NASA-CR-195125

IN-24-CR

204181

172P

E

RAL DESIGN CRITERIA FOR FILAMENT-WOUND
TE SHELLS

N
EN
S

4

PORT
tract: NAG-1-982

Manufacturing Technol
ond Building
lvania State University
Park, PA 16802

(NASA-CR-195125) STRUCTURAL DESIGN
CRITERIA FOR FILAMENT-WOUND
COMPOSITE SHELLS Final Report
(Pennsylvania State Univ.) 172 p

N94-24402

Unclas

G3/24 0204781

# TABLE OF CONTENTS

LIST OF FIGURES .......... iii

LIST OF TABLES .......... ix

SUMMARY .......... 1

1.0 INTRODUCTION .......... 3

2.0 FUNDAMENTALS OF FILAMENT WINDING .......... 7

- 2.1 Common Filament-Winding Materials .......... 8
- 2.2 Development of the Filament-Winding Pattern .......... 8
- 2.3 Curing Techniques .......... 14
- 2.4 Manufacturing Problems .......... 16

3.0 FLAT LAMINATES CONTAINING DEFECTS .......... 19

- 3.1 Experiments .......... 19
- 3.2 Analytical Models .......... 22

4.0 MANUFACTURE OF FILAMENT-WOUND CYLINDERS .......... 25

- 4.1 Materials Selection and Mandrel Design .......... 25
- 4.2 Determination of Optimal Manufacturing Procedures .......... 26
- 4.3 Manufacture of Cylinders for Compression Testing .......... 36
- 4.4 Conclusions .......... 49

5.0 MATERIAL AND GEOMETRIC CHARACTERIZATION .......... 53

- 5.1 Material Characterization .......... 53
- 5.2 Geometric Characterization .......... 57

6.0 COMPRESSIVE PERFORMANCE .......... 83

- 6.1 Test Equipment .......... 83
- 6.2 Experimental Procedures .......... 87
- 6.3 Data Reduction .......... 88
- 6.4 Results and Discussion .......... 90
- 6.5 Conclusions .......... 117

7.0 CLASSICAL BUCKLING AND STRENGTH ANALYSES .......... 119

- 7.1 Buckling Analysis .......... 119
- 7.2 Comparison of Buckling Analyses and Experimental Results .......... 130
- 7.3 Strength Analysis .......... 140
- 7.4 Design Criteria .......... 145

8.0 FINITE-ELEMENT ANALYSIS .......... 147

- 8.1 The Finite Element Model .......... 147
- 8.2 Effects of Material Modeling on Buckling Predictions .......... 151

8.3 Effects of Residual Thermal Strains on Buckling Predictions...... 154
9.0 CONCLUSIONS........ 157
10.0 RECOMMENDATIONS FOR FUTURE WORK........ 161
11.0 BIBLIOGRAPHY........ 163
11.1 Citations........ 163
11.2 Summary of Relevant Publications........ 166

# LIST OF FIGURES

Figure 2.1 Typical equipment layout used to produce filament-wound composite shells ........ 7

Figure 2.2 Common filament-winding patterns; a) hoop, and b) longitudinal ...... 9

Figure 2.3 The first stroke of a helical-winding pattern ........ 9

Figure 2.4 The first and second strokes of a helical-winding pattern with fiber crossovers circled ........ 9

Figure 2.5 Appearance of the mandrel at the beginning of the second pattern. In this case, the winding pattern consists of 2 circuits per pattern .......... 10

Figure 2.6 Complete helically-wound layer showing the regions which contain fiber undulations ........ 11

Figure 2.7 Fiber undulation geometry in a) woven and braided materials and b) filament-wound materials ........ 11

Figure 2.8 Mandrel coverage produced by each tow ........ 12

Figure 2.9 Length of the tow wound during one stroke ........ 13

Figure 2.10 Through-the-thickness view of the materials used for the shrink-tape curing technique ........ 15

Figure 2.11 Through-the-thickness view of the materials used for the vacuum-bag curing technique ........ 15

Figure 2.12 Moving melt front used to displace air and prevent voids during in-situ consolidation of thermoplastic filament winding........ 16

Figure 3.1 Flat laminate compression test fixture........ 21

Figure 3.2 Unit cell used to determine stiffness of fiber undulation regions ........ 22

Figure 3.3 Angular transformations involved in stiffness calculations of undulation regions........ 23

Figure 4.1 Schematic of the 57-mm diameter mandrel and endcaps designed by Fedro [13] ........ 26

Figure 4.2 Schematic of the 152-mm diameter mandrel and endcaps ........ 26

Figure 4.3 Original sensor-stand pulleys for winding dry fiber tows........ 27

Figure 4.4 Re-designed sensor stand a), and carriage pulleys b), for winding prepregged tows ........ 28

Figure 4.5 Infrared heater setup used for elevated-temperature winding........ 29

Figure 4.6 Circumferential cross-sectional view of Cylinder 072490 ................ 31

Figure 4.7 Circumferential cross-sectional view of Cylinder 073090 ................ 32

Figure 4.8 Circumferential cross-sectional view of Specimen 090190HS .......... 33

Figure 4.9 Circumferential cross-sectional view of Specimen 092390HS .......... 34

Figure 4.10 Circumferential cross-sectional view of Specimen 092690HS .......... 35

Figure 4.11 Circumferential cross-sectional view of Specimen 090190CC .......... 36

Figure 4.12 Circumferential cross-sectional view of Specimen 092390CC .......... 37

Figure 4.13 Circumferential cross-sectional view of Specimen 092690CC .......... 37

Figure 4.14 Circumferential cross-sectional view of Cylinder 062091. The microstructure shown here is typical of the cylinders manufactured for the In-Plane Crossover-Band Spacing experimental program ........... 40

Figure 4.15 Circumferential cross-sectional view of Cylinder 122990. The microstructure shown here is typical of all six-ply cylinders manufactured for the Cylinder Scale experimental program ............. 42

Figure 4.16 Circumferential cross-sectional view of Cylinder 010191 ................ 43

Figure 4.17 Circumferential cross-sectional view of Cylinder 012092. The microstructure shown here is typical of the cylinders manufactured for the Symmetry of the Laminated-Shell Regions experimental program .. 46

Figure 4.18 Circumferential cross-sectional view of Cylinder 012592. The microstructure shown here is typical of the cylinders manufactured for the Through-the-Thickness Crossover-Band Location experimental program ................................................................ 48

Figure 4.19 Crossover band configurations for cylinders manufactured for the Through-the-Thickness Crossover-Band Location experimental program ................................................................ 49

Figure 4.20 A map of the cylinder symmetry for the a) alternating, and b) wide/narrow, crossover-band configurations ............................. 50

Figure 4.21 Circumferential cross-sectional view of Cylinder 031392 ............... 51

Figure 5.1 Photomicrograph of Cylinder 062091 cut parallel to the winding direction in the neighborhood of a fiber-crossover band ................. 54

Figure 5.2 Experimental setup for measuring thicknesses of filament-wound cylinders ................................................................ 59

Figure 5.3 Typical displacement field of the filament-wound cylinder on the mandrel relative to a fixed reference position ............................. 60

Figure 5.4 Typical displacement field of the mandrel alone relative to a fixed reference position ........ 60

Figure 5.5 Position of the cylinder and mandrel surfaces measured for one stroke 61

Figure 5.6 Typical thickness field of the filament-wound cylinder ........ 61

Figure 5.7 Close-up of a filament-wound cylinder in the neighborhood of a twisted tow which demonstrates the sensitivity of the LVDT thickness-measurement technique ........ 62

Figure 5.8 Thickness distributions of a) a visually poor-quality cylinder (061991A) and b) a visually high-quality cylinder (070191B) ........ 63

Figure 5.9 First thickness field of Specimen 062191A measured to examine the consistency of the LVDT thickness-measurement technique ........ 64

Figure 5.10 Second thickness field of Specimen 062191A measured to examine the consistency of the LVDT thickness-measurement technique ........ 64

Figure 5.11 Third thickness field of Specimen 062191A measured to examine the consistency of the LVDT thickness-measurement technique ........ 65

Figure 5.12 Thickness field of Specimen 030992A which exhibits the non-intimate contact region ........ 66

Figure 5.13 A comparison of average thicknesses for the LVDT and micrometer thickness-measurement techniques ........ 68

Figure 5.14 A comparison of standard deviations for the LVDT and micrometer thickness-measurement techniques ........ 68

Figure 5.15 Algorithm for smoothing the thickness distributions. Each dot in the figure corresponds to a measured thickness location. The filled dots represent the point being smoothed ........ 69

Figure 5.16 Thickness field of Specimen 081291A a) before and b) after smoothing with the averaging technique ........ 70

Figure 5.17 Thickness field of Specimen 021192A a) before and b) after smoothing with the averaging technique ........ 71

Figure 5.18 Thickness field of Specimen 030592A a) before and b) after smoothing with the averaging technique ........ 72

Figure 5.19 Thickness field of Specimen 081291A smoothed with the truncation technique ........ 73

Figure 5.20 Thickness field of Specimen 021192A smoothed with the truncation technique ........ 73

Figure 5.21 Thickness field of Specimen 030592A smoothed with the truncation technique ........ 74

Figure 5.22 Filament-wound cylinder mounted in a lathe to be machined into compression specimens ........ 75

Figure 5.23 Schematic diagram of the equipment used to measure geometric imperfections of filament-wound cylinders ........ 76

Figure 5.24 Longitudinal distribution of a perfect cylinder aligned with the turntable axis, a perfect cylinder not on the spin axis, and typical data . 76

Figure 5.25 Geometric imperfections for the first scan of Specimen 062191B ........ 77

Figure 5.26 Geometric imperfections for the second scan of Specimen 062191B ... 78

Figure 5.27 Geometric imperfections for the third scan of Specimen 062191B ...... 78

Figure 5.28 Geometric imperfections of unidirectional-prepreg cylinders measured by Chryssanthopoulos, Giavotto, and Poggi [22] ........ 79

Figure 6.1 Equipment setup for compression testing ........ 84

Figure 6.2 End plates used to support the loaded ends of the filament-wound cylinders ........ 85

Figure 6.3 Typical buckled mode shape for [±30] cylinders ........ 88

Figure 6.4 Typical load/end-shortening displacement plot ........ 90

Figure 6.5 Typical buckling mode of [±30] filament-wound cylinders ........ 91

Figure 6.6 Buckled shape of Specimen 011692A ........ 92

Figure 6.7 Buckled mode shape and strain-gage locations for Specimen 062591B ........ 93

Figure 6.8 Axial compressive strains in Specimen 062591B ........ 93

Figure 6.9 Axial compressive strains in Specimens a) 063091A and b) 070191A . 95

Figure 6.10 Axial bending strains in Specimens a) 063091A and b) 070191A ....... 96

Figure 6.11 Buckling-load degradation with number of buckling cycles ........ 97

Figure 6.12 End-shortening displacement at buckling degradation with number of buckling cycles ........ 97

Figure 6.13 Stiffness degradation with number of buckling cycles ........ 98

Figure 6.14 Acoustic energy observed with Specimen 062191A ........ 98

Figure 6.15 Effect of circumferential crossover-band spacing on the buckling stress of 57-mm diameter [±30] filament-wound cylinders ........ 100

Figure 6.16 Axial compressive strains in Specimen 062391A ........ 101

Figure 6.17 Axial bending strains in Specimen 062391A .............................. 101

Figure 6.18 Buckled mode shape of Specimen 030692A; typical of the 152-mm diameter, [±30] specimens .................................................. 103

Figure 6.19 Acoustic energy of Specimen 030692B.................................... 103

Figure 6.20 Fracture pattern of Cylinder a) 121490 and b) 122990 .................. 106

Figure 6.21 Compressive fracture of Cylinder 010191................................ 107

Figure 6.22 Fractures of a) six and b) eighteen-ply specimens with helical layers on the outer surfaces of the cylinder....................................... 108

Figure 6.23 Fractures of a) six and b) eighteen-ply specimens manufactured with 0° layers on the inner an outer surfaces of the cylinder and ±60° layers in the interior ............................................................ 109

Figure 6.24 Transverse displacement of Specimen 012092A......................... 110

Figure 6.25 Non-linear load/end-shortening response of a typical specimen manufactured for the Through-the-Thickness Crossover-Band Location experimental program ............................................. 112

Figure 6.26 Typical fracture locations for the stacked crossover-band configuration ............................................................... 113

Figure 6.27 Typical fracture locations for the alternating crossover-band configuration ............................................................... 114

Figure 6.28 Typical fracture locations for the wide/narrow crossover-band configuration ............................................................... 114

Figure 7.1 Geometry and coordinate system for Cheng and Hou's [26] analysis.. 120

Figure 7.2 Comparison of sequential errors near a solution.......................... 123

Figure 7.3 Error of the relaxed boundary condition as a function of the axial load. A step size of 175 N/m was used to produce this figure................. 124

Figure 7.4 Buckled surface of [$\pm30/90_2/\pm30$] cylinder for a step size of 1750 N/m using Donnell's theory................................................ 125

Figure 7.5 Buckled surface of [$\pm30/90_2/\pm30$] cylinder for a step size of 875 N/m using Donnell's theory.................................................... 125

Figure 7.6 Buckled surface of [$\pm30/90_2/\pm30$] cylinder for a step size of 175 N/m using Donnell's theory.................................................... 126

Figure 7.7 Buckled surface of [$\pm30/90_2/\pm30$] cylinder for a step size of 17.5 N/m using Donnell's theory.................................................... 126

Figure 7.8 Buckled surface of [±30/$90_2$/±30] cylinder for a step size of 1750 N/m using Flügge's theory ........ 128

Figure 7.9 Buckled surface of [±30/$90_2$/±30] cylinder for a step size of 875 N/m using Flügge's theory ........ 128

Figure 7.10 Buckled surface of [±30/$90_2$/±30] cylinder for a step size of 175 N/m using Flügge's theory ........ 129

Figure 7.11 Buckled surface of [±30/$90_2$/±30] cylinder for a step size of 17.5 N/m using Flügge's theory ........ 129

Figure 7.12 Torsional buckling mode shape typical for 57-mm diameter, [±30] cylinders ........ 133

Figure 7.13 Accuracy of the In-Plane Crossover-Band Spacing specimens as a function of the normalized crossover-band spacing using Flügge's theory ........ 133

Figure 7.14 Checkerboard buckled shape observed for Specimen 010891 using Donnell's and Flügge's theories ........ 136

Figure 7.15 Buckled mode shape of Specimen 012592B computed with Flügge's theory: surface plot ........ 138

Figure 7.16 Buckled mode shape of Specimen 012592B computed with Flügge's theory: contour plot ........ 138

Figure 7.17 Accuracy of the Through-the-Thickness Crossover-Band Location specimens as a function of the minimum crossover-band spacing....... 139

Figure 7.18 Accuracy of the buckling-load predictions as a function of the geometric imperfection amplitude using Flügge's theory ........ 146

Figure 8.1 Convergence of the buckling load ........ 148

Figure 8.2 Model and mode shape with mesh level 3 ........ 149

Figure 8.3 Model and mode shape with mesh level 4 ........ 149

Figure 8.4 Model and mode shape with mesh level 5 ........ 150

Figure 8.5 Model and mode shape with mesh level 6 ........ 150

Figure 8.6 Model and mode shape with mesh level 7 ........ 151

Figure 8.7 Buckling mode shape for Material Set 1 ........ 153

Figure 8.8 Buckling mode shape for Material Set 3 ........ 153

Figure 8.9 Thermally deformed shape of the cylinder ........ 154

Figure 8.10 Buckling mode shape of thermally deformed cylinder ........ 155

## LIST OF TABLES

Table 3.1 Material properties of Amoco T650-35/1902 .......... 20

Table 4.1 Winding and curing parameters for cylinders manufactured for the Manufacturing Optimization study .......... 30

Table 4.2 Winding and curing parameters for cylinders manufactured for the In-Plane Crossover-Band Spacing experimental program .......... 39

Table 4.3 Winding and curing parameters for cylinders manufactured for the Cylinder Scale experimental program .......... 41

Table 4.4 Manufacturing parameters used to produce compression specimens for the Symmetry of the Laminated-Shell Regions experimental program .. 45

Table 4.5 Manufacturing parameters used to produce compression specimens for the Through-the-Thickness Crossover-Band Location experimental program .......... 47

Table 4.6 Summary of results for the manufacture of filament-wound cylinders .. 52

Table 5.1 Fiber volume fractions of selected filament-wound cylinders obtained by acid digestion .......... 55

Table 5.2 Void contents of selected filament-wound cylinders obtained by image analysis of the photomicrographs .......... 56

Table 5.3 Thicknesses and lengths of compression specimens measured by hand .......... 58

Table 5.4 Results of the thickness consistency study .......... 65

Table 5.5 Thickness parameters measured with the LVDT technique of cylinders manufactured for compression testing .......... 67

Table 5.6 Geometric parameters obtained for the consistency study .......... 79

Table 5.7 Geometric parameters for cylinders manufactured for compression testing .......... 80

Table 6.1 Data acquisition parameters used with the Locan-AT acoustic emission test equipment .......... 86

Table 6.2 Compression results for the In-Plane Crossover-Band Spacing experimental program .......... 99

Table 6.3 Compression results for the Mandrel Material experimental program ... 102

Table 6.4 Compression results for the Cylinder Scale experimental program ...... 104

Table 6.5 Compression results for the Symmetry of the Laminated-Shell Regions experimental program .......... 111

Table 6.6 Compression results for the Winding Sequence experimental program 111

Table 6.8 Compression results for the Through-the-Thickness Crossover-Band Location experimental program ........................................... 115

Table 6.9 Compression results for the Heated Winding experimental program.... 116

Table 7.1 Material constants used for the classical laminated-shell buckling analyses. The subscripts 1 and 2 refer to the fiber and transverse directions in the material respectively ...................................... 123

Table 7.2 Results of buckling force calculations computed to examine the step-size convergence of the computer program DON........................... 124

Table 7.3 Results of buckling force calculations for the examination of step-size convergence for computer program FLUGGE........................... 127

Table 7.4 Material properties and cylinder geometry reported in Tasi, Feldman, and Stang [7] used for model verification. The subscripts 1 and 2 refer to the fiber and transverse directions in the material respectively.. 130

Table 7.5 Results of buckling load calculations for the In-Plane Crossover-Band Spacing experimental program............................................. 132

Table 7.6 Results of buckling load calculations for the Mandrel Material experimental program..................................................... 134

Table 7.7 Results of buckling load calculations for the Cylinder Scale experimental program..................................................... 134

Table 7.8 Results of buckling load calculations for the Symmetry of the Laminated-Shell Regions experimental program......................... 135

Table 7.9 Results of buckling load calculations for the Winding Sequence experimental program..................................................... 136

Table 7.10 Results of buckling load calculations for the Through-the-Thickness Crossover-Band Location experimental program.......................... 137

Table 7.11 Results of buckling load calculations for the Heated Winding experimental program..................................................... 140

Table 7.12 Material constants used for the strength analysis .......................... 140

Table 7.13 Results of compressive strength calculations for the In-Plane Crossover-Band Spacing experimental program......................... 141

Table 7.14 Results of compressive strength calculations for the Mandrel Material experimental program..................................................... 142

Table 7.15 Results of compressive strength calculations for the Cylinder Scale experimental program..................................................... 143

Table 7.16 Results of compressive strength calculations for the Symmetry of the Laminated-Shell Regions experimental program .......... 143

Table 7.17 Results of compressive strength calculations for the Winding Sequence experimental program .......... 144

Table 7.18 Results of compressive strength calculations for the Through-the-Thickness Crossover-Band Location experimental program .......... 144

Table 7.19 Results of compressive strength calculations for the Heated Winding experimental program .......... 145

Table 8.1 Details of models used in Mesh Convergence Study .......... 148

Table 8.2 Material constitutive property sets for the FEM model .......... 151

Table 8.3 Stiffness of laminate and undulation regions .......... 152

Table 8.4 Buckling loads for different material properties .......... 152

# SUMMARY

Advanced composite cylinders, manufactured by filament winding, provide a cost-effective solution to many present structural applications; however, the compressive performance of filament-wound cylinders is lower than comparable shells fabricated from unidirectional tape. The objective of this study was to determine the cause of this reduction in thin filament-wound cylinders by relating the manufacturing procedures to the quality of the cylinder and to its compressive performance. The experiments on cylinder buckling were complimented by eigenvalue buckling analysis using a detailed geometric model in a finite element analysis. The applicability of classical buckling analyses was also investigated as a design tool.

The manufacturing phase of this research was divided into two parts. First, various winding and curing procedures were examined to determine which combination resulted in cylinders with the best microstructural quality and most uniform surfaces. The best technique involved winding the prepreg tow at an elevated temperature and then curing the cylinder with the use of high-temperature shrink tape. The second part of the manufacturing investigation involved fabricating cylinders for compression testing. Due to the complexity of the heated-winding apparatus, these cylinders were wound at room temperature and cured with shrink tape. Seven different experiments were designed to determine the effects of crossover-band spacing, scale, winding sequence, mandrel material, symmetry of the laminated-shell regions, through-the-thickness crossover-band location, and winding temperature. Compression specimens were machined from these cylinders with a nominal length-to-radius ratio of 3 and radius-to-thickness ratios of 160, 86, 60, and 18.

To account for the sensitivity of the buckling load to initial imperfections in the material and geometry, each specimen was examined to quantify the imperfection level. Thickness distributions were measured at many points on the surface of each specimen and the average and standard deviation of the distributions were determined. The thickness imperfections observed in this study were caused by twisting and misalignments of the tow during winding. Geometric imperfections were measured after the end fixtures were attached to the specimens prior to compression testing. Most imperfections of this type are caused by thermal residual stresses and mechanical stresses induced during the attachment of the loading fixtures.

Specimens were loaded to failure while monitoring the end-shortening displacement, local strains, local transverse displacement, and acoustic emission. Single-layer specimens with radius-to-thickness ratios of 160 and 60 buckled in the characteristic diamond-shaped mode and exhibited a stable postbuckling response. Some damage was induced in the specimens by the prebuckling and buckling process. Little additional damage was induced in these specimens when they were buckled multiple times. Multi-layer cylinders with radius-to-thickness ratios of 60 fractured immediately after buckling with no postbuckling strength. Specimens with radius-to-thickness ratios of 18 failed in compression. Material imperfections, which arise due to the presence of fiber undulations in the helical and circumferential-crossover bands, reduce the buckling load most when the shape of the winding pattern and the buckling mode are similar. Improvements in performance were observed when cylinders were wound with symmetric laminated-shell regions and crossover-bands staggered through the thickness.

A quantification of the sensitivity of buckling performance to fiber undulations inherent in the filament-wound cylinders was attempted by performing experiments and developing models to predict the stiffness of fiber-undulation regions. The experiments consisted of testing coupons, containing fiber undulations and ply defects, in compression. The undulations were analytically modeled using two approaches namely modified classical

lamination theory (MCLT) and the finite element method (FEM). In the MCLT, the stiffness of the fiber tow was transformed through an angle representing the undulation at a point and the classical lamination theory was applied pointwise along the fiber undulation. The finite element analysis addressed through-the-thickness effects in a fiber undulation region.

The stiffness of the undulation regions obtained using the analytical model was used in a finite element analysis of an entire filament wound cylinder. The fiber undulation regions were also included in the global model. The effect of using progressively complicated levels of material distribution on the accuracy of the buckling prediction was studied. Also, the importance of incorporating thermal deformation in determining the buckling response was investigated. The buckling load predicted by FEM was within 5 percent of the experimentally observed value.

Flügge's and Donnell's thin-shell theories were used to compute the critical buckling loads and modes of laminated, geometrically-perfect cylinders loaded in axial compression with clamped ends. When the results of this analysis were compared to the experiments, load reductions between 10 and 60 percent were observed due to the presence of material and geometric imperfections and non-membrane prebuckling effects. The Tsai-Wu failure criterion was able to correctly identify the failure mode of filament-wound cylinders and can be used to estimate the amount of damage induced during buckling.

# 1.0 INTRODUCTION

A current trend in high performance structures is to replace traditional unreinforced metals with advanced composite materials. The high specific stiffness and strength, excellent fatigue resistance, and mechanical integrity within many hostile environments often offsets the additional raw material and manufacturing costs of these materials thus making them viable alternatives. With the rapid rise in the use of advanced composites, has been a need to validate and improve the theoretical and analytical models for these materials. Anisotropic plate and shell theories have been developed and verified to a limited extent for unidirectional fiber laminates; however, composites manufactured with complex fiber geometries have not been studied extensively. Knowledge of higher-order behavior, such as non-linear dynamic response, large strain behavior, and buckling, is particularly limited for these materials.

The compressive buckling of structures fabricated from isotropic homogeneous materials has been studied extensively, as indicated by Singer [1]. Excellent models exist to predict the response of shells including prebuckling deformations, buckling loads, buckling modes, and postbuckling deformations provided sufficient documentation of the boundary conditions, material properties, and initial geometry of the shell are known. Additional complexities, such as stiffeners, cutouts, scale, and non-linear material behavior have also been examined and as such, the behavior of isotropic shells is generally assumed to be well understood.

Early investigations of the stability of advanced composite shells benefited greatly from the knowledge of isotropic shell behavior. Many of the complexities associated with buckling analyses and experimentation of isotropic shells have been investigated for cylinders laminated from unidirectional reinforcements according to Tennyson [2]. These include large displacement theories, plasticity, experimental determination of boundary conditions, and imperfections in the initial shape of the cylinder. Several important issues have also been identified that are unique to anisotropic shells such as, the importance of shear deformation in relatively thin shells, prebuckling deformations caused by material coupling, and the increased likelihood of material inhomogeneities.

Composite cylinders manufactured from unidirectional tape have been studied extensively by Tennyson and Muggeridge [3] and Booton and Tennyson [4] who have carefully documented the initial geometric imperfections of their compression specimens. Non-membrane type prebuckling displacements and statistical representations of the measured initial geometric imperfections are included in their analysis which resulted in a 15 percent improvement in the prediction of the compressive buckling load compared to analyses without these effects. Throughout these studies, the material is assumed to be free of imperfections such as voids, thickness variations, and curved fibers. Material imperfections are introduced experimentally by Abu-Farsakh and Lusher [5] who studied the response of cylinders fabricated from woven fabrics. The curved fibers resulting from the weaving process were not included in their analysis or discussion of the compressive behavior.

One of the most common techniques used to manufacture axisymmetric composite shells is filament winding. Filament winding is a readily automatable method which is commonly used to fabricate tubes, cylinders, pressure bottles, and rocket motor cases. Although this technique is attractive because of its cost effectiveness, shells which are filament wound contain complex fiber geometries in regions where the material is interwoven during winding. Card [6], Tasi, Feldman, and Stang [7], and Boresi, Langhaar, and Miller [8] use filament-wound cylinders to investigate the accuracy of several anisotropic shell theories with limited success. The discrepancies between the experimentally and theoretically determined buckling loads are attributed to initial imperfections; however, little investigation is reported to verify this claim.

The effect of material imperfections on the effective stiffness properties, which arise due to the interweaving of layers during filament winding, is reported by Brito [9]. Specimens with different amounts of interweaving were loaded in tension, by internal pressurization, and in torsion to determine the effective elastic constants. Results from these tests indicate an improvement in the longitudinal, transverse, and shear stiffnesses, and burst strength as the amount of interweaving increases. An increase in the fiber volume content with the amount of interweaving is also reported and could account for these improvements in performance.

One of the most difficult analytical problems encountered with composite materials is predicting failure response. Imperfections such as voids and delaminations, which initiate failure, complicate geometrical modeling. Fiber undulations, which are inherent in filament-wound structures, provide additional complications in attempts to characterize the structural behavior. Therefore, one of the important aspects of the present study was the characterization of the structural response of fiber undulations under compressive loads.

The structural response of a fiber undulation was characterized by both experimentally and analytically. In the experiments, specimens with simulated large-scale undulations as well as those with filament-wound undulations were studied. Three modeling techniques were used to gain more insight into the experimental results. The first was the classical lamination plate theory, based on the laminate lay-ups. The second was a modified classical lamination theory, based on the localized geometry of the undulation region. The third method was finite element modeling, based on the particular specimen geometry.

Micromechanical models of the regions containing interwoven fibers were examined by Hipp and Jensen [10], Jensen and Pai [11], and Jensen and Pickenheim [12]. Hipp and Jensen [10] and Jensen and Pickenheim [12] used three-dimensional finite elements to predict the elastic material properties of these regions. Hipp and Jensen [10] also used a modification of classical lamination theory developed for woven fabrics to estimate the effective extensional, coupling, and bending stiffness matrices for these regions. Jensen and Pai [11] reduced the three-dimensional constitutive relationships to two dimensions to predict the effective in-plane material response. The effective elastic material properties were used as material imperfections in finite-element stability analyses of filament-wound cylinders. Both Hipp and Jensen [10] and Jensen and Pai [11] reported reduced buckling loads due to the presence of these imperfections.

The objective of this study was to determine the relationships between manufacturing procedures, quality, and performance of thin filament-wound cylinders subjected to axial compressive buckling to establish guidelines for aiding the development of design criteria for thin filament-wound cylinders. The approach taken was to systematically vary the winding and curing parameters to investigate how they can be altered to improve the quality and compressive performance. To determine the effectiveness of the winding and curing techniques, each manufactured cylinder was examined to determine the quality of the cured structure. Cylinder quality was examined at the microscopic level to determine the presence of voids and fiber misalignments, and at the macroscopic level to determine the level of initial shape and thickness imperfections. The structural response was then evaluated by loading each specimen to failure. During testing, the applied load, end-shortening displacement, local strains and displacements, and acoustic emission were monitored. Finally, the compressive strength, buckling load, and mode shape were computed using linear buckling analyses and classical lamination theory, neglecting the influence of material imperfections, to investigate the applicability of these analytical techniques.

The buckling response was also investigated using the finite element method. The effects of material discontinuity, stiffness coupling in the fiber undulation regions, and the effect of thermal deformation on the buckling of the cylinders were studied.

The remainder of this document contains a detailed description of the work performed. Chapter 2 contains a discussion of how filament-wound cylinders are manufactured and the important winding parameters. The influence of curved fibers and other artificial defects on the compressive performance of flat laminates is described in Chapter 3. A detailed discussion of the winding and curing procedures which were used to fabricate cylinders for this study are presented in Chapter 4. The qualitative and quantitative quality assessment of each cylinder is discussed in Chapter 5. Chapter 6 contains a description of the equipment and testing procedures to measure the compressive performance and a discussion of the experimental results; especially, how the compression results relate to the quality and manufacturing procedures. Classical predictions of the compressive buckling behavior and strength are discussed in Chapter 7. Computation of the buckling load, using the finite-element method, is discussed in Chapter 8. Finally, Chapters 9 and 10 contain the conclusions and recommendations for future work, respectively.

## 2.0 FUNDAMENTALS OF FILAMENT WINDING

The most economical way to incorporate composite materials into large structures is to use automated production techniques. Filament winding is one such technique. Large quantities of raw materials can be quickly and accurately wound onto a mandrel with the use of a computer-controlled filament-winding system. The major components of a filament-winding system include the tensioner, filament winder, and mandrel, as shown schematically in Figure 2.1. The tensioner and sensor stand are used to apply a uniform tension to the material during winding. The mandrel acts as the take-up mechanism; while the carriage and payout eye on the filament winder move in unison to wind the fibers in the desired orientation. A computer is often used to create and store complex winding patterns and to control the motions of the filament winder.

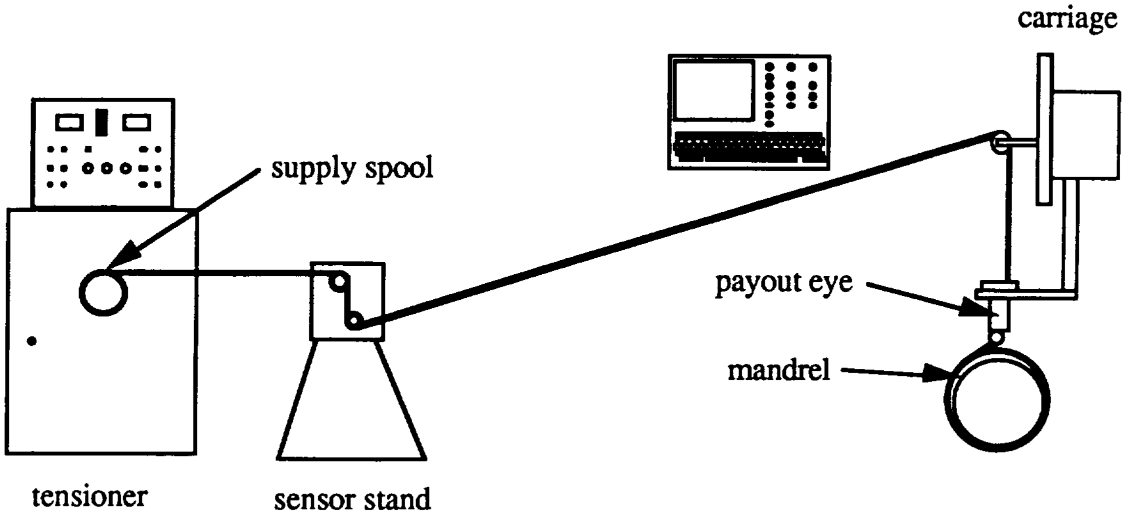

Figure 2.1: Typical equipment layout used to produce filament-wound composite shells.

The mandrel dictates the internal geometry of the structure acting as a form, much like a mold in casting procedures. The external shape of the structure is determined by the materials wound on the mandrel and additional materials such as cores for sandwich structures. Mandrels can be made from many different materials such as metal, plastic, composite, wood, foam, and elastomeric compounds. The major requirements of the mandrel material are stiffness, thermal stability, and the ability to create a smooth surface. A stiff material is required since fiber tension and the weight of the mandrel induce stresses which may cause unwanted deformations. A thermally stable material is required if a high processing temperature is used or if the matrix exhibits a large exotherm during cure since the mandrel typically remains in place during all phases of manufacture. A smooth, non-porous surface is needed to prevent physical bonding between the composite and mandrel. In addition to the material requirements, the mandrel must also be convex. Concave winding is not generally possible since the tensioned fibers will simply bridge the section rather than conforming to the desired shape.

## 2.1 Common Filament-Winding Materials

Almost any advanced composite material system can be filament wound. The most common of these materials include either continuous strands of glass, graphite, silicon carbide, or polymer fibers and either thermosetting or thermoplastic polymer matrices. Boron and some ceramic fibers are not used extensively due to their large minimum bend radii. Metal and ceramic matrix composites are also not typically filament wound due to the difficulty of mixing the fibers and matrices and the extreme processing conditions.

The two most common methods of filament winding with thermosetting polymer matrices are wet and dry winding. Wet filament winding refers to the process where dry fibers are impregnated during winding between the tensioner and the filament winder. The resin and hardener are first mixed and placed in a temperature controlled impregnator. As the fibers pass through the impregnator, they are coated with resin either by traveling over a drum coated with resin or by being immersed in the resin and then passed through a metering die. Although wet winding is often messy, it is usually the most economical method since the fibers and matrix are combined on-line. Dry filament winding uses fibers which have been mixed with resin prior to winding. Fibers which have been impregnated with resin and then partially cured to a "B-stage" are called prepregged tows if only one yarn of fibers is used. Prepregged tapes, two or more tows placed side by side, are often used to wind large parts. This technique is cleaner than wet winding since no liquid resins are used; however, it is more expensive since a separate manufacturing step is required and the prepregged materials must be stored at low temperatures. After winding, the structure is generally cured in a separate step to complete the consolidation and cure processes.

Thermoplastic matrix materials are also filament wound with similar techniques. Solutions of polymer and a suitable solvent can be used to impregnate dry strands of fibers while winding. This technique is not often used since hazardous solvents and/or complex solvent recovery systems must be used. Prepregged tows and tapes with thermoplastic matrices are the most common material form which are filament wound. One thermoplastic material form which does not have a thermoset counterpart is commingled yarns. The polymer is first spun into small diameter fibers and then mixed with the reinforcing fibers. The commingled bundle of fibers is then wound as if it was a prepreg tape.

## 2.2 Development of the Filament-Winding Pattern

Three winding paths are commonly used in filament winding. A hoop-winding pattern is obtained by winding on a very shallow helix where each tow is placed adjacent to the previously wound tow. Consequently, the mandrel is covered with one layer of material during one stroke; a stroke is the motion of the filament winder from one end of the mandrel to the other. The fiber angle within a hoop layer depends on the diameter of the mandrel and the width of the material being wound, ie. the bandwidth, according to the following relationship,

$$\alpha = \cos^{-1} \frac{b_w}{2\pi R} \tag{2.1}$$

where, $\alpha$ represents the hoop-winding angle, the radius of the mandrel is represented by $R$, and $b_w$ represents the bandwidth of the material being wound. A longitudinal pattern results from winding fiber tows parallel to the longitudinal axis of the mandrel. Figure 2.2 contains plan-view schematics of these winding patterns on cylindrical mandrels.

The helical-winding pattern develops when the tow is wound at a moderate angle to the longitudinal axis. When winding a helical layer, the tow begins at the left hand end of the mandrel and is wound at a constant angle to the right end of the mandrel, as shown in

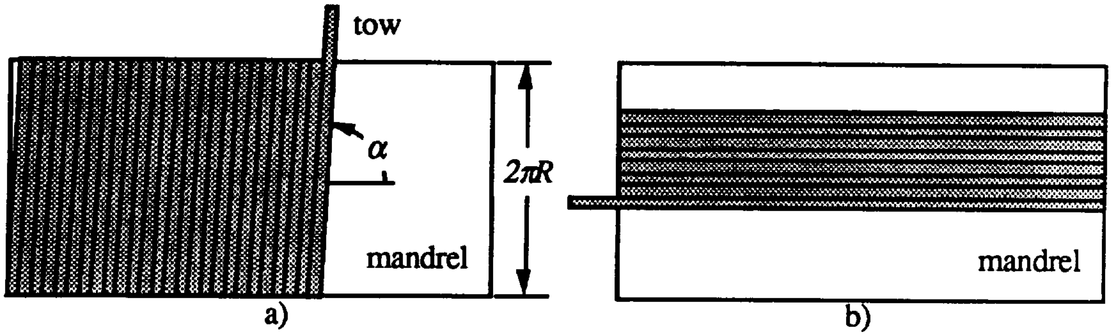

Figure 2.2: Common filament-winding patterns; a) hoop, and b) longitudinal.

Figure 2.3 in plan view. During the first stroke, the entire tow is wound against the mandrel or the layer immediately below the current layer. After reaching the right end, the transverse motion of the payout eye is halted while the mandrel continues to rotate. The angle of rotation is called the dwell angle. This rotation is necessary to allow the tow to change direction. Next, the tow is wound toward the left end of the mandrel (the second stroke) at the same angle and rotates through the dwell angle again, as shown in Figure 2.4. Since the first stroke has placed some material on the mandrel, the second stroke will cross over the first stroke in several locations. The combination of two dwell rotations, a left-to-right stroke, and a right-to-left stroke, is called a circuit.

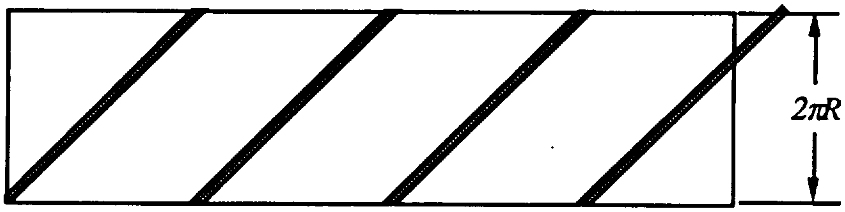

Figure 2.3: The first stroke of a helical-winding pattern.

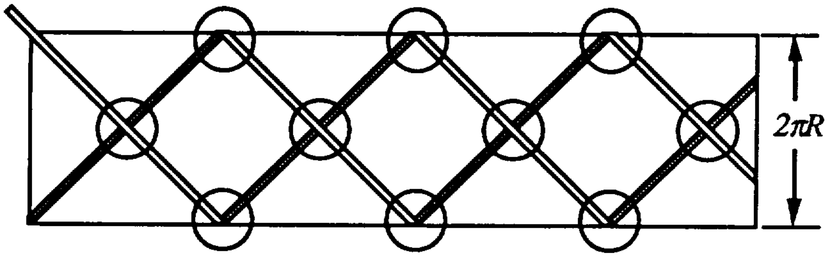

Figure 2.4: The first and second strokes of a helical-winding pattern with fiber crossovers circled.

At the end of the first circuit, the tow is typically not in the neighborhood of the starting position of the first stroke. Consequently, when the second circuit is wound, it will not be placed next to the first circuit. The filament winder will continue to wind circuits until the spacing between all tows is uniform; this collection of circuits is called a pattern. After winding one pattern, the tow will be adjacent to the starting position of the first stroke. The filament winder will then place the first stroke of the second pattern next to the first stroke of the first pattern, as shown in Figure 2.5. Patterns will continue to be wound until the surface of the mandrel is uniformly covered.

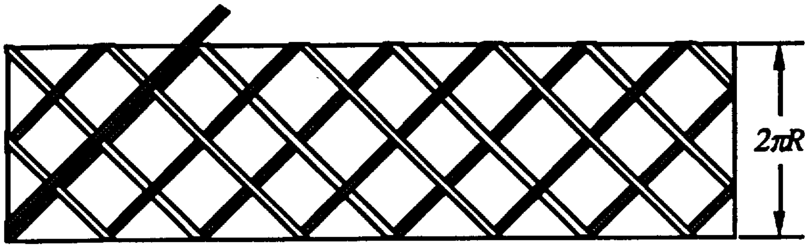

Figure 2.5: Appearance of the mandrel at the beginning of the second pattern. In this case, the winding pattern consists of 2 circuits per pattern.

During the second stroke, and on each subsequent stroke except the last one, the tow will alternately be wound against the mandrel and on top of previously wound material. As the tow either crosses from the mandrel to wound material or vice versa, the fibers must bend to accommodate the change in thickness. These transition regions are shown schematically in Figure 2.6 where the tows change color. Since any helically-wound layer contains these regions, they are classified as intrinsic material imperfections. Intrinsic imperfections are defined as those anomalies which cannot be removed from the structure or material by changing the winding and/or curing procedures. As suggested by research with fabric and wavy layer composites, the presence of these undulations may affect the structural response of the shell, since these regions have different effective material properties than the surrounding material and act as pre-microbuckled regions. Layers wound with circumferential and longitudinal-winding patterns do not contain intrinsic material imperfections.

Undulations in filament-wound materials have a different geometry than those produced in woven and braided materials. In these textile forms, the fibers which bend out-of-plane start on one side of the layer, traverse to the other side and back in a very short distance, as shown in Figure 2.7a. In filament-wound materials, the fibers within the undulation traverse from one side to the other and then stay on that side for an appreciable distance, as shown in Figure 2.7b. This distance varies from one bandwidth to many times the bandwidth depending on the position of the tow within the winding pattern.

In helically-wound layers, fiber undulations are grouped into two regions. One region forms a band of undulations along a helical path around the cylinder parallel to the winding angle. This region is called the helical-crossover band and the undulations are aligned next to one another, as shown in Figure 2.6. The other band of undulations is oriented in the circumferential direction and is called the circumferential-crossover band. Undulations in this band zig-zag as they progress around the cylinder. The combination of the helical and circumferential-crossover bands form the diamond-shaped repeating pattern characteristic of filament-wound materials, where the circumferential-crossover bands divide the pattern into equal triangular regions, and the helical-crossover bands form the edges of the region. The regions between the crossover bands consist of unidirectional fibers which are laminated in a $+\beta/-\beta$ orientation in half of the triangles and a $-\beta/+\beta$ orientation in the other half. Since the crossover bands contain a material which behaves differently than the surrounding laminated-shell regions, their location may be important to the mechanical response of the structure.

Three winding parameters are generally considered to be inflexible when specifying most winding patterns: the diameter of the mandrel (or the layer to be wound), the length

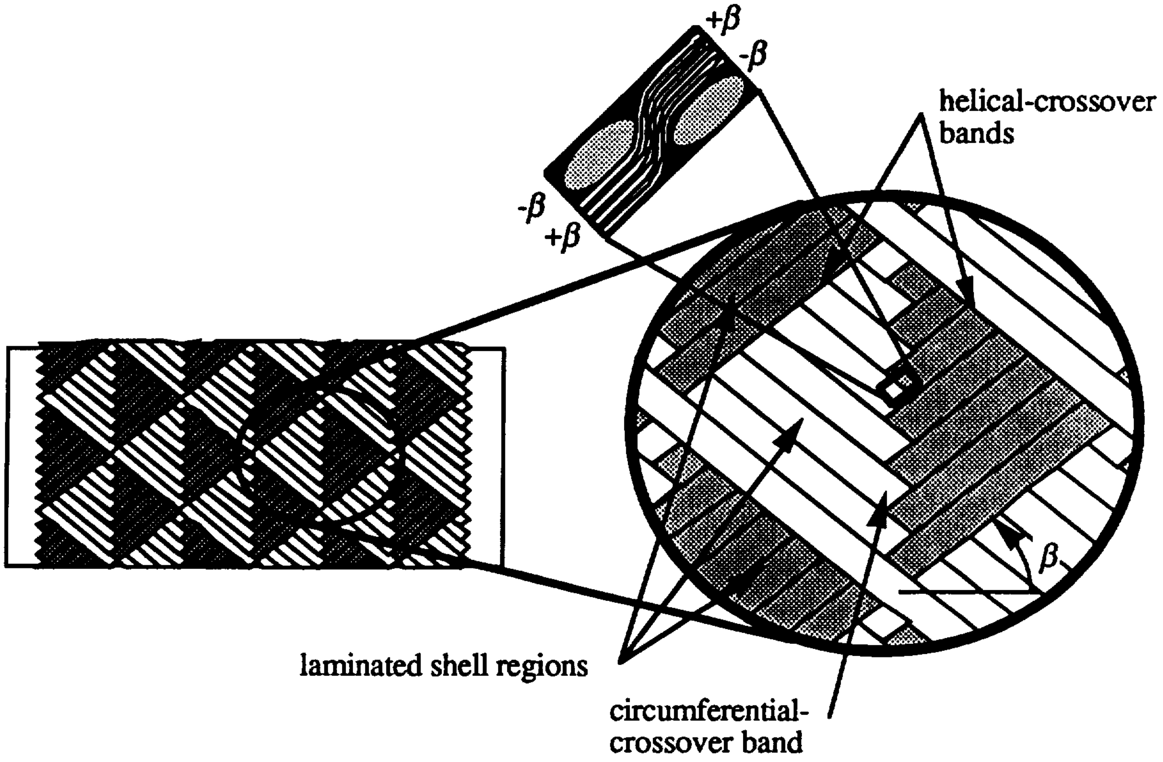

+β
-β
-β
+β
helical-crossover bands
laminated shell regions
circumferential-crossover band
β

Figure 2.6: Complete helically-wound layer showing the regions which contain fiber undulations.

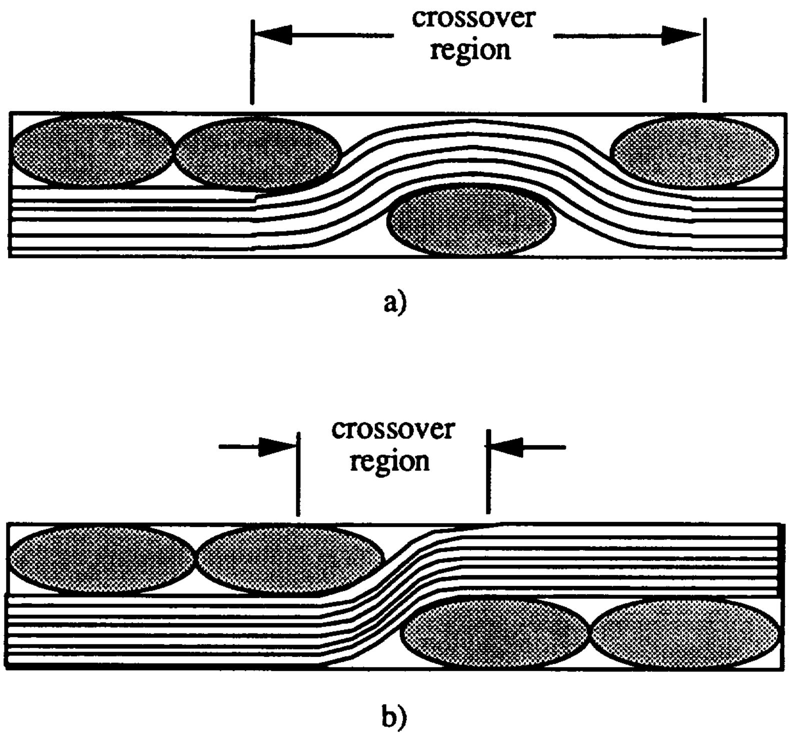

crossover region
a)
crossover region
b)

Figure 2.7: Fiber undulation geometry in a) woven and braided materials and b) filament-wound materials.

of the cylinder, and the winding angle. Two other winding parameters must also be specified before the winding pattern can be considered unique: the bandwidth and the dwell angle. The final choice of the winding parameters must satisfy the constraint of uniform coverage. The remainder of this section contains a discussion of how the winding parameters are chosen for a circular cylinder. More complex geometries would necessitate a more general set of equations.

To determine the number of circuits needed to cover the mandrel twice (once at $+\beta$ and once at $-\beta$), the bandwidth must first be determined. Winding with a bandwidth which is too large will yield gaps in the layer coverage and may trap air, producing voids in the cured material. Conversely, too much overlap will produce a thicker part with a nonuniform thickness due to the overlapping material. The amount of mandrel coverage in the circumferential direction which each tow makes during winding, $s_y$, is shown in Figure 2.8. This distance can be related to the winding angle, $\beta$, and the bandwidth, $b_w$, as follows,

$$s_y = \frac{b_w}{\cos\beta} \tag{2.2}$$

The ratio of mandrel circumference to the distance $s_y$ is equivalent to the number of circuits per coverage, $N_c$, and can be written as follows,

$$N_c = \frac{2\pi R\cos\beta}{b_w} \tag{2.3}$$

By definition, $N_c$ must be an integer, consequently, the expression above must be solved iteratively for $N_c$ by adjusting the bandwidth. The logical starting point for this iteration is to use the actual width of the material being wound since the curing conditions will tend to fill in minor gaps and smooth the thickness. Typically, only small deviations from the actual width of the tow are needed to satisfy Equation 2.3.

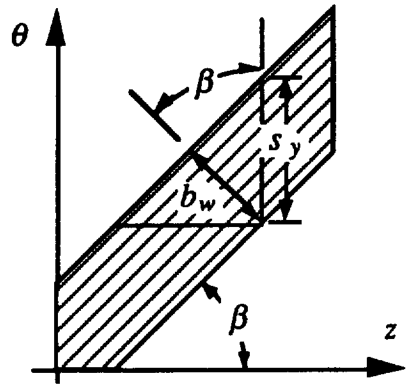

Figure 2.8: Mandrel coverage produced by each tow.

The start and stop positions of the carriage on the filament winder are specified by the size of the mandrel. The distance the mandrel rotates during one stroke, $s_{stroke}$, shown in Figure 2.9, can be computed with the following equation,

$$s_{stroke} = L_w \tan\beta \tag{2.4}$$

where, $L_w$ is the length of the mandrel being wound. Since $s_{stroke}$ is actually a distance around the circumference of the mandrel, the angle of rotation during one stroke, $\theta_{stroke}$, is given by the following expression in degrees,

$$\theta_{stroke} = \frac{180 L_w \tan\beta}{\pi R} \tag{2.5}$$

One circuit is composed of two strokes and two dwells; thus, the total angle of rotation for one circuit, $\theta_{cir}$, is related to the other winding parameters as follows:

$$\theta_{cir} = 2\left[\frac{180 L_w \tan\beta}{\pi R} + \theta_{dwell}\right] \tag{2.6}$$

where, $\theta_{dwell}$ represents the dwell angle in degrees.

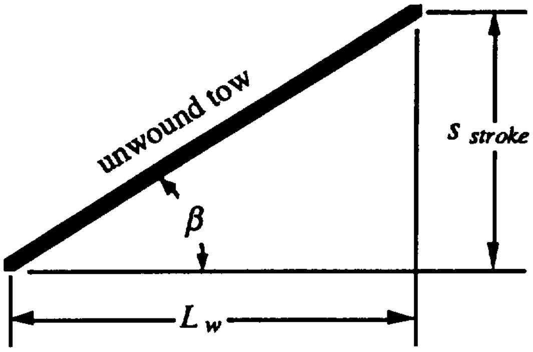

Figure 2.9: Length of the tow wound during one stroke.

The circumferential distance which the tow moves during the dwell, $s_{dwell}$, is,

$$s_{dwell} = R\theta_{dwell}\frac{\pi}{180} \tag{2.7}$$

The circumferential distance between the beginning of two sequential circuits is designated $s_f$, and the corresponding angle in degrees is $\theta_f$, where,

$$s_f = R\theta_f\frac{\pi}{180} \tag{2.8}$$

This angle can be computed from $\theta_{cir}$ as follows,

$$\theta_f = \theta_{cir} - Int\left(\frac{\theta_{cir}}{360}\right)360 \tag{2.9}$$

where *Int(x)* means the integer portion of the argument *(x)*. Since the position of the tow at the beginning and end of winding the layer is the same, the distance between two sequential circuits, multiplied by the number of circuits per pattern, $N_p$, must be an integer number of revolutions, as follows,

$$N_p\theta_f = 360m + \frac{360}{N_c} \tag{2.10}$$

where, $m$ represents an undetermined integer. Typically, $N_c$ is known from Equation 2.3, so $m$ can be determined from the following expression by substituting Equations 2.6 and 2.9 into Equation 2.10,

$$N_p\left[\frac{L_w \tan\beta}{\pi R} + \frac{\theta_{dwell}}{180} - Int\left(\frac{L_w \tan\beta}{\pi R} + \frac{\theta_{dwell}}{180}\right)\right] = m + \frac{1}{N_c} \tag{2.11}$$

At this point an iteration must be performed to solve this equation for $\theta_{dwell}$, $N_p$, and $m$. Notice, several solutions can be obtained for different values of these parameters. Bounds on the iteration are often determined by the dwell angle. If the dwell angle is too small, the fibers will slip on the mandrel; if the angle is large, excessive material waste will occur.

The circumferential-crossover band spacing, $w$, can be related to the radius, winding angle, and the number of circuits per pattern, as follows,

$$w = \frac{\pi R}{N_p \tan\beta} \tag{2.12}$$

Using $w$, the number of diamonds around the cylinder and other specific details about the winding pattern can be determined with simple trigonometric relations.

The bandwidth, number of circuits per coverage, dwell angle, and rotation per stroke computed by other methods may differ from the present discussion. These differences can be attributed to the need for the filament-winding machine to accelerate and decelerate at the end of each stroke which was not accounted for in the present analysis. If the acceleration is instantaneous, the analyses will yield the same winding parameters.

One method which can be used to evaluate different winding patterns is based on the crossover-band spacing. Another technique is to compare the amount of waste. To wind a cylinder of length $L_w$, the length of tow used to wind the cylindrical section, $w_{L_w}$ , is,

$$w_{L_w} = \frac{2N_c L_w}{\cos\beta} \tag{2.13}$$

and,

$$\hat{w}_{L_w} = \frac{2N_c}{\cos\beta} = \frac{w_{L_w}}{L_w} \tag{2.14}$$

is the length of tow per unit length of the mandrel. If the dwell is assumed to occur on the cylindrical surface of the mandrel, the length of material wound during one dwell rotation, $w_{L_d}$, can be estimated as follows,

$$w_{L_d} = \frac{\pi R \theta_{dwell}}{180} \tag{2.15}$$

Since there are two dwells during each circuit, the material wound during all dwell rotations, $w_{dwell}$, is computed as follows,

$$w_{dwell} = 2 w_{L_d} N_c = \frac{\pi R N_c \theta_{dwell}}{90} \tag{2.16}$$

Typically the material wound during the dwell rotation is not used as part of the final structure since fibers in this region are not oriented in the desired direction. If a length $L_l$ is trimmed from the left end of the cylinder, and $L_r$ from the right end, the amount of waste can be written as,

$$w_{total} = 2N_c \left\{ \frac{L_l + L_r}{\cos\beta} + \frac{\pi R \theta_{dwell}}{180} \right\} \tag{2.17}$$

Finally, using the areal weight of the tow, the mass of the wasted material can be determined.

## 2.3 Curing Techniques

Many techniques can be used to consolidate and/or cure the composite material into the final structure. The choice of which technique is most applicable depends on the type of matrix material, the desired quality of the finished material and structure, and cost. A discussion of the most common curing techniques is logically divided by which type of matrix is being considered: thermoset or thermoplastic.

Structures which use a room or low temperature thermosetting resin are typically cured by slowly rotating them on the filament winder or within an oven. The rotation prevents non-uniform resin flow around the structure which could cause sag marks, runs, and thickness changes. The cured material is typically resin rich and can contain a large void content since the only source of compaction pressure, which causes resin flow and void-size reduction, arises from the winding tension.

Further improvements in the quality of the structure can be achieved if external pressure is applied during cure. An external pressure will help to consolidate the laminate, remove voids by squeezing them to the surface, and reduce the size of trapped voids. External pressure will also increase the radial pressures which cause resin flow and may increase the likelihood of layer wrinkling. If the pressure is applied by the use of high-temperature shrink tape, the likelihood of layer waviness can be increased by allowing the resin to flow from the composite through gaps in the shrink tape, as shown in Figure 2.10.

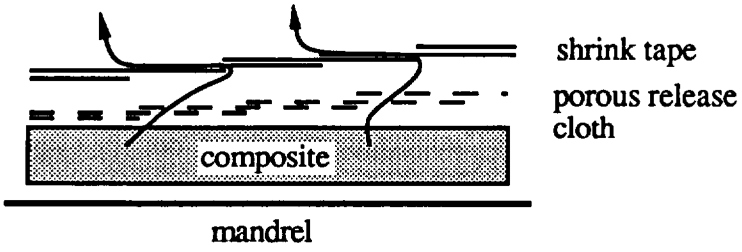

Figure 2.10: Through-the-thickness view of the materials used for the shrink-tape curing technique.

External pressure can also be applied with standard vacuum bagging materials. If a vacuum pump is used in conjunction with a layer of breather and a vacuum bag, approximately 100 kPa can be applied to the laminate. Although the use of vacuum is very helpful in removing voids from the wound material, it decreases the pressure within the void which causes an increase in diameter. To avoid this problem, an external pressure should also be used in conjunction with vacuum pressures or the vacuum must be released prior to solidification of the matrix. Unlike shrink tape, the vacuum bag technique can be used to apply very high compaction pressures; however, the breather and/or bleeder layers may wrinkle and these wrinkles will be transferred to the composite, as shown in Figure 2.11. The only way to prevent these wrinkles from developing is to wind the cure materials tightly over the composite, or to use materials which have a large bending stiffness (ie. effectively an exterior mold).

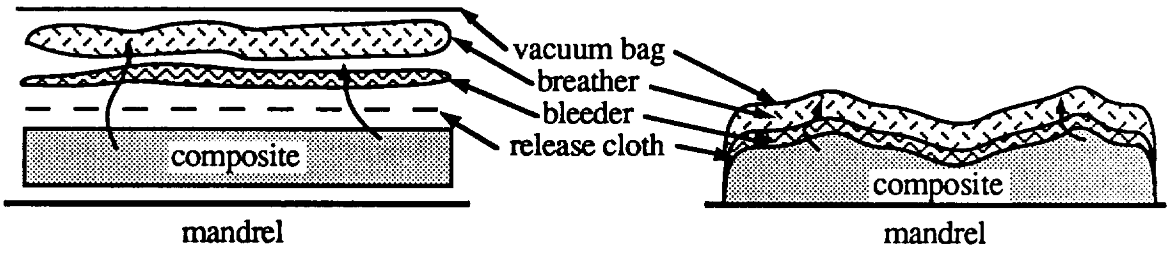

Figure 2.11: Through-the-thickness view of the materials used for the vacuum-bag curing technique.

The increase in quality which can be obtained with the use of external pressure during the curing of filament-wound structures must be balanced against the additional cost. Shrink tape, release ply, bleeder and breather layers, and vacuum bags all add to the cost of the manufacturing process as does the additional time required to apply these materials and remove them after curing. The greatest costs would be associated with the autoclave required for curing with the vacuum bag/external pressure technique.

Thermoplastic matrix composites can be consolidated in-situ or after winding. Due to the high temperatures and pressures used to consolidate thermoplastics, an autoclave or matched metal molds must be used to obtain sufficient quality if consolidation is performed after winding. The cost savings associated with in-situ consolidation are quite evident; at the completion of winding, manufacture of the structure is complete. Many techniques have been developed to apply the required pressures and temperatures to the material as it is being wound. Gas flames, lasers, and infrared heaters are typically used to apply heat in conjunction with heated mandrels and/or compaction rollers. One such technique has been developed by Fedro [13] for use with commingled yarns. Another novel technique which shows promise is to use an ultrasonic horn to apply the pressure and induce the mobility of the polymer chains necessary for consolidation.

As with thermosetting resins, some resin flow is required to develop intimate contact between the wound layers; however, since the minimum viscosity is larger in the case of thermoplastics, layer wrinkling is not generally a concern. Void removal does not easily occur by resin flow in thermoplastic processing, rather, the voids are either shrunk to an acceptable size with the use of large external pressures or the trapped air is displaced by a moving melt front during in-situ processing, as shown in Figure 2.12.

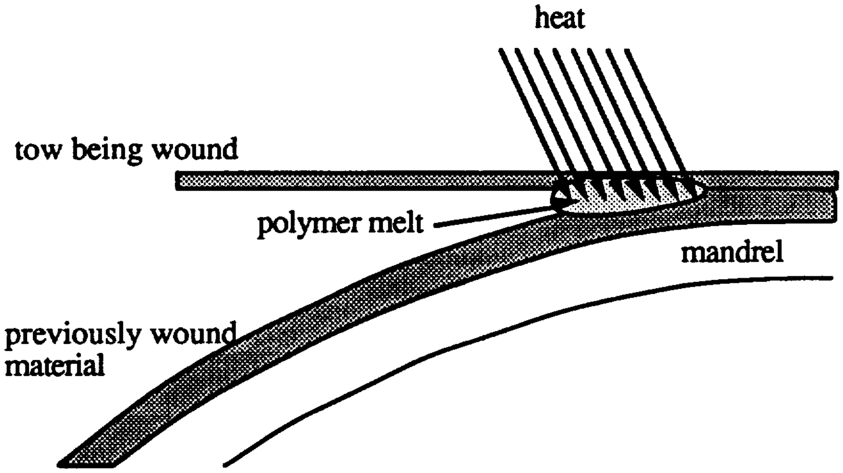

Figure 2.12: Moving melt front used to displace air and prevent voids during in-situ consolidation of thermoplastic filament winding.

## 2.4 Manufacturing Problems

The imperfections which develop due to improper manufacturing procedures are called extrinsic imperfections since they can usually be eliminated by changing the manufacturing parameters. This class of imperfections includes voids, regions of microbuckled fibers, thickness variations from nonuniform applied pressure, wrinkles in individual layers, and gaps or excessive overlapping of individual tows during winding. If the tow is not placed in the proper orientation on the mandrel during winding, gaps or excessive overlapping of the tows can occur. These imperfections can be caused by using an improper bandwidth when computing the winding parameters, slippage of the material after it has been placed on the mandrel, or improper rotation of the payout eye. Thickness variations can also develop if the wound tow twists before being placed on the mandrel. Twists cause nonuniformities in the coverage of an individual layer. Within the twist, the width of the tow narrows and the thickness increases. When subsequent layers are wrapped over the twist, air can be trapped within the material which may not be completely removed during cure; i.e., a void is created. Twists are caused by the angle between individual contact points along the fiber delivery path. If this angle is sufficient, the tow will fold because the tension on the tow tries to keep the material in a straight line. Twisting can be reduced if properly shaped pulleys and rotational payout-eye control are used.

When external pressures are applied during cure with the use of shrink tape, inconsistencies in the number of layers of shrink tape or release materials will cause thickness changes in the cured material. If the shrink tape is not applied uniformly, the result is a nonuniform application of pressure to the composite material. When the viscosity of the resin drops during cure, the resin will flow from regions of high pressure to regions with lower pressure. Usually only small thickness changes are associated with this type of imperfection.

When a structure is filament wound, the tow is tensioned which induces radial, longitudinal, and tangential stresses in the material. A compressive radial stress will squeeze some resin and trapped air out of the underlying layers. The outward resin flow will also cause the fibers to move inward. The inward motion of the layer will cause the circumferential length of the layer to shorten, effectively reducing the tensile circumferential stress in the layer. If sufficient resin flow is present either during winding or subsequent curing, the stress in the layer may become compressive, which will cause the fibers to buckle. The resulting waviness of the buckled layer may also affect the neighboring layers. A balance between a high tension required to keep the void content low yet prevent layer wrinkling must be achieved either through the use of processing models or trial and error.

Another manufacturing problem is the development of residual stresses in the filament-wound structure. Residual stresses can develop by three mechanisms: mechanical stresses, thermal stresses, and stresses introduced by chemical processes. The fiber tension used during winding will typically induce a compressive radial stress and a tensile circumferential stress in the as-wound material. Residual mechanical stresses can be controlled by the amount of winding tension and resin flow used during manufacture.

Thermal residual stresses are induced in the composite due to the mismatches in the coefficient of thermal expansion between the fibers and matrix and between the composite and mandrel. The residual stresses induced by mismatches in fiber and matrix coefficients of thermal expansion is the same for other composite lamination techniques. Thermal expansion of the mandrel during cure can induce a radial traction to the inner surface of the composite which will increase the resin pressure and fiber tension.

The final source of residual stress is chemical changes in the resin during manufacture. Polymerization, cross-linking, and chemical bond realignment cause volumetric changes in thermosetting resin composites to varying degrees. These volumetric changes in the matrix material may not be relaxed by resin flow or viscoelastic relaxation. Chemical residual stresses in thermoplastic matrix composites can also be induced by changes in crystallinity of the polymer during manufacture.

PAGE 18 INTENTIONALLY BLANK

PRECEDING PAGE BLANK NOT FILMED

# 3.0 FLAT LAMINATES CONTAINING DEFECTS

The compressive performance of a filament-wound cylinder can be degraded by unavoidable fiber curvatures in the crossover bands. These crossover bands contain fiber undulations which influence the compressive strength, stiffness, and failure mechanisms in a filament-wound structure. The primary objective of this part of the study was to characterize the compressive behavior of ply undulations. Compression tests were performed to identify failure mechanisms and to measure the compressive strength and stiffness of test specimens which contained varying amounts of undulations. The experimental results were complimented by analytical predictions of strength and stiffness. Three different analytical approaches were used in the analysis, namely, classical lamination theory, modified classical lamination theory, and the finite element method.

## 3.1 Experiments

Specimens with defects were designed to investigate the effects of ply and tow defects on the compressive strength and modulus of flat laminates by Hipp [14]. The ply defects studied were discontinuous unidirectional layers, layer undulations, and delaminated layers. The specimens manufactured with undulated fibers helped to identify the effects of fiber curvature which occur in filament-wound structures. Specimens containing discontinuous fibers, provided insight into the load transferring mechanisms which exist near the regions with reduced stiffness. As previously discussed, the fiber crossovers which occur in helical layers provide additional locations for voids or resin-rich regions. As a result, there are possibilities for weakened interfaces between a helical and an adjacent layer. Consequently, the specimens manufactured with induced delaminations were designed to investigate this defect type.

In a further study, Jensen and Pickenheim [12], compressive tests were conducted on flat-panel specimens which were developed to model the mechanics of large-scale fiber undulation regions in filament-wound composite cylinders. A total of 52 specimens were tested. Approximately half the specimens were hand laid-up with large scale, simulated fiber undulations. The undulations were created using unidirectional graphite/epoxy prepregs. These specimens were studied to better understand the behavior of fiber undulations under progressive compressive loading. The second set of specimens were obtained from longitudinally cut and flattened filament-wound cylinders. This set incorporated specimens with two different types of crossover bands found in filament-wound cylinders; namely, helical and circumferential crossover bands.

All specimens were cut from panels manufactured using Amoco T650-35/1902 unidirectional graphite/epoxy prepreg tape and Amoco T650-35/1908 prepreg tow material system. The nominal dimensions were 40.6 mm long by 19.1 mm wide by 3.05 mm thick for the hand laid-up specimens and 34.3 mm long by 12.7 mm wide by 2.16 mm thick for the filament-wound specimens. These dimensions precluded the occurrence of Euler's wide-column buckling. The failure stress was estimated using classical laminated plate theory in conjunction with Tsai-Wu failure criterion. The nominal material properties, used in the failure calculations are summarized in Table 3.1.

The specimens which were fabricated with ply drops and ply cuts contained defects located both symmetrically and non-symmetrically about the laminate midplane. In the specimens with ply cuts, the plies were cut perpendicular to the loading direction. Similarly, plies were dropped perpendicular to the loading direction and extreme care was taken to align both the dropped and cut regions through the thickness. The specimens containing filament-wound undulations were manufactured as flat laminates by winding

Table 3.1: Material Properties of Amoco T650-35/1902

| Property | Modulus (GPa) | Strength (MPa) |
|---|---|---|
| Longitudinal Tension | 146.7 | 1860.3 |
| Longitudinal Compression | 133.7 | 1653.6 |
| Transverse Tension | 9.7 | 62 |
| Transverse Compression | 9.7 | 137.8 |
| Shear | 5.5 | 82.68 |

several ±45° layers on a 15.25 mm diameter mandrel using a McClean-Anderson W70SP three-axis filament winder. The layers were carefully removed from the mandrel and flattened. Tow movement and buckling were minimized by the large mandrel diameter and low winding tension. Once in the flattened form, the layers were used to lay-up the laminates for the specimens. A nonporous Teflon®-coated release film was used to induce the delaminations, simulating the weakened interface of the filament-wound specimens.

Laminates were processed using the manufacturer's recommended cure and post-cure cycles, and a standard vacuum-bagging technique. The cured laminates were machined to the proper gage length and width on a precision wafering machine with a diamond-coated saw blade. Extreme care was taken during machining to ensure that all edges were straight and parallel.

The compression tests were conducted using a NASA short-block compression fixture. All testing was performed using a Tinius Olsen 270 kN (60 kip) screw-type testing machine. A hemispherical alignment device was used with the test fixture to ensure that the upper and lower test platens remained parallel. The specimens with ply defects and those designed to examine the effects of fiber curvatures were instrumented with Micro-Measurements EA-06-062ED120 electrical resistance strain gages. The gages were placed back-to-back at the center of the test section. The dropped-ply specimens however, had two pairs of gages placed above and below the defect line, respectively.

The specimens which contained delaminated layers were not instrumented with strain gages. Since the delaminated region occupied a majority of the gage area, an accurate strain reading could not be obtained by a surface-mounted strain sensor. Alternatively, two linear variable differential transformers (LVDT) were used to measure the global displacement of the specimen during the test, as illustrated in Figure 3.1. All of the tests were performed at a constant crosshead speed of 0.635 mm per minute until failure. The load data from the testing machine, local strain data, and voltages from the LVDT's were recorded using an Omega ® 900 data acquisition system controlled by Labtech Notebook on an IBM compatible PC/AT.

The specimens with induced defects were tested in compression and compared with control groups to determine the consequences of defects which arise naturally during the fabrication of filament-wound structures. The compressive response of all specimens manufactured from unidirectional prepreg was linear to failure. Failure was catastrophic in all cases with no prior warning, either visually, audibly, or from the strain gages. As expected, the induced defects resulted in a significant reduction in the ultimate failure stress. The average failure stresses for the specimen groups with ply defects are within 3.0% of each other, and approximately 40% below the control group. The specimens

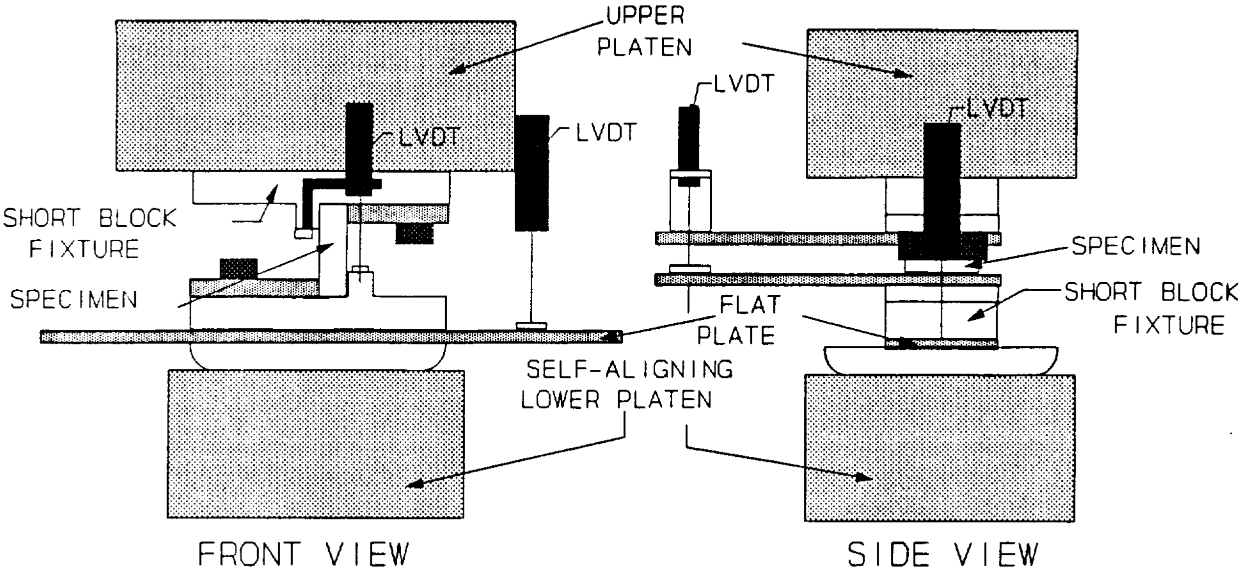

Figure 3.1: Flat laminate compression test fixture.

containing fiber curvatures had a failure stress 32% lower than the ply control group. The stiffness reduction in the specimens with unsymmetric ply cuts was 8%, while the symmetric ply cut group had a 16% reduction.

This study also addressed the relationship between the reduction of structural properties in thick filament-wound structures to the percentage of weak interfaces. Increasing the thickness of filament-wound structures causes a corresponding increase in the number of interfaces which include fiber crossovers. All of the specimens exhibited non-linear behavior. The experimental compressive moduli were nearly identical for the specimens having similar thicknesses.

The thin delaminated specimen failure stress was reduced by 5%, while the thin filament-wound specimens had a 41% reduction in failure stress. The increased number of weakened interfaces in the thick delaminated specimens reduced the failure stress by 20%, while the thick filament-wound specimens showed a 46% reduction. The additional number of delaminated layers was more detrimental to the structure than the increased number of filament-wound layers. The premature failure of the filament-wound specimens resulted in the lower failure strains. However, the filament-wound specimens exhibited increased toughness by carrying higher loads after initial damage compared to the other specimens. The presence of fiber undulations lowers the failure stress of the composite, but not as severely as ply defects, such as cut or dropped plies.

In the additional set of experiments performed [12], the stiffness of a laminate reduced from 3% to 51% due to fiber crossovers. Comparing the results for different in-plane crossover band orientations, it is seen that generally, larger stiffness reduction occurred for the perpendicular crossover bands, compared to the 45° crossover band orientation. This confirms that compressive stiffness reduction is greatest in the direction of the ply undulation.

The hand laid-up specimens with a single undulation had a slightly larger compressive stiffness reduction ranging from 8% to 23%, compared to the stiffness reduction ranging from 3% to 19% for the filament-wound specimens with helical crossovers. It is likely that the symmetry and smaller out-of-plane undulation angles of the filament-wound plies resulted in a smaller reduction in axial compressive stiffness. The largest stiffness reduction occurred for the filament-wound specimens with circumferential crossover bands. These specimens showed a significant decrease in stiffness ranging from 25% to 51%, versus the reduction in stiffness ranging from 3% to 19% for the filament-wound specimens containing helical crossover bands. Comparison of the two sets of filament-wound specimens with helical crossovers shows that the lay-up of the outer layers significantly influence the reduction in stiffness results. In all cases it was conjectured that failure of the specimens was dominated by interlaminar stresses leading to delaminations in the undulation region.

## 3.2 Analytical Models

Two modeling techniques, in addition to classical lamination theory, were used to gain more insight into the experimental results. The first was a modified classical lamination theory (MCLT) based on the localized geometry of the undulation region. The second method was finite element modeling (FEM) based on the unique specimen geometry. The material properties for Amoco T650-35/1902 summarized in Table 3.1 were used in the analysis.

Chou and Ishikawa's approach [15] was used to develop a model of fiber undulations in filament-wound structures. The major differences between Ishikawa and Chou's model and that proposed by Jensen and Hipp [16] were in the undulation shape and the nonorthogonality of the cross-over geometry. Based on photomicrographs taken from the manufactured cylinders, the general shape of fiber undulations was identified as a sinusoid. The nonorthogonality was accounted for with a transformation of the layer properties through an in-plane angle before calculating the average stiffness. The unit cell used in the study is shown in Figure 3.2.

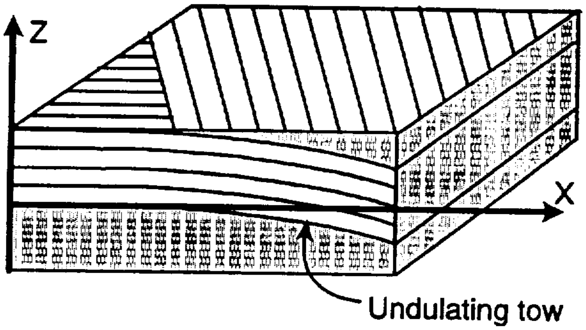

Figure 3.2: Unit cell used to determine stiffness of fiber undulation regions.

In the MCLT, laminated plate theory was assumed to be applicable at discrete locations along the length of the undulation. The principal stiffness constants, $Q_{ij}$, for the undulating layer were calculated as a function of the through-the-thickness off-axis angle due to the fiber undulation. The principal material stiffness, $Q_{ij}$, was then transformed to the principal coordinate axis through the in-plane angle, which was the filament winding angle. The transformed stiffness constants for the undulating and the non-undulating layers were used to calculate the expressions for laminate constitutive properties ($A_{ij}$, $B_{ij}$, and $D_{ij}$) at a point along the undulation. The average stiffness properties for the undulation of a filament-wound tow were determined by numerically integrating the expressions for $A_{ij}$, $B_{ij}$, and $D_{ij}$ applying the mean value theorem. The material properties were averaged over half the undulation length to prevent the vanishing of bending-extension coupling due to the antisymmetrical undulation shape.

Next, a three-dimensional finite element model of the entire fiber crossover was developed by Hipp [14] to include the through-the-width effect for a non-orthogonal intersection of filament-wound tows. Midplane strains and curvatures were applied individually and all thirty-six stiffness coefficients ($A_{ij}$, $B_{ij}$, $D_{ij}$) were directly calculated using constitutive relations from classical lamination theory.

The analytical model based on modified classical lamination theory (MCLT) predicted a drop in the $A_{11}$, $A_{12}$ and $A_{66}$ and corresponding $D_{ij}$ terms for all winding angles. A better approximation of the bending-extension coupling $B_{ij}$ (compared to the Fiber-Crimp model of Chou and Ishikawa [15] was achieved with the half undulation model using MCLT. The finite element analysis showed similar trends in the case of the Aij and Dij terms. The data from the MCLT and finite element analyses did not show much agreement in the case of the bending-extension coupling, Bij. The differences can be attributed to the percentage of undulations being modeled in each case. The modified CLT analysis predicted higher coupling stiffness than predicted by classical lamination theory. It was also observed that winding angles which orient undulations closer to the loading direction result in greater reduction in both extensional and bending stiffness.

An alternate approach for determining the stiffness properties of fiber crossover in filament-wound cylinders has been proposed by Jensen and Pai [17]. First, the fiber undulation was represented as a sinusoid and the undulation angle at a particular location was determined as the inverse tangent of the slope of the sinusoid at that particular location. Hence, each point along the undulation was characterized by the in-plane angle (the filament-winding angle) and out-of-plane angle (undulation angle) as shown in Figure 3.3

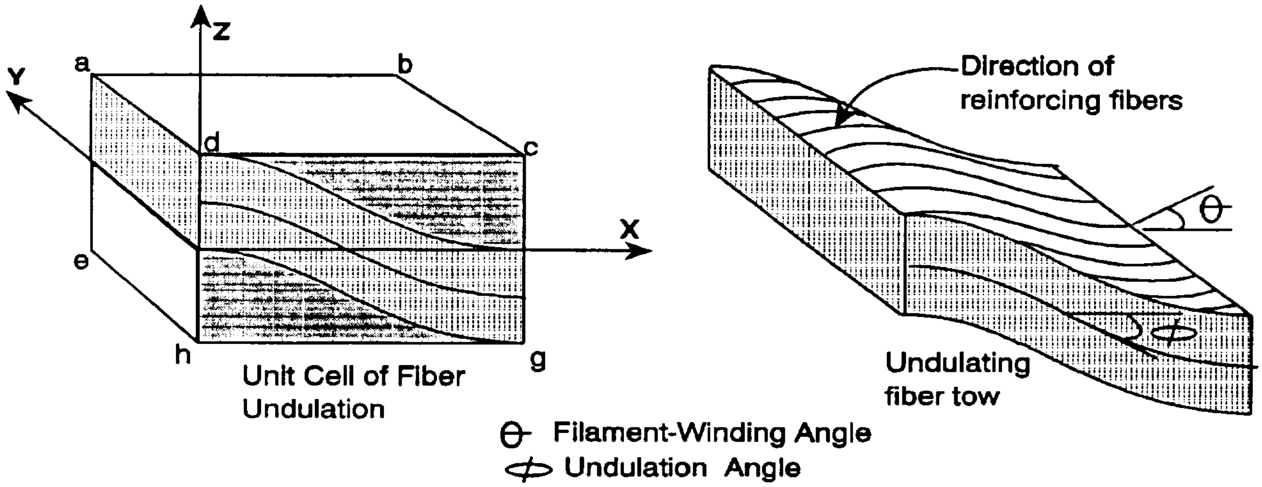

Figure 3.3: Angular transformations involved in stiffness calculations of undulation regions.

Next, the three-dimensional transversely-isotropic stiffness matrix for the undulating ply was transformed through the two angles to obtain the stiffness contribution of the undulating ply at a point along the undulation length. Then, the three-dimensional stiffness matrix was converted to a two-dimensional stiffness matrix using the classical assumptions of plate theory. The resulting two-dimensional effective stiffness of the undulating ply, along with the effective stiffness matrix of the nonundulating ply was used to calculate the stretching ($A_{ij}$), coupling ($B_{ij}$), and bending ($D_{ij}$) stiffness matrices. Classical lamination theory was used to determine the stiffness at a point along the undulation length. The effective property of the undulation regions were obtained by integrating the expressions for the A, B, and D matrices and applying the mean value theorem. As before, only half the undulation length was considered to preserve all terms of the extension-bending stiffness matrix.

The stretching-shearing ($A_{i6}$) and bending-twisting ($D_{i6}$) were unaffected by the out-of-plane undulation angle. The presence of the non-undulating tow was found to have no influence on the Poisson's coupling ($A_{12}$, $D_{12}$) shear ($A_{66}$) and twisting ($D_{66}$) terms. The longitudinal/transverse stretching ($A_{11}/A_{22}$) and longitudinal/transverse bending ($D_{11}/D_{22}$) showed a slight decrease with increasing undulation angles. This approach predicted the existence of $A_{16}$, $A_{26}$, $D_{16}$, $D_{26}$, $B_{11}$, $B_{12}$, $B_{66}$ coupling terms, which cannot be predicted using classical lamination theory applied to a ± laminate. However, due to the averaging of the stiffness over the undulation length involved in the present approach, the values obtained for stretching-twisting ($B_{16}$) and bending-shearing ($B_{26}$) terms were less than those predicted by the classical lamination theory approach.

Thus, it was observed that the classical lamination theory does not provide accurate coupling stiffness values for the undulation region. The next step in the analysis was to incorporate the stiffness values of the undulation region provided by the two analytical approaches into a global finite element model of the filament-wound cylinder as material properties.

# 4.0 MANUFACTURE OF FILAMENT-WOUND CYLINDERS

Many winding and curing parameters can influence the fiber microstructure, especially in the neighborhood of fiber crossovers. Controlling fiber placement also introduces an additional question: what combination of manufacturing parameters is best for a particular design? Specifically, the following questions have been identified as critical to the design of a compressively loaded, filament-wound cylinder:

- How does the crossover pattern -- i.e., the number and location of circumferential and helical-crossover bands -- affect the compressive structural response of a single layer, helically-wound cylinder?
- How does the anti-symmetry of the laminated-shell region affect the compressive structural response?
- How does the relative location of crossover bands within a multiple layered cylinder affect the compressive structural response?
- Can the results of a subscale experiment be used to predict the response of larger structures?
- Can the quality and load carrying capability of a filament-wound cylinder be improved by winding at an elevated temperature?
- Can other winding parameters such as mandrel material, winding sequence, and thickness affect the performance of filament-wound cylinders?

In an attempt to answer these questions, this research was divided into seven experimental programs: in-plane crossover-band spacing, mandrel material, cylinder scale, symmetry of the laminated-shell regions, winding sequence, through-the-thickness crossover-band location, and heated winding. Before discussing these experiments, the design of the mandrels, the materials used, and the development of optimal manufacturing methods will be discussed.

## 4.1 Materials Selection and Mandrel Design

The composite material chosen for this research program consisted of Thornel® T650-35 fibers and Amoco ERL 1908 thermosetting epoxy combined into 12000 filament prepregged tows. The tows contained approximately 32 percent resin by weight and were approximately 8.23-mm wide. Although the resin was B-staged, i.e. the polymerization and crosslinking reactions were advanced to an intermediate stage, the surface tack of this system was substantial. This improved the ability of the material to conform to complex contours and to adhere to the mandrel.

Two mandrel designs were used to fabricate specimens during this study. The first mandrel was designed by Fedro [13] and consisted of a 57-mm diameter, 304-mm long tube fitted with internal end fixtures, as shown schematically in Figure 4.1. Each end fixture was attached with four equally spaced and recessed screws. Mandrels of aluminum and steel were used during the research program. The second mandrel design consisted of a 152-mm diameter tube fitted with aluminum endcaps, as shown in Figure 4.2. Each endcap was drilled with 72 equally spaced holes for pins to hold the tow in place during winding. One 457-mm long steel mandrel was manufactured for use during the early stages of the research program and was later replaced by 608-mm long mandrels of aluminum and steel. The longer mandrels allowed two compression specimens to be machined from each cured cylinder.

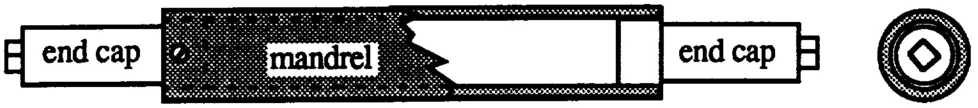

Figure 4.1: Schematic of the 57-mm diameter mandrel and endcaps designed by Fedro [13].

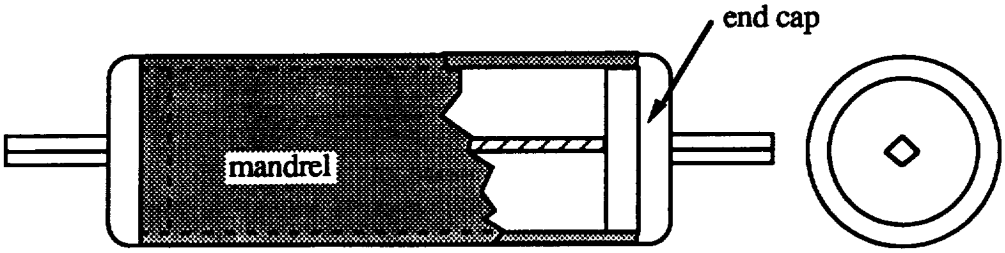

Figure 4.2: Schematic of the 152-mm diameter mandrel and endcaps.

## 4.2 Determination of Optimal Manufacturing Procedures

Several cylinders were wound and cured to investigate the manufacturing techniques discussed in Chapter 2. The goal of this work was to develop manufacturing procedures which could be used to consistently produce high quality filament-wound cylinders. Cylinders, manufactured for this phase of the research, were evaluated visually, both at the microscopic and macroscopic levels. Based on this evaluation, the manufacturing technique for the compression specimens was chosen. Quantitative quality measurements, such as fiber-volume fraction and void content, were made on selected cylinders and will be discussed in Chapter 5.

### 4.2.1 General Practices

The first step in manufacturing cylinders by filament winding is to prepare the mandrel and the pulleys or rollers along the fiber delivery path. The pulleys and rollers were cleaned with acetone to prevent any dirt or oil on the rollers from transferring to the prepreg during winding. This contamination could reduce the mechanical behavior of the material. To prevent chemical bonding between the matrix and the surface of the mandrel, each mandrel was carefully degreased with acetone and cleaned with methanol. Next, a light layer of either Airtech Release-All® 100 or Monocoat® E-63, non-fluorocarbon based release agents, was applied with a lint free cloth. The mandrel was placed in an oven at 177°C for approximately 30 minutes to evaporate the solvents in the release agent and to provide a more durable surface finish. After cooling, the mandrel was coated and baked again. This process was repeated six times. One air-dried layer of release agent was applied to the mandrel just prior to winding to fill in any scratches due to handling or removal of the previously cured cylinder.

In addition to the preparation of the mandrel, the software which controls the motion of the filament winder was programmed before winding. Since most cylinders in this research program were wound with a unique set of winding parameters, the programming step was performed for each cylinder. The McClean-Anderson filament winder (model W70-TAX/CT) is controlled with a computer program called Compositrak® [18]. This program is menu driven and very easy to use; consequently, rather than discussing the programming process, only the critical winding parameters for each cylinder will be discussed.

To begin winding, the supply spool was placed on the tensioner (American Sham model HE-1002 A), the tow was threaded along the fiber delivery path, and tied to the mandrel. The tensioner was then set for the desired tension. A constant fiber tension was maintained throughout the winding of each cylinder. If the winding was stopped for any appreciable length of time, the tensioner was turned off so that the tow would not damage the supply spool. During the prepregging operation the tow was wound on cardboard supply spools with very little tension in the fibers. Consequently, any appreciable diametrical force would cause the tows to stick together and split when they were unwound. After securing the tow to the mandrel, the filament winder was started and winding commenced. Oftentimes it was necessary to press the tow against the mandrel during the dwell rotation to keep it from slipping toward the center of the mandrel. Usually this was only necessary for the first pattern if the first layer was helically wound and was not needed if the first layer was hoop wound.

Tow twisting was occasionally observed during winding at three separate locations along the fiber delivery path. As the tow unwound from the supply spool it often rolled toward the middle of the spool due to the tension on the tow and the angle between the end of the spool and the sensor stand. This problem was compounded by poor alignment of the fiber delivery path and/or insufficient distance between the tensioner and the sensor stand. The second location of fiber twisting was on the sensor stand pulleys. These pulleys were originally designed for winding dry fibers and have a "U"-shaped cross section, as shown in Figure 4.3. During winding, the adhesive nature of the resin, coupled with the slight angle which was incurred by the width of the supply spool, caused the tow to climb up the sides of the pulley until it rolled over. The pulley on the carriage was of similar cross-sectional shape, constituting the third location of fiber twisting.

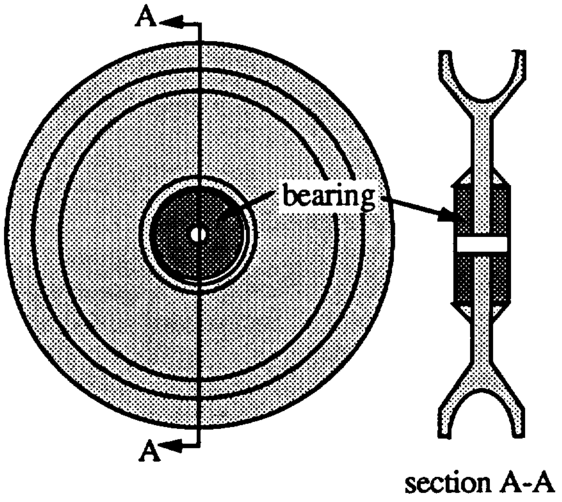

Figure 4.3: Original sensor-stand pulleys for winding dry fiber tows.

New pulleys were designed and manufactured for the sensor stand and the carriage positions. The new sensor-stand design consisted of a long cylindrical shaped pulley with small raised ends to restrain the tow, as shown in Figure 4.4a. This design allowed the tow to move horizontally along the pulley as it unwound from the supply spool and moved laterally with the carriage. The new carriage pulley, shown in Figure 4.4b, was parabolic in shape which allowed the tow to climb the sides of the pulley as the angle of winding changed. When the parabola was sufficiently shallow, the tow slid toward the bottom of the pulley without damage. These pulleys significantly reduced the amount of tow twisting.

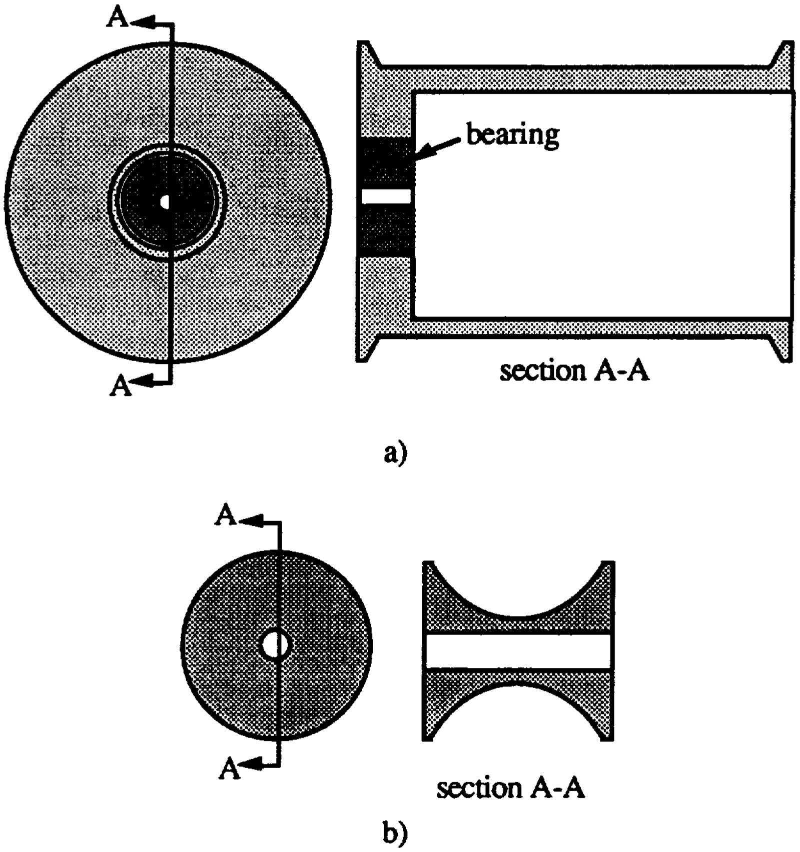

Figure 4.4: Re-designed sensor stand a), and carriage pulleys b), for winding prepregged tows.

The majority of experiments completed during this study were performed at room temperature; however, several cylinders were wound at an elevated temperature to increase the amount of resin flow during winding. Elevated temperature winding was accomplished by employing an infrared heater (Research Inc. model 4184) attached to the payout eye of the filament winder, as shown in Figure 4.5. The amount of heat was adjusted so that visible resin flow occurred as the tow was wound. Since the tow cooled as it passed around the mandrel and as the carriage progressed down the mandrel, the output of the heater was also adjusted according to the winding angle and winding speed. In addition to improving the consolidation of each layer, the flowing resin displaced air and filled in depressions around gaps, tow twists, and fiber crossovers. The heat was carefully regulated since too much heat can cause the epoxy to cure prematurely or thermally degrade.

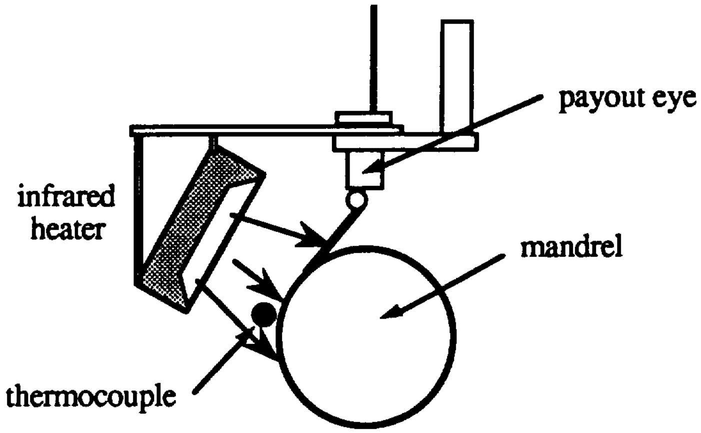

Figure 4.5: Infrared heater setup used for elevated-temperature winding.

After the layers were wound, the tow was cut near the mandrel and rewound on the supply spool. Next, the wound layers were trimmed by cutting them with a razor blade approximately 50 mm from each end. This allowed the material wound over the endcaps to be removed and allowed the cure materials to be attached to the mandrel. The cure materials were then wound over the composite. Typically, this was performed in the filament winder with the endcaps attached since the winder was used to rotate the cylinder as the materials were applied; however, the endcaps were removed prior to cure. The specific procedures for applying the cure materials will be discussed in the following sections.

### 4.2.2 Autoclave Curing Technique

The most common technique for producing high quality flat laminates is to use a vacuum bagging scheme in conjunction with an autoclave. Rather than relying solely on fiber tension for consolidation and resin flow in filament-wound structures, the autoclave curing technique employs externally applied pressures to improve the quality of the composite. To investigate this technique, Cylinder 072490 was wound on the 152-mm diameter, 457-mm long steel mandrel with a $[90/\pm30_2/90]$ winding sequence. Each cylinder can be identified by a 6 digit number which corresponds to the date of manufacture: two digits for the month, day, and year, respectively. When more than one curing technique was used or multiple compression specimens were machined from the same cylinder, additional letters were used to identify each specimen. The same winding parameters were used for the internal and external ±30° layers, and are listed in Table 4.1. The thicknesses listed in the table are the average of ten measurements made with a ball-end micrometer at locations chosen randomly around the circumference of each cylinder. Pins, pressed into each endcap, were used during winding to help hold the tow in place. Since the length of the fiber delivery system was quite short and the tow was forced around the pins, a large amount of tow twisting was observed during winding.

Prior to curing, the composite material was trimmed around the pins and the cylinder was loosely wrapped with one layer of porous Teflon®-coated glass fabric. One layer of bleeder material was applied to absorb resin, air, and volatiles during cure, as shown in Figure 2.11. To limit the amount of resin flow, one layer of nonporous release film, perforated with approximately 1 pin hole per 4 square inches, was used to cover the bleeder cloth. The layers outside of the nonporous film consisted of breather cloth and vacuum bagging film, respectively. The entire assembly was suspended inside the autoclave and a thermocouple was taped to the inner surface of the mandrel to control the

Table 4.1: Winding and curing parameters for cylinders manufactured for the Manufacturing Optimization study.

| Cylinder Number | Winding Sequence | Mandrel (mm) | Bandwidth (mm) | Dwell (rev.) | Circuits per Coverage | Circuits per Pattern | Circ. X-Over Band Spacing (mm) | Winding Tension (N) | Manuf. Method | Thickness (mm) |
|---|---|---|---|---|---|---|---|---|---|---|
| 072490 | $[90/\pm30]_{as}$ | 152 steel | 3.48 | 0.05108 | 119 | 2 | 207 | 8.9 | autoclave | 14.0 |
| 073090 | $[90/\pm30]_{as}$ | 57 steel | 2.77 | 0.19760 | 55 | 1 | 152 | 8.9 | autoclave | 16.5 |
| 090190HS | $[90/\pm30]_{as}$ | 57 steel | 2.77 | 0.19760 | 55 | 1 | 152 | 22 | none | 2.03 |
| 092390HS | $[90/\pm30]_{as}$ | 57 al | 2.77 | 0.18705 | 59 | 5 | 30.5 | 5.8 | none | 1.91 |
| 092690HS | $[90/\pm30]_{as}$ | 57 al | 2.77 | 0.29907 | 55 | 4 | 38.1 | 5.8 | none | 1.57 |
| 100490HS | $[90/\pm30]_{as}$ | 152 steel | 2.79 | 0.25296 | 148 | 1 | 414 | 8.9 | none | 1.57 |
| 090190CC | $[90/\pm30]_{as}$ | 57 steel | 2.77 | 0.19760 | 55 | 1 | 152 | 22 | S.T.(2) | 1.78 |
| 092390CC | $[90/\pm30]_{as}$ | 57 al | 2.77 | 0.18705 | 59 | 5 | 30.5 | 5.8 | S.T.(2) | 1.60 |
| 092690CC | $[90/\pm30]_{as}$ | 57 al | 2.77 | 0.29907 | 55 | 4 | 38.1 | 5.8 | S.T.(2) | 1.52 |
| 100490CC | $[90/\pm30]_{as}$ | 152 steel | 2.79 | 0.25296 | 148 | 1 | 414 | 8.9 | S.T.(2) | 1.52 |

S.T.(#) -- Refers to the shrink tape manufacturing technique where the number in parentheses indicates the number of layers of shrink tape

autoclave during cure. A Baron model BAC-7 autoclave was used to cure the cylinder with 586 kPa external and full vacuum pressure according to the manufacturer's recommended cure cycle.

During the vacuum check, several longitudinal wrinkles were observed in the outer bag and breather material. These wrinkles were caused by the change in diameter of the cure materials as the vacuum was applied. The external pressure increased the amount of compaction of the bleeder and breather materials, further increasing the severity of the wrinkles. Resin flow during cure from the interior of the composite into the bleeder, also caused the fibers to move toward the mandrel surface with a corresponding loss of fiber tension. The resulting outer surface of the composite cylinder contains many small wrinkles which are parallel to the longitudinal axis and are distributed uniformly about the circumference of the cylinder. After trimming the ends of the cured cylinder, it was evident that these wrinkles contained fibers. Helical dents could also be observed in portions of the cylinder. These regions were caused by tow twisting which was observed in the ±30° layers. Although the vacuum bagging materials and pressures applied to the composite during cure caused wrinkles to develop in the outer surface, no appreciable voids were observed within the cured material.

Several sections of Cylinder 072490 were machined parallel to the circular cross section, potted in a mixture of epoxy resin and hardener (Shell Epon® 815 and Versamid® 140 respectively), polished, and examined under a microscope to determine the distribution of fibers and voids within the material. Figure 4.6 contains a photomicrograph of a representative portion of the cylinder in the neighborhood of a wrinkle. Corresponding to the thickness change is a visible change in the fiber-volume fraction. Resin rich regions are particularly apparent between the inner 90° and the first ±30° layer. Several small voids can be seen in this resin rich region; however, these voids are very small and do not appreciably contribute to the changes in the total laminate thickness.

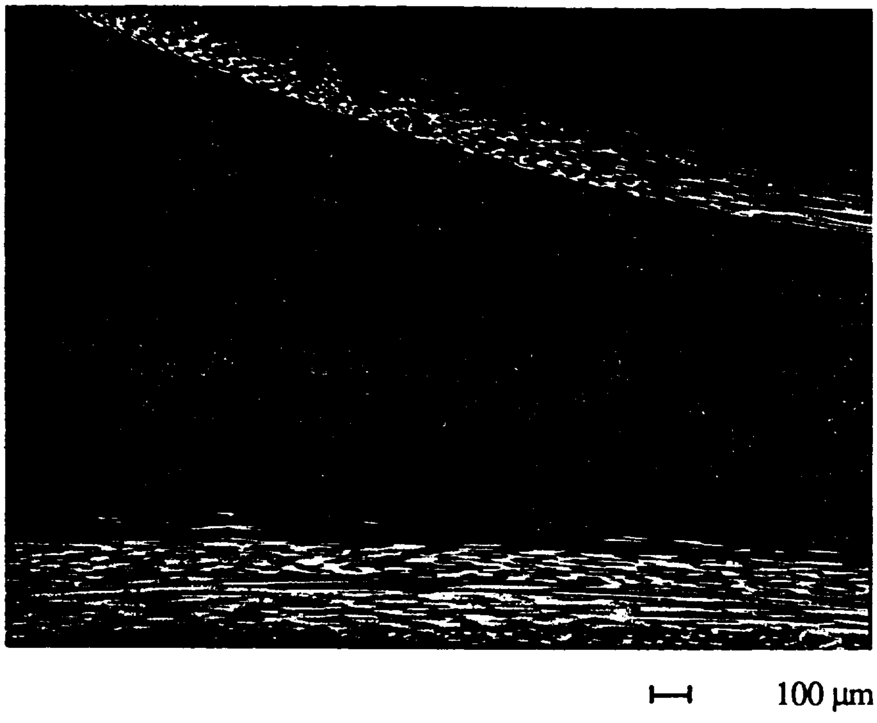

Figure 4.6: Circumferential cross-sectional view of Cylinder 072490.

Cylinder 073090 was manufactured using a similar autoclave curing technique to determine the role of resin flow in the development of wrinkles in filament-wound shells. The 57-mm diameter cylindrical steel mandrel was wound with a [90/±30$_2$/90] winding sequence while maintaining 8.9 N of tension. Several twists occurred during winding; yet, the number of twists was significantly less than those within Cylinder 072490. Following winding, the composite was covered with a nonporous release cloth, one layer of breather material, and a vacuum bag. The nonporous release material was used to reduce the amount of resin removed from the composite and, hopefully, to reduce the layer wrinkling. As vacuum pressure was applied, the vacuum bag and breather materials were smoothed by hand to help reduce the number of wrinkles.

After curing the cylinder with vacuum and external pressures, the cylinder was removed from the vacuum bag and trimmed. Although the number of wrinkles was reduced with this manufacturing technique, several large wrinkles were observed in the longitudinal direction. Examination of the cut section revealed few voids, as shown in Figure 4.7, yet wrinkles were apparent in the fibers as well as the resin coating on the outer surface. The thickness of this cylinder is significantly larger than the Cylinder 072490, 1.65 mm versus 1.40 mm respectively, due to the lack of resin flow out of the composite.

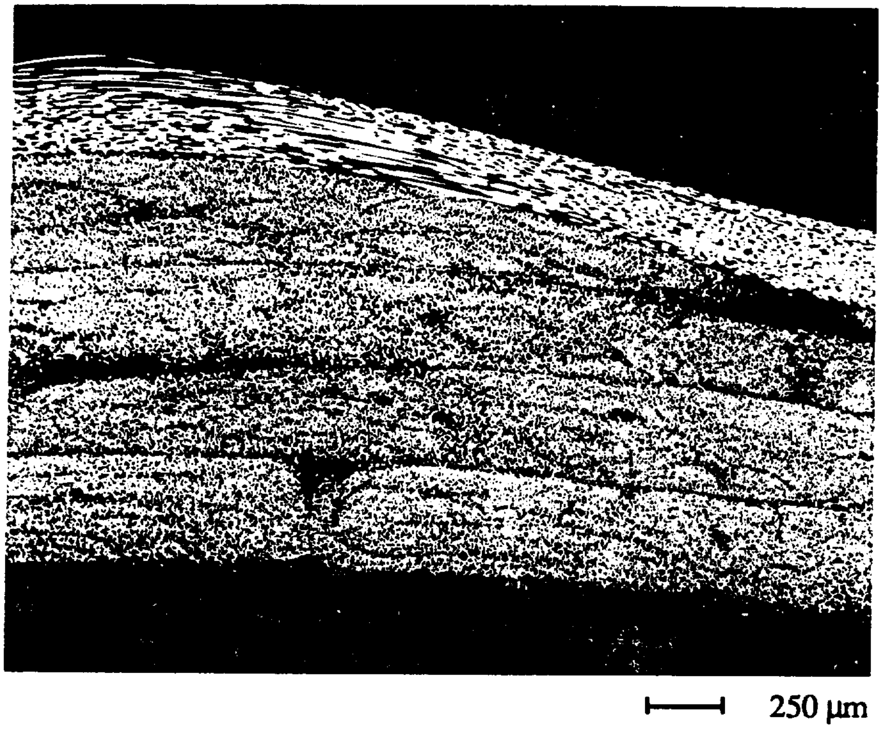

Figure 4.7: Circumferential cross-sectional view of Cylinder 073090.

Autoclave curing of Cylinders 072490 and 073090 demonstrated that this technique is attractive since the void content of the composite material is very small. However, wrinkles which developed in these cylinders will probably adversely affect the structural performance of the composite shell. Since the wrinkles are large and contain fibers, this curing technique was not used to manufacture specimens for compression testing.

### 4.2.3 Oven Curing Without Pressure

Typically, a wet wound part is cured by slowly rotating the mandrel and cylinder in a convection oven. To form a basis of comparison, Cylinder 090190 was wound on the

57-mm diameter steel mandrel with a $[90/\pm30_2/90]$ winding sequence and the winding parameters listed in Table 4.1. Since the void content and degree of consolidation are primarily dependent on the winding tension with this curing technique, a tension of 22 N was used. After winding, the ends of the composite were trimmed and a narrow strip of material was removed from the center of the remaining material so that two curing techniques could be compared irrespective of differences in the winding procedure. One-half of the composite cylinder (Specimen 090190HS) was loosely wrapped with porous release cloth prior to curing. Since no external pressure was applied during cure, the possibility of outer layer wrinkling was minimized; however, the cured cylinder is quite thick compared to previous manufacturing attempts and contains many large voids, as shown in Figure 4.8. Specimen numbers with the suffix HS were used to identify the portion of a cylinder cured without external compaction pressure.

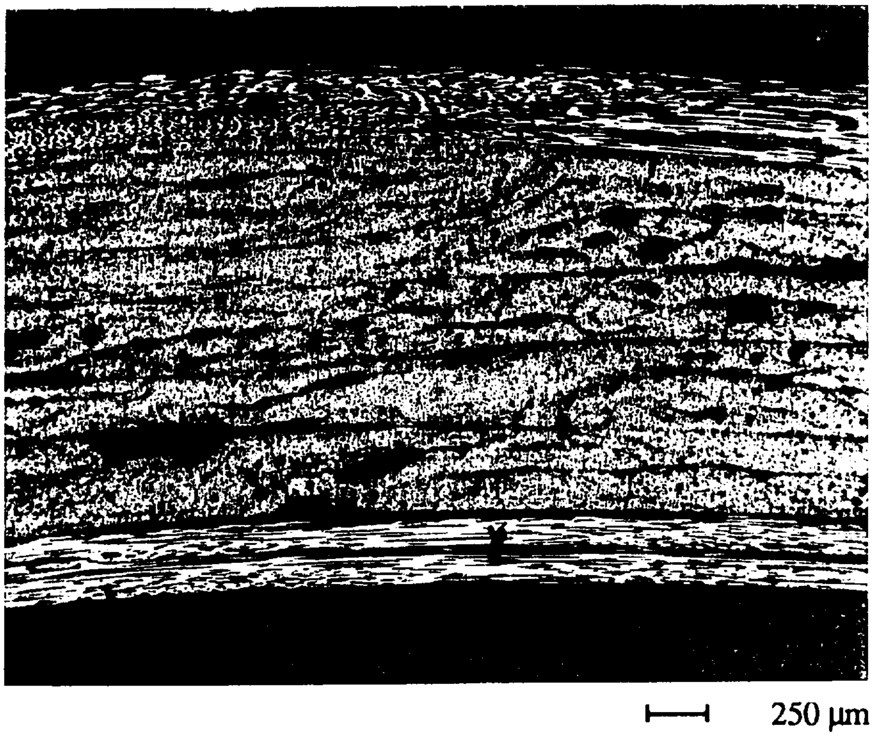

Figure 4.8: Circumferential cross-sectional view of Specimen 090190HS.

Cylinder 092390 was manufactured with a slightly different winding and curing procedure to reduce the void content observed with Specimen 090190HS. The 57-mm diameter aluminum mandrel was heated to approximately 80°C with the infrared heater setup shown in Figure 4.5. A $[90/\pm30_2/90]$ winding sequence was used with the winding parameters listed in Table 4.1 and 5.8 N of tension. A lower tension was used due to problems with the calibration of the tensioner. Very few twists in the fiber tow were observed during winding and overall placement of the prepreg tow was excellent.

After winding, the composite material was trimmed and divided as with Cylinder 090190 and one section (Specimen 092390HS) was covered with 25-mm wide strips of porous release cloth under slight tension. A convection oven was used to cure the cylinder as described previously. The exterior of the cured cylinder has a mottled surface because the resin did not evenly wet the release cloth. A uniform cylinder thickness was obtained, yet voids are still apparent in the material as evident from the photomicrograph shown in

Figure 4.9. Compared to Specimen 090190HS, the voids appear to be much smaller and more uniformly distributed due to the elevated winding temperature.

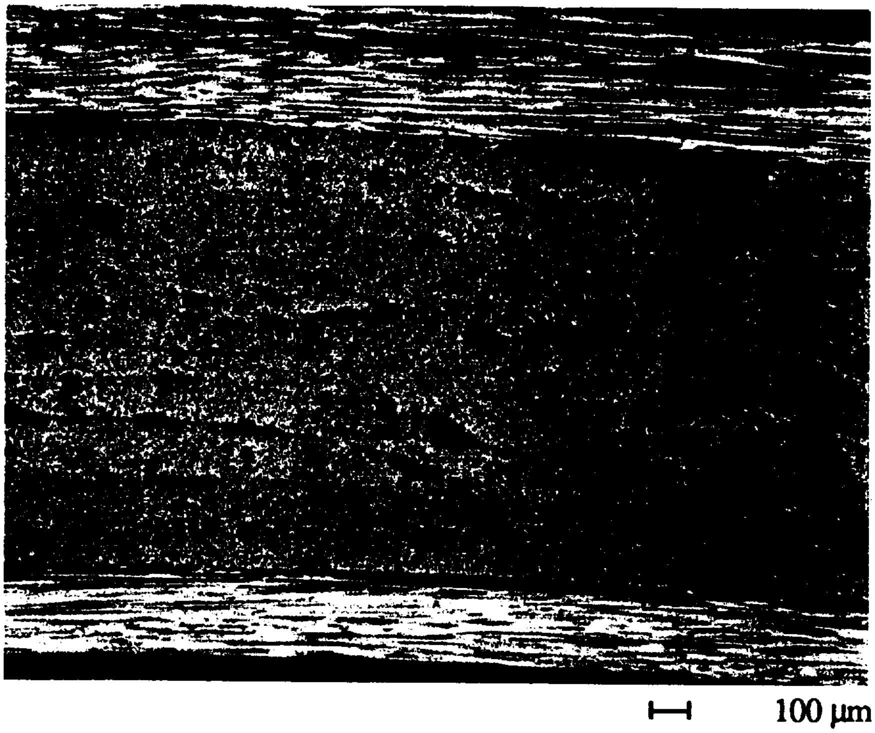

Figure 4.9: Circumferential cross-sectional view of Specimen 092390HS.

Cylinder 092690 was also manufactured on the 57-mm diameter aluminum mandrel with a [90/±$30_2$/90] winding sequence. Winding was performed with 5.8 N of fiber tension and at 80°C as with Cylinder 092390. The major difference in the manufacturing technique for this cylinder is the manner in which the cure materials were applied. The cylinder was wrapped tightly with porous release cloth strips approximately 25-mm wide to provide some compaction of the underlying composite material. A high-temperature adhesive tape was wrapped over the release cloth to increase the resin and compaction pressures. This technique produced a cylinder with a very uniform thickness and low void content, as shown in Figure 4.10.

Due to the quality of Cylinder 092690, Cylinder 100490 was wound at room temperature on the 152-mm diameter, 407-mm long steel mandrel and cured with the same divided-cylinder technique to determine if the manufacturing procedures could be scaled. Prior to winding, the pins in the endcaps were removed to reduce the twisting observed in Cylinder 072490. The computer controller on the filament winder was programmed so that the tow passed over the endcaps during the helical winding to hold the tow in the desired position. Accurate tow placement and few twists were observed during winding.

After trimming the composite material, cure materials were applied as with Cylinder 092690 and the wound mandrel was placed in an autoclave for curing. No external or vacuum pressures were used, rather, the autoclave was used to accurately control the temperature of the cylinder. Appearance of interior and exterior surfaces of the cured cylinder is nearly identical to Cylinder 092690. Visual inspection of the cross section indicated a low void content despite room-temperature winding and the use of a steel mandrel.

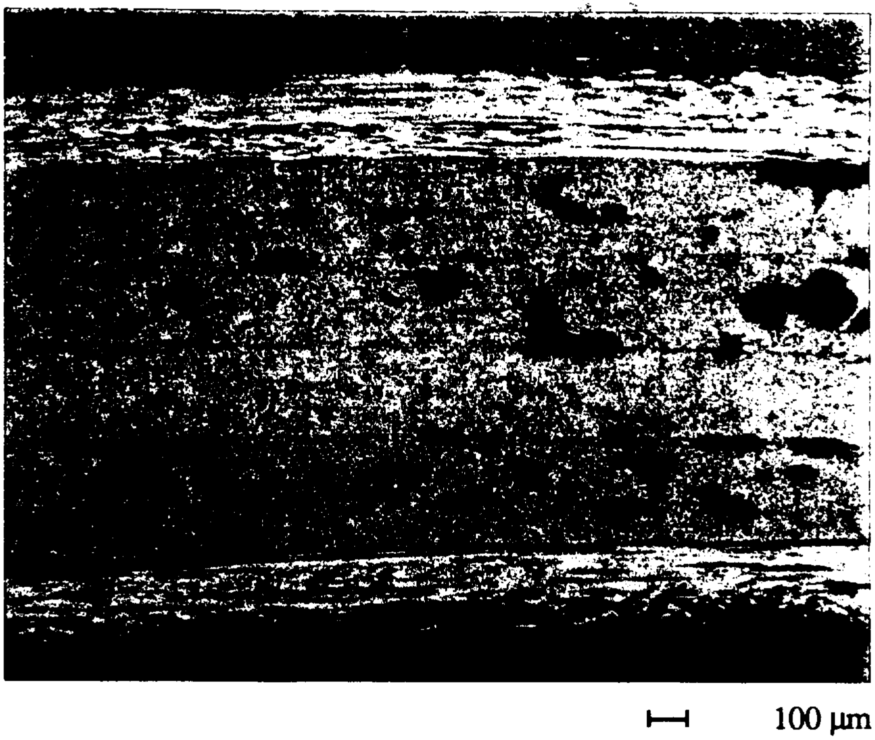

Figure 4.10: Circumferential cross-sectional view of Specimen 092690HS.

### 4.2.3 Oven Curing with Shrink Tape

To attempt to minimize the void content without producing wrinkles, the other half of Cylinder 090190 was cured with temperature-sensitive shrink tape. The shrink tape used in this research consisted of a nonporous 0.05-mm thick biaxially-oriented polyamide film (Airtech International Inc. High Shrink Tape A575). Specimen numbers with the suffix CC were used to identify the portions cured with shrink tape. The outer surface of Specimen 090190CC was loosely wrapped with porous release cloth, then wrapped with approximately two layers of shrink tape, as shown in Figure 2.10. Since narrow strips of shrink tape were used, some resin was allowed to flow out of the composite and between the layers of shrink tape.

After the cure cycle was completed and the cure materials were removed, several small longitudinal indentations were observed in the outer surface. These imperfections were caused by the lack of tension in the release cloth during cure. As the temperature in the oven increased, the shrink tape applied a compaction pressure to the composite material, thus, producing a compressive stress in the release cloth. Wrinkles in the release cloth developed and were transferred to the composite. Thickness variations were also observed in the longitudinal direction and were attributed to nonuniformities in the number of shrink tape layers from point to point. Irrespective of the indentations in the outer surface and the thickness variations, the quality of Specimen 090190CC is much better than Specimen 090190HS. Since the cylinders were wound under identical conditions, the differences in quality are attributed to the use of shrink tape during cure. Improvements in the microstructure are apparent by comparing Figures 4.8 and 4.11.

To prevent wrinkles in the release cloth, three layers of shrink tape were wrapped directly on the filament-wound composite material during the manufacture of Specimen 092390CC. According to the manufacturer, the tape should release from most epoxies. After removing the cylinder from the oven, it could not be removed. Thickness uniformity

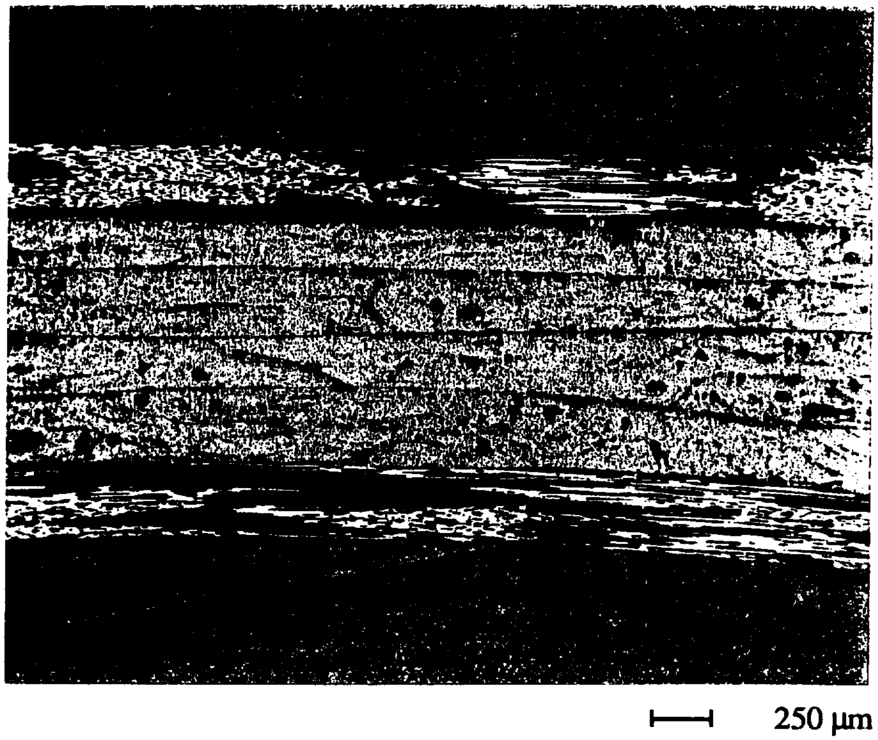

Figure 4.11: Circumferential cross-sectional view of Specimen 090190CC.

and void content , as shown in Figure 4.12, appear to be improved compared to Specimens 090190CC and 092390HS. This specimen demonstrates that the improvement in material quality which accompanies heated winding is much larger than the quality reduction associated with a decrease in the winding tension.

The other half of Cylinder 092690 was wrapped with shrink tape rather than with the high temperature adhesive tape as described previously. Comparing the two halves of the cylinder, Specimen 092690CC has better thickness uniformity and a lower void content, as shown in Figure 4.13. The quality of Specimen 092690CC is lower than Specimen 092390CC despite similar winding conditions. No explanation for the observed reduction in quality could be determined. The quality of Specimen 100490CC was similar to Specimen 092390CC.

## 4.3 Manufacture of Cylinders for Compression Testing

The following section contains a discussion of the manufacturing procedures used to wind and cure cylinders for subsequent compression testing. In most of the experimental programs, the objective was to remove the effects of the curing procedure from the cylinder quality and compressive response so that the effects of the winding parameters could be determined. The heated winding and mandrel material experiments were used to study the effects of the manufacturing procedures irrespective of the winding pattern.

### 4.3.1 In-Plane Crossover-Band Spacing

The location of the circumferential and helical-crossover bands within a helically wound layer can be changed without changing the winding angle; consequently, the amount of material which undulates and its location within the shell can be controlled. The

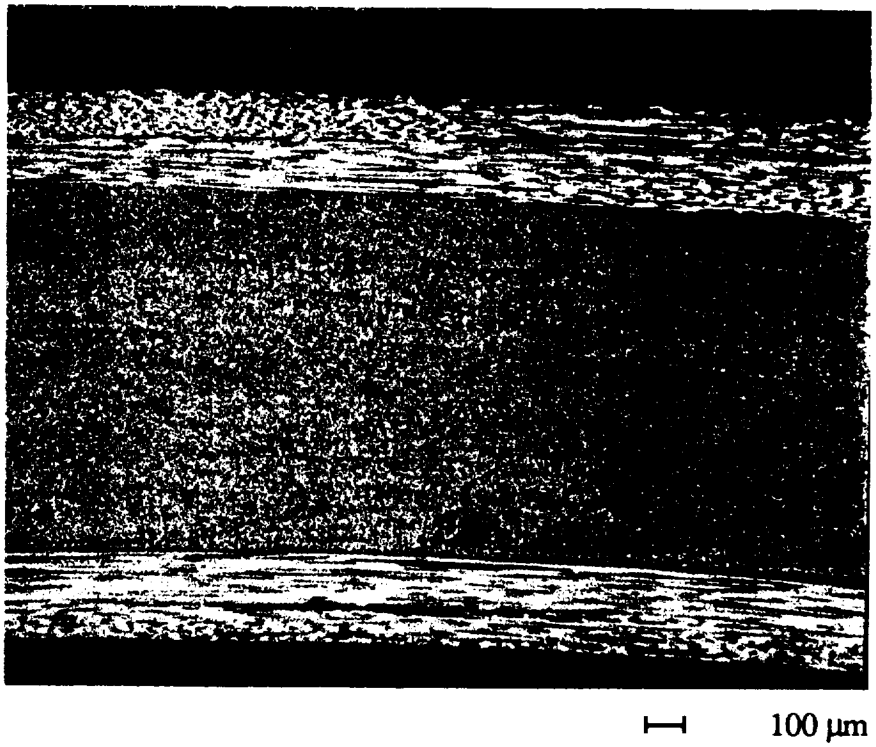

Figure 4.12: Circumferential cross-sectional view of Specimen 092390CC.

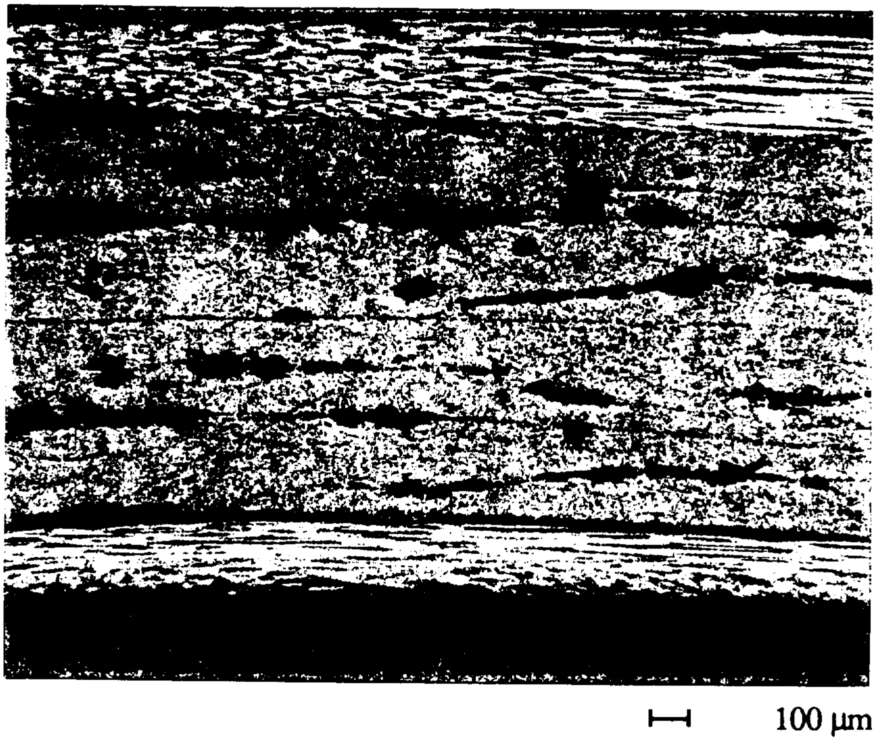

Figure 4.13: Circumferential cross-sectional view of Specimen 092690CC.

influence of these regions on the compressive performance of thin shells was investigated by systematically altering the location and number of crossover bands in the plane of the cylinder. Crossover location was varied by adjusting the number of circuits per pattern and the dwell angle. Cylinders wound during this experiment consist, of only one ±30° layer wound on a 57-mm diameter aluminum mandrel with circumferential crossover-band spacings of 155, 76, 51, 30, 14, and 6.9 mm. These crossover-band spacings correspond to having 0, 1, 2, 3, 5, and 11 circumferential-crossover bands within a 84-mm long test section, respectively. Although Cylinder 011692 was wound without circumferential-crossover bands, two helical-crossover bands were included. The specific winding parameters for these cylinders are listed in Table 4.2.

To obtain a uniform level of quality during this experiment, an attempt was made to maintain the same winding and curing procedures for each specimen. In most cases, the cylinders were wound with a tension of 22 N and a bandwidth of 4.2 mm then covered with two layers of porous release cloth and four layers of shrink tape. Cylinders 061991, 062291, and 062491 contained a larger number of twisted tows which formed gaps and ridges in the cured cylinder. These winding patterns were rewound to form Cylinders 062091, and 062591. Figure 4.14 contains a photomicrograph of Cylinder 062091 which is typical of the specimens manufactured for this study. Photomicrographs for each cylinder manufactured during the course of this research program is included in Claus, Hahn, and Jensen [19].

### 4.3.2 Mandrel Material

To investigate the effect of mandrel material, two cylinders were wound on 57-mm diameter, 3.2-mm thick mandrels manufactured from aluminum and steel to produce Cylinders 062191 and 062391, respectively. Each cylinder was wound with a [±30] winding sequence, a tension of 22 N, and a circumferential-crossover band spacing of 51 mm and then cured with four layers of shrink tape. Only very slight differences in thickness were recorded; 4.22 mm versus 4.27 mm for the aluminum and steel, respectively. Microscopic examination of the material revealed nearly identical quality as did visual examination of the internal and external surfaces.

### 4.3.3 Cylinder Scale

When large cylindrical shells are designed, often there is no experimental evidence to support the predicted behavior of the cylinder with that particular radius, thickness, length, and lamination sequence. A scaling rule which is based on experimental evidence, is invaluable for this particular design problem. Due to the anisotropy of composite materials, scaling laws for isotropic materials may not be valid. The goal of this experimental program was to investigate the effects of scale on filament-wound cylinders. The effect of cylinder diameter was investigated with single-layer cylinders wound on 57-mm and 152-mm diameter mandrels. Thickness effects were investigated by comparing $[90/\pm30_2/90]$, $[\pm30/90_2/\pm30]$, and $[0/\pm60_2/0]$ cylinders to $[90_3/\pm30_3/\pm30_3/90_3]$, $[\pm30_3/90_3/90_3/\pm30_3]$, and $[0_3/\pm60_3/\pm60_3/0_3]$ cylinders wound on a 152-mm diameter mandrel. Each cylinder was wound at room temperature and cured with the use of temperature-sensitive shrink tape.

Cylinder 061991 was wound with a [±30] winding sequence on the 57-mm diameter aluminum mandrel with 31 N of fiber tension and a circumferential-crossover band spacing of 76 mm. Selected winding parameters for the Cylinder Scale experimental program are listed in Table 4.3. During winding, the fiber tow twisted appreciably due to the length of the fiber delivery system and the humidity within the room. The wound material was trimmed, covered with two layers of porous release cloth, and two layers of shrink tape. A convection oven was used to cure the material as described in Section 4.2. When the cured cylinder was removed from the mandrel, the gaps in the layer formed

Table 4.2: Winding and curing parameters for cylinders manufactured for the In-Plane Crossover-Band Spacing experimental program.

| Cylinder Number | Winding Sequence | Mandrel (mm) | Bandwidth (mm) | Dwell (rev.) | Circuits per Coverage | Circuits per Pattern | Circ. X-Over Band Spacing (mm) | Winding Tension (N) | Manuf. Method | Thickness (mm) |
|---|---|---|---|---|---|---|---|---|---|---|
| 011692 | [±30] | 57 al | 3.20 | 0.43258 | 48 | 1 | 155 | 22 | S.T. (4) | 0.432 |
| 061991 | [±30] | 57 al | 3.23 | 0.40206 | 47 | 2 | 76.2 | 31 | S.T. (2) | 0.462 |
| 062091 | [±30] | 57 al | 3.23 | 0.40206 | 47 | 2 | 76.2 | 22 | S.T. (4) | 0.427 |
| 062191 | [±30] | 57 al | 3.23 | 0.31695 | 47 | 3 | 50.8 | 22 | S.T. (4) | 0.422 |
| 062291 | [±30] | 57 al | 3.23 | 0.31695 | 47 | 3 | 30.5 | 22 | S.T. (4) | 0.414 |
| 062491 | [±30] | 57 al | 3.23 | 0.47889 | 48 | 5 | 30.5 | 22 | S.T. (4) | 0.427 |
| 062591 | [±30] | 57 al | 3.23 | 0.37473 | 48 | 43 | 30.5 | 22 | S.T. (4) | 0.429 |
| 063091 | [±30] | 57 al | 3.23 | 0.04139 | 48 | 11 | 14.2 | 22 | S.T. (4) | 0.427 |
| 070191 | [±30] | 57 al | 3.23 | 0.41639 | 48 | 23 | 6.89 | 22 | S.T. (4) | 0.450 |

S.T.(#) -- Refers to the shrink tape manufacturing technique where the number in parentheses indicates the number of layers of shrink tape

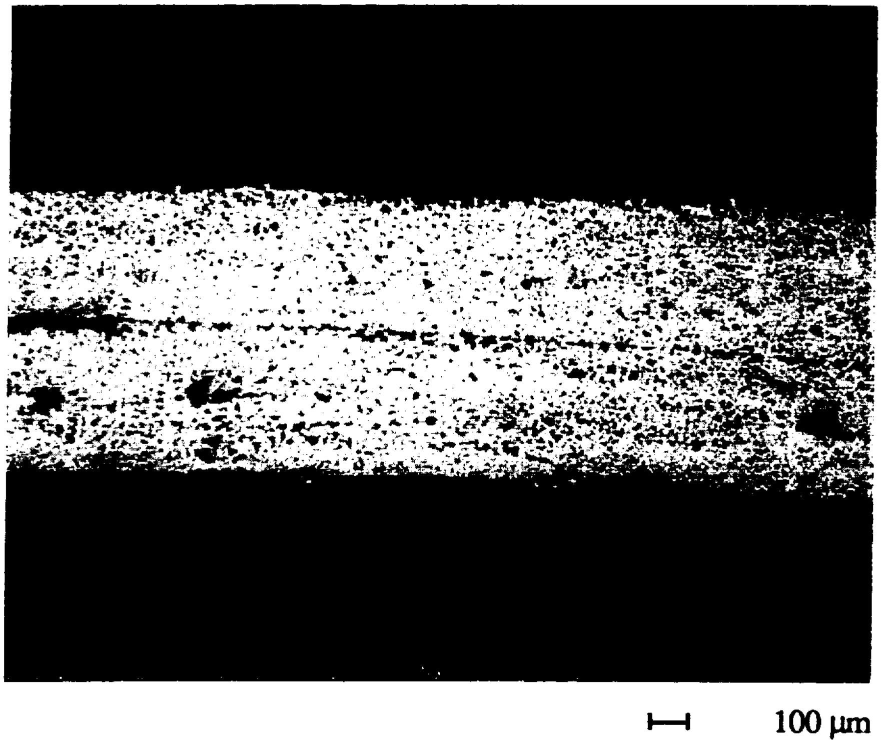

Figure 4.14: Circumferential cross-sectional view of Cylinder 062091. The microstructure shown here is typical of the cylinders manufactured for the In-Plane Crossover-Band Spacing experimental program.

where the tow twisted were filled in on the inside surface; however, the twists formed ridges and valleys in the outer surface despite the large winding tension and the use of shrink tape.

Cylinder 062091 was manufactured with the same winding parameters as Cylinder 061991 and a winding tension of 22 N. Tow twisting was dramatically reduced by careful alignment of the fiber delivery path. Four layers of shrink tape were used, two wound left-to-right and two wound right-to-left, to increase the consolidation pressure during cure and reduce the number of gaps observed in Cylinder 061991. The improvements in the winding procedure and increased consolidation pressure resulted in a slightly thinner cylinder with better visual quality, as seen in Figure 4.14.

Cylinders which are 152-mm in diameter with [±30] winding sequences were manufactured to examine the effects of diameter on the compressive response. Cylinder 070291 was wound and cured on a 152-mm diameter steel mandrel with 104 mm between circumferential-crossover bands. A short section of the ±30 layer near one endcap was also wound with several hoop layers to help separate the cylinder and mandrel after cure. The cylinder was covered with two layers of porous release cloth and four layers of shrink tape as with Cylinder 062091. After cure, many techniques were tried to remove the cylinder from the mandrel without success. When a stripping die was used on the reinforced region of the cylinder, the thin portion quickly buckled and then fractured. To remove the rest of the composite material from the mandrel, the cylinder was slit along its length and the material was pried off. This problem was related to the lack of release agent on the mandrel during cure and the thickness of the cylinder.

Cylinder 081291 was wound on a 608 mm long aluminum mandrel with similar winding and curing parameters as Cylinder 070291. To prevent the cylinder from bonding to the mandrel, the amount of release agent on the mandrel was increased. Due to high

Table 4.3: Winding and curing parameters for cylinders manufactured for the Cylinder Scale experimental program.

| Cylinder Number | Winding Sequence | Mandrel (mm) | Bandwidth (mm) | Dwell (rev.) | Circuits per Coverage | Circuits per Pattern | Circ. X-Over Band Spacing (mm) | Winding Tension (N) | Manuf. Method | Thickness (mm) |
|---|---|---|---|---|---|---|---|---|---|---|
| 061991 | [±30] | 57 al | 3.23 | 0.40206 | 47 | 2 | 76.2 | 31 | S.T. (2) | 0.462 |
| 062091 | [±30] | 57 al | 3.23 | 0.40206 | 47 | 2 | 76.2 | 22 | S.T. (4) | 0.427 |
| 070291 | [±30] | 152 steel | 3.20 | 0.12555 | 129 | 4 | 104 | 22 | S.T. (4) | stuck |
| 081291 | [±30] | 152 al | 3.23 | 0.44937 | 129 | 1 | 104 | 22 | S.T. (4) | 0.452 |
| 030692 | [±30] | 152 al | 3.20 | 0.45709 | 129 | 4 | 104 | 22 | S.T. (4) | 0.457 |
| 122990 | $[90/\pm30]_{as}$ | 152 steel | 2.77 | 0.28501 | 127 | 14 | 29.7 | 18 | S.T. (2) | 1.35 |
| 010891 | $[\pm30/90]_{as}$ | 152 steel | 2.79 | 0.28501 | 127 | 14 | 29.7 | 20 | S.T. (2) | 1.45 |
| 022591 | $[0/\pm60]_{as}$ | 152 steel | 3.25 | 0.13281 | 73 | 5 | 27.7 | 22 | S.T. (2) | 1.42 |
| 010191 | $[90_3/\pm30_3]_{as}$ | 152 steel | 3.25 | 0.21727 | 129 | 13 | 31.2 | 22 | S.T. (2) | 4.37 |
| 030991 | $[\pm30_3/90_3]_{as}$ | 152 steel | 3.28 | 0.32714 | 129 | 13 | 31.8 | 22 | S.T. (2) | 4.11 |
| 053091 | $[0_3/\pm60_3]_{as}$ | 152 steel | 3.28 | 0.13281 | 73 | 5 | 27.7 | 22 | S.T. (2) | 4.06 |

S.T.(#) -- Refers to the shrink tape manufacturing technique where the number in parentheses indicates the number of layers of shrink tape

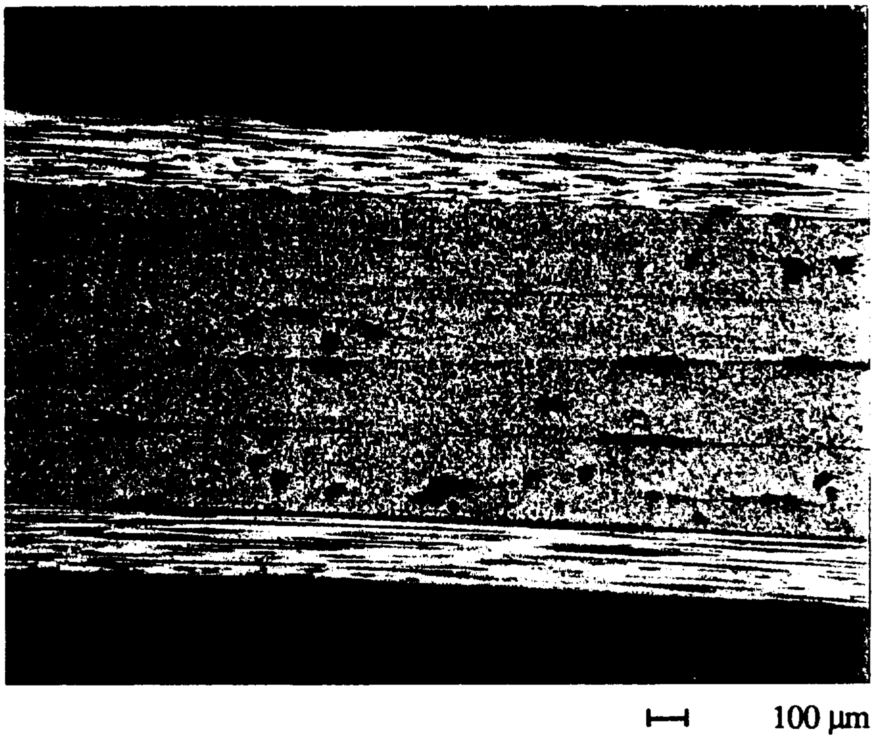

Figure 4.15: Circumferential cross-sectional view of Cylinder 122990. The microstructure shown here is typical of all six-ply cylinders manufactured for the Cylinder Scale experimental program.

room temperature and humidity during winding, the prepreg tow twisted excessively, producing many ridges and gaps in the cured cylinder. The surface quality of this cylinder is similar to Cylinder 061991. Cylinder 030692 was wound with the same winding and curing parameters as Cylinder 081291 when room temperature and humidity conditions were more favorable with a corresponding improvement in quality. The quality of this cylinder was comparable to Cylinder 062091.

The effects of thickness type scaling on cylinder quality and compressive response were investigated with cylinders wound with more than one winding angle. A quasi-isotropic, $\pi/3$, laminate was chosen for this experimental program based on an analytical study by Hahn, Jensen, Claus, and Hipp [20] which demonstrated that a $[90/\pm30]_s$ cylinder had the largest buckling load for a 6-ply laminated cylinder chosen from $[90/\pm\theta]_s$, $[\pm\theta/90]_s$, $[0/\pm\theta]_s$, and $[\pm\theta/0]_s$ lamination sequences. Each cylinder in this experimental program was wound at room temperature and cured with two layers of shrink tape.

A $[90/\pm30_2/90]$ winding sequence was used to produce Cylinder 122990. To help prevent gaps in the layer coverage compared to previous winding trials, the amount of tow overlap was increased by decreasing the bandwidth to 3.3 mm. Microscopic examination, shown in Figure 4.15, revealed a good distribution of fibers and a modest void content. The microstructure of this cylinder was typical of all six-ply specimens produced during this experimental program.

Ply order was investigated by changing the order of the layers to $[\pm30/90_2/\pm30]$ to produce Cylinder 010891. This cylinder was wound and cured in a fashion similar to Cylinder 122990. Although this cylinder was slightly thicker (1.45 mm versus 1.35 mm for Cylinder 122990), the void content, and internal and external surfaces are comparable.

The effects of winding mechanics was examined by rotating the quasi-isotropic winding sequence to produce Cylinder 022591 which consisted of a $[0/\pm60_2/0]$ winding sequence. Bandwidth and circumferential crossover-band spacing were matched with Cylinder 122990 so that mechanical results could be compared irrespective of the crossover pattern. While winding the 0° layers, the prepreg tow was wound approximately 180° around the end cap to maintain fiber tension. Several tows on the inside 0° layer slipped near the endcap and produced gaps in the cured material. Slippage was prevented in the outer layer by the adhesive nature of the previously-wound plies.

Each of the previous six-ply cylinders was manufactured again with a thickness scale factor of 3. Cylinder 010191 was wound with a $[90_3/\pm30_6/90_3]$ winding sequence and the same crossover pattern as its thin companion, Cylinder 122990. Although the winding and curing parameters for this cylinder were the same as those used previously, the visual quality of the cured material is lower. These procedures resulted in a larger void content and an increased per-ply thickness, as seen in Figure 4.16.

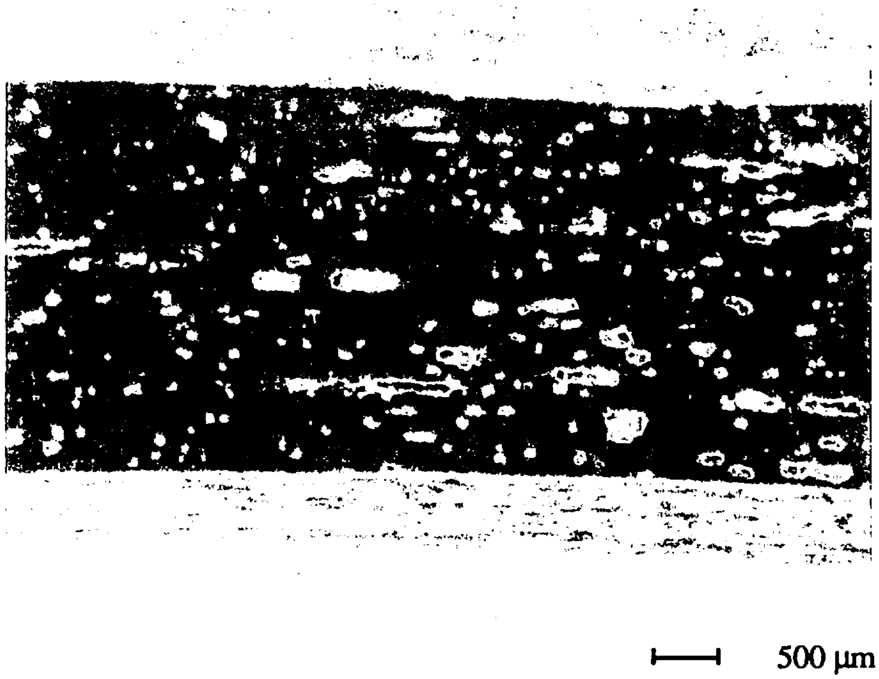

Figure 4.16: Circumferential cross-sectional view of Cylinder 010191.

Cylinder 030991 was wound on the 152-mm diameter, 457-mm long steel mandrel with a $[\pm30_3/90_6/\pm30_3]$ winding sequence. Circumferential-crossover band spacing and winding procedures were similar to Cylinder 010891. To reduce the void content from that observed in Cylinder 010191, one layer of breather material was stretched over the two layers of shrink tape. A vacuum bag was then placed over the breather and fitted with a vacuum port. During cure, -254 mm of Hg was applied to the vacuum bag to help remove entrapped air and volatiles. No external pressure, other than the shrink tape, was applied to the cylinder during cure and the vacuum bag was vented to the atmosphere prior to gelation to prevent the formation of wrinkles. No wrinkles were observed in the cured material and subsequent micrographic inspection of this cylinder, revealed a void content similar to Cylinder 010191.

Cylinder 053091 was manufactured with a $[0_3/\pm60_6/0_3]$ winding sequence and with the same winding pattern as the Cylinder 022591. After winding, the cylinder was covered with two layers of porous release cloth and two layers of shrink tape. In an attempt to reduce the void content in this cylinder compared to the previously manufactured 18-ply cylinders, two additional layers of shrink tape were applied. No changes were made to the curing procedure and the resulting surface finish of this cylinder is similar to the previously manufactured 18-ply cylinders. By comparing the microstructure of the cured cylinders, the increased number of shrink-tape layers seems to have reduced the size and quantity of voids.

### 4.3.4 Symmetry of the Laminated-Shell Regions

The goal of this experimental program was to study the effect of symmetry in the laminated-shell regions on the compressive response. Since antisymmetric laminates will deform out of plane prior to failure due to extension-bending coupling, the critical buckling loads of cylinders with antisymmetric winding sequences may be different than symmetrically-wound cylinders. The cylinders wound for this experiment consisted of two ±30° layers with the circumferential-crossover bands stacked through the thickness.

Cylinder 012092 was wound with one layer directly on top of the other on the 152-mm diameter, 608-mm long aluminum mandrel and cured with two layers of porous release cloth and four layers of temperature-sensitive shrink tape. This produced a [+30/-30/+30/-30] laminate configuration in one half of the laminated regions and a [-30/+30/-30/+30] laminate configuration in the other half, i.e. an antisymmetric laminate. Since the laminated-shell regions were the location of interest, a winding pattern with three circumferential-crossover bands along the length of the compression specimen was chosen. The winding parameters for this experimental program are shown in Table 4.4.

The same winding parameters were used to manufacture Cylinder 021192; however, the winding procedure was slightly different. After the first helical layer was wound, the mandrel was removed from the winding machine, the left and right ends of the mandrel were reversed without rotating the mandrel about its longitudinal axis, and the mandrel was reinstalled in the winding machine to wind the second layer. This procedure resulted in [-30/+30/+30/-30] and [+30/-30/-30/+30] laminated-shell regions; i.e., a symmetric laminate. Although Cylinder 012092 contained slightly more tow twists than Cylinder 021192, the microstructural quality for both cylinders is similar to that shown in Figure 4.17.

### 4.3.5 Winding Sequence

The effect of winding sequence was investigated by altering the ply order of a $[90/\pm30_2/90]$ cylinder to obtain a $[\pm30/90_2/\pm30]$ winding sequence. This variation was studied by comparing Cylinders 122990 and 010891. Details of the manufacture of these cylinders can be found in Section 4.3.3.

### 4.3.6 Through-the-Thickness Crossover-Band Location

In filament-wound shells with more than one helically-wound layer, the relative position of the crossover bands from layer to layer may influence the compressive behavior of the shell. Alternating the position of the circumferential-crossover bands, or varying their spacing, may improve the postbuckling strength or delay the initiation of fracture. To investigate the effect of the through-the-thickness crossover-band location, three cylinders were manufactured on the 152-mm diameter 608-mm long steel mandrel with $[\pm30/90_2/\pm30]$ winding sequences. An antisymmetric configuration was chosen so that results from the present study can be compared to cylinders manufactured for the Winding Sequence experimental program.

Cylinder 012592 was wound with both helical layers containing crossover-band spacings of 83 mm and the same carriage starting and stopping positions. This procedure

Table 4.4: Manufacturing parameters used to produce compression specimens for the Symmetry of the Laminated-Shell Regions experimental program.

| Cylinder Number | Winding Sequence | Mandrel (mm) | Bandwidth (mm) | Dwell (rev.) | Circuits per Coverage | Circuits per Pattern | Circ. X-Over Band Spacing (mm) | Winding Tension (N) | Manuf. Method | Thickness (mm) |
|---|---|---|---|---|---|---|---|---|---|---|
| 012092 | $[\pm30]_{as}$ | 152 al | 3.23 | 0.38190 | 128 | 5 | 82.8 | 22 | S.T. (4) | 0.912 |
| 021192 | $[\pm30]_{s}$ | 152 al | 3.23 | 0.38190 | 128 | 5 | 82.8 | 22 | S.T. (4) | 0.869 |

S.T.(#) -- Refers to the shrink tape manufacturing technique where the number in parentheses indicates the number of layers of shrink tape

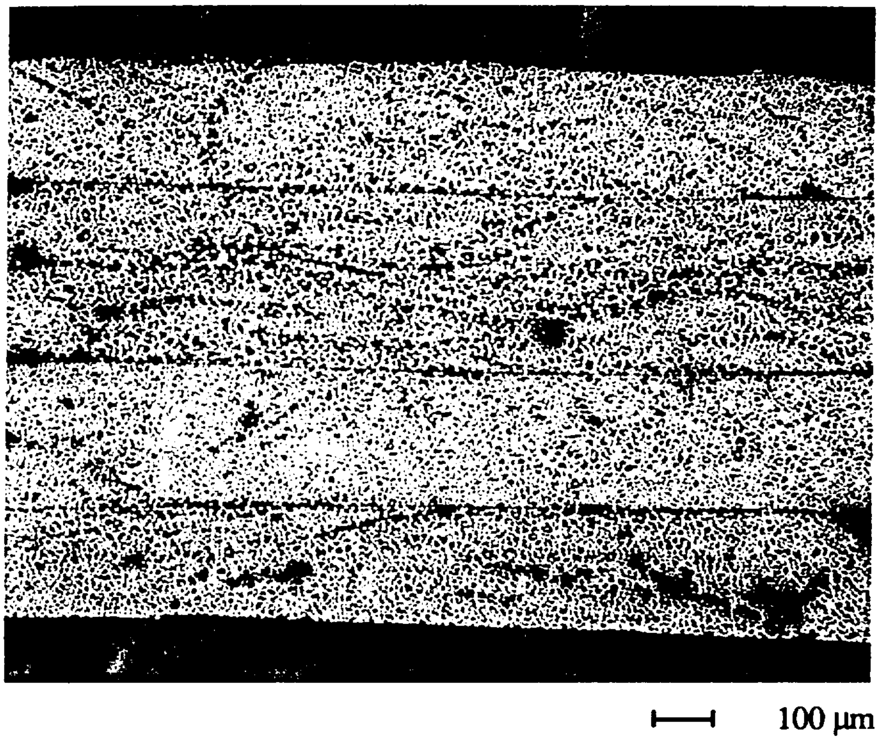

Figure 4.17: Circumferential cross-sectional view of Cylinder 012092. The microstructure shown here is typical of the cylinders manufactured for the Symmetry of the Laminated-Shell Regions experimental program.

resulted in the circumferential and helical-crossover bands stacked through the thickness. The winding parameters used for the helical layers in this cylinder, shown in Table 4.5, were the same as Cylinder 012092. All cylinders manufactured for this experimental program were cured with two layers of porous release cloth and four layers of shrink tape. Figure 4.18 contains a photomicrograph of Cylinder 012592 which is representative of the cylinders manufactured for the Through-the-thickness Crossover-Band Location experimental program.

An alternating configuration of circumferential-crossover bands was used to manufacture Cylinder 013092 . To achieve this configuration, both layers were wound with the same crossover-band spacing; however, the carriage start and stop positions for the second layer were shifted to the left by exactly one-half of the circumferential-crossover band spacing. Unfortunately, the room temperature during winding was quite high and the prepreg tow twisted many times. The cylinder was covered and cured with the same procedures as Cylinder 012592; however, the tow twisting caused many ridges and gaps in the cured cylinder. Cylinder 030592 was wound on a cooler day which reduced the amount of tow twisting. The winding parameters used for this cylinder were the same as Cylinder 013092 and the cured surfaces of this cylinder are much smoother than the previous attempt.

The third winding configuration (Cylinder 030992) consisted of a wide circumferential crossover-band spacing on the outside of the cylinder and a narrow spacing on the inside. The narrow crossover-band spacing was exactly half of the wide spacing. Unfortunately, since the carriage start and stop positions were the same, the crossover bands did not stack through the thickness as expected. The bands on the outside bisected

Table 4.5: Manufacturing parameters used to produce compression specimens for the Through-the-Thickness Crossover-Band Location experimental program.

| Cylinder Number | Winding Sequence | Mandrel (mm) | Bandwidth (mm) | Dwell (rev.) | Circuits per Coverage | Circuits per Pattern | Circ. X-Over Band Spacing (mm) | Winding Tension (N) | Manuf. Method | Thickness (mm) |
|---|---|---|---|---|---|---|---|---|---|---|
| 012592 | $[\pm 30/90]_{as}$ | 152 steel | 3.23 | 0.38190 | 128 | 5 | 82.8 | 22 | S.T. (4) | 1.34 |
| 013092 | $[\pm 30/90]_{as}$ | 152 steel | 3.23 | 0.38190 | 128 | 5 | 82.8 | 22 | S.T. (4) | 1.36 |
| 030592 | $[\pm 30/90]_{as}$ | 152 steel | 3.23 | 0.38190 | 128 | 5 | 82.8 | 22 | S.T. (4) | 1.36 |
| 030992i | $[\pm 30/90]_{as}$ | 152 steel | 3.25 | 0.43151 | 127 | 10 | 82.8 | 22 | S.T. (4) | 1.34 |
| 030992o | | | 3.23 | 0.38190 | 128 | 5 | 41.4 | | | |

S.T.(#) -- Refers to the shrink tape manufacturing technique where the number in parentheses indicates the number of layers of shrink tape

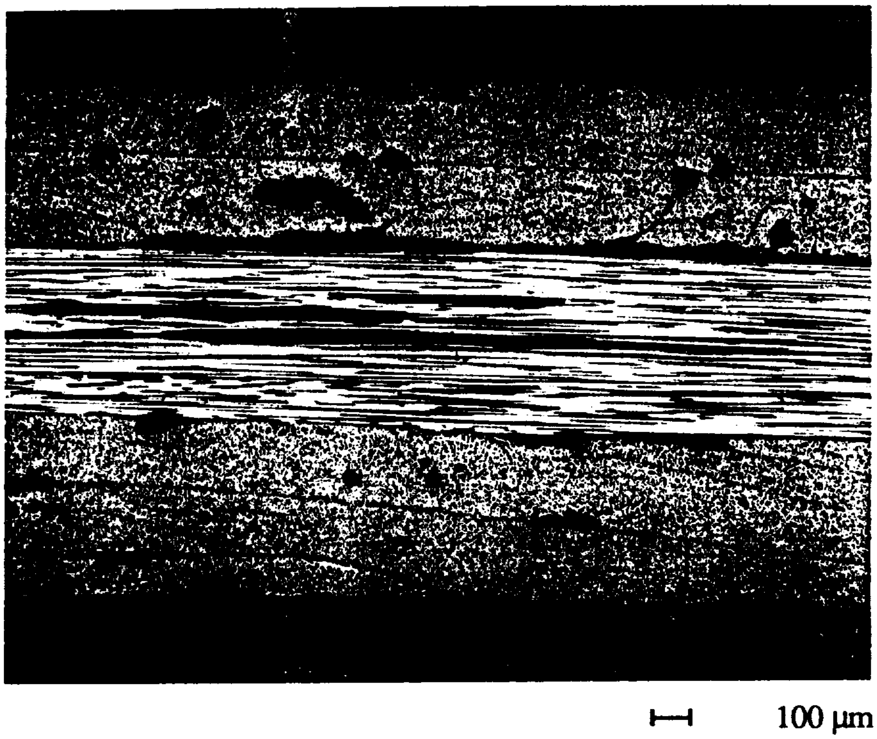

Figure 4.18: Circumferential cross-sectional view of Cylinder 012592. The microstructure shown here is typical of the cylinders manufactured for the Through-the-Thickness Crossover-Band Location experimental program.

the inner layer producing alternating circumferential-crossover bands. A schematic of the cross section of each cylinder manufactured for this experimental program is shown in Figure 4.19.

As discussed in the Section 4.3.4, stacking the crossover bands through the thickness creates an antisymmetric cylinder if the crossover-band spacing is the same for each layer. When the alternating and wide/narrow configurations were wound, some regions of the cylinder were symmetrically laminated, as shown in Figure 4.20. These regions may affect the prebuckling and postbuckling deformations differently than the antisymmetric regions due to the differences in the extension-bending stiffnesses. The amount of symmetrically laminated material is 0, 62.5, and 50 percent for the stacked, alternating, and wide/narrow crossover-band configurations respectively.

### 4.3.7 Winding Temperature

Due to the microstructural quality obtained when a heater was used to promote resin flow and compaction during early winding investigations, the effect of heated winding on the compressive response of filament-wound cylinders was examined. Two cylinders with $[90/\pm30_2/90]$ winding sequences were manufactured to investigate the effects of heated winding on the compressive response. Cylinder 031092 was wound on the 152-mm diameter, 608-mm long aluminum mandrel with stacked crossover bands. The heater, shown in Figure 4.5, was used to elevate the temperature of the tow until resin flow was observed. This cylinder was cured in the oven without additional materials on the exterior surface. Since the cylinder was not rotated during cure, the outside surface of the cured cylinder is quite resin rich with many sag marks in the resin and drips along one side. Several locations in the excess resin contain bubbles which were either squeezed out of the cylinder during manufacture or are a result of outgassing of the resin.

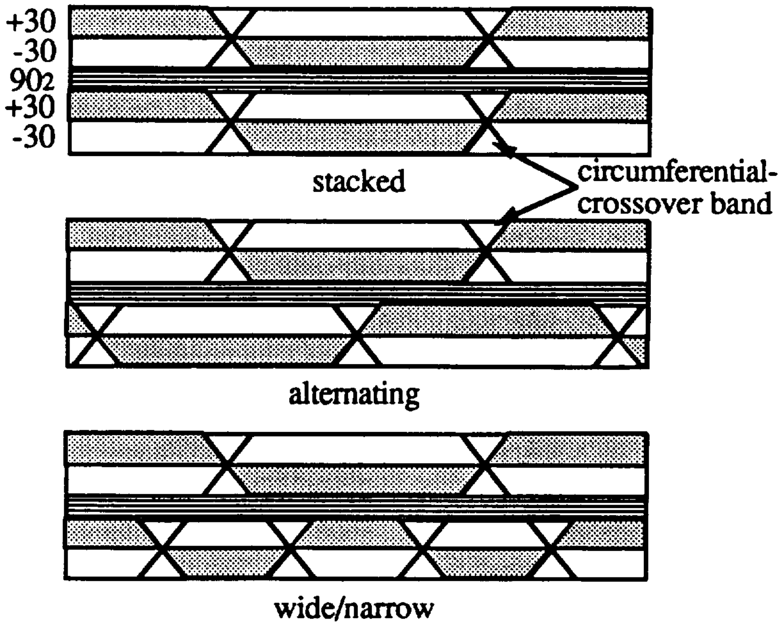

Figure 4.19: Crossover band configurations for cylinders manufactured for the Through-the-Thickness Crossover-Band Location experimental program.

Cylinder 031392 was wound with the same winding procedure as Cylinder 031092, however, this cylinder was covered with porous release cloth and shrink tape. The shrink tape produced a thinner cylinder with a very uniform wall thickness, as shown in Figure 4.21. The winding parameters for both heated cylinders are the same as Cylinder 012592 except for the sequence of layers.

## 4.4 Conclusions

Many combinations of winding and curing parameters have been investigated to produce filament-wound cylinders with a uniform thickness, minimum void content, and a high fiber-volume fraction. A summary of these parameters and the resulting qualitative visual quality is listed in Table 4.6. Heated winding improves the microstructural quality of small diameter filament-wound cylinders; however initially, large diameter cylinders appeared to have similar quality when wound at room temperature. Although the use of standard vacuum-bagging procedures yields composite cylinders with a very low void content, it is not a practical technique due to the added complexity and increased likelihood of wrinkling. Curing without external pressure, or pressure due to hand-wound release cloth alone, is unacceptable due to the large void content and relatively poor fiber-volume fraction. The preferred production technique is to wind porous release cloth tightly over the cylinder and cover it with shrink tape to apply an external compaction pressure.

When the shrink-tape technique was used to manufacture the cylinders for compression testing, the cured quality was quite consistent. Differences in the visual appearance were typically due to inaccuracies in the winding rather than the cure procedures. Tow twisting was a recurrent problem which was hampered by high room temperatures and humidity. Another common defect was caused by misplacement of the tows during winding either from inaccurate rotation of the payout eye or slippage of the tow on the mandrel.

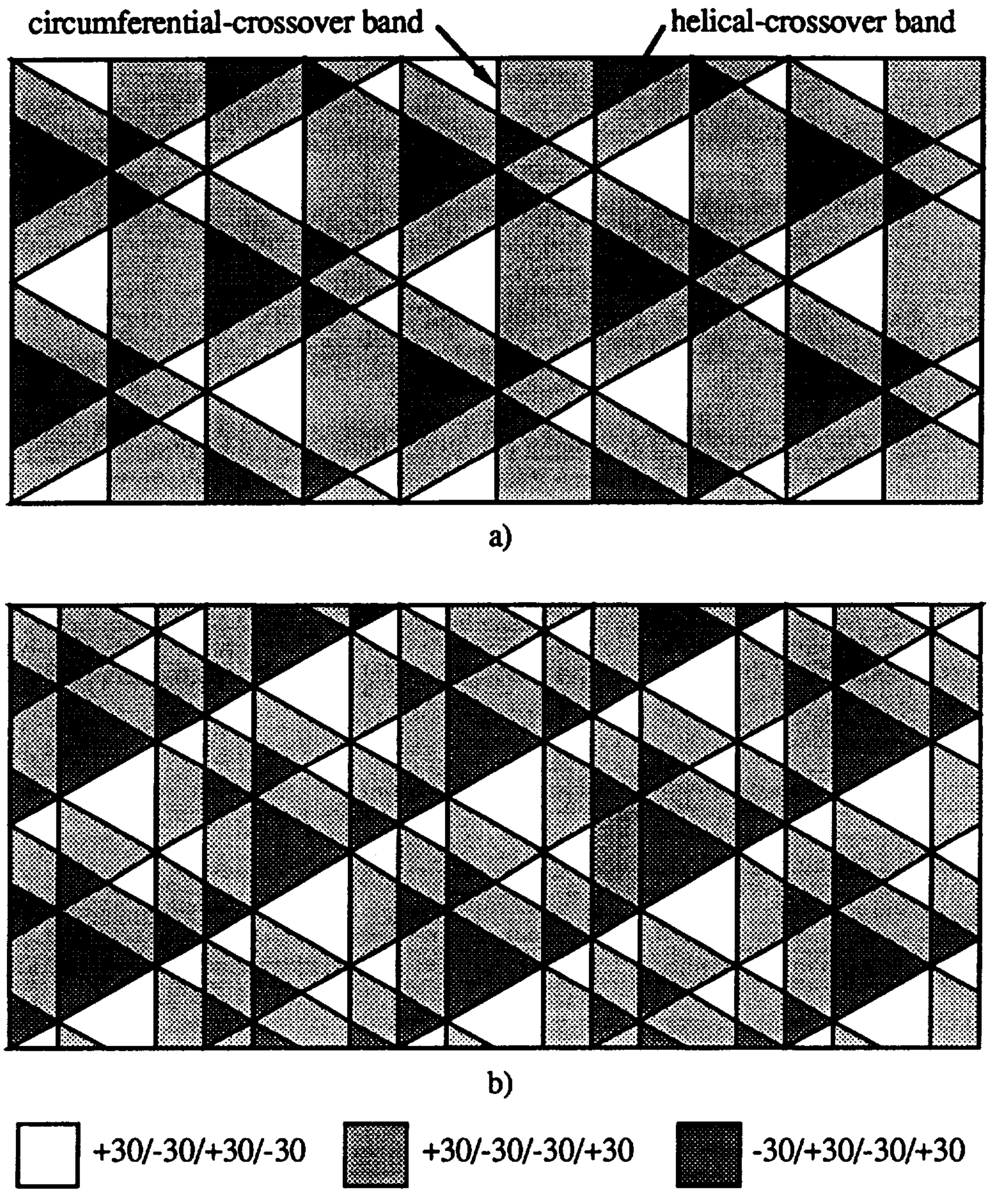
circumferential-crossover band
helical-crossover band
+30/-30/+30/-30
+30/-30/-30/+30
-30/+30/-30/+30

a)

b)

Figure 4.20: A map of the cylinder symmetry for the a) alternating, and b) wide/narrow, crossover-band configurations.

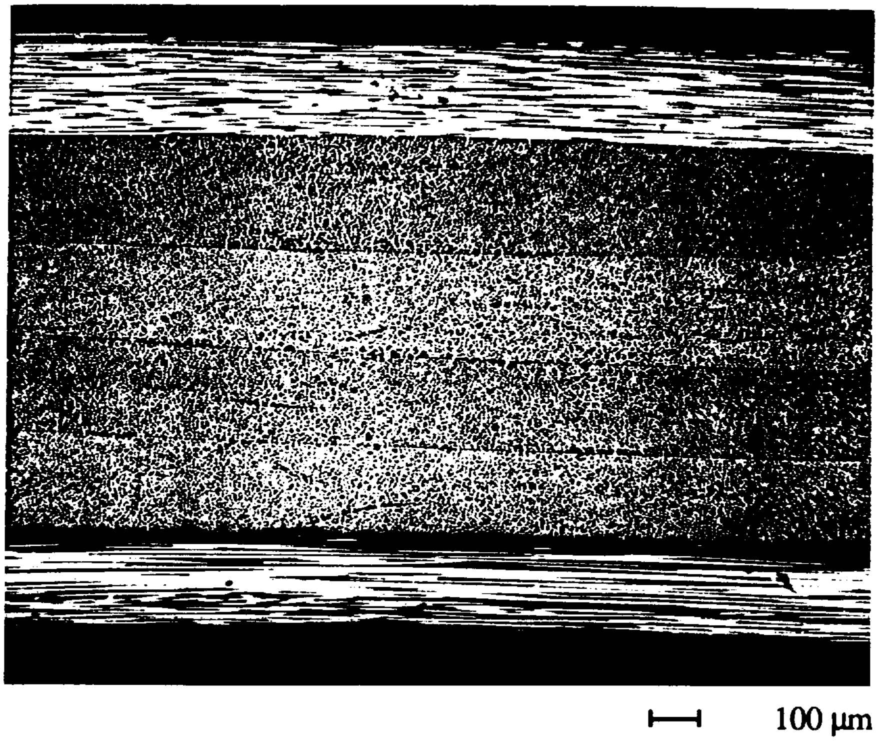

Figure 4.21: Circumferential cross-sectional view of Cylinder 031392.

The effects of scale on the visual quality of filament-wound cylinders is quite evident in the multi-layered specimens. The differences in the six-ply, 57-mm and 152-mm diameter specimens is quite small, indicating little influence of diameter on quality. When the 18-ply cylinders were manufactured, the cured material contained larger and more numerous voids than the 6-ply cylinders with the same winding sequence.

Use of an elevated winding temperature can improve the quality of filament-wound cylinders by simultaneously lowering the void content and increasing the fiber-volume fraction. Although the manufacturing procedures are slightly more complex, the improvement in quality of the 6-ply cylinders is readily apparent. Similar improvements in thick cylinders might be obtained by using an elevated winding temperature.

Table 4.6: Summary of results for the manufacture of filament-wound cylinders.

| Diameter | Winding Sequence | Amnt. of Twisting | Room Temp. and Humidity | Winding Temp. | Pressureization Method | Microscopic Quality | Macroscopic Quality |
|---|---|---|---|---|---|---|---|
| large | $[90/\pm30]_{as}$ | low | moderate | room | auto. w/ bleed | poor | poor |
| small | $[90/\pm30]_{as}$ | low | moderate | room | auto. w/o bleed | poor | poor |
| small | $[90/\pm30]_{as}$ | low | moderate | room | none | very poor | poor |
| small | $[90/\pm30]_{as}$ | low | moderate | elevated | little | very poor | fair |
| large | $[90/\pm30]_{as}$ | low | moderate | room | some | fair | good |
| small | $[90/\pm30]_{as}$ | low | moderate | room | shrink | fair | good |
| small | $[90/\pm30]_{as}$ | low | moderate | elevated | shrink | very good | very good |
| large | $[90/\pm30]_{as}$ | low | moderate | room | shrink | very good | very good |
| small | $[\pm30]$ | low | moderate | room | shrink | good | very good |
| large | $[\pm30]$ | high | high | room | shrink | fair | fair |
| small | $[\pm30]$ | low | moderate | room | shrink | good | very good |
| large | $[\pm30]$ | high | high | room | shrink | fair | fair |
| large | $[\pm30/90]_{as}$ | low | moderate | room | shrink | good | very good |
| large | $[\pm30/90]_{as}$ | high | high | room | shrink | fair | fair |
| large | $[90/\pm30]_{as}$ | low | moderate | elevated | none | excellent | poor |
| large | $[90/\pm30]_{as}$ | low | moderate | elevated | shrink | excellent | excellent |

# 5.0 MATERIAL AND GEOMETRIC CHARACTERIZATION

The quality of composite structures is difficult to quantify. Depending on the specific application, the quality may be governed by the appearance, microstructure, void content, geometry, stiffness, strength, damage tolerance, or any combination of these parameters. According to Tennyson and Muggeridge [3], when thin-cylindrical shells are subjected to axial compression, the critical quality issue which affects the performance is the extent of initial geometric imperfections. In this research, the quality of the filament-wound shells was examined to determine the relationships between the compressive performance and the manufacturing parameters. The quality was characterized at two levels. First, the microstructure of the composite material was examined qualitatively by visual examination using photomicrographs and quantitatively with fiber volume fraction and void content measurements. The second quality level involved the macroscopic appearance, thickness distribution, and geometric similarity to a perfect cylinder. In the following sections, the equipment, procedures, and results of the material and geometric characterizations are discussed.

## 5.1 Material Characterization

Defects in filament-wound materials often consist of voids, resin rich regions, wrinkles, twisted tows, and fiber crossovers. During the development of the optimal manufacturing method and manufacture of specimens for compression testing, visual techniques were used to examine the microstructure, and interior and exterior surfaces to judge the overall quality of the cylinder. The following sections contain additional procedures, results, and discussion of the visual examination, fiber volume fraction, and void content of filament-wound cylinders used to develop the optimal manufacturing techniques and relate the manufacturing procedures to the compressive performance.

### 5.1.1 Visual Examination

Small sections were machined from each cured cylinder for microscopic examination of the material quality. Most sections were cut perpendicular to the longitudinal axis of the cylinder; however, several sections were also machined parallel to the winding angle in the neighborhood of a crossover band. Each sample was encapsulated in room-temperature curing epoxy as described in Section 3.2.2. A postcure was often performed for several hours at 70°C to increase the hardness of the potting resin thus making it easier to grind and polish. The samples were hand ground and polished using standard metallurgical procedures. Photomicrographs of the 2, 4, 6, and 18-ply specimens were taken with an inverted microscope with an attachment for Polaroid® single sheet film.

The distribution of fibers, matrix, and voids can be clearly observed from the photomicrographs. Although only a small section can be observed at one time, representative sections can be quickly identified prior to photographing. When cylinders are wound at room temperature, air can become trapped when the tow crosses an uneven surface such as a tow twist or crossover band. Voids within a crossover can be observed in Figure 5.1.

### 5.1.2 Fiber-Volume Content

The fiber-volume content of selected cylinders was measured using the procedure set forth in ASTM D 3171-90 [21]. This procedure consisted of machining small (6.4 mm by 6.4 mm) sections from the cylinder and then dissolving the matrix in a solution of

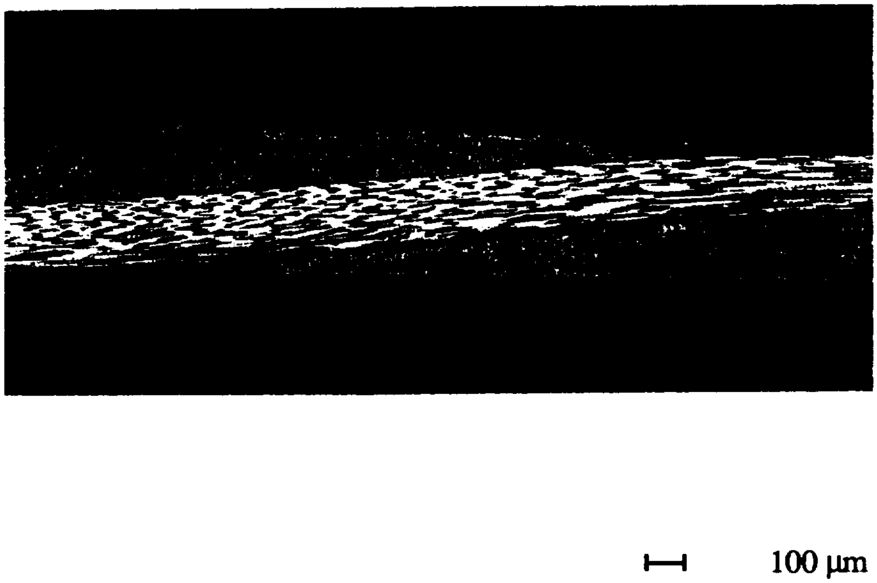

Figure 5.1: Photomicrograph of Cylinder 062091 cut parallel to the winding direction in the neighborhood of a fiber-crossover band.

concentrated sulfuric acid and 30 percent hydrogen peroxide. The density of the sample was measured before digestion and the fiber weight was measured after washing and drying the fibers to remove any residual acid. Using the manufacturer's fiber density value of 1.75 g/cc, the fiber-volume content can be computed with the following relationship,

$$V_f = \frac{W}{w}\frac{\rho_c}{\rho_f} \tag{5.1}$$

where, $V_f$ represents the fiber volume fraction, $W$ is the weight of the fiber after digestion, $w$ represents the weight of the composite, $\rho_f$ represents the density of the fibers, and $\rho_c$ represents the density of the composite. The results from these tests are listed in Table 5.1.

Several visual observations which were made in the manufacturing optimization study, are verified with the volume-fraction results. Curing room-temperature wound cylinders without the use of external pressure, as with Specimen 090190HS, resulted in a thick part with many voids; likewise, the fiber-volume content of Specimen 090190HS is much lower than Specimen 092690CC which was wound at an elevated temperature and cured with the use of shrink tape. Cylinder 031092 was also wound at an elevated temperature and contained few voids. This cylinder has a slightly lower fiber-volume content than Specimen 092690CC since no external pressure was applied to this cylinder during cure, resulting in a resin rich layer on the outer surface of the cylinder. The additional vacuum pressure used during cure of Cylinder 030991 made little difference in the amount or size of voids; however, the fiber-volume content is slightly higher, as expected since four layers of shrink tape were used compared to two layers used to manufacture Cylinder 122990.

Winding procedures can also affect the quality of the material. When Cylinder 022591 was wound, several twists were observed in the 0° layers which resulted in resin rich regions and a larger void content than Cylinders 122990 and 011191. Since each

Table 5.1: Fiber volume fractions of selected filament-wound cylinders obtained by acid digestion.

| Cylinder Number | Winding Sequence | Circ. X-Over Band Spacing (mm) | Composite Density (g/cc) | Fiber Wt. Content (%) | Fiber Vol. Content (%) |
|---|---|---|---|---|---|
| 090190HS | $[90/\pm30]_{as}$ | 152 | 1.38 | 65.4 | 51.6 |
| 092690CC | $[90/\pm30]_{as}$ | 3.81 | 1.50 | 72.5 | 62.2 |
| 122990 | $[90/\pm30]_{as}$ | 30.5 | 1.50 | 71.1 | 60.9 |
| 022591 | $[0/\pm60]_{as}$ | 27.9 | 1.41 | 68.5 | 55.2 |
| 010191 | $[90_3/\pm30_3]_{as}$ | 30.5 | 1.47 | 67.5 | 56.7 |
| 030991 | $[\pm30_3/90_3]_{as}$ | 33.0 | 1.40 | 69.0 | 57.5 |
| 011692 | [±30] | 155 | 1.55 | 73.4 | 65.0 |
| 061991 | [±30] | 76.2 | 1.55 | 71.8 | 63.6 |
| 062091 | [±30] | 76.2 | 1.58 | 73.0 | 65.9 |
| 062191 | [±30] | 50.8 | 1.58 | 74.6 | 67.4 |
| 062291 | [±30] | 30.5 | 1.54 | 72.7 | 64.0 |
| 062491 | [±30] | 30.5 | 1.59 | 74.0 | 67.2 |
| 062591 | [±30] | 30.5 | 1.58 | 72.5 | 65.5 |
| 063091 | [±30] | 14.2 | 1.58 | 73.8 | 66.6 |
| 070191 | [±30] | 6.86 | 1.56 | 70.9 | 63.2 |
| 021192 | $[\pm30]_s$ | 85.3 | 1.50 | 74.6 | 63.9 |
| 030992 | $[\pm30/90]_{as}$ | 85/41 | 1.40 | 73.0 | 58.4 |
| 031092 | $[90/\pm30]_{as}$ | 85.3 | 1.49 | 71.8 | 61.2 |

cylinder was covered with two layers of shrink tape and cured in the same fashion, the lower fiber-volume content of Cylinder 022591 is attributed to tow twisting. A comparison of the 57-mm diameter, [±30] cylinders demonstrates that the number of crossovers within a helical layer does not affect the fiber-volume content.

### 5.1.3 Void Content

In an attempt to quantify the void content in selected cylinders, image analysis was performed on the photomicrographs of selected specimens to estimate the amount of voids contained in the composite material. To perform this analysis, the photomicrographs were digitized with a 256-level greyscale scanner at a resolution of 24 dots per millimeter (600 dots per inch). This image was then imported into Image 1.36, a computer software package, for subsequent analysis.

A scale for each image was specified by equating the height of each image to the thickness of the cylinder measured with a ball-end micrometer. The area of the image which corresponded to the entire composite was first measured. Next, the image was converted from a greyscale picture to a black and white image by setting a level of gray which delineated black from white; ie. a threshold. The threshold was adjusted so that the entire image of the composite was white with the exception of the voids. The software was used to measure the black area and the void content was computed as the ratio of the black area to the total area. Results from this analysis are shown in Table 5.2.

Table 5.2: Void contents of selected filament-wound cylinders obtained by image analysis of the photomicrographs.

| Cylinder Number | Winding Sequence | Circ. X-Over Band Spacing (mm) | Winding Temp. | Cure Technique | Void Content (%) |
|---|---|---|---|---|---|
| 090190HS | $[90/\pm30]_{as}$ | 152 | Room | no press. | 4.3 |
| 092690CC | $[90/\pm30]_{as}$ | 3.81 | High | S.T. (2) | 9.0 |
| 122990 | $[90/\pm30]_{as}$ | 30.5 | Room | S.T. (2) | 2.1 |
| 022591 | $[0/\pm60]_{as}$ | 27.9 | Room | S.T. (2) | 6.0 |
| 010191 | $[90_3/\pm30_3]_{as}$ | 30.5 | Room | S.T. (2) | 8.8 |
| 030991 | $[\pm30_3/90_3]_{as}$ | 33.0 | Room | S.T. (2) | 14 |
| 011692 | [±30] | 155 | Room | S.T. (4) | 1.5 |
| 061991 | [±30] | 76.2 | Room | S.T. (2) | 1.1 |
| 062091 | [±30] | 76.2 | Room | S.T. (4) | 0.50 |
| 062191 | [±30] | 50.8 | Room | S.T. (4) | 0.39 |
| 062291 | [±30] | 30.5 | Room | S.T. (4) | 0.40 |
| 062491 | [±30] | 30.5 | Room | S.T. (4) | 0.57 |
| 062591 | [±30] | 30.5 | Room | S.T. (4) | 1.2 |
| 063091 | [±30] | 14.2 | Room | S.T. (4) | 0.053 |
| 070191 | [±30] | 6.86 | Room | S.T. (4) | 0.13 |
| 021192 | $[\pm30]_s$ | 85.3 | Room | S.T. (4) | 6.9 |
| 030992 | $[\pm30/90]_{as}$ | 85/41 | Room | S.T. (4) | 4.3 |
| 031092 | $[90/\pm30]_{as}$ | 85.3 | High | no press. | 1.1 |

S.T.(#) -- Refers to the shrink tape manufacturing technique where the number in parentheses indicates the number of layers of shrink tape

The results of the void content measurements follow the general quality discussions in Chapter 4. The 57-mm diameter [±30] cylinders consistently exhibit the lowest void content. When the number of plies is increased, as in Cylinders 090190HS and 092690CC, the void content increases substantially. Diameter seems to have little influence on the void content as evident by comparing the thick 57-mm cylinders to Cylinders 122990 and 022591, rather, the accuracy of the placement of the tows during winding and the amount of tow twisting seems to be important. Further increases in the number of plies is paralleled by an increase in the void content as was observed in the photomicrographs. The void content for Cylinder 031092 was substantially lower than the other six-ply 152-mm diameter cylinders. This improvement in quality was attributed to the elevated winding temperature.

### 5.1.4 Conclusions

The material quality observed in the present research depends strongly on the manufacturing procedures. Many of these effects were observed in the photomicrographs, as discussed in Chapter 4, and are reflected in the fiber volume fraction and void content measurements. Although the winding pattern does not seem to affect the material quality, tow twisting produces voids, resin rich regions, and thickness variations which are detrimental to the material quality. The improved quality which results from winding at an elevated temperature was also evident from the visual, fiber volume fraction, and void content observations. In conclusion, the manufacturing procedures can greatly affect the quality of filament-wound cylinders and the techniques discussed in Section 5.1 can be used to quantify the material quality.

## 5.2 Geometric Characterization

According to Singer [1], the discrepancy between analytical buckling models of perfect cylinders made of isotropic homogeneous materials and experimental observations are generally attributed to initial geometric imperfections. The extent of imperfection sensitivity of composite cylinders is not as well understood due to the more complex behavior of these materials. In addition to initial geometric imperfections, the anisotropy and transverse-shear sensitivity of these materials can induce substantial prebuckling displacements which may adversely affect the compressive performance. These effects can be accommodated in an advanced analysis of the structure, although the initial geometry of the shell must be determined a priori. The geometry of the cylinders manufactured for this research were evaluated locally by examining the thickness of the shell at many points and globally by measuring the shape of the shell and comparing it to a perfect cylinder.

### 5.2.1 Imperfections in Thickness

Many of the imperfections mentioned previously in the manufacturing and material quality discussions were associated with local changes in thickness. Two techniques were used to quantify the thickness of each cylinder. First, a ball-end micrometer with a resolution of 0.0025 mm was used at random locations around the circumference; five on each end of the specimen. The mean thickness, number of measurements, and standard deviation of the thickness, and length of each compression test specimen are listed in Table 5.3. This technique resulted in a rapid measure of the thickness; however, the defects induced during winding and cure were difficult to quantify since the micrometer can only be used near the machined edges, only a small number of measurements were made, and the diameter of the spherical end is large compared to many of the imperfections. A caliper, with a 0.025-mm resolution, was used to measure the length of each 57-mm diameter cylinder at a number of locations chosen randomly around the circumference of the cylinder. An engineer's scale was used to measure the length of the 152-mm diameter cylinders.

The second thickness-measurement technique was developed to measure each specimen over its entire surface. This technique utilized the McClean-Anderson filament winder and a spring loaded Linear Voltage Displacement Transformer (LVDT, Lucas Schaevitz Model PCA-116) with a 1.6 mm spherical contact tip, clamped to the payout eye of the filament winder, as shown in Figure 5.2. The filament winder was programmed with a zero-degree winding pattern which caused the LVDT to trace longitudinal paths on the cylinder. Output from the LVDT was recorded with an Omega OM-900 data-acquisition system and a Standard 386 personal computer.

An LVDT senses position by the relative location of a ferromagnetic core within a stationary electric coil. Changes in position of the core are linearly related to the changes in voltage within the coils. In this experiment, measured voltages were both positive and negative depending on the position of the core. The LVDT is only capable of measuring relative positions unless some point is arbitrarily chosen as a reference point. For this experiment, the zero point within the LVDT was assumed to be the reference point. The LVDT was calibrated before each experiment by alternately placing a glass microscope slide of known thickness between the LVDT and the mandrel. The measured change in voltage was divided by the thickness of the slide to obtain the calibration constant. The sensitivity of this measuring technique depended on the performance of the LVDT and the OM-900

Table 5.3: Thicknesses and lengths of the compression specimens measured by hand.

| Cylinder Number | Winding Sequence | Cylinder Length (mm) | Mean Thickness (mm) | Number of Measurements | Standard Deviation (x10^-2 mm) |
|---|---|---|---|---|---|
| 122990 | [90/±30]$_{as}$ | 229 | 1.35 | - | - |
| 010891 | [±30/90]$_{as}$ | 229 | 1.45 | - | - |
| 022591 | [0/±60]$_{as}$ | 229 | 1.42 | - | - |
| 010191 | [90$_3$/±30$_3$]$_{as}$ | 229 | 4.37 | - | - |
| 030991 | [±30$_3$/90$_3$]$_{as}$ | 229 | 4.11 | - | - |
| 053091 | [0$_3$/±60$_3$]$_{as}$ | 229 | 4.06 | - | - |
| 061991A | [±30] | 86.1 | 0.445 | 10 | 1.48 |
| 061991B | [±30] | 86.1 | 0.481 | 9 | 3.30 |
| 062091 | [±30] | 86.2 | 0.426 | 9 | 1.20 |
| 062191A | [±30] | 86.2 | 0.416 | 10 | 4.37 |
| 062191B | [±30] | 82.3 | 0.432 | 10 | 2.59 |
| 062291A | [±30] | 85.0 | 0.410 | 11 | 5.11 |
| 062291B | [±30] | 86.5 | 0.419 | 11 | 4.01 |
| 062391A | [±30] | 86.8 | 0.437 | 10 | 2.62 |
| 062391B | [±30] | 85.8 | 0.414 | 10 | 3.02 |
| 062491A | [±30] | 85.4 | 0.406 | 10 | 2.04 |
| 062491B | [±30] | 85.6 | 0.425 | 10 | 1.88 |
| 062591A | [±30] | 85.2 | 0.428 | 10 | 2.67 |
| 062591B | [±30] | 85.7 | 0.429 | 10 | 2.19 |
| 063091A | [±30] | 87.0 | 0.431 | 10 | 1.54 |
| 063091B | [±30] | 85.7 | 0.422 | 10 | 2.51 |
| 070191A | [±30] | 85.8 | 0.447 | 10 | 2.53 |
| 070191B | [±30] | 85.5 | 0.452 | 10 | 2.06 |
| 011692A | [±30] | 84.9 | 0.425 | 9 | 2.47 |
| 011692B | [±30] | 83.8 | 0.437 | 9 | 2.92 |
| 081291A | [±30] | 196 | 0.456 | 10 | 1.85 |
| 081291B | [±30] | 192 | 0.449 | 10 | 1.79 |
| 030692A | [±30] | 206 | 0.454 | 10 | 2.10 |
| 030692B | [±30] | 208 | 0.458 | 10 | 1.78 |
| 012092A | [±30]$_{as}$ | 231 | 0.910 | 10 | 2.19 |
| 012092B | [±30]$_{as}$ | 229 | 0.915 | 10 | 1.79 |
| 021192A | [±30]$_{s}$ | 230 | 0.857 | 10 | 2.34 |
| 021192B | [±30]$_{s}$ | 235 | 0.878 | 10 | 1.31 |
| 012592A | [±30/90]$_{as}$ | 231 | 1.34 | 10 | 2.54 |
| 012592B | [±30/90]$_{as}$ | 227 | 1.33 | 10 | 2.25 |
| 013092A | [±30/90]$_{as}$ | 235 | 1.36 | 10 | 2.45 |
| 013092B | [±30/90]$_{as}$ | 228 | 1.36 | 10 | 3.40 |
| 030592A | [±30/90]$_{as}$ | 235 | 1.36 | 10 | 1.67 |
| 030592B | [±30/90]$_{as}$ | 229 | 1.35 | 10 | 3.33 |
| 030992A | [±30/90]$_{as}$ | 235 | 1.33 | 10 | 1.27 |
| 030992B | [±30/90]$_{as}$ | 228 | 1.34 | 10 | 1.29 |
| 031092A | [90/±30]$_{as}$ | 235 | 1.33 | 10 | 6.05 |
| 031092B | [90/±30]$_{as}$ | 228 | 1.35 | 10 | 6.83 |
| 031392A | [90/±30]$_{as}$ | 228 | 1.21 | 10 | 2.30 |
| 031392B | [90/±30]$_{as}$ | 228 | 1.21 | 10 | 2.31 |

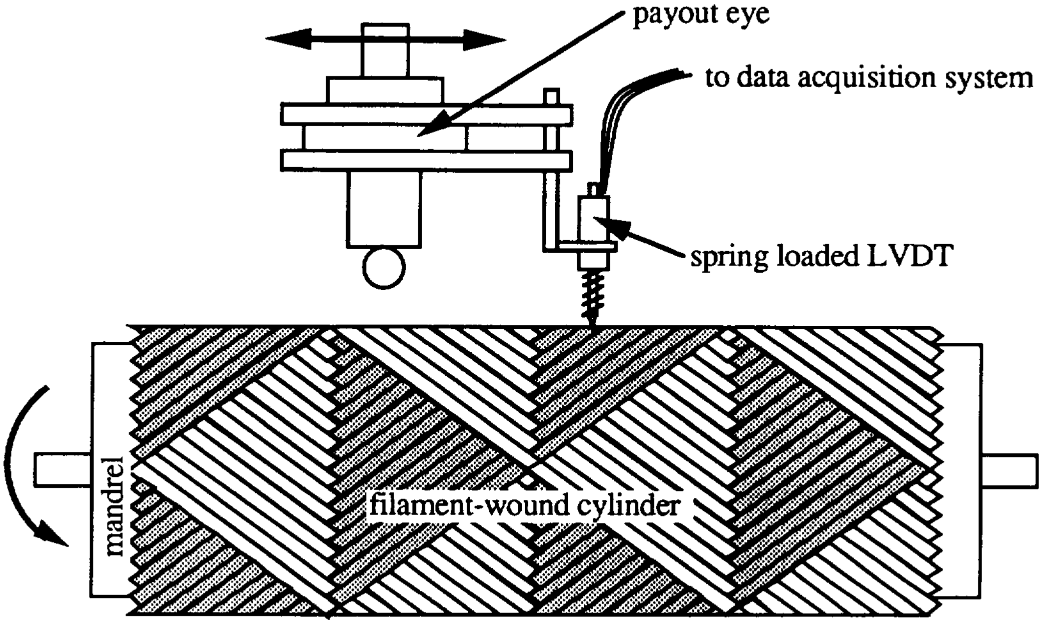

Figure 5.2: Experimental setup for measuring thicknesses of filament-wound cylinders.

system. Since the LVDT is an analog device, its sensitivity is very good; 2.4 mV/V/0.0254 mm. The major errors in this measuring technique are associated with the analog to digital translation of the LVDT signal. Using a ±2 Volt supply voltage, this system had a sensitivity of ±0.983 μm.

To begin testing, the specimen was placed on the mandrel used during manufacture and the zero degree position of the mandrel was marked on the cylinder for future reference. The filament winder was started and data acquisition was initiated either when the LVDT began to move or when it passed a known position on the cylinder. The angular resolution of the thickness data was twice the angular increment programmed into the filament winder (data was only recorded while moving left to right); typically, 6° and 4° for the 57-mm and 152-mm diameter specimens, respectively. The data acquisition rate coupled with the carriage speed dictated the longitudinal spacing of the data points; typically, 1 mm and 4 mm for the 57-mm and 152-mm diameter specimens, respectively.

Four sources of error were identified with this technique. First, the starting point in each scan depended on the coordination of the operator since a keystroke was required to initiate data acquisition. Second, if data acquisition was started when the LVDT began to move, data was recorded during acceleration of the filament winder at the beginning of each stroke. Since the data-acquisition speed was uniform, the data near the starting and ending points was skewed. This problem was minimized by starting data acquisition after full speed of the filament winder was achieved and halting acquisition before the winder began to decelerate. Third, the assumption was made that the inner surface of the filament-wound cylinder and the outer surface of the mandrel were in intimate contact. The fourth source of error was misalignments of the mandrel with respect to the carriage motion. Wobbles were observed in the data which were caused by misalignments of the cylinder axis and the spin axis of the filament winder. Also, the carriage moved at a slight angle to the axis of the cylinder which caused the magnitude of the wobble to vary along the length of the specimen.

To remove the wobble displacements from the cylinder data, the mandrel was scanned with the same winding program. After measuring the outer surface of the cylinder, the composite cylinder was carefully slid along the mandrel until it was outside of the measuring area. The filament winder was started and data was recorded in the same area as the cylinder. Typical scans of the cylinder on the mandrel and the mandrel alone are shown in Figures 5.3 and 5.4, respectively. The resulting data, shown for one stroke of the filament winder in Figure 5.5, consists of two arrays of points measured from the same reference position in the LVDT. Consequently, the thickness of the cylinder is simply the difference between the mandrel data and the cylinder data. As is evident by Figure 5.6, the thickness distribution is devoid of the wobbling motion.

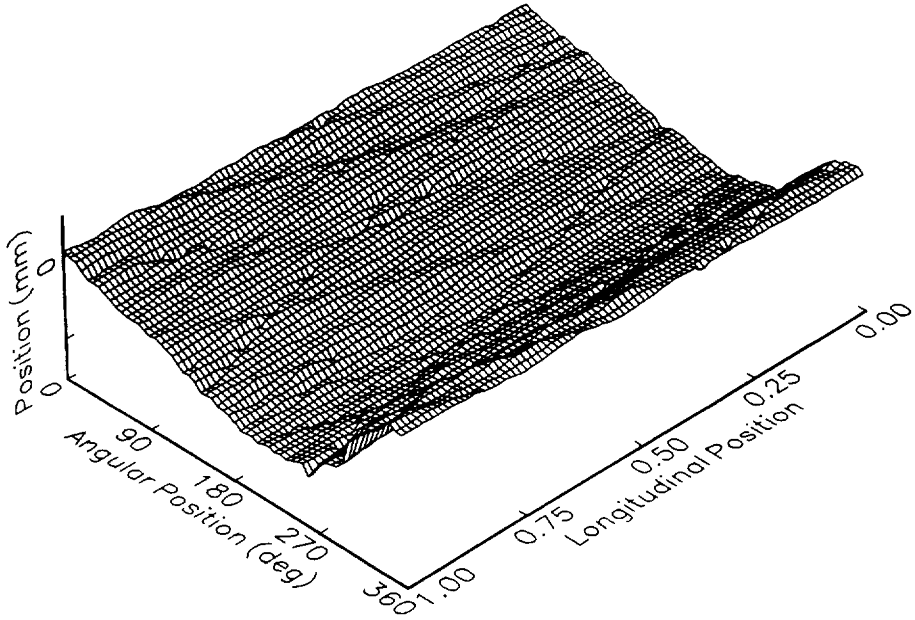

Figure 5.3: Typical displacement field of the filament-wound cylinder on the mandrel relative to a fixed reference position.

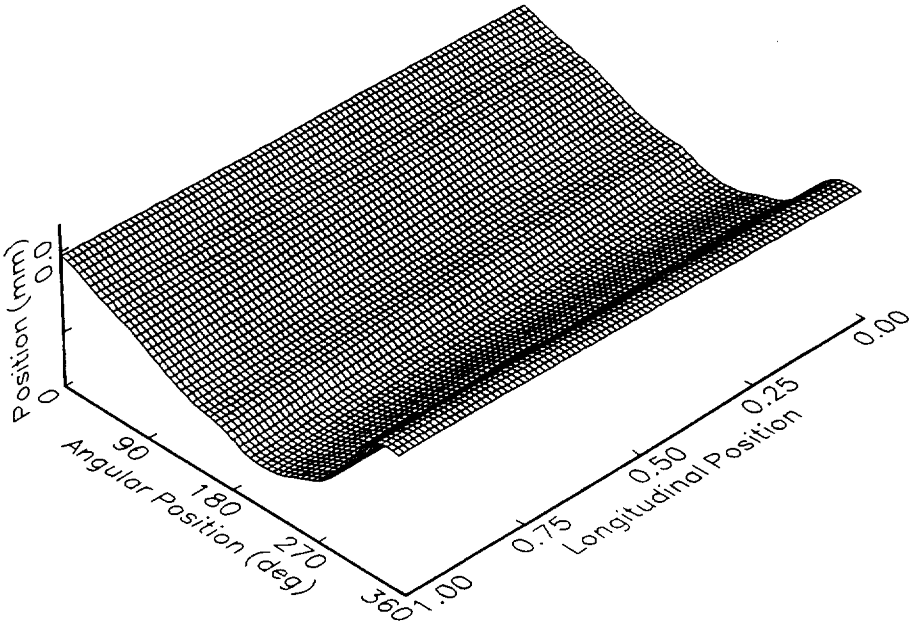

Figure 5.4: Typical displacement field of the mandrel alone relative to a fixed reference position.

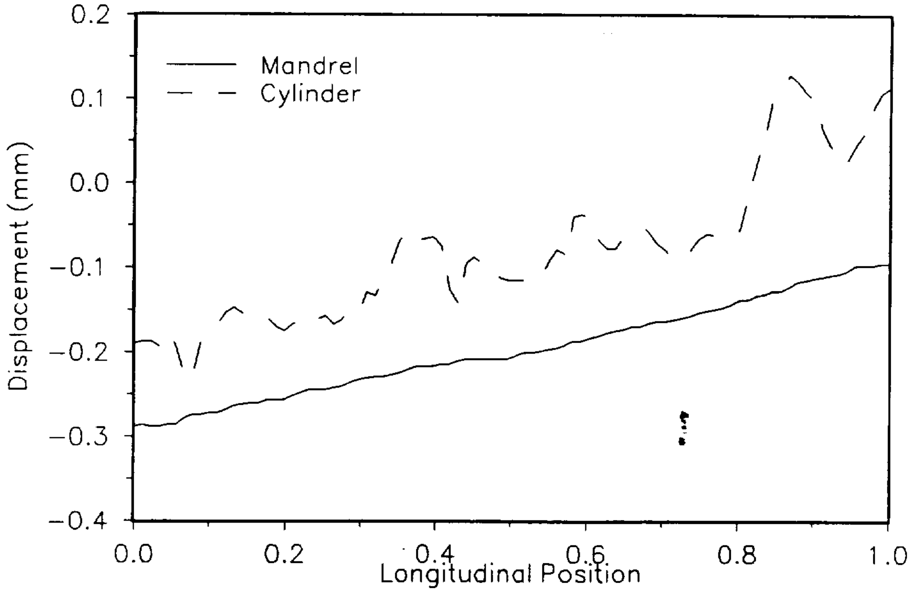

Figure 5.5: Position of the cylinder and mandrel surfaces measured for one stroke.

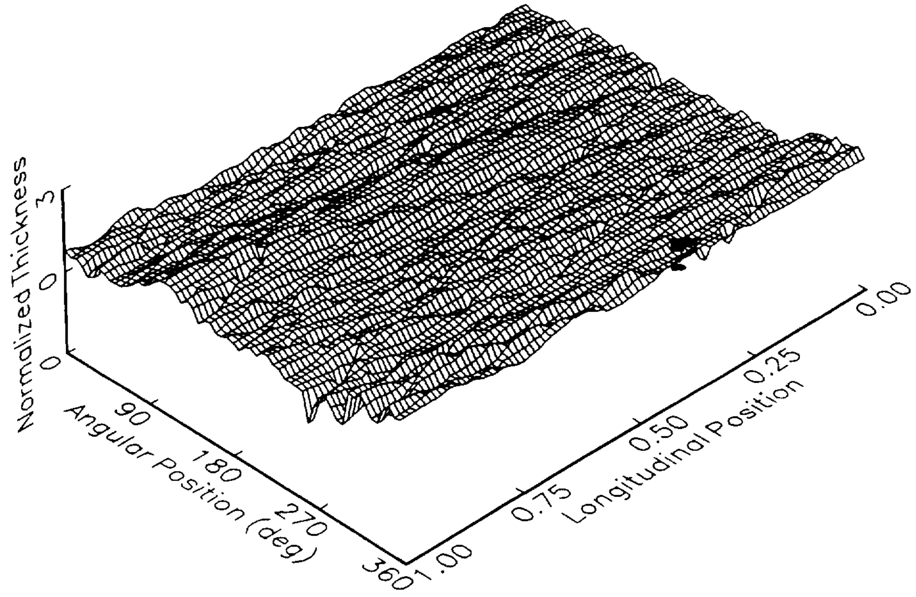

Figure 5.6: Typical thickness field of the filament-wound cylinder.

A Fortran computer program was written to convert the measured LVDT data into thickness distributions and compute statistical parameters on the thickness field such as the mean, standard deviation, root mean square, minimum, maximum, and range. This measuring technique was very sensitive to local thickness imperfections, as shown in Figure 5.7. The photograph and thickness plot correspond to a region of a [±30] cylinder in the neighborhood of a tow which twisted during winding. Figure 5.8 contains the thickness distributions of a a) visually poor-quality cylinder, and a b) high-quality cylinder.

Both specimens were wound at room temperature with similar winding parameters and cured with the shrink-tape technique; however, the effects of tow twisting and fiber misalignment are readily apparent.

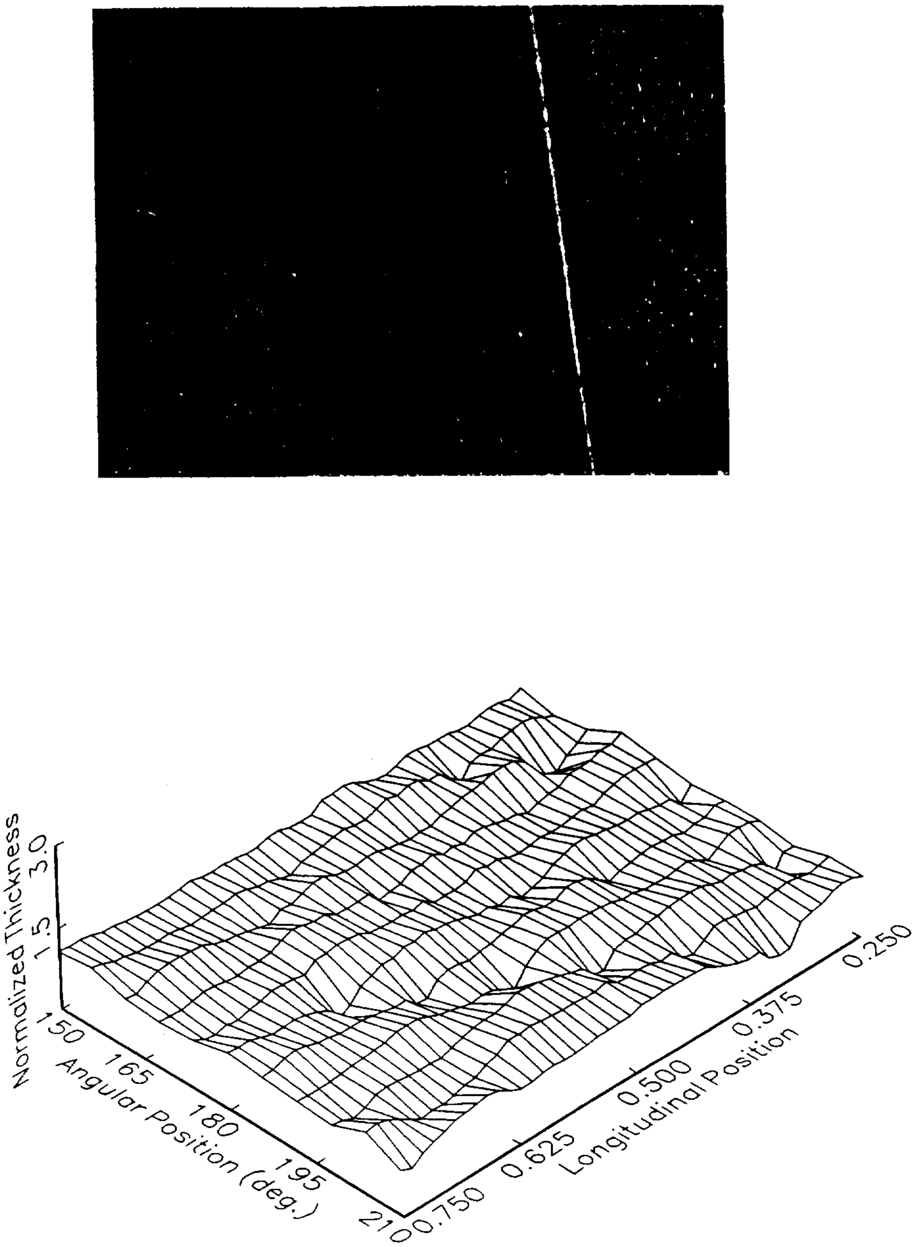

Figure 5.7: Close-up of a filament-wound cylinder in the neighborhood of a twisted tow which demonstrates the sensitivity of the LVDT thickness-measurement technique.

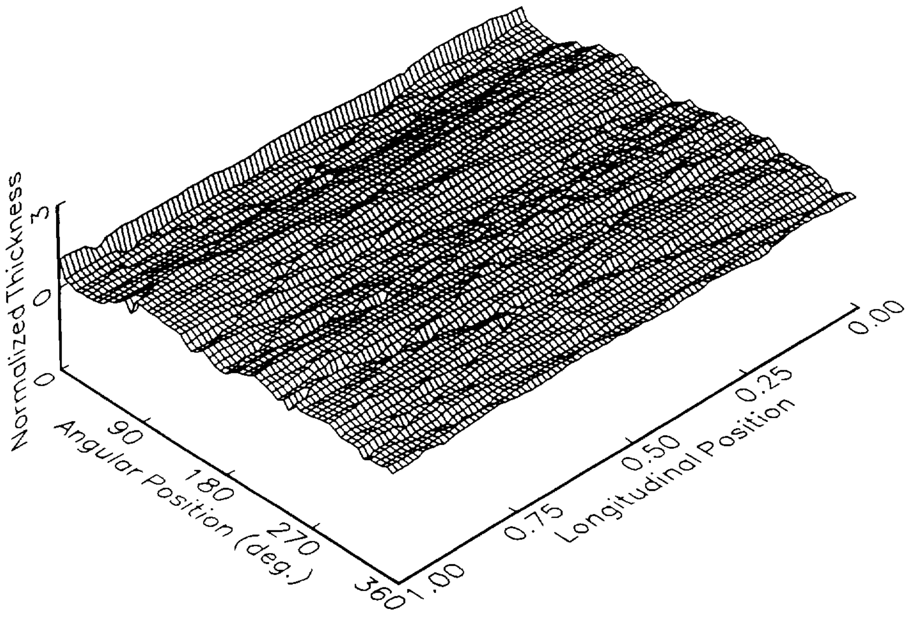

a)

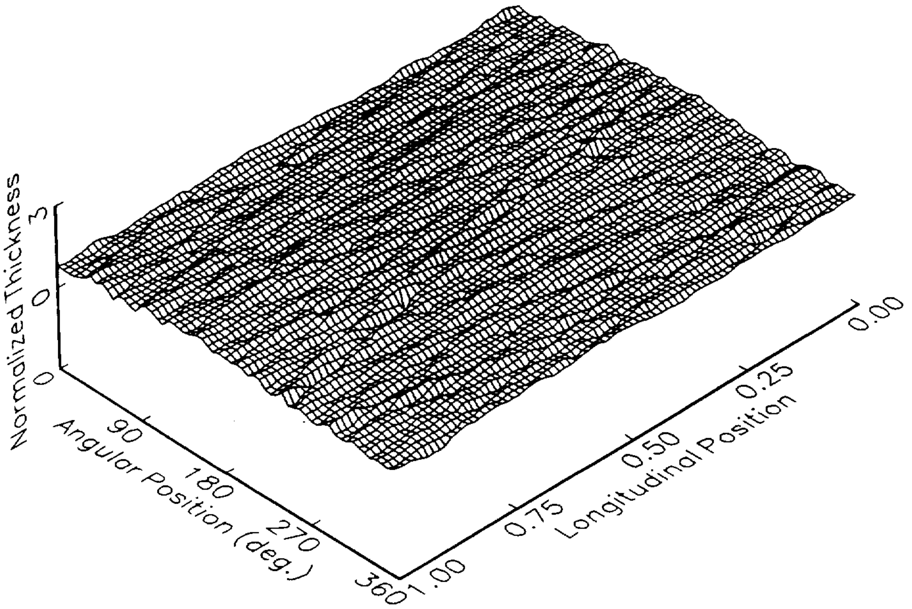

b)

Figure 5.8: Thickness distributions of a) a visually poor-quality cylinder (061991A) and b) a visually high-quality cylinder (070191B).

To examine the consistency of this technique, Specimen 062191A was measured three times and the data reduced with the computer code. Each experiment involved removing the mandrel completely from the filament winder. The resulting thickness distributions are shown in Figures 5.9-5.11 and appear to be nearly identical. Results of this study are listed in Table 5.4.

The six-ply cylinders often exhibited a small deviation in the thickness data, as shown in Figure 5.12. Visual examination of the cylinders did not reveal the cause of this

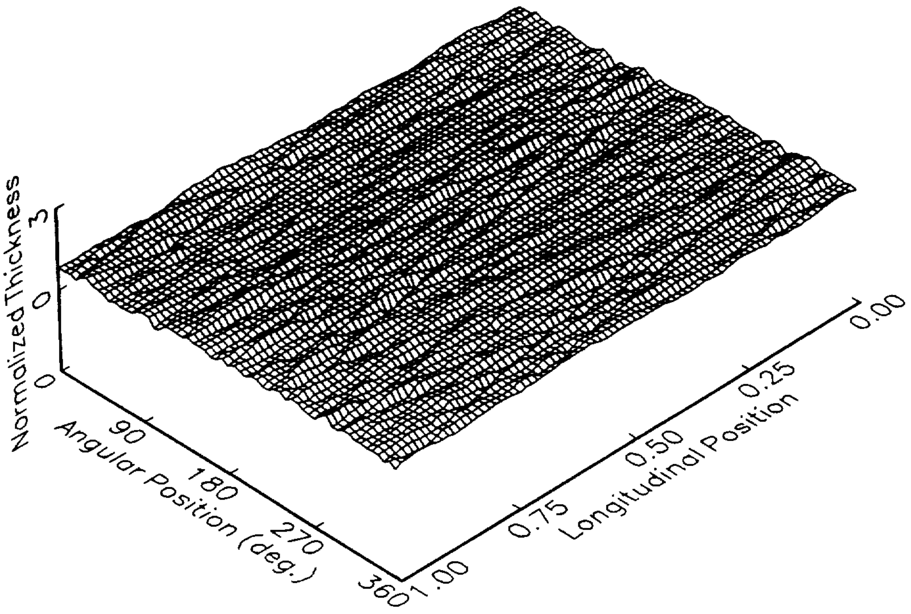

Figure 5.9: First thickness field of Specimen 062191A measured to examine the consistency of the LVDT thickness-measurement technique.

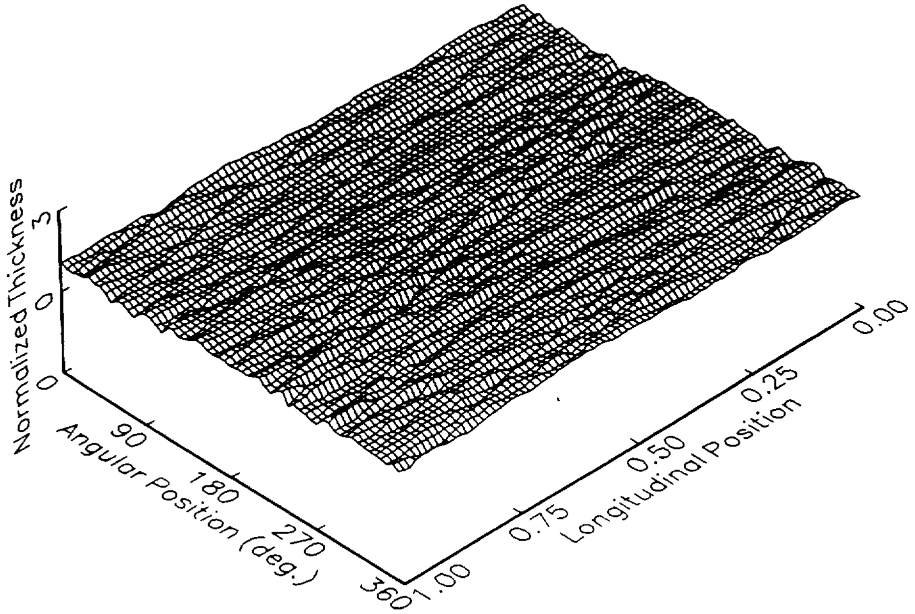

Figure 5.10: Second thickness field of Specimen 062191A measured to examine the consistency of the LVDT thickness-measurement technique.

anomaly; consequently, the regions were assumed to be caused by the lack of intimate contact between the cylinder's inner surface and the outer surface of the mandrel. Table 5.5 contains the statistical results for each specimen wound for compression testing. Several of the 57-mm diameter compression specimens could not be tested with this

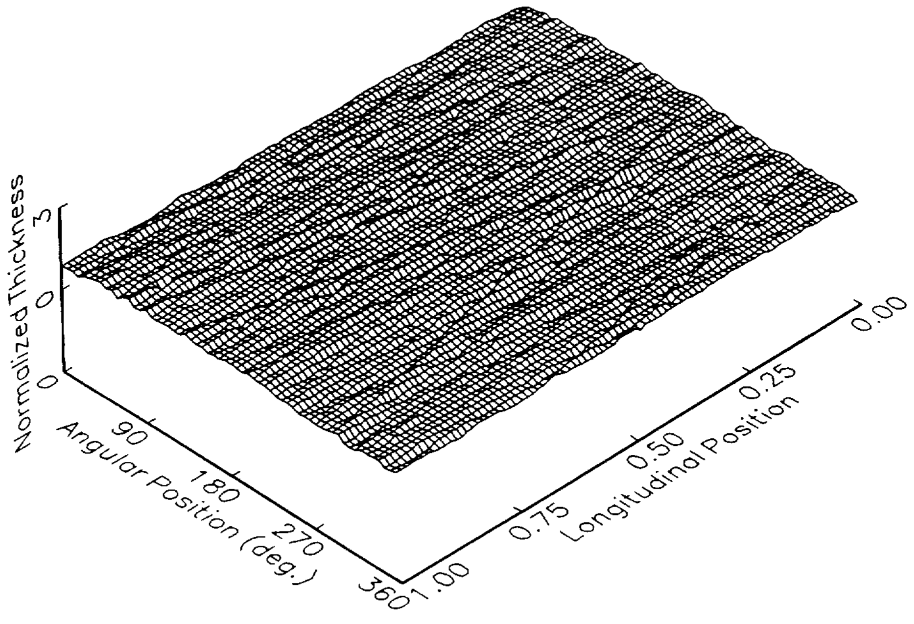

Figure 5.11: Third thickness field of Specimen 062191A measured to examine the consistency of the LVDT thickness-measurement technique.

Table 5.4: Results of the thickness consistency study.

| Test Number | Minimum Thickness (mm) | Maximum Thickness (mm) | Mean Thickness (mm) | Standard Deviation (mm) | R.M.S. Thickness (mm) |
|---|---|---|---|---|---|
| 1 | 0.213 | 0.622 | 0.428 | 0.0654 | 0.433 |
| 2 | 0.156 | 0.559 | 0.398 | 0.0590 | 0.402 |
| 3 | 0.201 | 0.586 | 0.418 | 0.0523 | 0.421 |

technique since strain gages were bonded to the inner surface and would have been damaged by placing the cylinder on the mandrel.

In general, the thickness measurements obtained with this technique follow the visual observations of the outer surface of each cylinder. Where thickness imperfections were observed in the outer ply due to incorrect placement of the shrink tape, wrinkles in the cure materials, or regions of twisted tows, the thickness distributions also exhibited these imperfections. The thickness distributions and their associated statistics, do not depend on the mandrel material, in-plane crossover location, or the position of the crossover bands through the thickness. If Cylinder 061991 is compared to the other [±30] 57-mm diameter cylinders, the effects of the increased winding tension and fewer shrink tape layers do not make a difference on the average thickness; however, the larger standard deviation indicates a slightly rougher surface. This observation can be explained by the large amount of tow twisting which was observed during winding.

When the diameter of the cylinder is changed, the larger diameter cylinders seem to be slightly thicker than the smaller diameter cylinders. The cause for the increased

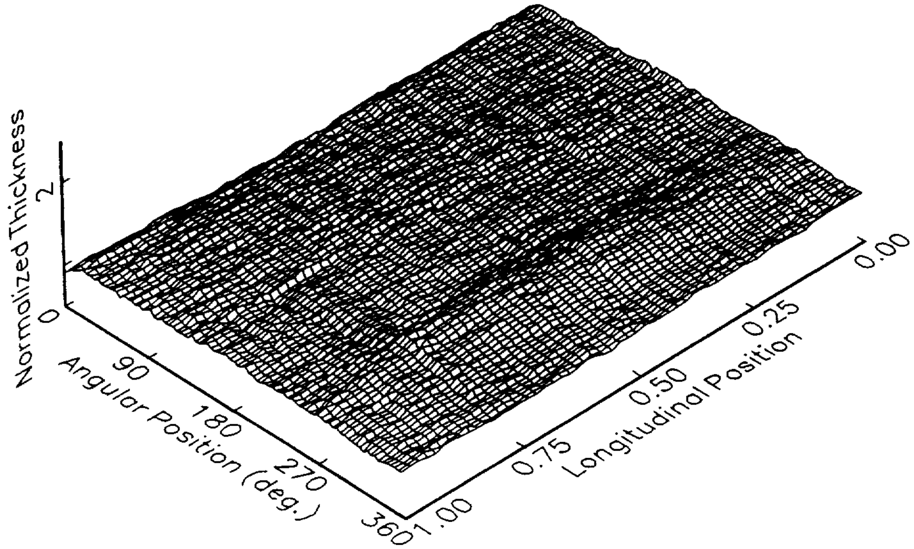

Figure 5.12: Thickness field of Specimen 030992A which exhibits the non-intimate contact region.

thickness is most likely due to the reduced pressure applied by the shrink tape. If the standard deviation for the large and small diameter cylinders is examined on a per-ply basis, scaling the diameter has no affect on the surface roughness. Increasing the number of plies resulted in a dramatic reduction in the standard deviation. This observation is expected since the helical layers will nest together to effectively reduce the influence of a single twisted or misplaced tow.

When the symmetric and antisymmetric cylinders are compared, the average thickness of the antisymmetric cylinder is slightly larger because more tow twisting was observed during winding. These twists are not evident when the thickness distribution or standard deviations are examined.

An elevated winding temperature had the most dramatic effect on the thickness of filament-wound cylinders. Cylinders wound with an elevated temperature and cured with shrink tape have a thinner per-ply thickness than any other manufacturing technique; however, the standard deviation for these cylinders is larger than the other six-ply cylinders. The cause for the increased deviation could be related to either the winding sequence or the elevated winding temperature. Evidence from the [±30] and [±30/±30] cylinders seems to indicate that multiple adjacent helical layers improves the surface smoothness. Since Cylinder 031392 was wound with adjacent ±30° plies, the elevated temperature is the most likely cause for the larger standard deviation. The precise mechanism; however, is unknown.

Another comparison of interest is the accuracy of the thicknesses measured with the LVDT technique versus those measured with the ball-end micrometer. The thickness of cylinders wound with only one helical layer are nearly the same for the two techniques; however, as the number of plies increases, the LVDT technique indicates a larger thickness than the micrometer technique as shown in Figure 5.13. This observation may be somewhat biased by the lack of intimate contact observed with the six-ply cylinders. If the standard deviations for the two techniques are similarly compared, the LVDT technique

Table 5.5: Thickness parameters measured with the LVDT technique of cylinders manufactured for compression testing.

| Cylinder Number | Winding Sequence | Minimum Thickness (x10^-2 mm) | Maximum Thickness (x10^-2 mm) | Mean Thickness (x10^-2 mm) | Standard Deviation (x10^-2 mm) | R.M.S. Thickness (x10^-2 mm) |
|---|---|---|---|---|---|---|
| 061991A | [±30] | -3.72 | 62.5 | 39.8 | 12.2 | 41.6 |
| 061991B | [±30] | -5.57 | 70.0 | 29.0 | 13.4 | 31.9 |
| 062091 | [±30] | -- | -- | -- | -- | -- |
| 062191A | [±30] | 21.3 | 62.2 | 41.5 | 5.89 | 43.3 |
| 062191B | [±30] | -10.2 | 58.7 | 42.7 | 9.95 | 108 |
| 062391A | [±30] | -- | -- | -- | -- | -- |
| 062391B | [±30] | 18.6 | 60.5 | 44.0 | 4.54 | 44.2 |
| 062491A | [±30] | 8.39 | 96.3 | 51.5 | 17.2 | 54.3 |
| 062491B | [±30] | 34.4 | 59.5 | 45.8 | 3.88 | 45.9 |
| 062591A | [±30] | 27.2 | 60.0 | 46.1 | 3.75 | 46.3 |
| 062591B | [±30] | -- | -- | -- | -- | -- |
| 063091A | [±30] | -- | -- | -- | -- | -- |
| 063091B | [±30] | 34.0 | 58.5 | 46.6 | 3.28 | 46.7 |
| 070191A | [±30] | -- | -- | -- | -- | -- |
| 070191B | [±30] | 25.6 | 58.8 | 43.2 | 5.04 | 43.4 |
| 011692A | [±30] | 25.3 | 61.5 | 46.4 | 4.34 | 47.0 |
| 011692B | [±30] | 27.8 | 58.5 | 47.0 | 3.95 | 46.6 |
| 081291A | [±30] | 30.5 | 78.8 | 49.8 | 4.93 | 50.0 |
| 081291B | [±30] | 27.4 | 65.9 | 47.8 | 4.55 | 48.0 |
| 030692A | [±30] | 28.9 | 60.0 | 43.7 | 4.33 | 43.9 |
| 030692B | [±30] | 36.6 | 69.3 | 46.8 | 4.44 | 47.3 |
| 012092A | $[\pm30]_{as}$ | 85.1 | 112 | 97.3 | 3.97 | 97.4 |
| 012092B | $[\pm30]_{as}$ | 71.0 | 116 | 99.4 | 4.94 | 99.5 |
| 021192A | $[\pm30]_{s}$ | 67.4 | 103 | 86.1 | 4.91 | 86.3 |
| 021192B | $[\pm30]_{s}$ | 85.0 | 116 | 98.0 | 4.78 | 98.1 |
| 012592A | $[\pm30/90]_{as}$ | 119 | 165 | 144 | 5.20 | 145 |
| 012592B | $[\pm30/90]_{as}$ | 124 | 166 | 150 | 6.50 | 150 |
| 013092A | $[\pm30/90]_{as}$ | 110 | 158 | 140 | 6.54 | 140 |
| 013092B | $[\pm30/90]_{as}$ | 102 | 167 | 141 | 7.23 | 141 |
| 030592A | $[\pm30/90]_{as}$ | 131 | 172 | 146 | 5.56 | 146 |
| 030592B | $[\pm30/90]_{as}$ | 119 | 161 | 143 | 4.84 | 143 |
| 030992A | $[\pm30/90]_{as}$ | 111 | 166 | 141 | 6.86 | 142 |
| 030992B | $[\pm30/90]_{as}$ | 113 | 164 | 141 | 6.95 | 142 |
| 031092A | $[90/\pm30]_{as}$ | 142 | 224 | 164 | 7.92 | 164 |
| 031092B | $[90/\pm30]_{as}$ | 123 | 216 | 138 | 9.08 | 146 |
| 031392A | $[90/\pm30]_{as}$ | 104 | 155 | 127 | 8.26 | 127 |
| 031392B | $[90/\pm30]_{as}$ | 105 | 152 | 123 | 8.44 | 124 |

consistently yields larger values, as shown in Figure 5.14, because the end of the LVDT has a smaller diameter which can fit into smaller imperfections and the entire cylinder was examined.

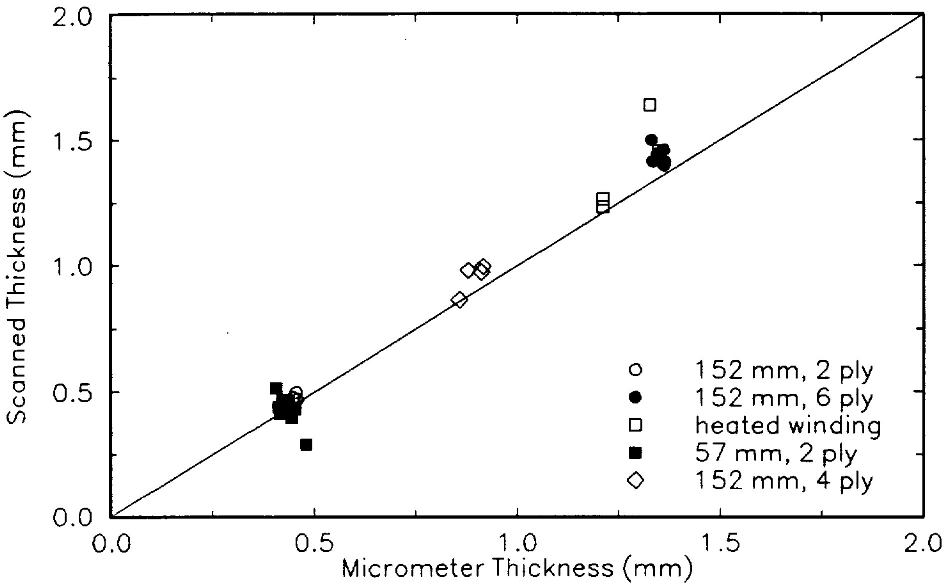

Figure 5.13: A comparison of average thicknesses for the LVDT and micrometer thickness-measurement techniques.

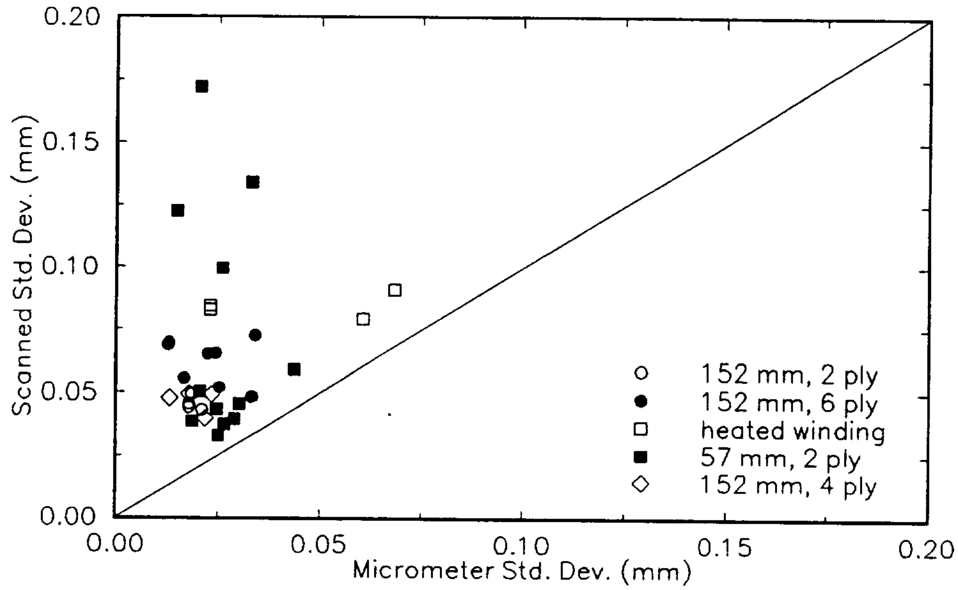

Figure 5.14: A comparison of standard deviations for the LVDT and micrometer thickness-measurement techniques.

To improve the identification of poor quality regions, two smoothing approaches were used. Some of the surface roughness which was apparent in the thickness distributions was caused by the porous release cloth used during processing. This material created a textured surface in the resin on the outer surface of the cylinders which can be seen in Figure 5.7. The first smoothing approach involved averaging the thickness at each point with its nearest neighbors, as shown in Figure 5.15. Points along the edges of the scan and at each corner were smoothed using a similar procedure. The actual and smoothed thickness distributions for Specimens 081291A, 021192A, and 030592A are shown in Figures 5.16-5.18. The average micrometer thickness and length of each specimen, listed in Table 5.3, were used to nondimensionalize these thickness distributions. Much of the surface roughness is not visible with this technique while the major defects in the thickness are still apparent.

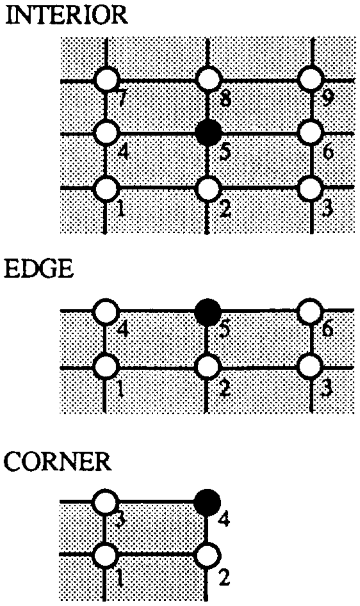

$t_{smooth} = \frac{1}{9}[t1+t2+...+t8+t9]$

$t_{smooth} = \frac{1}{6}[t1+t2+t3+t4+t5+t6]$

$t_{smooth} = \frac{1}{4}[t1+t2+t3+t4]$

Figure 5.15: Algorithm for smoothing the thickness distributions. Each dot in the figure corresponds to a measured thickness location. The filled dots represent the point being smoothed.

The second smoothing technique consisted of interrogating the thickness at each point and comparing it to the average thickness with regard to the standard deviation of the distribution. If the thickness at any point was within two standard deviations on either side of the mean thickness, the thickness was considered to be the mean thickness. For points which existed outside this band, the actual thickness was used. These truncated thickness distributions allow the major defects to be easily identified as shown in Figures 5.19-5.21.

### 5.2.2 Imperfections in Geometry

Imperfections in the geometry of the shell also exist at the global level. These imperfections can be caused by three factors: residual thermal stresses induced during manufacturing, inaccurate machining of the mandrel or cylinder, and stresses induced when attaching the loading fixtures. Residual thermal stresses, which are primarily due to the anti-symmetry of the helically-wound layers, can result in large geometric imperfections. Since the compression-twisting coupling terms of the laminated-shell regions are non-zero, thin cylinders with helical layers may have substantial geometric imperfections before loading. If the mandrel has not been accurately machined, geometric imperfections can be

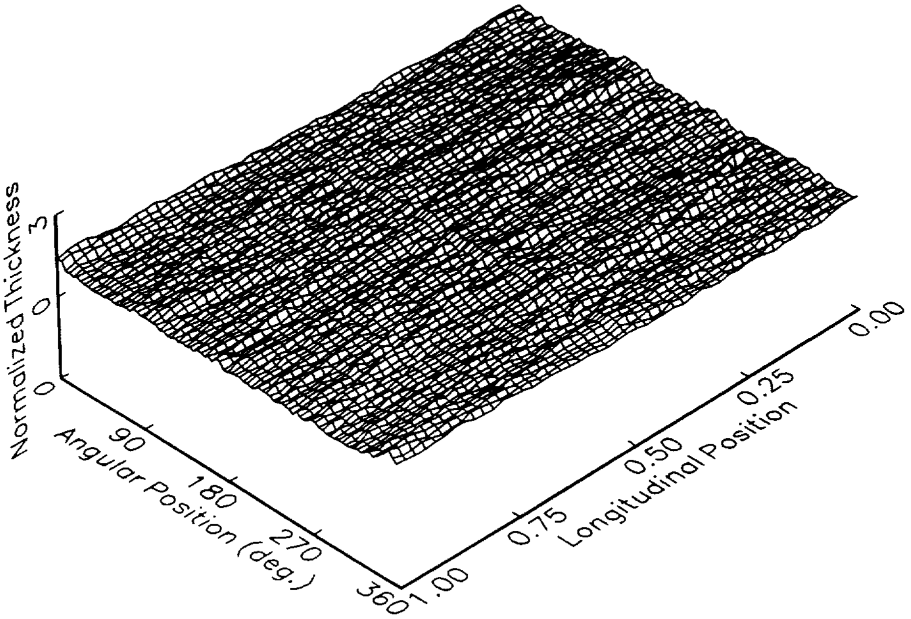

a)

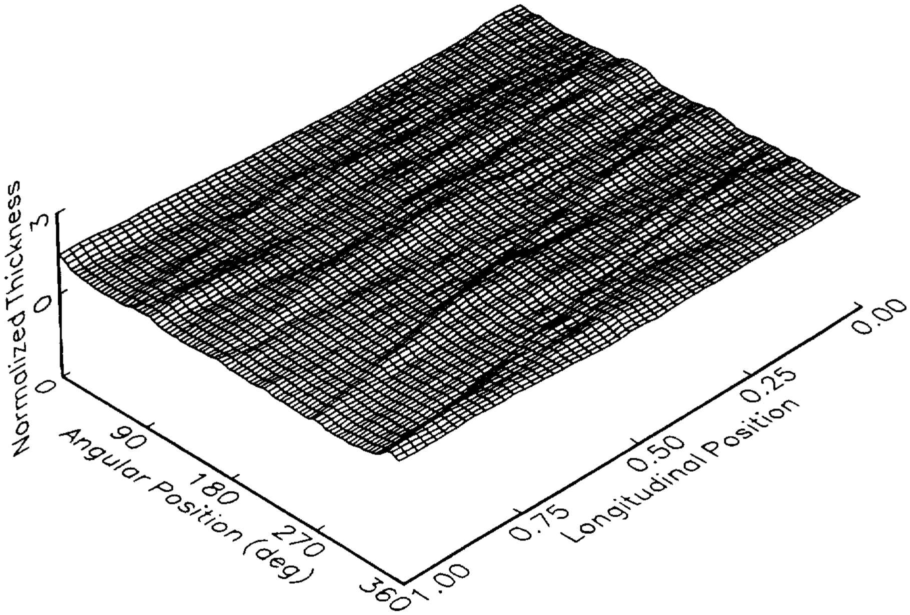

b)

Figure 5.16: Thickness field of Specimen 081291A a) before and b) after smoothing with the averaging technique.

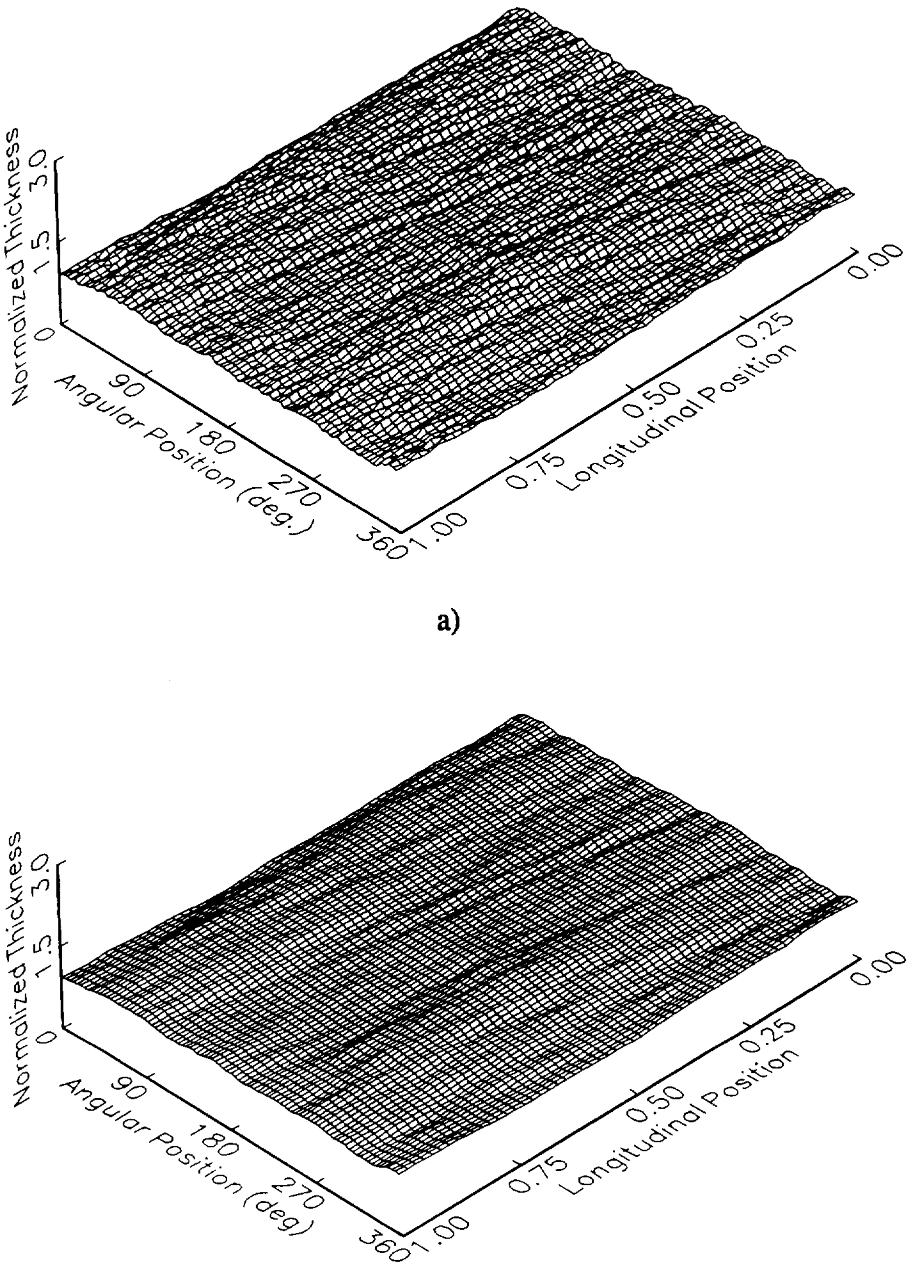

a)

b)

Figure 5.17: Thickness field of Specimen 021192A a) before and b) after smoothing with the averaging technique.

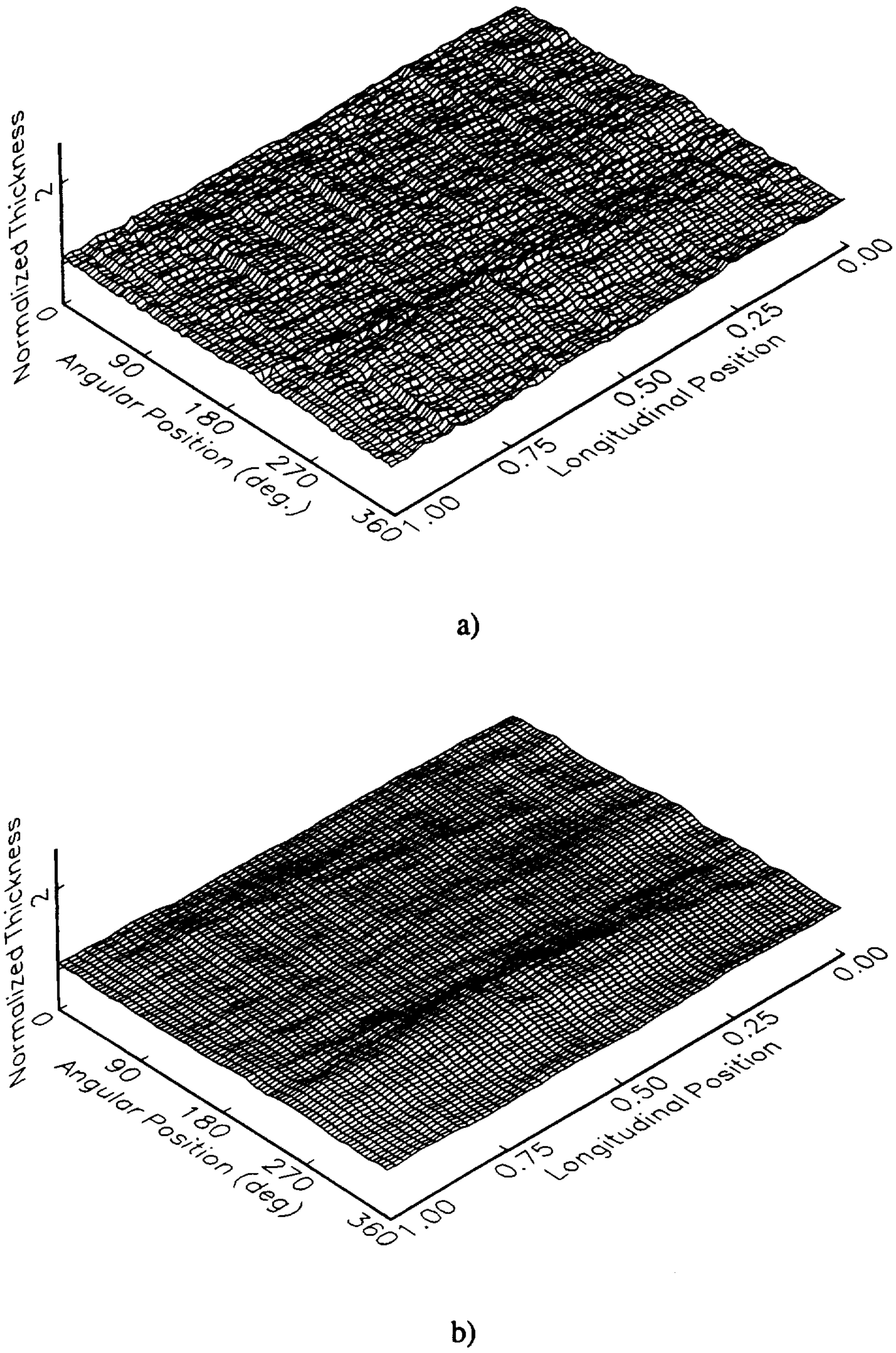

a)

b)

Figure 5.18: Thickness field of Specimen 030592A a) before and b) after smoothing with the averaging technique.

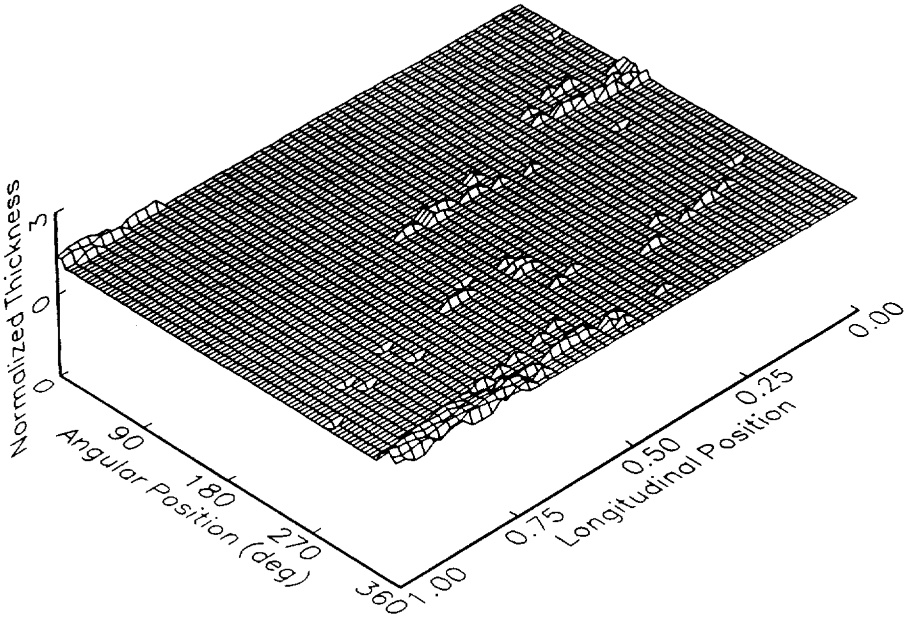

Figure 5.19: Thickness field of Specimen 081291A smoothed with the truncation technique.

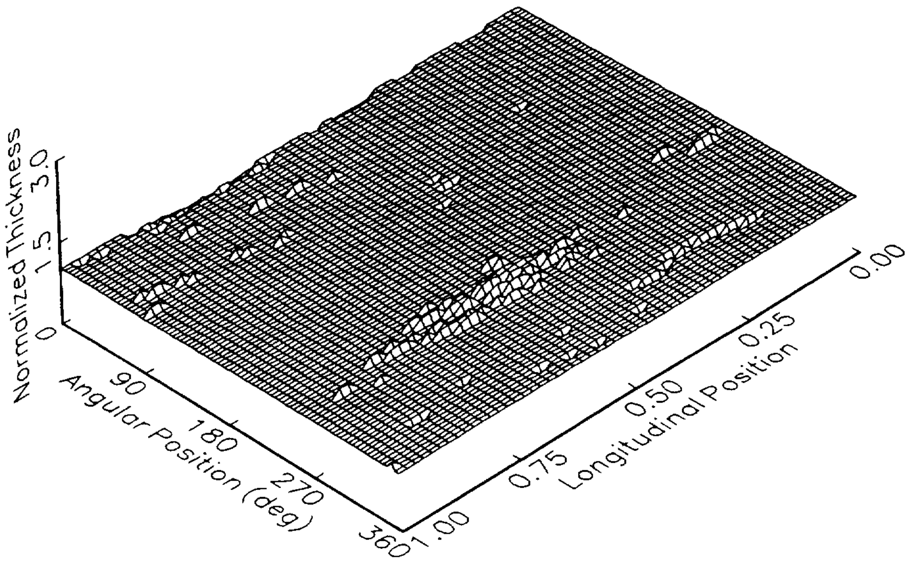

Figure 5.20: Thickness field of Specimen 021192A smoothed with the truncation technique.

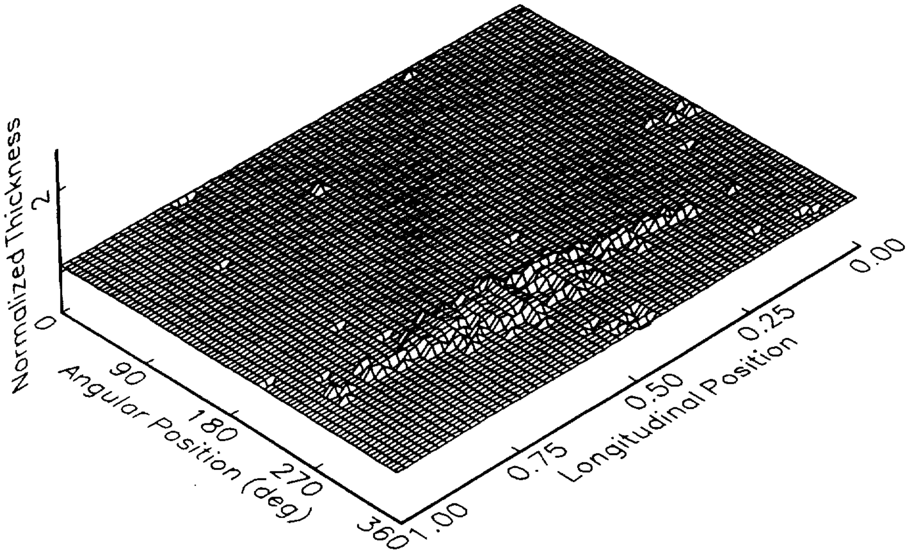

Figure 5.21: Thickness field of Specimen 030592A smoothed with the truncation technique.

induced since the manufacturing procedures force the composite material to reproduce the mandrel surface exactly. When machining the cured cylinder into compression specimens, it is necessary to cut the cylinder perpendicular to the longitudinal axis, otherwise, an elliptical cross section will result relative to the machined edge. The last cause of geometric inaccuracies is the deformations induced by attaching load introduction devices to the cylinder.

Compression specimens were machined from the cured cylinders using the equipment shown in Figure 5.22. Each cylinder was placed on a mandrel of the correct size and either held in place with hose clamps or adhesive tape. The mandrel was centered in the lathe grips to insure that the cylinders were cut perpendicular to the longitudinal axis of the cylinder. The actual cutting was accomplished by using a glass-fiber reinforced abrasive disk mounted in either a Dremel® Motor Tool or a flexible extension for a 9.53 mm electric drill attached to the tool rest. The lathe and abrasive disk were rotated in opposite directions and the tool rest was fed into the cylinder very slowly. This technique resulted in very accurately machined ends which were relatively free of damage.

Since the fixtures used to support the ends of the cylinder during compression testing can also change the geometry of the shell, each specimen was potted in the end fixtures prior to geometry testing. The end fixtures used during this study consisted of steel plates with machined grooves which were filled with Cerrobend®. Cerrobend® is a low melt-temperature alloy (70°C) which expands when cooled and is used to prevent brooming of loaded edges.

To begin the geometric testing, the potted cylinders were attached to a milling machine turntable with the aid of an adapter to ensure consistent alignment. Using a magnetic dial-gage holder, the spring-loaded LVDT was clamped horizontally against the cylinder, as shown in Figure 5.23. To measure the cylinder geometry, the turntable was rotated while the LVDT output was monitored with the data-acquisition and personal-computer system described previously. Data acquisition speed was very slow so that the

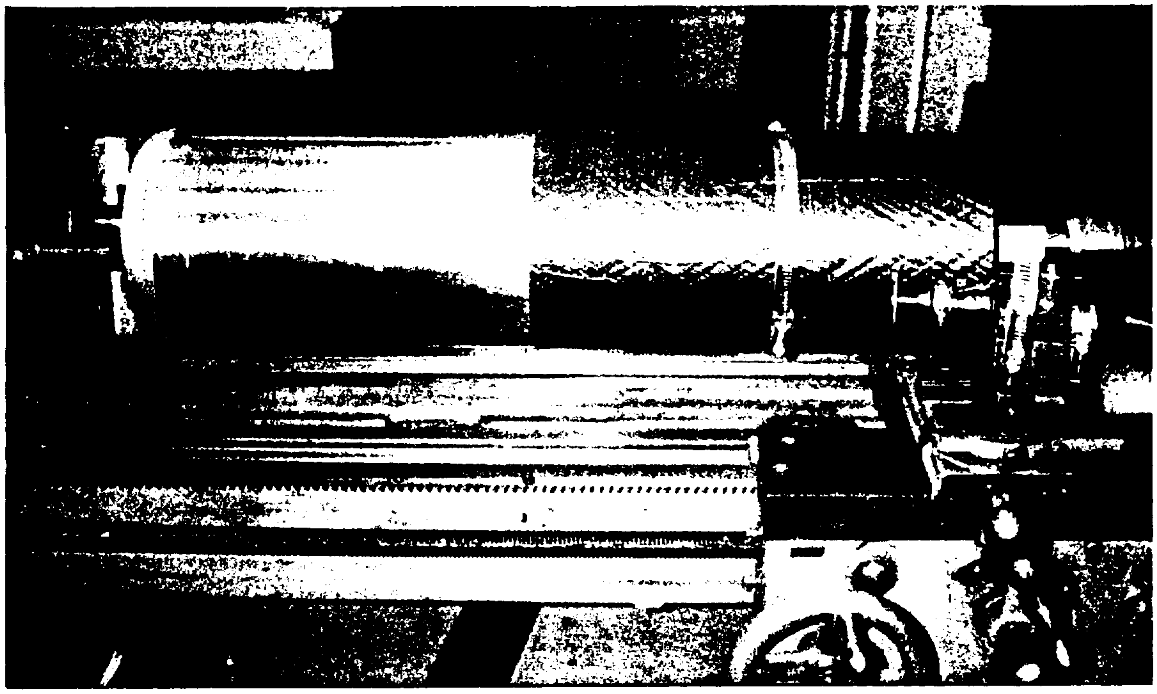

Figure 5.22: Filament-wound cylinder mounted in a lathe to be machined into compression specimens.

turntable could be rotated four degrees between each measurement. Measurements were made at 13-mm intervals along the length of the 57-mm diameter specimens and at 25-mm intervals for the 152-mm diameter specimens.

The LVDT output recorded by the computer, is a measure of the distance between the center of the LVDT and the surface of the cylinder. Using the average value of the calibration constant measured in the thickness distribution experiments, the LVDT output was converted from voltage into distance. Each data point was compared to all of the points measured at one horizontal position of the LVDT to compare the deviation of the actual cylinder from a geometrically perfect cylinder. The data was also compared by examining changes in the cross section along the length of the cylinder which indicated the similarity of the filament-wound specimen to a geometrically perfect cylinder.

When several preliminary results were plotted, the cross sections appeared to be ellipsoidal; whereas, visual examination did not support this observation. This discrepancy was attributed to errors in placing the cylinder in the Cerrobend® and attaching the end fixtures on the turntable. If the filament-wound cylinder had a circular cross section and was perfectly aligned with the turntable, the resulting data would appear as a horizontal straight line, as shown in Figure 5.24. If the longitudinal axis of this hypothetical cylinder is not aligned with the spin axis of the turntable, the data would appear to be sinusoidal. An elliptical cross section would appear as a linear combination of two sinusoids with different wavelengths.

To remove the errors associated with the misalignment of the cylinder on the turntable, the data from each scan was first fitted with a perfect circle. This was accomplished by plotting the data versus the sine of the difference between the angle of rotation and a phase angle. A linear least-squares analysis was then performed with different values of the phase angle until the best fit was obtained. When the LVDT was moved from one horizontal position to the next, it was necessary to loosen the clamp attached to the magnetic dial-gage holder. Consequently, the precise distance between the

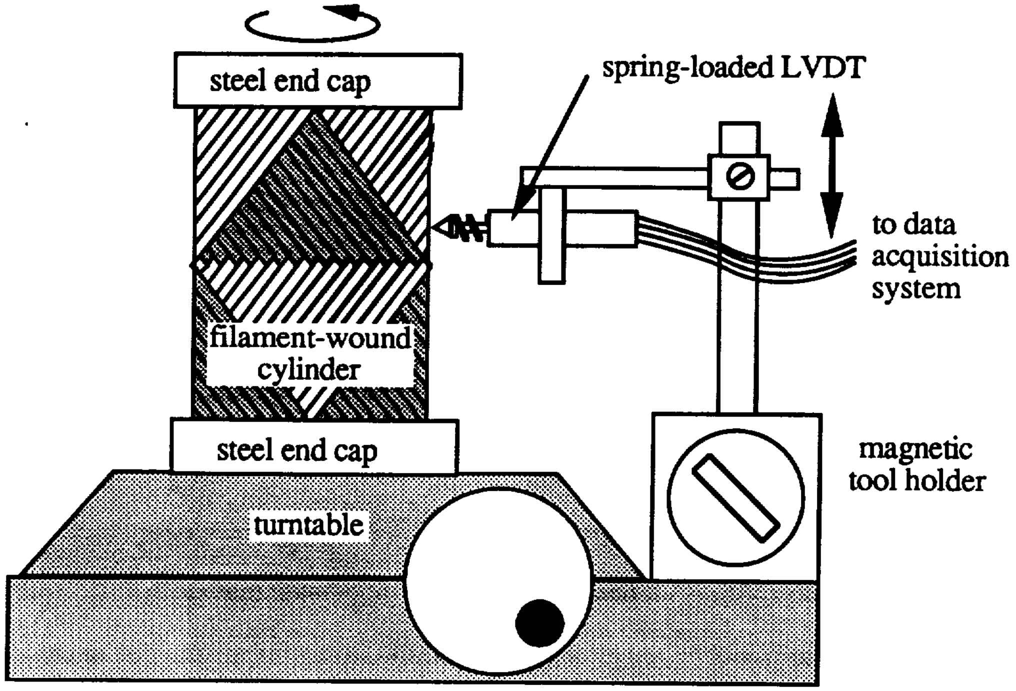
steel end cap
spring-loaded LVDT
to data acquisition system
filament-wound cylinder
steel end cap
magnetic tool holder
turntable

Figure 5.23: Schematic diagram of the equipment used to measure geometric imperfections of filament-wound cylinders.

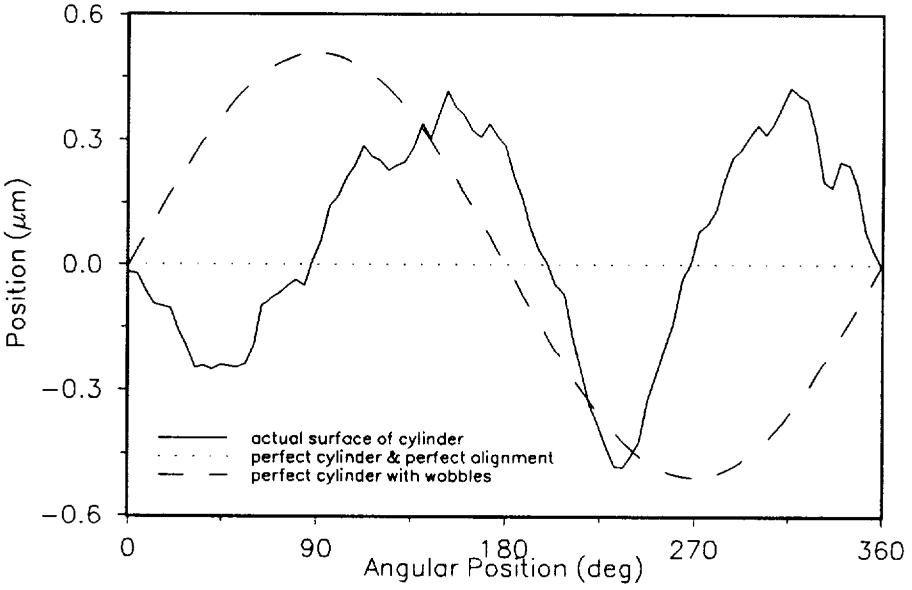

Figure 5.24: Longitudinal distribution of a perfect cylinder aligned with the turntable axis, a perfect cylinder not on the spin axis, and typical data.

LVDT and the surface of the cylinder was not maintained during testing. To compare each cross section it was assumed that the zero degree location on the filament-wound specimen was vertical. This assumption effectively removes any tilt of the cylinder with respect to the machined ends.

To remove the errors induced by misalignments, the average of each perfect circle was used to create the perfect cylinder. The difference between this perfect cylinder and the actual data is the geometric imperfection amplitude. To quantify the magnitude of the geometric imperfections, several statistical parameters were examined. The arithmetic mean of the distribution was invariably extremely small since the circumference of the cylinder does not change. The standard deviation, root mean square, and range of the geometric imperfections were also calculated.

To confirm the consistency of this experimental procedure, Specimen 062191B was examined three times. Plots of the imperfection amplitudes are shown in Figures 5.25-5.27 and are nearly identical. Table 5.6 contains the statistical results of each experiment. The results of this exercise demonstrate excellent consistency of the geometric imperfection testing technique.

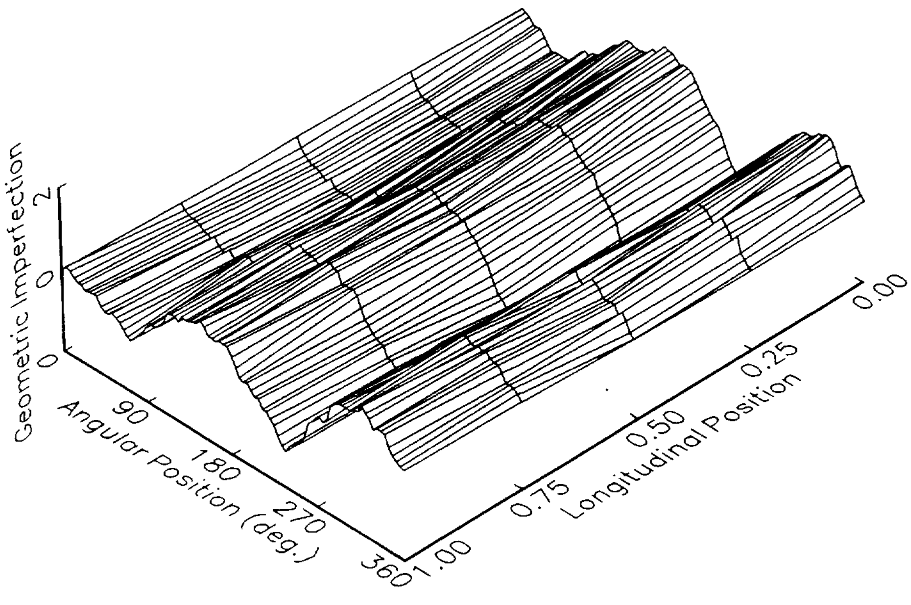

Figure 5.25: Geometric imperfections for the first scan of Specimen 062191B.

The geometric imperfections observed in the filament-wound cylinders differ dramatically from those reported by Chryssanthopoulos, Giavotto, and Poggi [22] who investigated the geometric imperfections of symmetric cross-ply and angle-ply cylinders fabricated by hand from unidirectional-prepreg sheets. Many of the local imperfections in the filament-wound cylinders are not apparent in their specimens, as shown in Figure 5.28; however, the large ridges are absent in filament-wound cylinders. Geometric imperfections in filament-wound cylinders are primarily caused by residual stresses in the antisymmetric laminated-shell regions while, the ridges in Figure 5.28 are caused by overlapping of the prepreg layers.

The geometric imperfections for the In-Plane Crossover-Band Spacing study were similar to those shown in Figure 5.25; however, the magnitude of the imperfection varies considerably, as shown in Table 5.7. The large variations in amplitude, especially apparent near the ends of some cylinders, were also visible in the specimens prior to potting them in

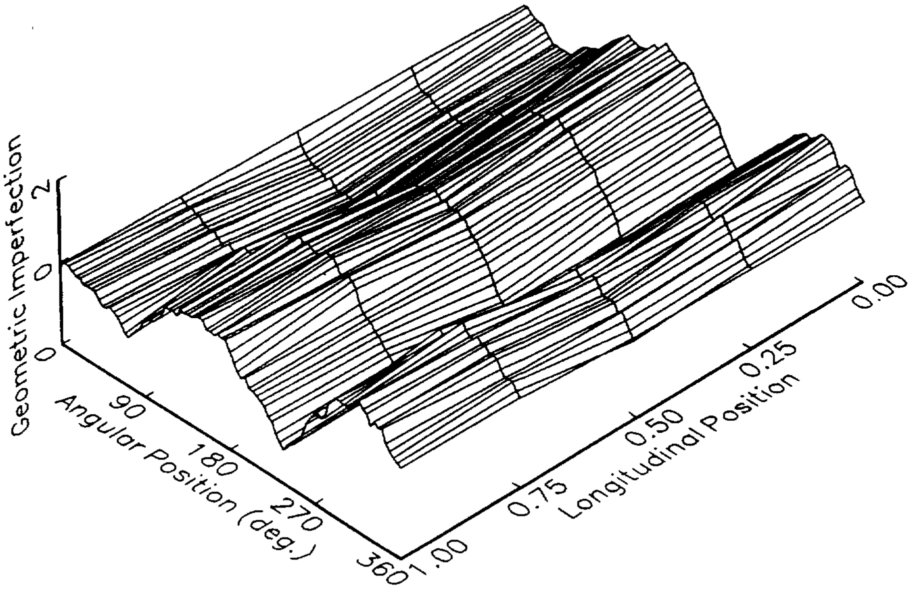

Figure 5.26: Geometric imperfections for the second scan of Specimen 062191B.

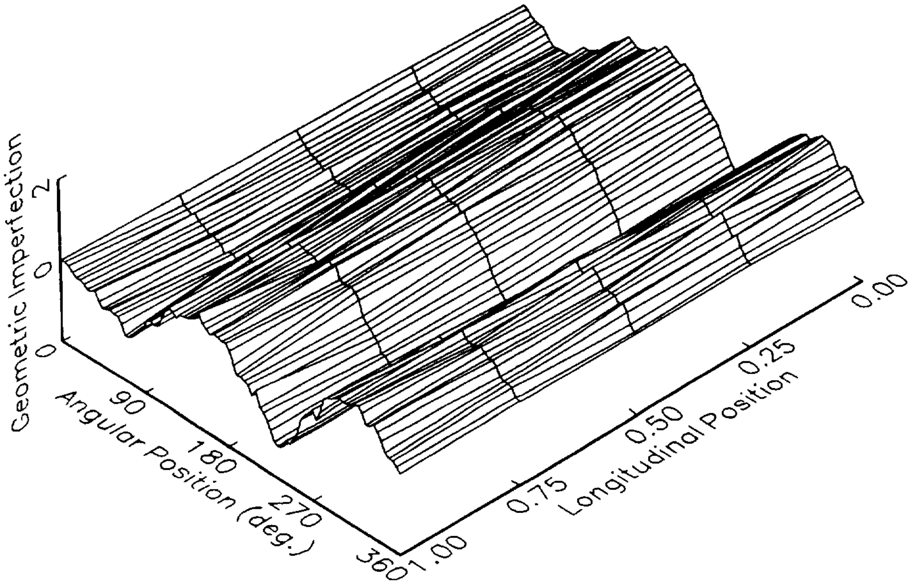

Figure 5.27: Geometric imperfections for the third scan of Specimen 062191B.

the compression fixtures. When the range of the imperfections was examined as a function of the circumferential crossover-band spacing, no correlation was evident. As the crossover-band spacing increases, the imperfection range for all of the specimens was approximately constant; however, the scatter in the measured ranges increased substantially. This effect was caused by inaccuracies in machining the compression specimens with respect to the winding pattern from the wound cylinders. If the crossover-band spacing is very small, the cylinder is more effectively homogeneous and the location

Table 5.6: Geometric parameters obtained for the consistency study.

| Test Number | R.M.S. Geo. Impf. (mm) | Standard Deviation (mm) | Range Geo. Impf. (mm) | Range/ Thick* |
|---|---|---|---|---|
| 1 | 0.299 | 0.296 | 1.23 | 2.845 |
| 2 | 0.291 | 0.290 | 1.10 | 2.545 |
| 3 | 0.275 | 0.273 | 1.05 | 2.430 |

* micrometer thickness

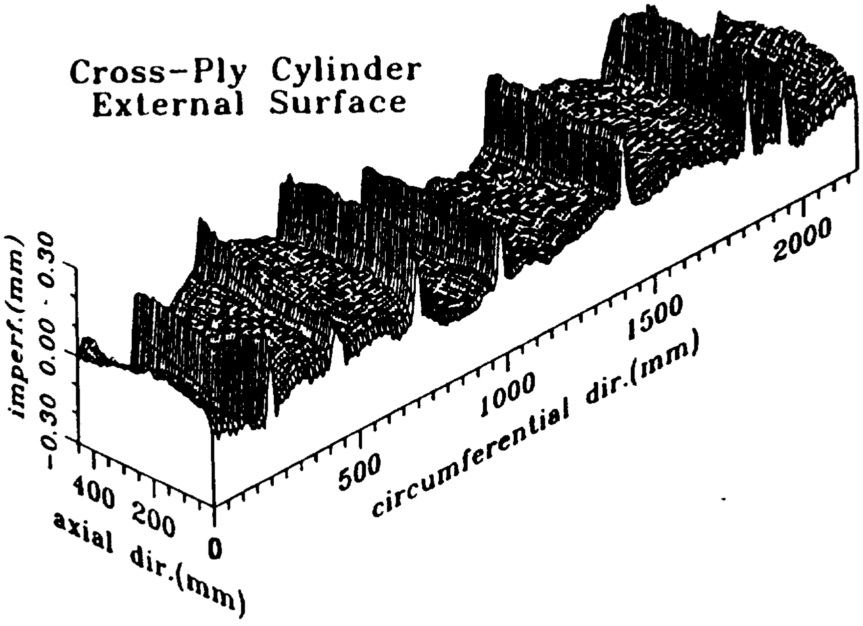

Figure 5.28: Geometric imperfections of unidirectional-prepreg cylinders measured by Chryssanthopoulos, Giavotto, and Poggi [22].

of the machined edge is not as critical as when the cylinder is wound with few crossover bands.

Although the mandrel material does not affect the magnitude of the geometric imperfection, the scale of the cylinder produces a substantial effect. When the 57-mm diameter [±30] cylinders were compared to the 152-mm diameter cylinders (Specimens 061991A, 061991B, and 062091 versus Specimens 081291A, 081291B, 030692A, and 030692B) based on the range of the geometric imperfections, the small diameter cylinders were more nearly perfect.

When the symmetric and antisymmetric cylinders were compared, the advantages of a symmetric lamination sequence were immediately apparent. Although the range of the imperfection was similar for Specimens 021192A, 021192B, 012092A, and 012092B, Cylinder 021192 was much more consistent since this cylinder was manufactured with

Table 5.7: Geometric parameters for cylinders manufactured for compression testing.

| Cylinder Number | Winding Sequence | R.M.S. Geo. Impf. (x10^-2 mm) | Standard Deviation (x10^-2 mm) | Range Geo. Impf. (x10^-2 mm) | Range/ Thick* |
|---|---|---|---|---|---|
| 061991A | [±30] | 6.44 | 6.40 | 35.5 | 0.7981 |
| 061991B | [±30] | 19.5 | 19.6 | 95.1 | 1.978 |
| 062091 | [±30] | 21.7 | 21.7 | 105 | 2.474 |
| 062191A | [±30] | 12.8 | 13.3 | 67.8 | 1.630 |
| 062191B | [±30] | 26.5 | 26.3 | 112 | 2.606 |
| 062391A | [±30] | 13.2 | 13.2 | 71.0 | 1.624 |
| 062391B | [±30] | 9.02 | 9.02 | 49.8 | 1.203 |
| 062491A | [±30] | 12.1 | 12.1 | 70.3 | 1.733 |
| 062491B | [±30] | 9.02 | 8.52 | 55.8 | 1.314 |
| 062591A | [±30] | 20.5 | 20.5 | 99.7 | 2.326 |
| 062591B | [±30] | 15.2 | 15.2 | 86.1 | 2.005 |
| 063091A | [±30] | 6.28 | 6.28 | 42.4 | 0.9853 |
| 063091B | [±30] | 14.1 | 14.1 | 61.2 | 1.486 |
| 070191A | [±30] | 16.9 | 16.9 | 77.1 | 1.727 |
| 070191B | [±30] | 19.4 | 19.3 | 100 | 2.220 |
| 011692A | [±30] | 24.0 | 23.9 | 139 | 3.265 |
| 011692B | [±30] | 9.59 | 9.79 | 51.3 | 1.175 |
| 081291A | [±30] | 20.6 | 20.1 | 113 | 2.480 |
| 081291B | [±30] | 55.2 | 54.9 | 256 | 5.607 |
| 030692A | [±30] | 48.5 | 48.2 | 198 | 4.354 |
| 030692B | [±30] | 14.1 | 14.0 | 80.2 | 1.751 |
| 012092A | $[\pm30]_{as}$ | 22.0 | 21.9 | 105 | 1.155 |
| 012092B | $[\pm30]_{as}$ | 12.4 | 11.7 | 60.6 | 0.6623 |
| 021192A | $[\pm30]_{s}$ | 13.4 | 13.3 | 72.2 | 0.8429 |
| 021192B | $[\pm30]_{s}$ | 14.1 | 14.0 | 79.7 | 0.9080 |
| 012592A | $[\pm30/90]_{as}$ | 16.5 | 16.4 | 87.7 | 0.6521 |
| 012592B | $[\pm30/90]_{as}$ | 17.4 | 17.3 | 101 | 0.7593 |
| 013092A | $[\pm30/90]_{as}$ | 21.6 | 21.5 | 113 | 0.8274 |
| 013092B | $[\pm30/90]_{as}$ | 16.3 | 16.2 | 92.9 | 0.6807 |
| 030592A | $[\pm30/90]_{as}$ | 19.5 | 19.4 | 94.2 | 0.6919 |
| 030592B | $[\pm30/90]_{as}$ | 19.3 | 19.2 | 88.2 | 0.6522 |
| 030992A | $[\pm30/90]_{as}$ | 9.80 | 9.74 | 55.5 | 0.4158 |
| 030992B | $[\pm30/90]_{as}$ | 19.2 | 19.0 | 110 | 0.8227 |
| 031092A | $[90/\pm30]_{as}$ | 19.6 | 19.5 | 92.7 | 0.6990 |
| 031092B | $[90/\pm30]_{as}$ | 28.9 | 28.7 | 143 | 1.057 |
| 031392A | $[90/\pm30]_{as}$ | 15.0 | 14.9 | 66.1 | 0.5455 |
| 031392B | $[90/\pm30]_{as}$ | 10.1 | 10.0 | 54.2 | 0.4476 |

* micrometer thickness

symmetric laminated-shell regions. As with the In-Plane Crossover-Band Spacing specimens, this indicates the strong dependence of the geometric imperfections on the thermal residual stresses.

The cylinders manufactured for the Through-the-Thickness Crossover-Band Location study have slightly larger geometric imperfections than those manufactured for the

Symmetry of the Laminated-Shell Regions experiments. Results for the stacked and alternating specimens were more consistent than the specimens wound with a wide crossover-band spacing for the outside and a narrow spacing for the inner ply. This finding is contrary to the results from the In-Plane Crossover-Band Spacing study.

Cylinders wound at an elevated temperature and cured with shrink tape (Specimens 031392A and 031392B) exhibited the smallest range-to-radius ratio of all specimens tested. Unfortunately, the effects of heat alone cannot be differentiated from the effects of winding sequence since Cylinders 121490 and 122990 were not measured for geometric imperfections prior to compression testing. The most plausible explanation for this improvement is the circumferential bending stiffness of the specimens. Since the hoop layers are located on the inner and outer surfaces of Cylinder 031392, less imperfection is expected compared to cylinders manufactured with the hoop layers on the inside of the material.

### 5.2.3 Conclusions

The geometry of filament-wound cylinders is strongly dependent on the manufacturing technique. At the local level, the cylinder thickness depends on the amount of twisted and misplaced tows which cause local ridges and valleys in the material. In multiple-layer cylinders, the thickness is more uniform when the helically-wound plies are placed adjacent to one another since the fibers tend to nest with one another. The average and truncated smoothing techniques can be used to easily identify regions of poor quality. The curing technique also affects the uniformity of the thickness since sags and drips in the resin affect the smoothness of the exterior surface.

At the global level, the geometry of filament-wound cylinders depends on the winding pattern, scale, and ply order. The winding pattern affects the size of the laminated-shell regions and their location relative to the machined edges. Since these regions are typically antisymmetric, the thermal residual stresses which are induced during curing will produce non-circular cross sections. As the diameter of the cylinder increases, the size of the imperfections increases since the circumferential bending stiffness of the cylinder is lower. As the number of plies increases, the size of the geometric imperfections decreases slightly in relation to the bending stiffness.

PAGE 82 INTENTIONALLY BLANK

PRECEDING PAGE BLANK NOT FILMED

# 6.0 COMPRESSIVE PERFORMANCE

The goal of this research was to vary the filament-winding process to improve the compressive structural response of thin cylindrical shells. Many factors can affect the stability of filament-wound shells including the winding pattern, curing technique, microstructural quality, and similarity to a geometrically perfect cylinder. In the preceding chapters, the manufacturing procedures and quality assessment have been discussed. The purpose of this chapter is to describe the test procedures, present results, and to compare the compressive response of the cylinders to the specific manufacturing parameters and quality levels. Correspondingly, this chapter is divided into five sections: test equipment, experimental procedures, data reduction, results and discussion, and conclusions. Due to the number of specimens which were tested, only representative data is included in the following sections. A complete collection of the load/end-shortening displacement data, local strains results, photographs of the buckled cylinders, sketches of the buckled shapes and fracture locations, and acoustic emission results is given in Claus, Hahn, and Jensen [19].

## 6.1 Test Equipment

Three different groups of testing equipment were used to evaluate the compressive buckling response of filament-wound cylinders: mechanical, acoustic emission, and visual recording equipment. A schematic of the most general testing configuration is shown in Figure 6.1. The mechanical test equipment included the compression testing machine, LVDTs and strain gages to monitor the deformation of the cylinder, and the data acquisition system for recording the response during testing. An acoustic emission (AE) system was used to monitor the ultrasonic signals emitted by the specimen during testing. Two types of visual recording equipment were used: still photographs were taken before and after failure, and video images were recorded during loading to examine the buckling and postbuckling processes. Specific details about this equipment are discussed in the following sections.

### 6.1.1 Mechanical Test Equipment

Each filament-wound cylinder was loaded through the use of 25 mm thick steel end plates. Two different sets of end plates were used to accommodate the 57-mm and 152-mm diameter cylinders, however, both sets of fixtures had the same general design, as shown in Figure 6.2. Each plate contained a circular groove, approximately 6.4-mm wide and 6.4-mm deep, to hold the cylinder and Cerrobend® as described in Section 4.2.2. A concentric recess was machined into one plate approximately 102 mm in diameter to hold the hemispherical aligner. The hemispherical aligner was used to compensate for misalignments between the end plates and the testing machine. Four holes were drilled and tapped at equal intervals around the end plate for attachment of the LVDTs. In the end plates used for the smaller diameter cylinders, four holes were drilled to accommodate pins to ensure the top and bottom end plates are properly aligned during potting. Additional holes were drilled in each end plate to allow air to flow freely from the inside of the cylinder during potting and for passage of the strain-gage lead wires.

Three LVDTs, Lucas Schaevitz model MHR-100, were mounted to the upper end plate at 90° intervals with the aid of aluminum mounting blocks. These LVDTs have a nominal linear range of ±2.54 mm and a sensitivity of 2.2 mV/V/0.0254 mm. The cores were mounted to core extension rods tailored to the length of the cylinder being tested. The

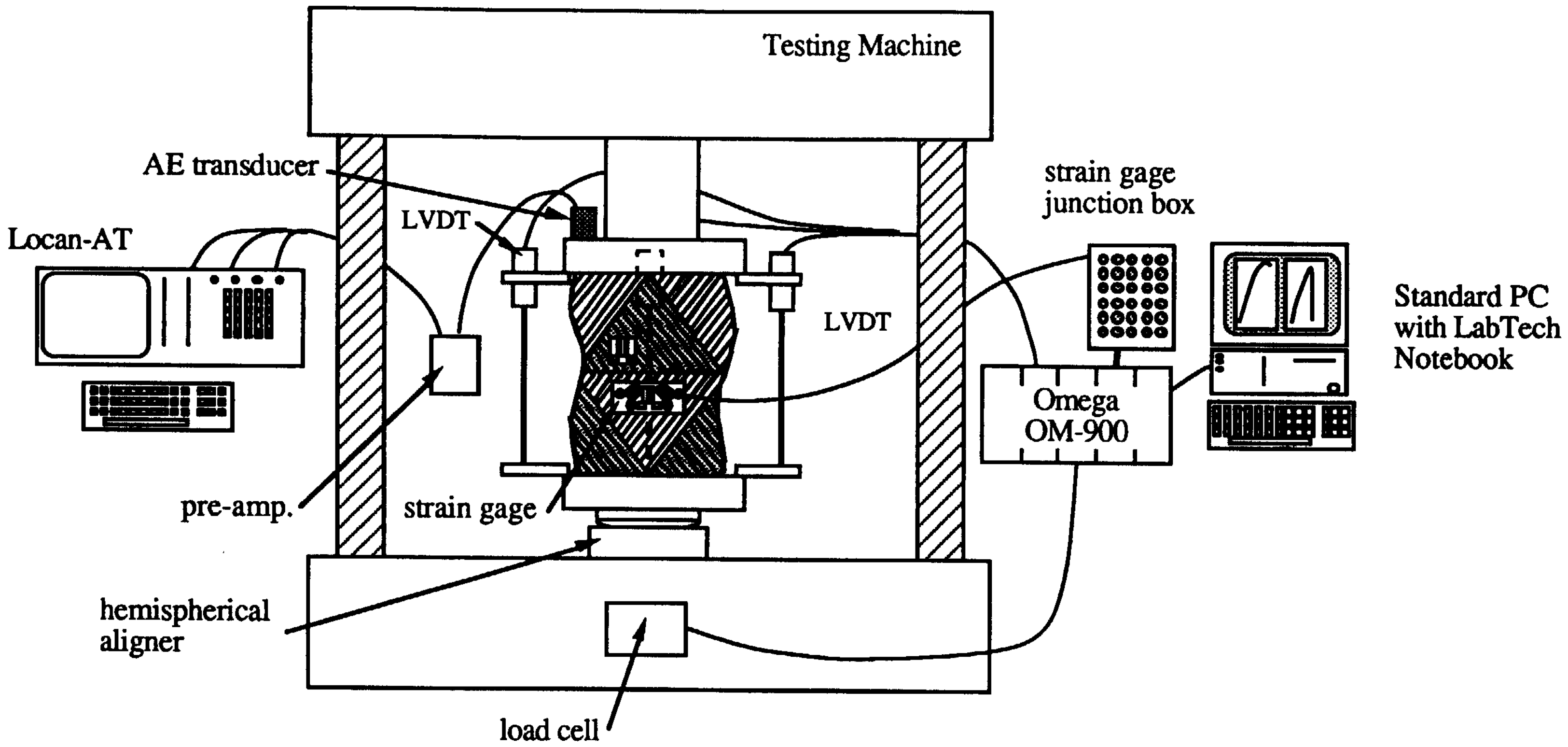
Testing Machine
AE transducer
Locan-AT
LVDT
LVDT
strain gage junction box
Standard PC with LabTech Notebook
Omega OM-900
pre-amp.
strain gage
hemispherical aligner
load cell

Figure 6.1: Equipment setup for compression testing.

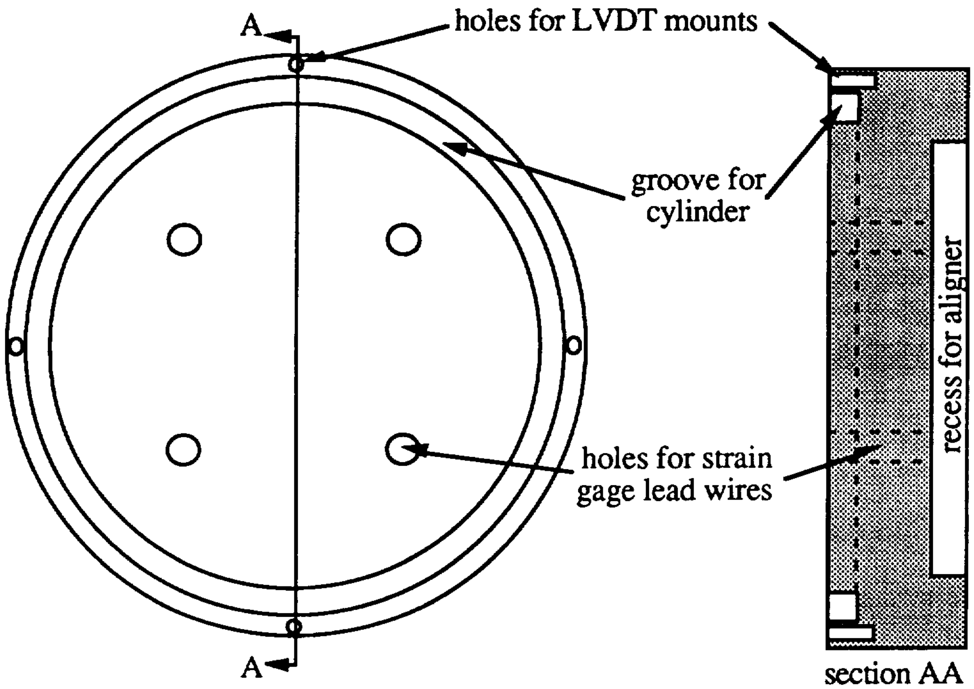

Figure 6.2: End plates used to support the loaded ends of the filament-wound cylinders.

mounting blocks were designed so that the position of the LVDTs could be adjusted to produce the greatest measurement range for each cylinder. Each core extension rod was placed in a small depression machined in either the lower end plate or in a special mounting block to maintain alignment.

A Tinius-Olsen screw-driven universal testing machine, capable of 270 kN (60000 lbs.), was used to load the two, four, and six-ply cylinders to failure. Eight different load-cell ranges are available with this machine: 1.3, 2.7, 5.3, 11, 27, 53, 130, and 270 kN (300, 600, 1200, 2400, 6000, 12000, 30000, and 60000 lbs). The load-cell range used during testing varied with each specimen configuration. During testing, a constant crosshead-displacement rate of 0.635 mm/min was used. A Baldwin hydraulic universal testing machine capable of 1.3 MN (300000 lbs) was used to load the eighteen-ply cylinders to failure.

To record the load cell, LVDT, and strain-gage values during testing, an Omega OM-900 data acquisition system and a Standard 386 personal computer were used with the LabTech Notebook software program. This is the same data acquisition system used for the thickness and geometry testing described in Chapter 4. Data acquisition rates depended on the number of channels being recorded. When only the load and axial LVDTs were monitored during testing, a data acquisition speed of 10 Hz. was used.

### 6.1.2 Acoustic Emission Test Equipment

Acoustic emission monitoring was used to determine when damage occurred during testing. Acoustic events are caused by sudden changes in the strain energy within a material or structure resulting from phase transformations, crack initiation, crack propagation, or buckling. Since no phase transformations were induced in the material and several thresholds were used to eliminate noise during testing, the acoustic events observed were caused by fracture of the composite material and buckling. No previous reference of acoustic emission monitoring during compressive buckling has been located.

The acoustic emission monitoring equipment used during this research program consisted of a Locan-AT system manufactured by Physical Acoustics Corporation. This device was used to process the incoming acoustic signals, perform several calculations, store these parameters on an internal hard disk, and display the acoustic events on a computer screen. Acoustic events were sensed at the end plate by a broadband transducer, Physical Acoustics Corporation model S9208, which has a nominal operating frequency range between 20 kHz and 1 MHz. An ultrasonic gel was used as the couplant between the end plate and the transducer. The transducer was connected by a mini-BNC coaxial cable to a pre-amplifier, Physical Acoustics Corporation model 1220A, which amplified the signal from the sensor by 40 dB.

From the pre-amplifier, the signal was split into three parts with the use of T-connectors and connected to three input channels on the Locan-AT. The input signal was split so that different threshold levels could be used with the same input signal. The channel with the lowest threshold provided the greatest sensitivity but also contained the most noise; whereas, the channel with the highest threshold only captured the most energetic events. Table 6.1 contains the data acquisition parameters used during compression testing. The peak definition time (PDT), hit definition time (HDT), and hit lockout time (HLT) are parameters which help quantify the incoming voltage signal from the AE transducer as an acoustic event. The PDT is used to define when the maximum amplitude peak has occurred during an acoustic event. The HDT is the maximum length of time in which a voltage signal can be considered as one acoustic event. Finally the HLT is the length of time after the HDT has expired in which the system ignores any voltages above the threshold. This parameter is helpful for eliminating unwanted reflections of the acoustic wave. A complete discussion of these parameters is given in [23].

Table 6.1: Data acquisition parameters used with the Locan-AT acoustic emission test equipment.

| Channel Number | Gain (dB) | Threshold (dB) | Peak Defination Time (µs) | Hit Defination Time (µs) | Hit Lockout Time (µs) |
|---|---|---|---|---|---|
| 1 | 20 | 40 | 50 | 200 | 300 |
| 2 | 20 | 55 | 50 | 200 | 300 |
| 3 | 10 | 70 | 50 | 200 | 300 |

### 6.1.3 Photographic and Video Test Equipment

Visual observation of the compression specimens before, during, and after failure, can often be the most informative data gathered during compression testing. Images of the cylinders were captured in two forms: still photographs using a 35 mm camera, and video tape. Photographs of each cylinder were taken just prior to testing and after failure. A standard-speed video camera was used with a VHS video cassette recorder (VCR) to document most tests during the entire compression test. Two compression specimens, Specimens 012592B and 031392B, were monitored with a high-speed video system operating at 2000 frames per second. These images were captured on a 19 mm wide magnetic tape and then copied to a standard VCR tape for review and permanent storage.

## 6.2 Experimental Procedures

Most cured cylinders were machined into two specimens which were designated with the cylinder number and the suffix A or B. After the thickness distributions were measured with the LVDT system, selected 152-mm diameter specimens were instrumented with foil-type strain gages. The 57-mm diameter compression specimens which were strain gaged were not tested to determine their thickness distributions. In each case, the gages were placed back to back so that bending and compressive strains could be differentiated. Where gages were mounted on the laminated-shell regions, the gages were located at the centroid of the region to minimize the effect of the crossover bands. The specific location of each gage will be discussed in Section 6.4 in conjunction with the compression results.

To mount the cylinders for compression testing, the steel end fixtures were placed on a hot plate and heated to melt the Cerrobend®. After melting, the end plate was removed from the hot plate and the specimen was inserted in the liquid Cerrobend® such that the cylinder was concentric with the end plate. A weight was placed on the end of the specimen to keep the edge of the cylinder at the bottom of the groove in the end plate. After cooling, the second end plate was attached with the same technique. When potting the second edge of the 57-mm diameter cylinders, four brass tubes were placed through the holes in the end plates to ensure alignment. The end plates for the 152-mm diameter specimens were aligned visually.

After the geometry measurements were completed, the specimen was placed in the testing machine and the LVDTs were attached to the upper end plate. The LVDTs were adjusted so that the center of the core was located at the center of the LVDT. Next, the LVDTs and strain gages were connected to the OM-900 system. The hemispherical aligner was placed under the 57-mm diameter specimens and on top of most of the 152-mm diameter cylinders and the entire system was placed in the center of the testing machine. Selected specimens were also monitored with the use of the spring-loaded LVDT used for thickness and geometry testing. When this instrument was used, it was attached to the specimen to monitor the transverse displacements during loading.

The axial LVDTs were calibrated with the use of two glass microscope slides. Both slides were placed under the core extension rod and several seconds of data were recorded with the data-acquisition system. The top slide was then removed and several more seconds of data were recorded. This process was repeated five times for each LVDT. Since microscope slides have a very uniform thickness, the change in voltage monitored with the data-acquisition system could be related to the thickness of the slide to determine the calibration constant. LVDT calibration was performed for each test so that differences in the experimental setup could be considered. When strain gages were mounted on the cylinder, the computer files containing the strain-gage data were checked to identify any problems with the gages or connections prior to testing.

Close-up photographs of the specimen were taken with a 35 mm camera. The camera was removed prior to testing and a video camera was installed in approximately the same location. Next, the mechanical and acoustic data-acquisition systems were initialized, the proper load-cell range was chosen, and the load cell was zeroed. The test was begun by starting the VCR, turning on the chart recorder on the testing machine, starting the testing machine, and simultaneously striking keys on the mechanical and acoustic emission computer keyboards to begin data acquisition. For the specimens which had a stable postbuckling behavior, the cylinder was loaded until either the mode shape no longer changed or until substantial fracture of the specimen was observed. Loading was halted immediately after fracture for the specimens which exhibited an unstable postbuckling behavior.

Photographs of the failed cylinders were taken prior to unloading the specimen. If the specimen contained out-of-plane deformations, a paint pen was used to trace the ridges in the deformation pattern. These ridges were formed either where the cylinder made the transition from cylindrical to buckled regions, or where two deformation regions interacted as shown in Figure 6.3. After drawing, the specimens were unloaded and the cylinder was removed from the testing machine.

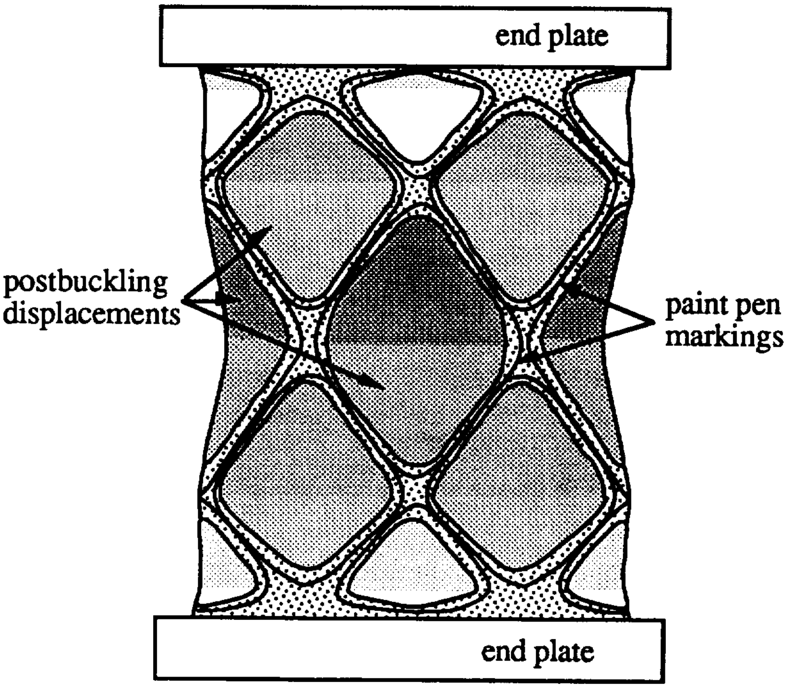

Figure 6.3: Typical buckled mode shape of [±30] cylinders.

In several cases, the [±30] cylinders were buckled multiple times to determine behavior of filament-wound shells to low-cycle buckling fatigue. The procedure for these experiments was nearly identical to that described previously with the following exception. As soon as the maximum load was reached, the testing machine was stopped to limit the amount of postbuckling damage. This procedure was repeated ten times while monitoring the LVDTs, loads, strains, and acoustic emission. Photographs were taken and deformations were sketched on the cylinder prior to unloading the first and after the tenth cycles. The tenth loading cycle was typically extended until the cylinder was well within the postbuckling regime.

## 6.3 Data Reduction

The calculations required to obtain the mechanical and acoustic emission parameters from the measured quantities are discussed in the following section. The quantities measured during the compression tests include the voltages from the LVDTs, strains from each strain gage, percentage of the full-scale load-cell range, voltages from the transversely mounted LVDT, and many acoustic emission parameters. The conversion of these quantities into the stiffness, buckling or fracture load, end-shortening displacement at buckling, transverse displacement, and global strain values were accomplished using Lotus 123, a spreadsheet computer program. Many of the acoustic emission parameters were

C-2

computed within the Locan-AT system and will not be described here; however, the binning process used to examine the statistical behavior of the acoustic response is described in Section 6.3.2. An excellent description of the methods used to determine the energy, counts, amplitude, and frequency of the acoustic emissions is given in Pollock [24].

### 6.3.1 Mechanical Data

The calculation of the calibration constants and displacements from the measured LVDT voltages is the same for the compression tests as for the thickness distribution testing described previously. The average of the calibration constants for the spring-loaded LVDT, measured during the thickness testing, was used for the compression testing. The average displacement measured by the three axially-located LVDTs was computed and used as the average end-shortening displacement for subsequent calculations.

Loads, measured by the load cells in the Tinius-Olsen testing machine, are recorded by a pen on the chart recorder. The chart recorder was calibrated so that its position was linearly related to the percentage of the full-scale load range for each load cell. A potentiometer was mounted to the pen drive mechanism and output from this device was calibrated so that the data-acquisition system also recorded the percentage of the full scale load. Consequently, to covert these values to the load on the specimen, the stored numbers were divided by 100 and multiplied by the value of the full-scale load. Often the load reading at the start of the test was not zero. To compensate for this inaccuracy, each subsequent value of load was shifted by this null-load value after testing. The stress on the specimen was computed from the load and the cross-sectional area of the specimen using the micrometer thickness value. The maximum measured load was considered to be the failure load; likewise, the average end-shortening displacement at the maximum load was considered to be the end-shortening displacement at failure. During many tests, noise in the load measurement was observed as sharp drops in the measured load.

The LabTech Notebook software was programmed with the gage factors necessary for the conversion of the Wheatstone Bridge voltages into strain values. As with the load cell data, the strain-gage data often indicated a strain when no load had been applied to the specimen. This strain value was subtracted from the corresponding data and the circumferential, hoop, and shear strains were calculated. Since the strain gages were usually placed on either a crossover band or on a laminated-shell region, the measured strains can not be related to the effective laminate Young's modulus due to the non-zero bending-extension coupling stiffnesses in these regions.

The stiffness of the cylinder was computed from the slope of the load versus average end-shortening displacement curve. Often, this curve was non-linear at the beginning of the test and near the maximum load, as shown in Figure 6.4. The initial linear region was used to compute the stiffness for each cylinder. When the compression specimen was buckled multiple times, the stiffness, buckling load, end-shortening displacement at buckling, and local strains were computed for each loading cycle to determine degradation in performance with repeated buckling.

### 6.3.2 Acoustic Emission Data

The conversion of the electronic signal from the acoustic emission transducer into parameters such as counts, energy, amplitude, and frequency were computed by the Locan-AT prior to storage on the hard drive. Each acoustic event was similarly handled and stored during the compression test. Binning, a common technique used to statistically examine acoustic emission data, was performed on the counts and energy parameters. When the data is binned, each parameter is summed over a short period of time. Consequently, acoustic events which occur in rapid succession are combined without a major reduction in the type of information presented. A Fortran computer program was written to bin the acoustic emission data recorded on all three channels during the

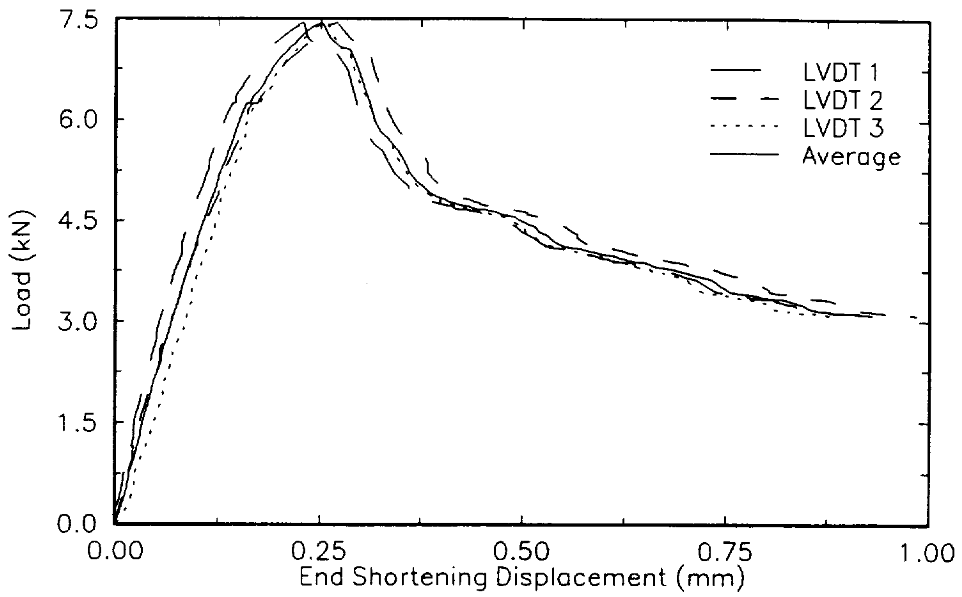

Figure 6.4: Typical load/end-shortening displacement plot.

compressive-buckling tests using a bin size of 0.16 sec. When the compression specimen was buckled multiple times, the acoustic emission data was binned for each loading cycle to examine the degradation in performance.

## 6.4 Results and Discussion

Many parameters are required to completely describe the manufacturing, quality, and compressive performance of thin filament-wound cylinders. The relationships between the manufacturing and quality parameters have been discussed in the previous chapters. The following discussion of the compressive results has been divided into the seven experimental programs: In-Plane Crossover-Band Spacing, Mandrel Material, Cylinder Scale, Symmetry of the Laminated-Shell Regions, Winding Sequence, Through-the-Thickness Crossover-Band Location, and Heated Winding.

### 6.4.1 In-Plane Crossover-Band Spacing

The objective of this study was to examine the effects of the in-plane circumferential crossover-band spacing on the compressive response. Each specimen was wound on a 57-mm diameter mandrel with a winding sequence of [±30] and cured with the shrink-tape technique. The number of circuits per pattern was varied to produce crossover-band spacings of 155, 76, 51, 30, 14, and 6.9 mm.

During testing, each specimen behaved in the same general fashion. As the specimens were loaded, they shortened in a linear fashion without appreciable bending. Some minor cracking was heard during the early stages of testing which increased with the load until buckling occurred. When the shell buckled, a loud pop was heard which corresponded to the appearance of the out-of-plane displacements and a sharp drop in load. Typically, the buckled mode shape consisted of diamond-shaped regions uniformly distributed around the circumference of the shell, as shown in Figure 6.5. The main ring of diamonds was centered along the mid-length of the cylinder and was approximately half of the cylinder in height. Each diamond was oriented with the corners pointing to the machined ends of the specimen with the widest section deformed inward. In several specimens, the regions between the main ring of diamonds and the end plates also contained diamond-shaped, out-of-plane deformations. These diamonds were typically not uniform from top to bottom due to the constraint caused by the clamped edge.

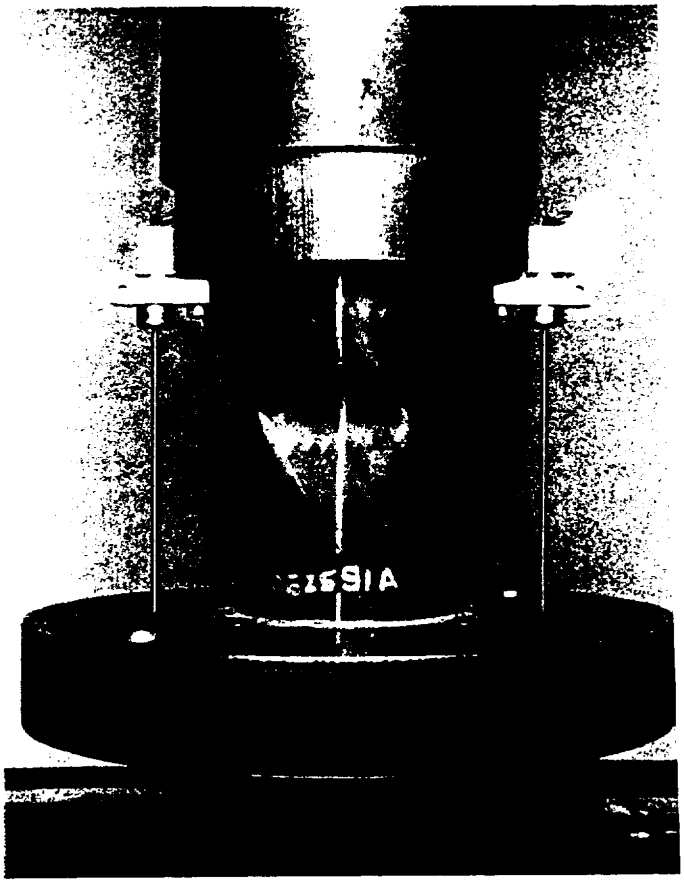

Figure 6.5: Typical buckling mode of [±30] filament-wound cylinders.

Although most specimens buckled and postbuckled in the same shape, the pattern of helical and circumferential-crossover bands did affect the compressive behavior. The regions of the buckled cylinder with the smallest radius of curvature, the edges and corners of the diamonds, are parallel to the winding angle, as is evident in Figure 6.5. Each edge was approximately one tow width away from the helical-crossover bands. Where the winding pattern was either smaller or larger than the buckled mode shape, the edges of the buckled diamonds are also aligned with the winding pattern; however, one buckled diamond often contained several laminated-shell regions.

The most striking exception to these observations occurred with Specimen 011692A which has a circumferential crossover-band spacing of 155 mm. This specimen contained several small diamond-shaped buckled regions which paralleled both sides of the helical-crossover bands, as shown in Figure 6.6. The regions far from the crossover bands did not contain out-of-plane deformations. Although the load-end shortening response for Specimen 011692B is nearly the same, this specimen buckled like the other winding patterns. One possible explanation for this behavior is indicated by the range of the geometric imperfection. This quality measure indicates that Specimen 011692A is much more non-cylindrical than other compression specimens in this study.

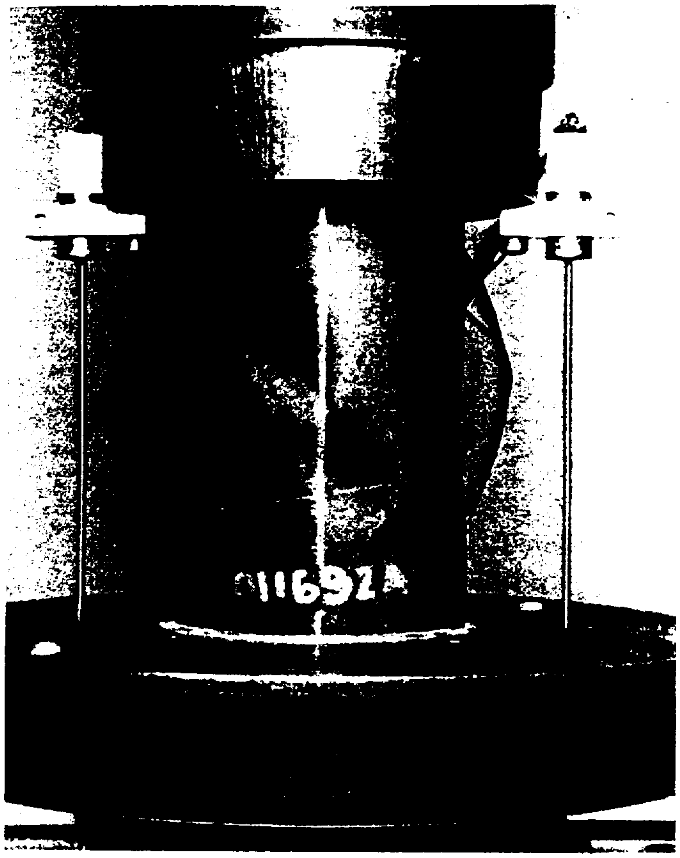

Figure 6.6: Buckled shape of Specimen 011692A .

When the specimens were postbuckled, the out-of-plane displacements increased in a stable fashion and additional cracking was heard as the out-of-plane regions began to interact. After the initial drop in load, the load increased slightly which continued until substantial cracks were induced. Very little coalescence of the buckling modes, ie. out-of-plane displacements associated with one buckling mode combining to form a different postbuckling mode, was observed. Visible cracks were observed in the regions between the buckling diamonds where the radius of curvature of the buckling mode was small. During unloading, the regions with out-of-plane deformations slowly diminished until the cylinder snapped back to its original shape. As with the initial buckling response, a loud pop was heard as the cylinder returned to its original conformation.

Four specimens in this experimental program were instrumented with strain gages to investigate the local deformation behavior of the shells during the prebuckling, buckling, and postbuckling stages of the experiment. The first instrumented specimen (062591B) was used to examine the variation of strain within one triangular region. The specimen was instrumented with Micro-Measurements model EA-06-062ED-120 gages using standard surface preparation and bonding techniques. Strain-gage position number 1 was located on a circumferential-crossover band and was aligned at +30°. Gages in position 3 were aligned at -30° and were placed on top of a helical-crossover band. Positions 2 and 4 were located at the centroid of neighboring triangular shell regions, as shown in Figure 6.7. Surprisingly, Positions 1 and 2 exhibited nearly the same compressive strains throughout the test. When the buckling mode was examined, these positions were located in the same general region of one buckling diamond, as shown in Figure 6.7. Position 3 was located near one edge of a buckled diamond and exhibited the largest compressive strain. Although

Position 4 is at the same general location as Position 2, the strain was smaller throughout the test. Position 4 is closer to the clamped edge of the cylinder which could explain this behavior. In each case, the compressive strains do not change sign during the experiment, as shown in Figure 6.8. The magnitude of the bending strains follows the same trends as the compressive strains; however, in each case the bending strains change sign after buckling. This indicates that the prebuckling and postbuckling shapes are different in these locations on the cylinder.

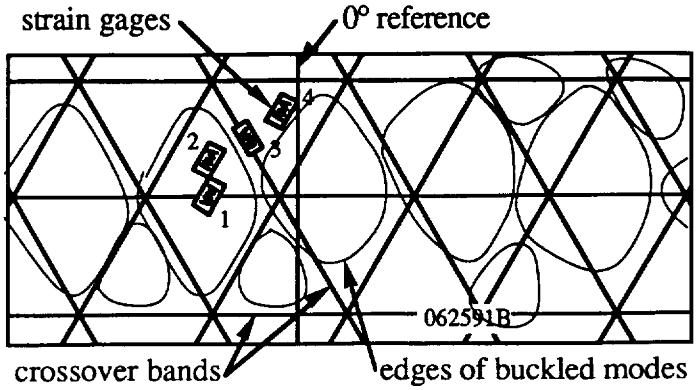

Figure 6.7: Buckled mode shape and strain-gage locations for Specimen 062591B.

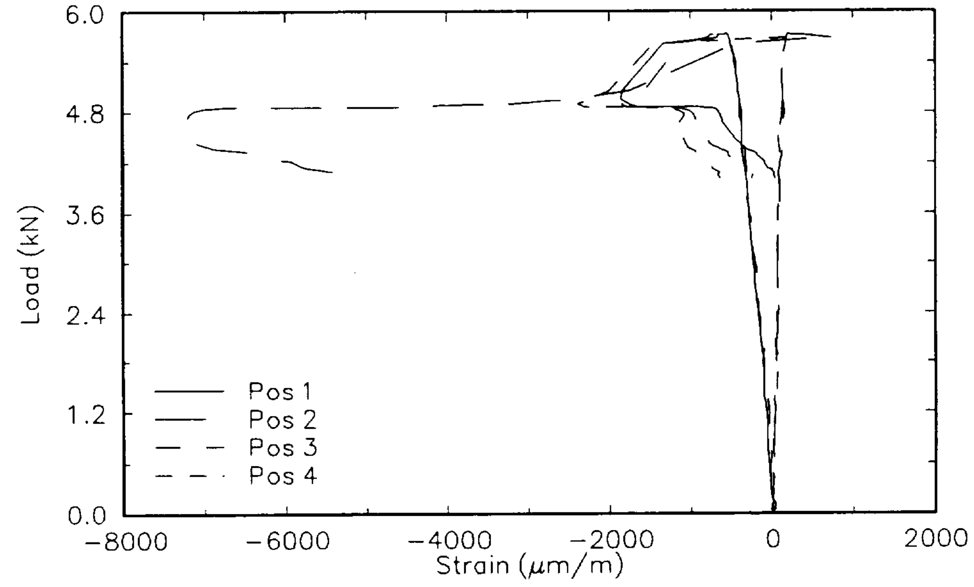

Figure 6.8: Axial compressive strains in Specimen 062591B.

The final three specimens which were instrumented with strain gages, utilized long gage-length rosettes to measure the complete state of strain; Micro-Measurements model CEA-06-125UW-120. Specimen 062091 had rosettes located at the centroid of two laminated-shell regions placed 180° apart. Longitudinal and transverse compression strains were similar for the two positions. After buckling, the compressive strains maintained their prebuckling sign which indicates a similarity in shape before and after buckling. The longitudinal bending strains for both positions were quite small in the prebuckling regime. Transverse bending strains were larger in magnitude than the longitudinal strains and differ in sign. Consequently, since the transverse bending strains were different on the opposite sides of the cylinder, the shape of the cylinder was not axisymmetric prior to buckling.

Specimens 063091A and 070191A were instrumented with strain-gage rosettes at only one position since the crossover-band spacing of these cylinders was very small. The long gage length of the strain gages effectively integrates the influence of several helical and circumferential-crossover bands. The compressive strain behavior of these specimens was very similar, as shown in Figure 6.9. The sharp vertical lines in these plots indicate either buckling or the formation of cracks during postbuckling. The bending strain behavior of Specimens 063091A and 070191A differed considerably, as shown in Figure 6.10. Specimen 063091A exhibited very little longitudinal bending which changed sign after buckling and grew quite large. The longitudinal bending strains of Specimen 070191A were also smaller than the transverse bending strains; however, the direction of curvature at this position in this specimen remained the same after buckling.

The behavior of the in-plane crossover location specimens was also examined by buckling selected specimens several times. Specimens 062091, 062191A, and 011692A were loaded just beyond buckling and then unloaded nine times while monitoring the load, end-shortening displacements, and strains on the specimens. Each specimen was then loaded well beyond the buckling load to observe the behavior of each cylinder in the postbuckling regime. In all cases, the buckling load dropped significantly from the first cycle to the second. The buckling load continued to drop in decreasing amounts with each cycle until the third or forth cycle, as shown in Figure 6.11. Reductions in the end-shortening displacement at buckling and stiffness with the buckling cycle, shown in Figures 6.12 and 6.13 respectively, are typically smaller than those seen in the buckling loads. The increase in the end-shortening displacement at buckling for the first three loading cycles of Specimen 011692A maybe caused either by bending or movement of the cylinder in the Cerrobend®. In each case, irrecoverable damage is induced in the filament-wound cylinder during buckling. Damage is also induced in subsequent buckling events; however, the additional increment in damage is much smaller and will even disappear after several cycles.

Results from the acoustic-emission testing support the previously made arguments regarding the reduction in performance during multiple buckling cycles. Specimen 062191A was loaded ten times while monitoring acoustic emission; whereas, Specimen 062191B was only loaded once. The first loading cycle of Specimen 062191A shows some damage occurring prior to buckling; however, the vast majority of damage was induced at the buckling load and in the initial portion of the postbuckling regime, as shown in Figure 6.14. Subsequent loading cycles showed very little damage. Examination of loading cycles 2 through 9 suggests that buckling also induced an ultrasonic acoustic event in addition to the loud pop heard during testing. In both specimens, the majority of damage occurred during the postbuckling phase of the experiment.

When the compressive response of each specimen was examined with respect to the quantifiable quality parameters, no clear correlations were observed. This result is expected since each specimen was manufactured with identical curing procedures; however, the lack of correlation with the range of the geometric imperfection was unexpected. As the fiber-volume content increased, the buckling strain decreased slightly. A corresponding increase in stiffness was observed for these specimens; however, the amount of scatter for this comparison was quite large as shown in Table 6.2.

Several trends were observed when the buckling load, stiffness, and end-shortening displacement at buckling were examined in terms of the manufacturing parameters. The most dramatic trend in these results was observed when the buckling stress was compared to the circumferential crossover-band spacing. Since the crossover bands contain curved fibers which alter the in-plane and bending stiffnesses of the

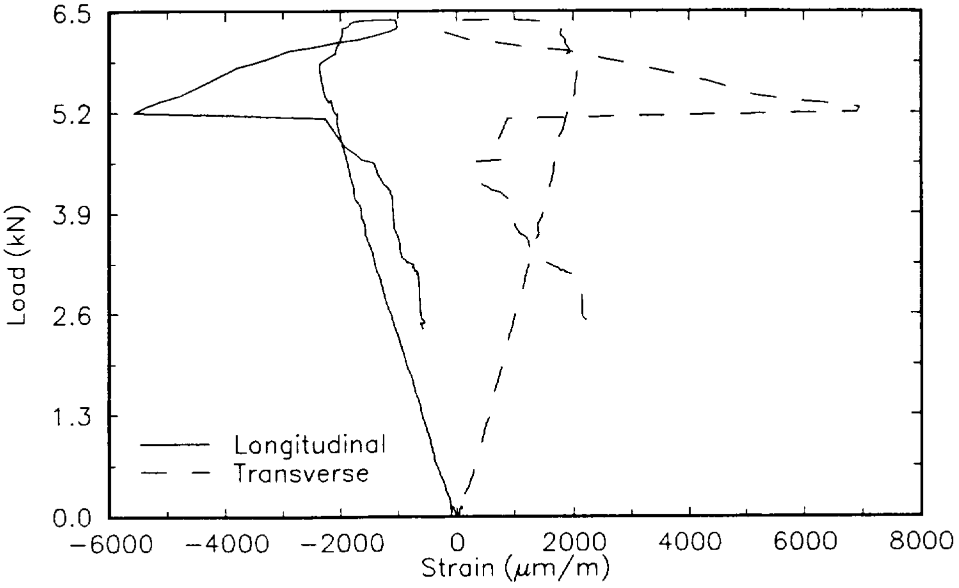

a)

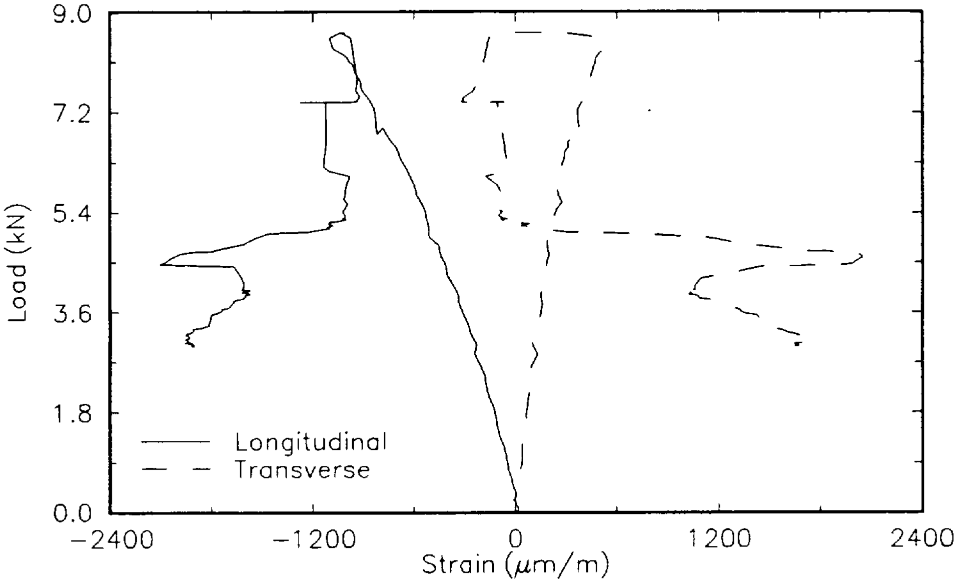

b)

Figure 6.9: Axial compressive strains in Specimens a) 063091A and b) 070191A.

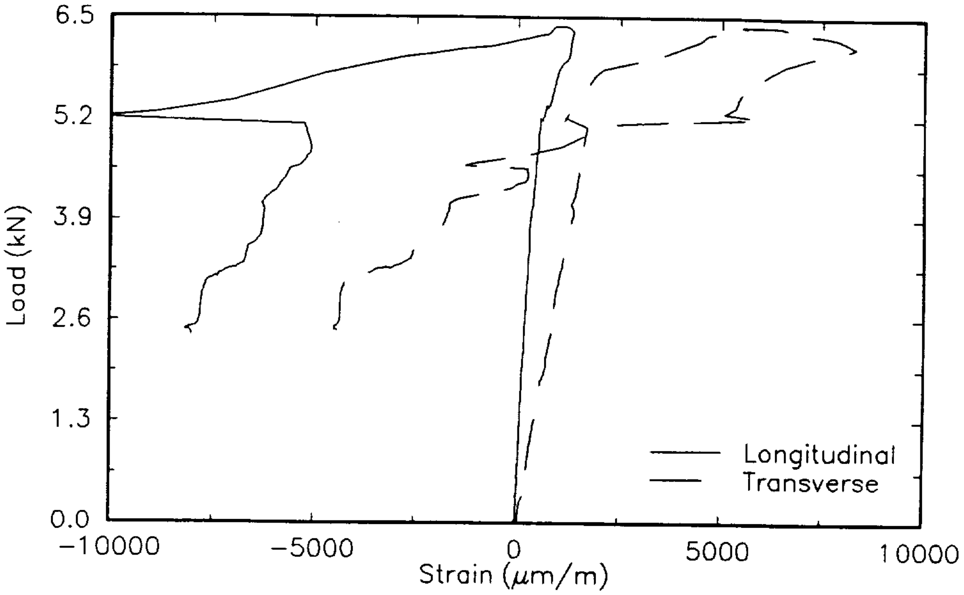

a)

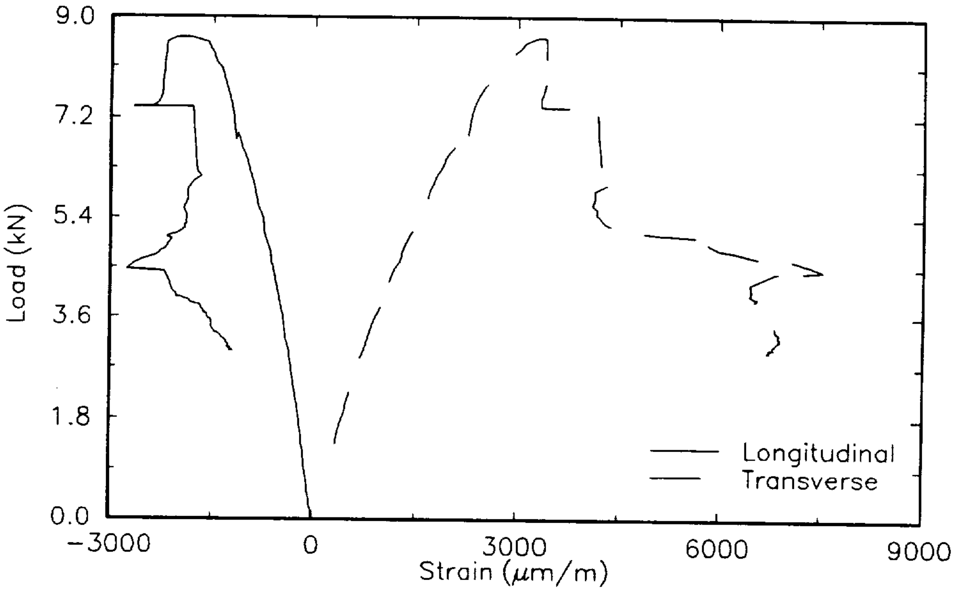

b)

Figure 6.10: Axial bending strains in Specimens 063091A and 070191A.

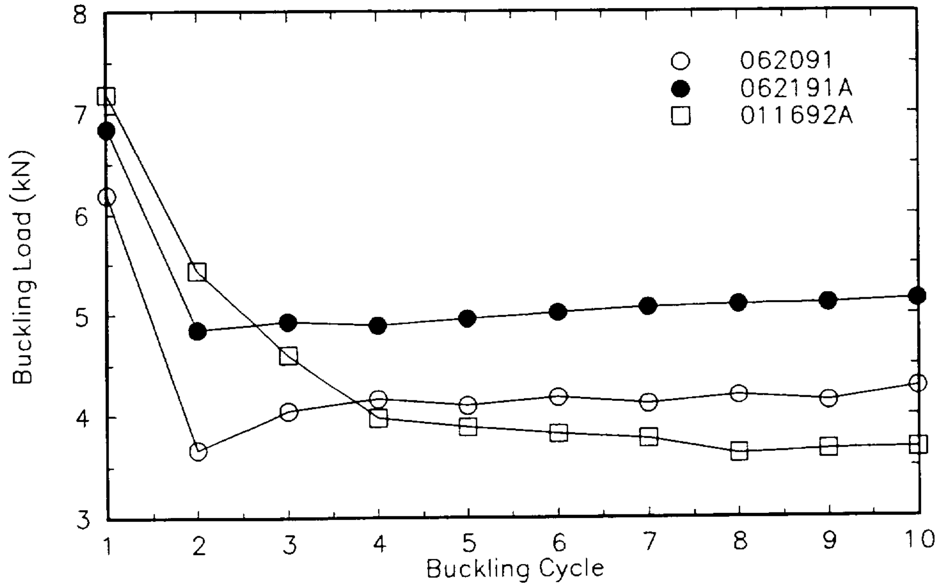

Figure 6.11: Buckling-load degradation with number of buckling cycles.

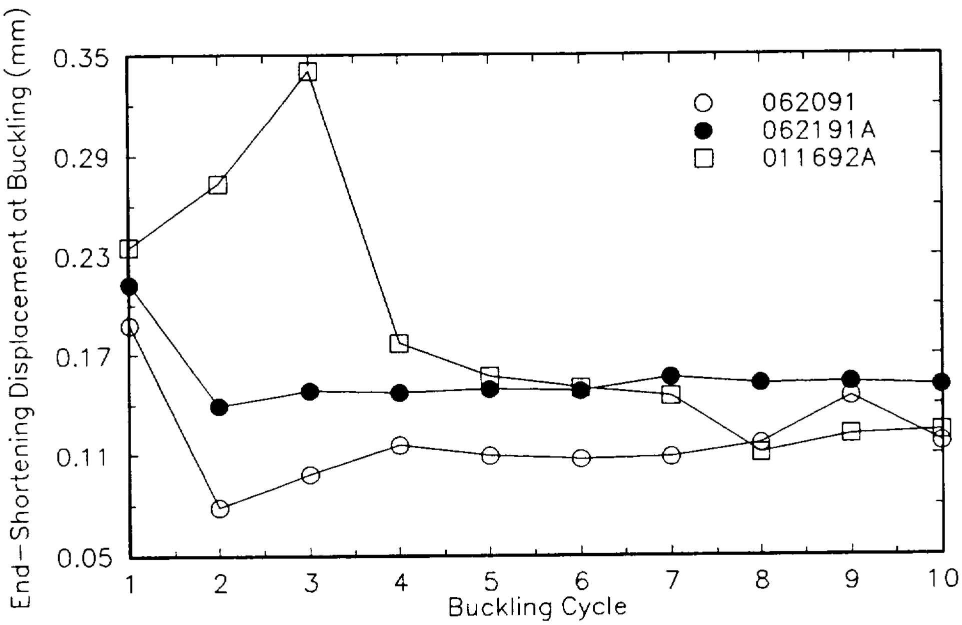

Figure 6.12: End-shortening displacement at buckling degradation with number of buckling cycles.

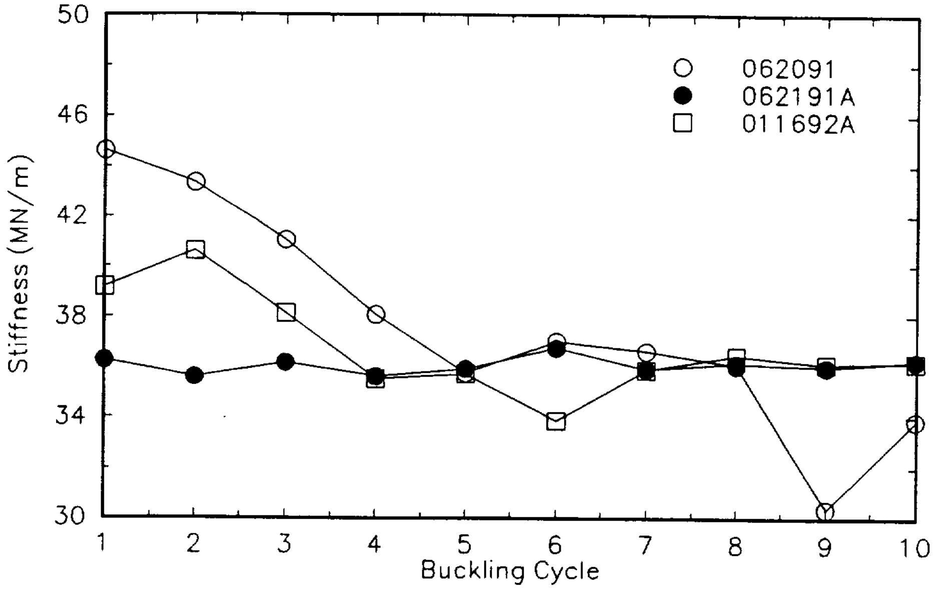

Figure 6.13: Stiffness degradation with number of buckling cycles.

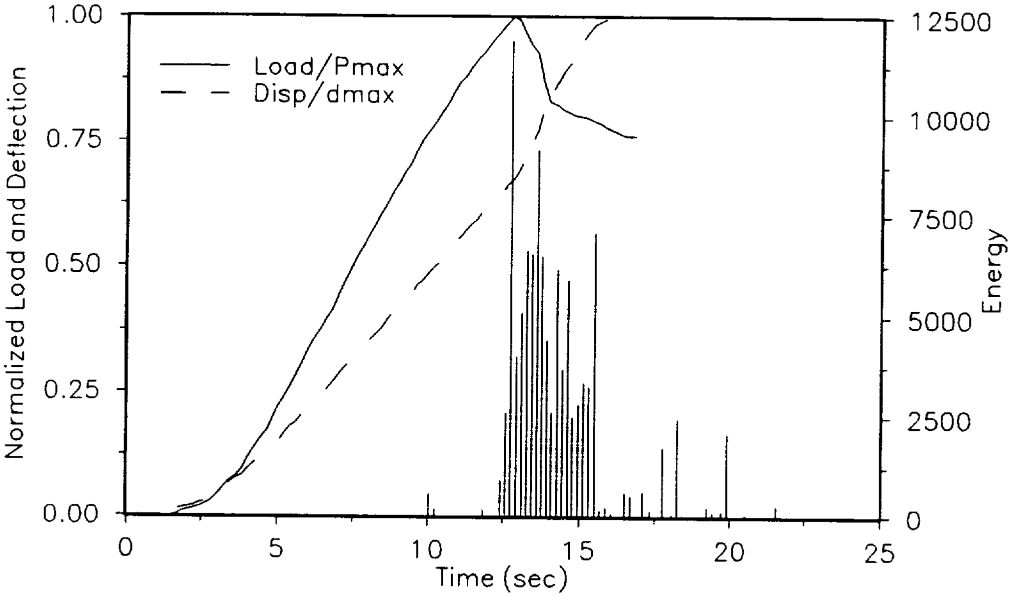

Figure 6.14: Acoustic energy observed with Specimen 062191A.

Table 6.2: Compression results for the In-Plane Crossover-Band Spacing experimental program.

| Cylinder Number | Circumferential Crossover Band Spacing (mm) | Stiffness (x10^-3 N/m) | End Short. Displ.@ Buck. (mm) | Buckling Stress (MPa) | Number of Circum. Waves |
|---|---|---|---|---|---|
| 061991A | 76.2 | 3.82 | 0.252 | 103 | 4 |
| 061991B | 76.2 | 3.13 | 0.287 | 82.5 | 5 |
| 062091 | 76.2 | 4.47 | 0.188 | 79.7* | 4 |
| 062191A | 50.8 | 3.63 | 0.212 | 90.5* | 6 |
| 062191B | 50.8 | 3.84 | 0.203 | 86.1 | 6 |
| 062291A | 30.5 | 3.61 | 0.206 | 94.6 | 6 |
| 062291B | 30.5 | 2.99 | -- | 87.5 | 5 |
| 062491A | 30.5 | 4.96 | 0.148 | 89.8 | 5 |
| 062491B | 30.5 | 3.87 | 0.167 | 72.3 | 5 |
| 062591A | 30.5 | 3.64 | 0.195 | 82.9 | 5 |
| 062591B | 30.5 | 3.59 | 0.189 | 73.4 | 5 |
| 063091A | 14.2 | 5.01 | 0.252 | 81.4 | 5 |
| 063091B | 14.2 | 3.70 | 0.231 | 87.1 | 5 |
| 070191A | 6.86 | 4.06 | 0.252 | 105 | 5 |
| 070191B | 6.86 | 3.29 | 0.312 | 108 | 5 |
| 011692A | 155 | 3.92 | 0.235 | 84.1* | -- |
| 011692B | 155 | 4.17 | 0.223 | 92.3 | 6 |

* first load cycle

laminate, the compressive response should depend on the number of crossovers within a specimen. As the length divided by the circumferential crossover-band spacing increased, (the number of crossovers in the specimen decreases) the buckling stress decreased initially and then rose, as shown in Figure 6.15. The mode number shown in this figure corresponds to the number of circumferential waves in the observed buckled shape. The buckling stress was smallest when the diamond shaped regions of the winding pattern and buckling mode coincided (i.e. when w = 30 mm). When the winding pattern was much smaller than the buckling mode, the buckling stress was 30 percent greater than when the winding and buckling patterns were the same size. A 15 percent increase in buckling stress was observed as the crossover-band spacing increased. Similar trends were observed when the end-shortening displacements at buckling were compared to the winding pattern. No clear correlation was observed between the winding pattern and the effective axial stiffness of the cylinder.

### 6.4.2 Mandrel Material

Mandrel material can affect filament-wound cylinders by changing the level of residual stress induced in the material and the pressure on the inner surface of the cylinder during cure. Cylinder 062191 was wound and cured on an aluminum mandrel while Cylinder 062391 was wound and cured with the same manufacturing parameters on a steel mandrel. When the load/end-shortening displacement behavior and buckling mode shapes were examined, little difference in the two cylinders was observed.

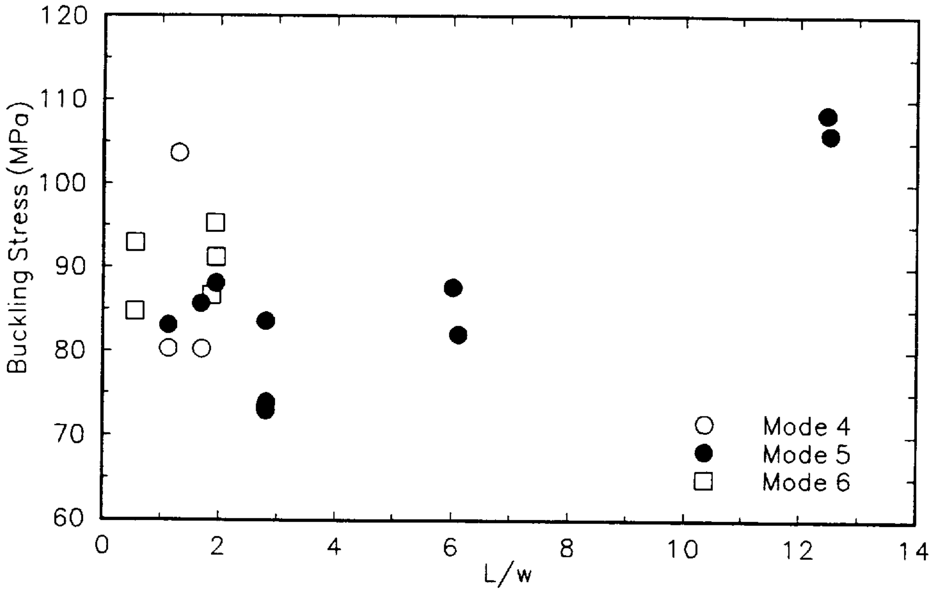

Figure 6.15: Effect of circumferential crossover-band spacing on the buckling stress of 57-mm diameter [±30] filament-wound cylinders.

Specimen 062391A was instrumented with strain gages located at the centroid of the each wound triangle around the circumference of the specimen. Micro-Measurements model CEA-06-125UR-120 gages were used at each location and were numbered sequentially around the circumference. The initial third of the loading range of this specimen exhibited a great deal of non-linear compressive strain behavior, as shown in Figure 6.16, which was also observed in the load-end shortening behavior. After this portion of the experiment, the slopes of the compressive strain lines were the same up to buckling which indicates that the specimen was loaded uniformly around the circumference. This non-linearity was thought to be caused by uneven potting of the cylinder in the Cerrobend®. The bending strains, shown in Figure 6.17, do not exhibit the initial non-linear behavior, however, the differing signs and slopes of the strains indicate that the amount of bending in the specimen depended on circumferential position. The bending strain behavior was relatively linear up to buckling with the exception of position number 1. The bending strains in this location changed sign prior to global instability. This behavior was expected since these shells exhibit extension-bending coupling behavior arising from the antisymmetry of the laminated shell and non-membrane prebuckling deformations. Only Positions 1, 2, and 6, which are located on one side of the specimen, changed sign after buckling.

Both specimens manufactured with the steel mandrel were buckled ten times to investigate their low-cycle fatigue behavior. Specimen 062391A responded very similarly to the 57-mm diameter specimens discussed in Section 6.4.1. The continued decrease in buckling load observed in Specimen 062391B was caused by the damage induced in the specimen since loading was not halted immediately after buckling. When the load history included moderate postbuckling deformations, the amount of induced damage was larger for each loading cycle with corresponding decreases in the stiffness, end-shortening displacement at buckling, and buckling load.

Examination of the compressive performance parameters, shown in Table 6.3 for the first load cycle, exhibited no trends in the buckling strains; however the stiffness and buckling stress of the specimens manufactured on the steel mandrel were slightly lower.

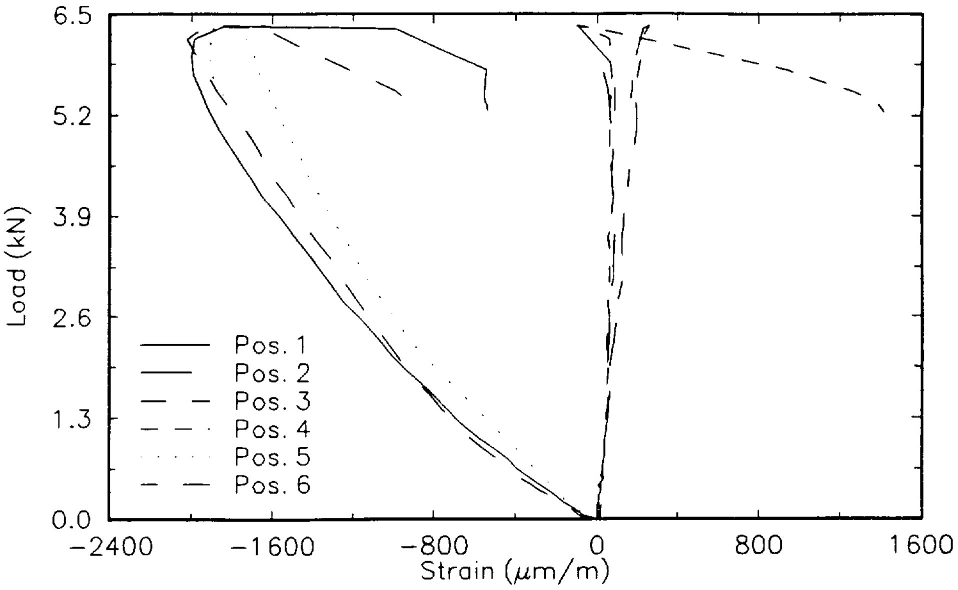

Figure 6.16: Axial compressive strains in Specimen 062391A .

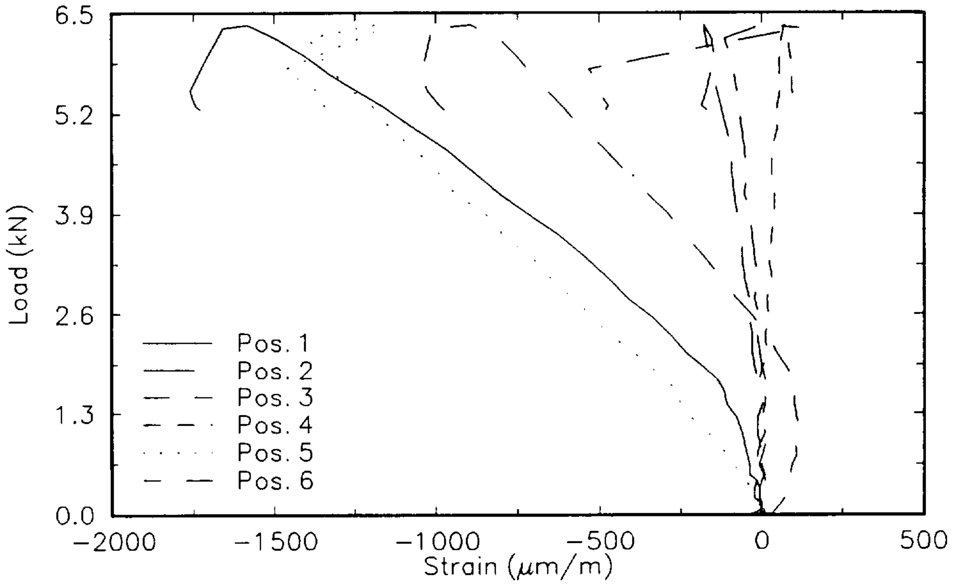

Figure 6.17: Axial bending strains in Specimen 062391A .

These differences may be caused by the fiber volume fraction of the two cylinders. Based on this study, the global stiffness and buckling load of a filament-wound cylinder does not depend on the type of mandrel material used to manufacture the cylinder.

### 6.4.3 Cylinder Scale

In this study, four combinations of cylinder diameter and thickness were used to examine the effects of scale on the compressive performance. The first comparison

Table 6.3: Compression results for the Mandrel Material experimental program.

| Cylinder Number | Mandrel Material | Stiffness (x10^-3 N/m) | End Short. Displ.@ Buck. (mm) | Buckling Stress (MPa) | Number of Circum. Waves |
|---|---|---|---|---|---|
| 062191A | Aluminum | 3.63 | 0.212 | 90.5* | 6 |
| 062191B | Aluminum | 3.84 | 0.203 | 86.1 | 6 |
| 062391A | Steel | 3.50 | 0.162 | 79.6* | 4 |
| 062391B | Steel | 3.22 | 0.264 | 85.1* | 5 |

* first load cycle

involved examining the response of [±30] cylinders wound on the 57-mm and 152-mm diameter mandrels. The second comparison was used to investigate the effects of thickness on multi-layered cylinders.

Cylinders 081291 and 030692 were manufactured with the 152-mm diameter mandrel and wound with a [±30] winding sequence with one circumferential-crossover band in the gage length of the specimen. Like the 57-mm diameter [±30] cylinders, these specimens responded linearly until the buckling load was reached. The load then immediately dropped and remained relatively constant in the initial postbuckling regime. Buckled shapes of the 152-mm diameter specimens, shown in Figure 6.18, contained the same diamond-shaped regions as their smaller counterparts; however, the number of diamonds was typically eight compared to five for the small-diameter cylinders. Another difference in the buckled-mode shape involved the rows of buckled diamonds near the ends of the specimens. These diamonds were much smaller and were quite deformed on the 57-mm diameter specimens; while, the regions were nearly identical to the center row of diamonds for the 152-mm diameter specimens. Damage initiation in the 152-mm diameter specimens required more extensive end-shortening displacement which was expected since the curvature within the buckled displacements was substantially less than observed in the smaller cylinders.

Specimen 030692B was buckled ten times to compare the accumulation of damage during buckling and its affect on the buckling load, strain, and the cylinder stiffness to the small-diameter cylinders. Since the internal energy level at buckling was much lower in the large-diameter specimens, the testing machine could be stopped faster which resulted in less postbuckling damage. Consequently, no appreciable degradation in the buckling load was observed after the first loading cycle.

The acoustic-emissions system was used to monitor each 152-mm diameter specimen during testing. Although Specimens 061991A, 061991B, and 062091 were not monitored acoustically, the large cylinders responded similarly to other 57-mm diameter specimens used for the In-Plane Crossover-Band Spacing experimental program. As observed with the audible cracking, the large-diameter cylinders seemed to be less damaged in the prebuckling, buckling, and initial postbuckling regimes, as shown in Figure 6.19.

The geometry of the 152-mm diameter specimens was designed so that the radius-to-length ratio was similar to the 57-mm diameter specimens. The radius-to-thickness and length-to-thickness ratios of the large specimens were approximately 2.6 times larger than the small specimens. The difference in scale did not affect the axial stiffness of the specimens; however, the buckling stress and end-shortening displacement at buckling were approximately one order of magnitude smaller for the large specimens, as shown in Table 6.4. When the manufacturing and quality parameters were examined to determine the cause

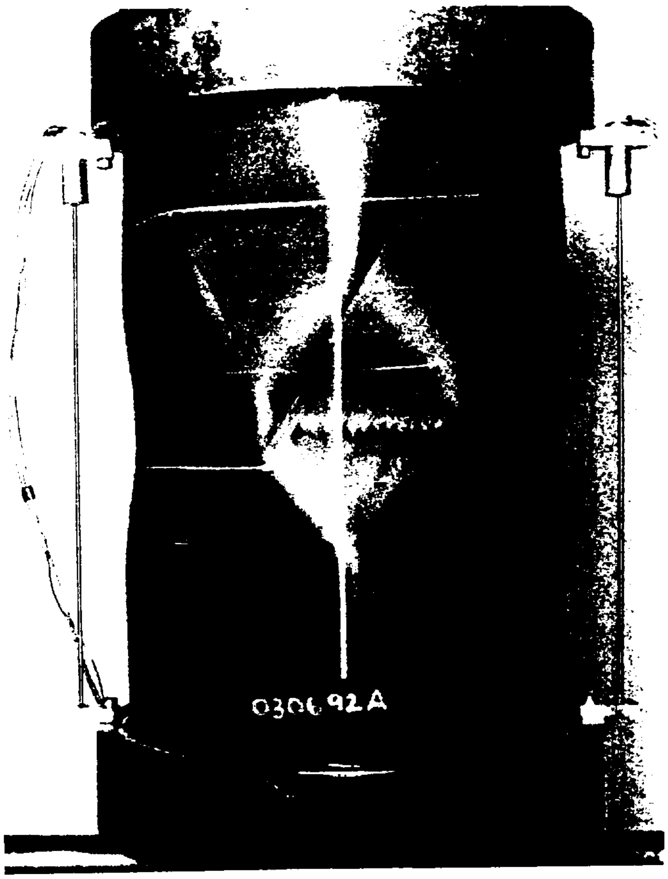

Figure 6.18: Buckled mode shape of Specimen 030692A; typical of the 152-mm diameter, [±30] specimens.

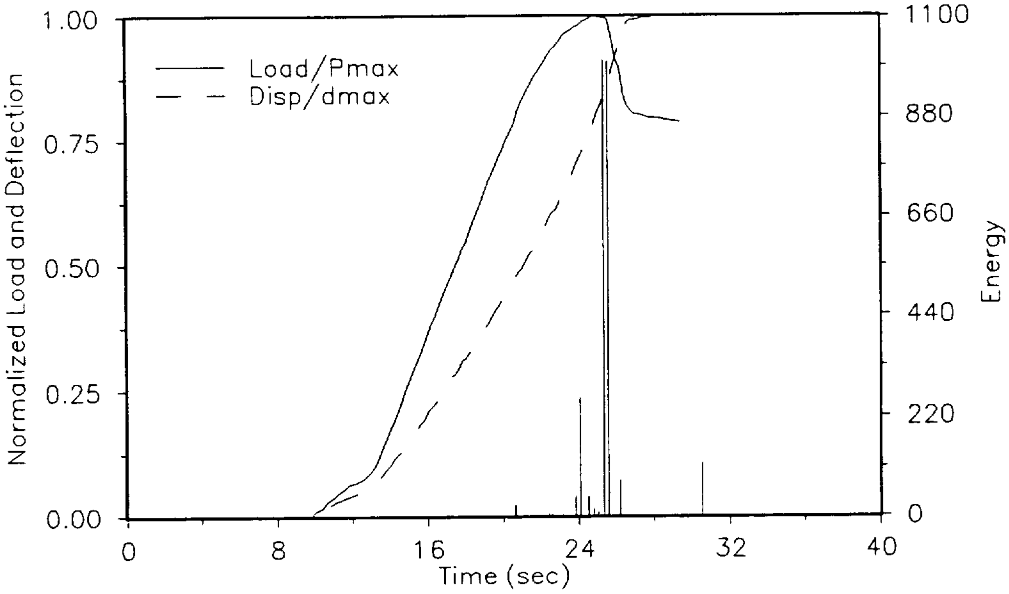

Figure 6.19: Acoustic energy of Specimen 030692B.

for these reductions in performance, no major causes were found. The standard deviation of the thickness distribution measured with the LVDT technique was much smaller for the 152-mm diameter specimens compared to Specimens 061991A, 061991B, and 062091; however, these values were similar to other 57-mm diameter specimens. Differences in the length-to-circumferential crossover-band spacing ratio between the two sizes of specimens was considered to be insignificant based on the findings of the In-Plane Crossover-Band Spacing experiment. Consequently, the differences in performance were attributed to the scale of the cylinder.

Table 6.4: Compression results for the Cylinder Scale experimental program.

| Cylinder Number | Winding Sequence | t/r (%) | Stiffness (x10^-3 N/m) | End Short. Displ.@ Buck. (mm) | Failure Stress (MPa) |
|---|---|---|---|---|---|
| 061991A | [±30] | 1.6 | 3.82 | 0.252 | 103 |
| 061991B | [±30] | 1.7 | 3.13 | 0.287 | 82.5 |
| 062091 | [±30] | 1.5 | 4.47 | 0.188 | 79.7* |
| 081291A | [±30] | 0.66 | 5.25 | 0.103 | 22.3 |
| 081291B | [±30] | 0.63 | 4.59 | 0.128 | 24.5 |
| 030692A | [±30] | 0.60 | 4.97 | 0.144 | 26.1 |
| 030692B | [±30] | 0.60 | 4.71 | 0.171 | 26.5* |
| 121490 | $[90/\pm30]_{as}$ | 1.4 | -- | -- | 202 |
| 122990 | $[90/\pm30]_{as}$ | 1.8 | -- | -- | 268 |
| 010891 | $[\pm30/90]_{as}$ | 1.9 | -- | -- | 272 |
| 022591 | $[0/\pm60]_{as}$ | 1.9 | -- | -- | 234 |
| 010191 | $[90_3/\pm30_3]_{as}$ | 5.7 | -- | -- | 336 |
| 030991 | $[\pm30_3/90_3]_{as}$ | 5.4 | -- | -- | 303 |
| 053091 | $[0_3/\pm60_3]_{as}$ | 5.3 | -- | -- | 264 |

* first load cycle

In conclusion, increasing the scale of a filament-wound cylinder by increasing the diameter, while maintaining the thickness, length, and winding parameters, induced four major changes in the compressive performance. First, the larger-diameter cylinders typically had more diamond-shaped buckling modes around the circumference. Second, those deformed regions next to the ends of the specimen were more developed on the large-diameter cylinders and look more like those in the center of the specimen. The third and fourth differences in performance were the smaller end-shortening displacement at buckling and buckling loads, respectively. Each of these differences in compressive performance was a result of the changes in the diameter of the cylinder, not the manufacturing procedures or quality of the specimen.

The second scaling experiment involved cylinders wound with more than one winding angle and six or eighteen plies. Cylinders 121490, 122990, 010891, and 022591 were wound with six layers and the same curing technique. Similarly, the eighteen-ply cylinders consisted of winding three layers of material in place of each ply in the six-ply cylinders. This method of scaling was necessary since helical winding cannot produce layers wound at +β and -β separately.

Most of these specimens were tested very early in this research program and the axial LVDTs were not used. A discussion of the procedures used to perform these tests was reported by Hipp [14]. The behavior of both the six and eighteen-ply cylinders was very different from either diameter of the [±30] specimens. The six-ply specimens emitted some cracking noises as the cylinder was loaded with more noise being emitted as the maximum load was approached. After the specimen failed, there was no evidence of buckling displacements; rather, a fracture was observed which circumnavigated the cylinder. When the video-tape recording was reviewed, the fracture seemed to appear instantaneously. In each case, negligible post-failure strength was observed. In some respects, the eighteen-ply cylinders responded in a similar fashion. Many cracks were heard prior to the ultimate load, no buckling deformations were observed, and very little post-failure strength was recorded.

Since the cylinders did not exhibit a stable postbuckling behavior and due to the testing procedures of Hipp [14], the six and eighteen-ply specimens can only be compared based on their ultimate loads and fracture patterns. In each case, the fracture patterns were substantially different for the different thicknesses. Cylinders 121490 and 122990 were manufactured with a $[90/\pm30_2/90]$ winding sequence with stacked crossover-band spacings of 34 and 30 mm, respectively. The visible damage in Cylinder 121490 was contained in a very narrow region around approximately two-thirds of the specimen and was visible at the same location on the inside and outside surfaces of the cylinder, as shown in Figure 6.20. The remaining portion of the fracture was oriented at approximately 45° to the longitudinal axis of the cylinder. Cylinder 122990 contained more visible damage than the previous specimen and only half of the cylinder contained a circumferentially-oriented crack. Examination of the inner surface revealed that the fracture passed directly through the thickness of the specimen. The outer hoop layers were delaminated in the region of the circumferential fracture which revealed that the fracture coincided with a circumferential-crossover band. Although the visual quality of both cylinders was nearly the same, Cylinder 122990 failed at a larger buckling stress which may have been caused by the smaller crossover-band spacing.

Cylinder 010191, the eighteen-ply equivalent to Cylinders 121490 and 122990, failed in a very different fashion. The fracture in this specimen ran through the thickness of the cylinder; however, the damaged zones around the fracture were much wider than the six-ply specimens and were oriented in V-shaped bands which spanned the entire length of the specimen, as shown in Figure 6.21. The extent of damage and orientation of the fractures in the six and eighteen-ply specimens, indicated different failure mechanisms. The localized damage in the six-ply specimens was probably the result of a buckling induced instability which immediately induced a fracture which propagated around the cylinder. A compression failure mode is proposed as the cause of failure of the eighteen-ply specimen.

Cylinders 010891 and 030991 were wound with ±30° plies on the inside and outside surfaces and contained 90° layers on the interior of the laminate. Response of these specimens was similar to the previous six and eighteen-ply cylinders; however, the fracture pattern was quite different. The width of the damage zone for Cylinder 010891 was quite large with many splits and delaminations in the inner and outer layers oriented in the fiber direction. Approximately 50 percent of the fracture was located on either a circumferential or helical-crossover band with fractures extending into the laminated shell regions. As with the previous six-ply cylinders, failure probably began as an instability of the shell which initiated a fracture which quickly propagated through the specimen.

The fracture pattern of Cylinder 030991 was aligned with the helical-crossover bands and often accompanied by delaminations but not splitting of the laminated-shell regions, as shown in Figure 6.22. Only approximately half of the fracture was aligned on the inner and outer surfaces unlike the six-ply specimen. In several areas, the delaminations were examined and found to exist at the interface between the helical and hoop layers. The failure progression in this specimen probably began with a delamination

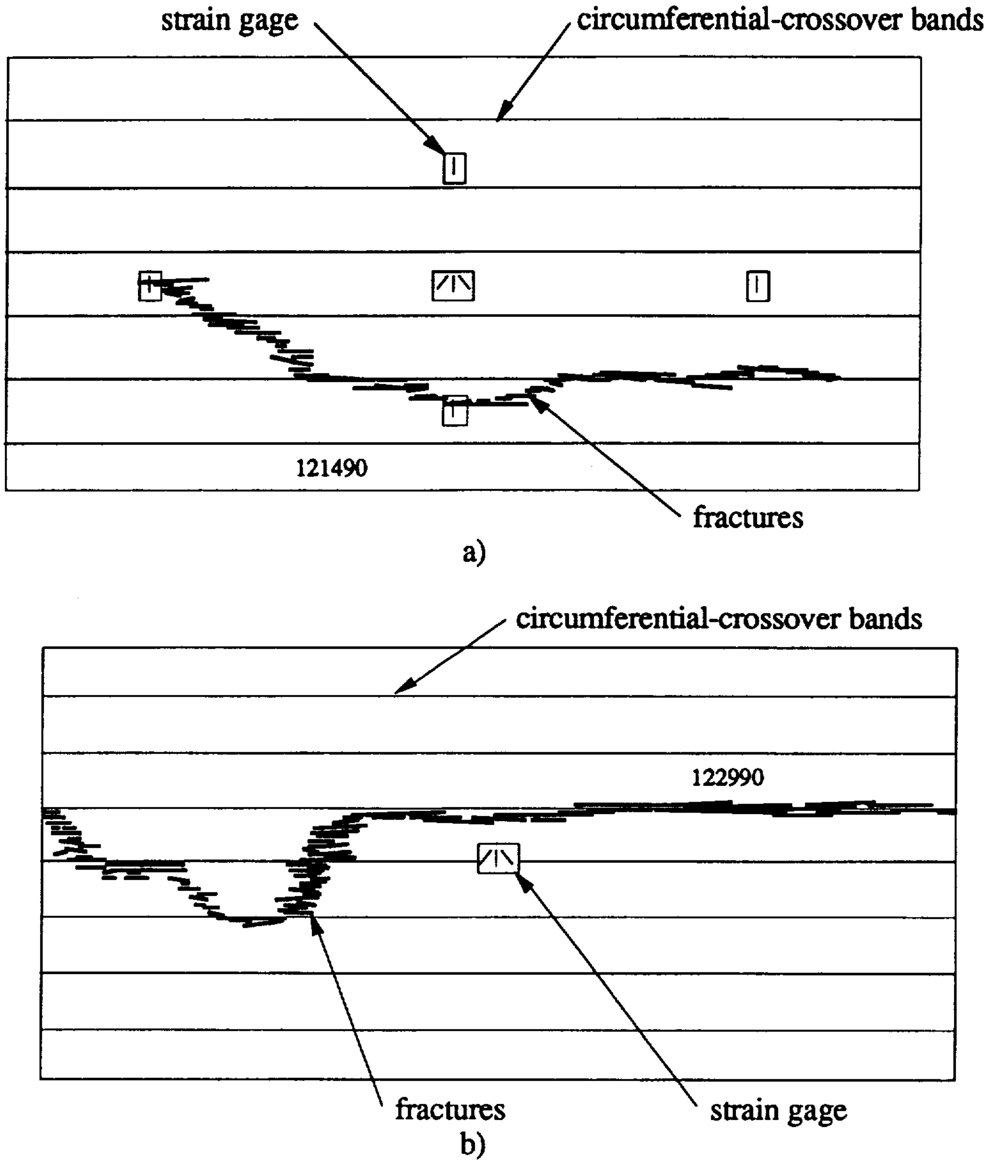
strain gage
circumferential-crossover bands
121490
fractures
circumferential-crossover bands
122990
fractures
strain gage

a)

b)

Figure 6.20: Fracture pattern of Cylinders a) 121490 and b) 122990.

which quickly caused a fracture to propagate through the helical layers in the neighborhood of the undulating fibers. Since only one drop in load was observed, the hoop layers probably did not fracture.

The final winding configuration used for the thickness scaling comparison, consisted of layers wound at 0° and ±60° to produce Cylinders 022591 and 053091. The behavior of Cylinder 022591 was similar to the other six-ply specimens since no out-of-plane displacements were observed and no post-failure strength was measured. The fracture progressed around the cylinder along a circumferential path and was located at approximately the same position on the inner and outer surfaces. The size of the damage zone was similar to Cylinder 010891, however, the actual fracture was very narrow and the visible damage was caused by splitting and delamination of the 0° layers. When the

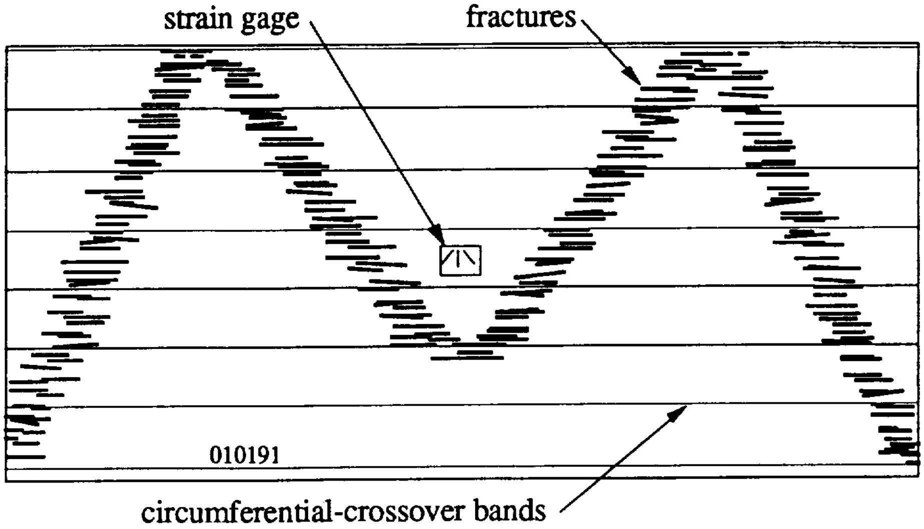

Figure 6.21: Compressive fracture of Cylinder 010191.

delaminations were examined, the surface of the ±60° layer could be observed and a circumferential-crossover band was located directly under the fracture. No damage was observed in the ±60° layers.

Failure of Cylinder 053091 exhibited some similarities to the previous eighteen-ply cylinders and Cylinder 022591. More audible cracking was observed during the test with many of the events seeming to have a longer duration than in previous specimens. When the maximum load was reached, there was a sharp drop in load as before; however, the cylinder still supported approximately 30 percent of the maximum load. This is in contrast to the other six and eighteen-ply specimens which exhibited no post-failure strength. The entire interior and exterior surfaces of the failed specimen were covered with many longitudinal splits and delaminations. As with Cylinder 022591, the delaminations existed between the axial and helical layers and often extended into the potted end of the specimen, as shown in Figure 6.23. Few circumferential cracks were observed in the 0° layers on either the inner or outer surfaces. The failure sequence of this specimen was clearly delamination followed by sublaminate (0° layers) buckling.

In conclusion, when the scale of a filament-wound cylinder is changed by increasing its thickness while maintaining the same diameter, length, and winding parameters, two changes in the compressive performance were observed. First, the maximum stress obtained in the specimen was greater for the thicker specimens. This increase in performance was caused by a change in the failure mode of the specimen. In each case, the thin specimens probably buckled then immediately fractured. The thick specimens failed due to a combination of compressive stresses, shearing stresses, delaminations, and sublaminate buckling.

### 6.4.4 Symmetry of the Laminated-Shell Regions

In this study, the influence of symmetry of the laminated-shell regions was investigated with cylinders wound with two plies of ±30° material. Cylinders 012092 and 021192 were manufactured with three circumferential-crossover bands in each specimen with antisymmetric and symmetric laminated-shell regions, respectively. The compressive behavior of these cylinders was quite different from the previously discussed specimens. As the specimens were loaded, the material emitted cracking sounds which built in intensity and frequency until the maximum load was reached. At this point, the specimens buckled

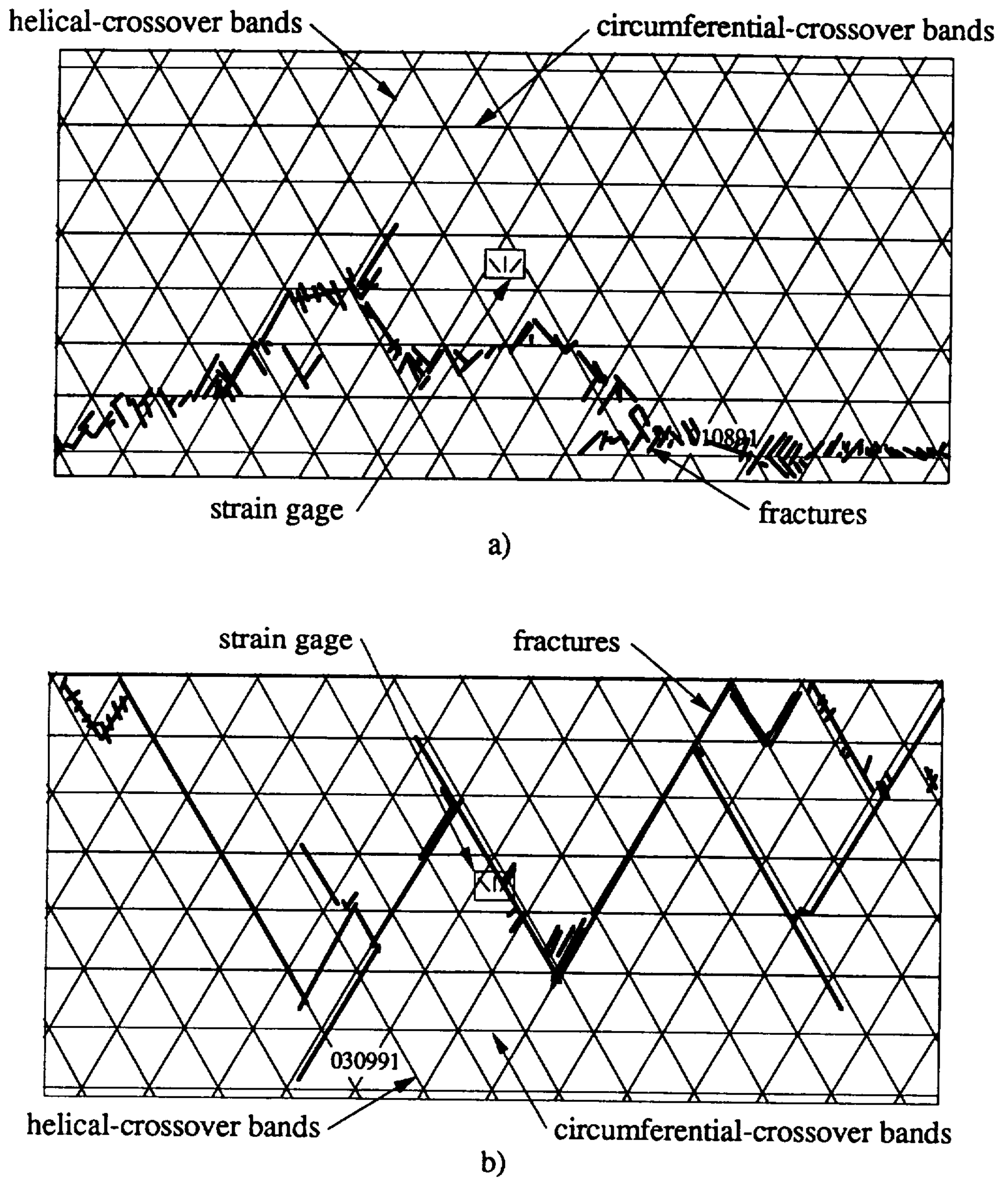
helical-crossover bands
circumferential-crossover bands
10891
strain gage
fractures
a)
strain gage
fractures
030991
helical-crossover bands
circumferential-crossover bands
b)

Figure 6.22: Fractures of a) six and b) eighteen-ply specimens with helical layers on the outer surfaces of the cylinder.

abruptly and the load dropped substantially. The ratio of postbuckling strength to maximum load for these specimens is smaller than the other ±30° cylinders, and much larger than the six and eighteen-ply specimens.

The buckled mode shape for most of the symmetric and antisymmetric specimens consisted of a single row of diamond shaped regions which were closer to one end. The regions were often distorted near the potted portion of each specimens, however, the diamonds were uniformly distributed around the circumference of the specimen. Specimen 012092A buckled at the center of the cylinder with a mode shape which closely resembled

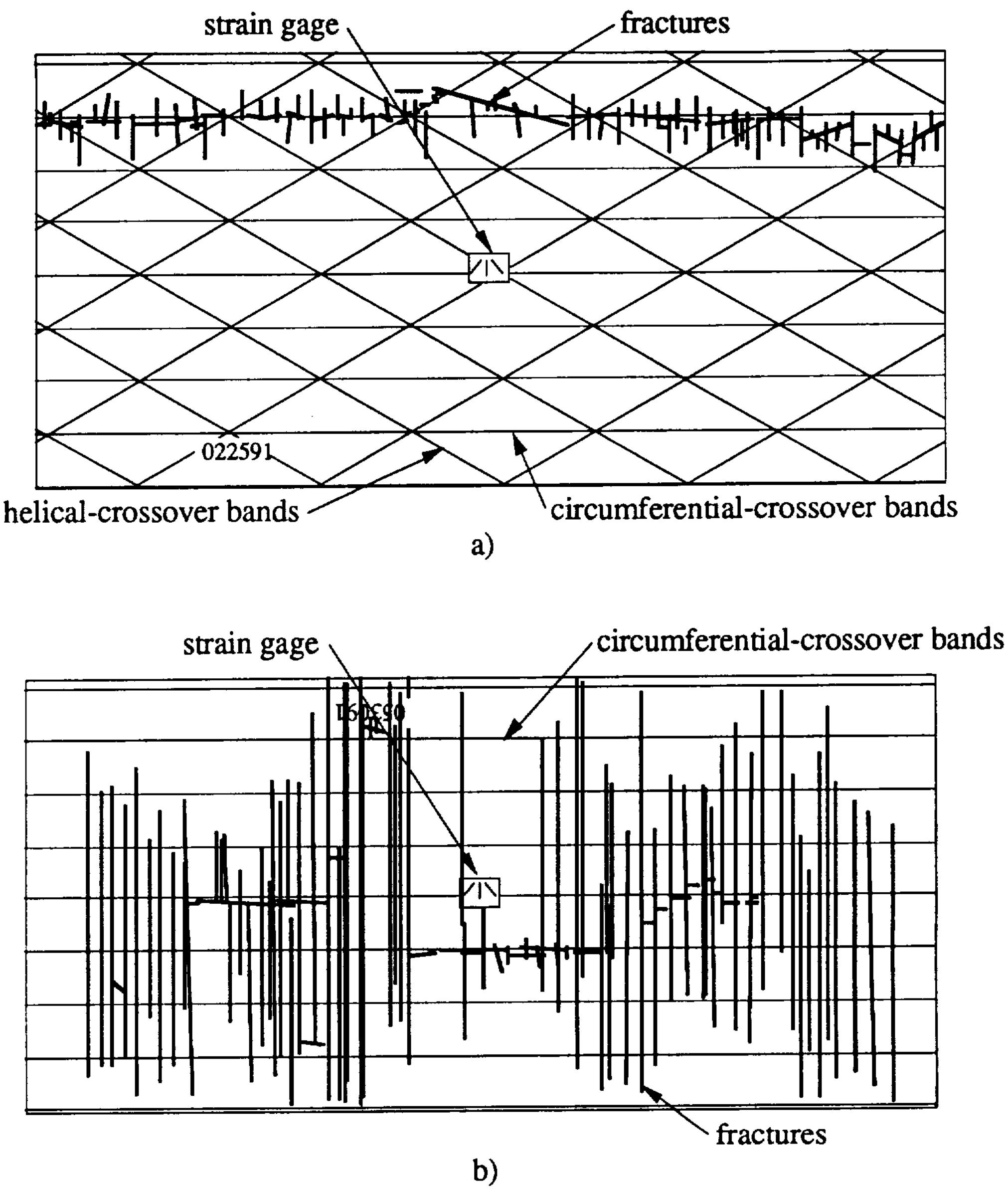
strain gage
fractures
022591
helical-crossover bands
circumferential-crossover bands
a)
strain gage
circumferential-crossover bands
fractures
b)

Figure 6.23: Fractures of a) six and b) eighteen-ply specimens manufactured with 0° layers on the inner an outer surfaces of the cylinder and ±60° layers in the interior.

the 57-mm diameter, [±30], specimens with three circumferential-crossover bands shown in Figure 6.5. At buckling, fractures appeared in each specimen in the region of largest bending curvature, but were quickly arrested.

Specimen 012092A was interrogated with the spring loaded LVDT used for the thickness and geometry testing. The LVDT was aligned so that it pointed in the radial direction at the centroid of a laminated shell region. During testing, this location began to move outward until approximately one-fourth of the maximum load was reached, as shown in Figure 6.24. This point then began to move towards the center of the cylinder. At approximately 50 percent of the maximum load, the point again changed direction and continued to expand outward until the buckling load was reached. An inward displacement was observed after buckling.

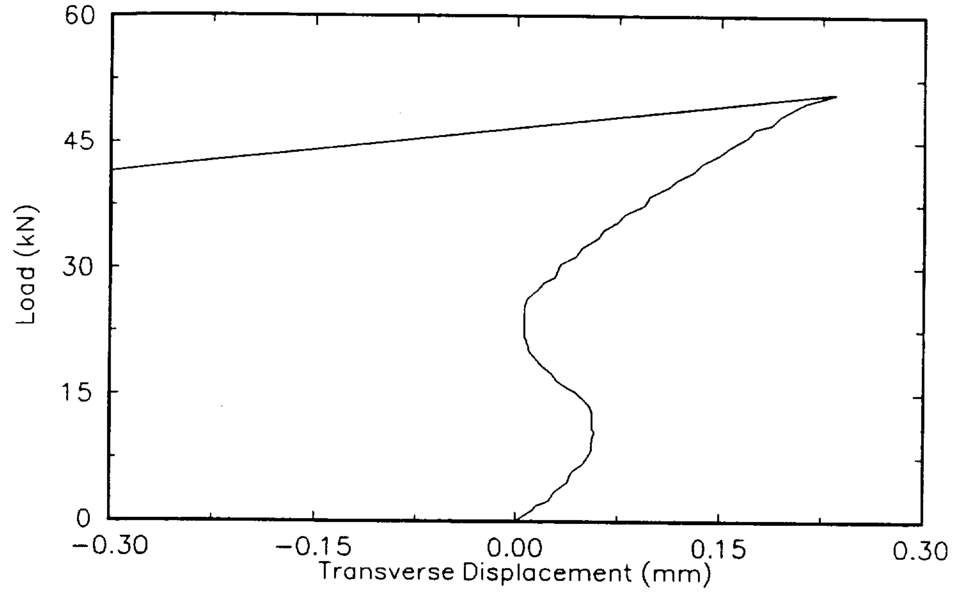

Figure 6.24: Transverse displacement of Specimen 012092A.

Strain-gage rosettes, Micro-Measurements model EA-06-125RA-120, were mounted back to back on Specimens 021192A and 012092A to measure the local strains at three locations during loading. The first position was located on the middle circumferential-crossover band equidistant from the helical-crossover bands. The second location was directly above the first at the centroid of the winding diamond. The last location was at the intersection of the middle circumferential-crossover band and two helical-crossover bands.

When the compressive performance parameters were examined, the stiffness, end-shortening displacement at buckling, and buckling stress are nearly identical for both types of specimens, as shown in Table 6.5. The greatest difference in performance was the state of strain measured at the intersection of the two helical and central circumferential-crossover bands. The axial bending strain in the antisymmetric specimen was much larger than in the symmetric specimen. When the strain gages located at the centroid of the laminated-shell regions were compared, the axial bending strain in both winding configurations was nearly zero. These results were surprising since the antisymmetric laminated-shell regions should exhibit bending strains which arise from the coupling behavior of the shell.

The conclusions which can be drawn from this investigation were somewhat surprising. For filament-wound cylinders with identical crossover-band spacings, location through the thickness, and similar quality levels, the effects of symmetry in the laminated-shell regions was negligible with regards to the global performance of the cylinder. Limited evidence indicates that local strains prior to buckling may differ between the two configurations; although, the amount of bending strain in the laminated-shell region of the antisymmetric specimen was much smaller than expected.

Table 6.5: Compression results for the Symmetry of the Laminated-Shell Regions experimental program.

| Cylinder Number | Winding Sequence | Stiffness (x10^-3 N/m) | End Short. Displ.@ Buck. (mm) | Buckling Stress (MPa) | Number of Circum. Waves |
|---|---|---|---|---|---|
| 021192A | $[\pm30]_s$ | 5.64 | 0.806 | 116 | 6 |
| 021192B | $[\pm30]_s$ | 8.00 | 0.728 | 126 | 6 |
| 012092A | $[\pm30]_{as}$ | 6.67 | 0.844 | 116 | 5 |
| 012092B | $[\pm30]_{as}$ | 7.76 | 0.724 | 118 | 6 |

### 6.4.5 Winding Sequence

The objective of this experiment was to investigate the effects of changing the sequence of layers on the quality and performance of filament-wound cylinders. Four specimens, Cylinders 122990, 010891, 010191, and 030991, were manufactured with $[90_n/\pm30_n/\pm30_n/90_n]$ and $[\pm30_n/90_n/90_n/\pm30_n]$ winding sequences in either six or eighteen-ply configurations (values of n of either 1 or 3). The behavior of each cylinder was discussed in Section 6.4.3: the compression results are listed again in Table 6.6 for completeness.

Table 6.6: Compression results for the Winding Sequence experimental program.

| Cylinder Number | Winding Sequence | t/r (%) | Maximum Stress (MPa) | Circumferential Crossover Band Spacing (mm) |
|---|---|---|---|---|
| 122990 | $[90/\pm30]_{as}$ | 1.8 | 268 | 29.7 |
| 010891 | $[\pm30/90]_{as}$ | 1.9 | 272 | 29.7 |
| 010191 | $[90_3/\pm30_3]_{as}$ | 5.7 | 336 | 31.2 |
| 030991 | $[\pm30_3/90_3]_{as}$ | 5.4 | 303 | 31.8 |

It has been shown that the bending strains at some locations in the cylinder can change sign during buckling; this corresponds to a change in curvature of the undeformed surface from convex to concave or vice versa. Cylinder 010891 had a lower bending stiffness in the circumferential direction than Cylinder 122990 and may have stored more energy in the form of prebuckling deformations. This difference may have been sufficient to alter the buckling load. The most drastic difference in performance of the six-ply cylinders was the fracture behavior. The exterior hoop layers in Cylinder 122990 prevented visible delaminations and seemed to constrain the fracture to the circumferential direction better than when helical layers were wound on the outside surfaces of the laminate. This observation was similar to the design recommendation made by Card [6].

Hoop-wound layers also constrained damage to a smaller area when the fracture patterns of Cylinders 010191 and 030991 were compared. When ±30° layers were placed on the surface of the cylinder, the plies failed by a combination of shear failures along helical-crossover bands and delamination of the helical layers from the hoop layers. The failure stresses seemed to be better shared between the different types of layers when the hoop layers were placed on the outside of the cylinder. The different failure mechanisms observed in these specimens are the probable causes for the lower maximum stress observed in Cylinder 030991 despite a better visual quality level.

### 6.4.6 Through-the-Thickness Crossover-Band Location

This experiment was designed to investigate the effects of through-the-thickness crossover-band location on the compressive performance of filament-wound cylinders. Three winding configurations were used to manufacture four cylinders: one cylinder with stacked crossover bands, two cylinders with alternating bands of the same width, and one cylinder with different crossover-band spacings. Each cylinder's load/end-shortening behavior was similar with little difference in response of the three axial LVDTs and no post-failure strength. Most specimens also exhibited some non-linear behavior near the beginning of the test, as shown in Figure 6.25. The specimens initially responded linearly until approximately 2 percent of the maximum load was reached at which time the structure softened slightly and then stiffened. The non-linear portion of the response was typically less than 10 percent of the total range of the cylinder's response.

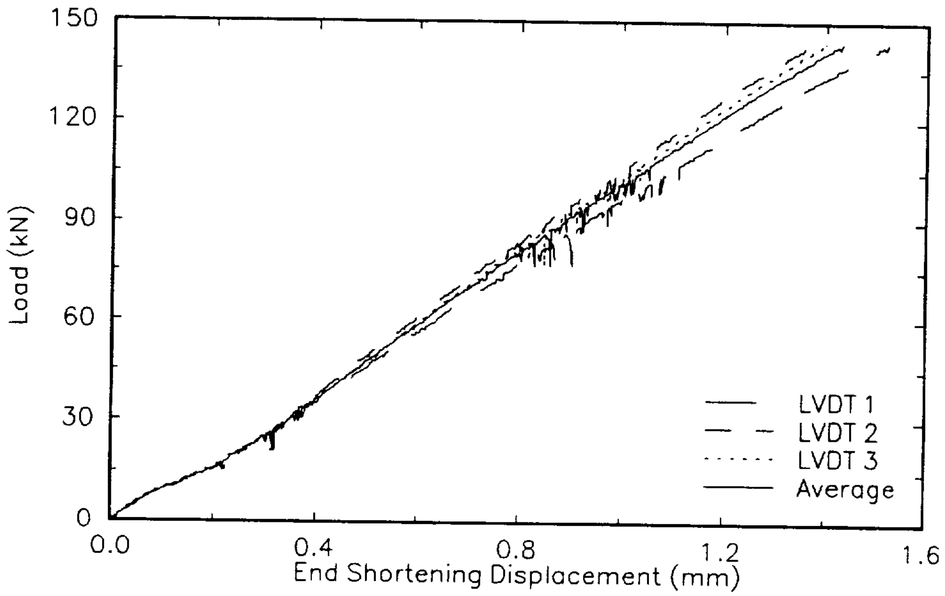

Figure 6.25: Non-linear load/end-shortening response of a typical specimen manufactured for the Through-the-Thickness Crossover-Band Location experimental program.

Strain-gage rosettes were mounted back to back on the inner and outer surfaces of selected specimens at the center circumferential-crossover band, at the centroid of a laminated shell region, and at the intersection of two helical-crossover bands. The non-linear behavior observed with the LVDTs was not evident in the axial compression data obtained with the strain-gage rosettes. Axial-compressive strains were linear to failure in each case and the strain at the circumferential-crossover band was the smallest in magnitude. Axial bending strains for the stacked specimen behaved non-linearly while the other configurations did not. Trends in the transverse compression and bending strains, were similar to the axial behavior.

Acoustic emission data was recorded for each specimen in this experiment. Audibly, cracks could be heard occasionally during each test. Just prior to the final fracture, the intensity and frequency of the sonic and ultrasonic activity increased dramatically. No discernible differences in the acoustic emission response was observed which could be related to the through-the-thickness crossover-band spacing.

Three different locations on the winding pattern were monitored with the transverse LVDT. Specimens 012592A, 013092A, 013092B, and 030592B were configured with the LVDT located at the centroid of a laminated shell region on the outside surface; the LVDT was placed near the intersection of two helical-crossover bands on Specimens 012592B, 030592A, and 030992B; and the LVDT was placed directly on top of the intersection of two helical-crossover bands on Specimen 030992A. When the results were examined with respect to either the location of the LVDT or the crossover bands through the thickness, no trends in the material response were evident. The LVDT response often varied substantially for the same location and winding pattern on different specimens.

The fracture locations are very consistent for the three laminate configurations. In each case, the extent of splitting and delamination damage was quite similar. For the specimens with the crossover bands stacked through the thickness, one circumferential fracture was observed directly on top of the middle crossover band, as shown in Figure 6.26. Regions of damage in specimens with alternating crossover bands were the same on the inner and outer cylinder surfaces and concentrated along either the inner or outer circumferential-crossover bands with some transition regions, as shown in Figure 6.27. The fractures observed in the specimens with the wide/narrow-winding configuration also were concentrated on circumferential-crossover bands; however, the fracture jumped between the crossover-band locations more often than when the crossover bands alternated through the thickness, as shown in Figure 6.28.

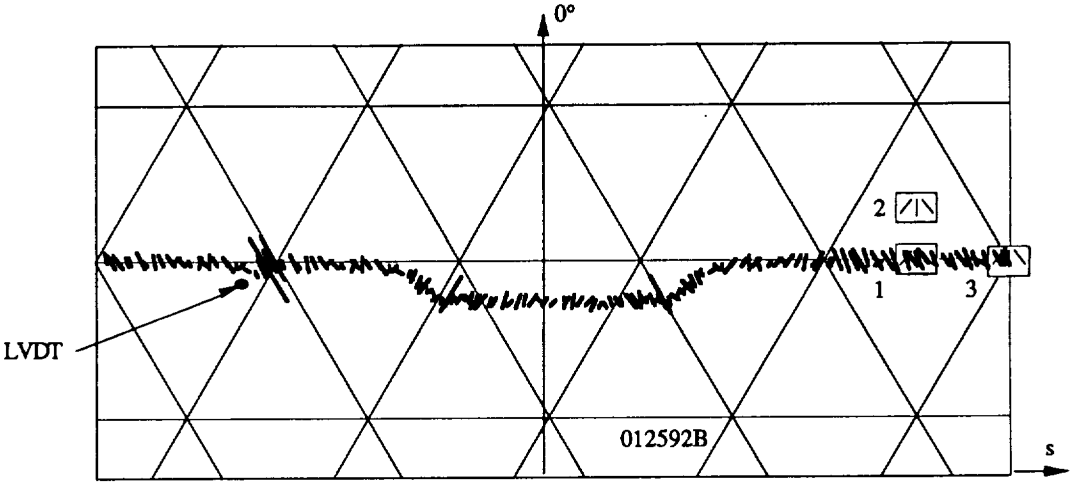

Figure 6.26: Typical fracture locations for the stacked crossover-band configuration.

When the compressive performance parameters were examined, several dramatic results were observed when cylinders of equal visual quality were compared (Cylinders 012592, 030592, and 030992). The failure stress of the stacked crossover-band configuration was the smallest of the configurations tested, as shown in Table 6.8. The alternating configuration was stronger by 8.4 percent compared to the stacked configuration; however, it was also 12.4 percent weaker than the wide/narrow

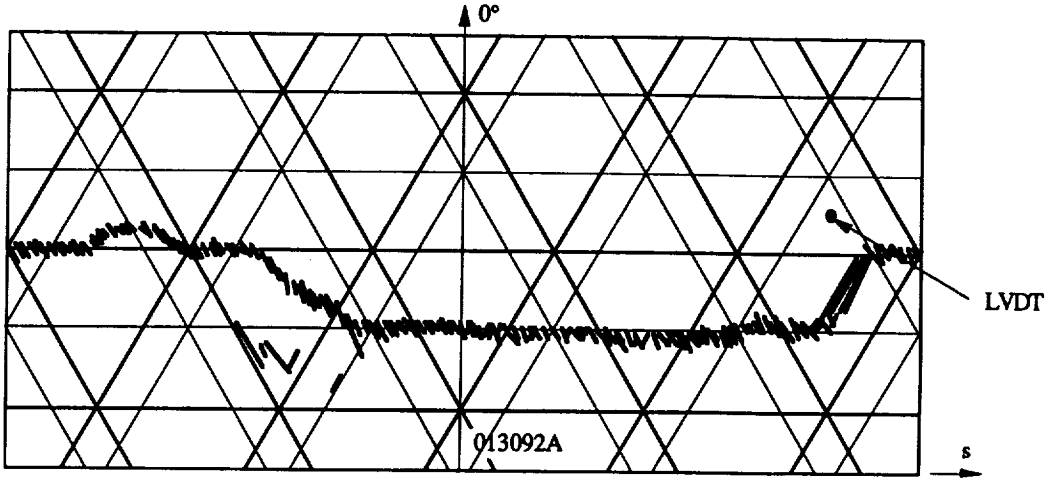

Figure 6.27: Typical fracture locations for the alternating crossover-band configuration.

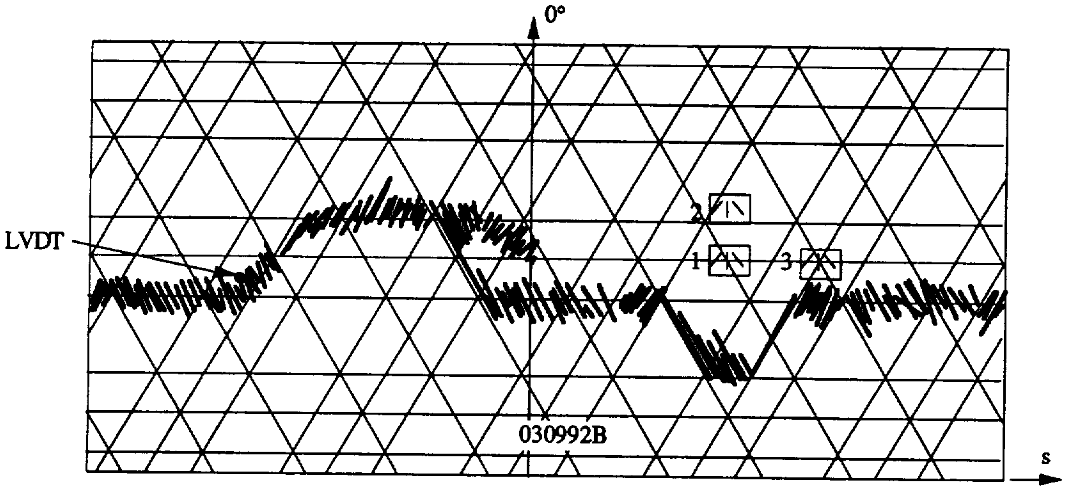

Figure 6.28: Typical fracture locations for the wide/narrow crossover-band configuration.

configuration. End-shortening displacements at failure for the stacked configuration were also lowest; although, the alternating and wide/narrow configurations were similar. Cylinder stiffness values were quite consistent for each specimen.

One exception to these trends was apparent when the compression parameters of Cylinder 013092 was compared to Cylinder 030592. Many tow twists were observed while winding Cylinder 013092 which resulted in a visually unappealing surface. Surprisingly, this cylinder buckled with a 10 percent larger stress than Cylinder 030592 which was wound and cured in the same manner. When the measured quality parameters were examined, no consistent differences were observed between the two cylinders. The cause for the improved performance was thought to arise from an increase in the bending stiffness of the shell caused by the twisted tows. Cylinder 062491 (a 57-mm diameter

Table 6.8: Compression results for the Through-the-Thickness Crossover-Band Location experimental program.

| Cylinder Number | T-T-T Configuration | Stiffness (x10^-3 N/m) | End Short. Displ.@ Buck. (mm) | Buckling Stress (MPa) | Circumferential Crossover Band Spacing (mm) |
|---|---|---|---|---|---|
| 012592A | stacked | 11.3 | 1.43 | 222 | 82.8 |
| 012592B | stacked | 11.6 | 1.43 | 246 | 82.8 |
| 013092A | alternating | 11.4 | 1.73 | 275 | 82.8 |
| 013092B | alternating | 11.4 | 1.72 | 275 | 82.8 |
| 030592A | alternating | 12.9 | 1.36 | 250 | 82.8 |
| 030592B | alternating | 10.8 | 1.76 | 261 | 82.8 |
| 030992A | wide/narrow | 11.4 | 1.74 | 291 | 41.4/82.8 |
| 030992B | wide/narrow | 11.5 | 1.60 | 292 | 41.4/82.8 |

[±30] cylinder with a 30 mm circumferential crossover-band spacing) also contained many twisted tows compared to Cylinder 062591; however, the difference in performance was not as dramatic as with the large-diameter cylinder.

### 6.4.7 Heated Winding

Two cylinders were wound at an elevated temperature to investigate how the improvements in quality which result from winding with a low viscosity resin to displace air and improve consolidation, affect the compressive response. Cylinders 031092 and 031392 behaved similarly to the previously discussed [$90/\pm30_2/90$] and [$\pm30/90_2/\pm30$] specimens. The non-linear end shortening behavior observed in the Through-the-Thickness Crossover-Band Location experimental program was also observed in Specimens 031092A and 031092B; however, this anomaly was absent in Specimens 031392A and 031392B which were cured with shrink tape. Each specimen exhibited very little post-failure strength.

The major difference in behavior of these specimens, was the relative lack of audible cracking during loading; especially for Specimens 031392A and 031392B. The reduction in acoustic activity might be related to the microstructural quality of the composite material. In the previously discussed cylinders, the laminates contained an appreciable number of voids. These voids acted as microcrack initiation sites which could have caused the acoustic events. Since the cylinders manufactured for this experiment had fewer voids, they are less likely to microcrack prior to ultimate failure.

The fracture patterns which developed during testing were similar to those observed in Cylinders 122990 and 011191. Each fracture was located at a circumferential crossover-band location with little deviation in location. Several out-of-plane deformations were observed in each specimen which straddled the fracture. These regions disappeared after unloading which indicated they were buckling induced. This observation lends credence to the hypothesis of buckling induced fracture as the failure mode for the six-ply cylinders. Poor microstructural quality and/or thicker laminates might explain why these out-of-plane displacements were not visible in the other six-ply specimens.

Specimen 031392B was instrumented with strain-gage rosettes which were aligned vertically on the specimen. Since hoop layers were wound on the outside and inside surfaces of this cylinder the helical-crossover bands could not be accurately located after cure. Consequently, two rosettes were placed longitudinally at the centroid of laminated shell regions and the third was placed on the circumferential-crossover band between them. Unfortunately, several gages did not function properly during the experiment. Despite these problems, the general trends in the strain-gage data were similar to the other six-ply cylinders.

The transversely mounted LVDT was used during testing and exhibited similar results as those mentioned in the previous section. The LVDT was located at the center of Specimen 031092B, which corresponded to a circumferential-crossover band. LVDT location with respect to the helical-crossover bands could not be determined due to the presence of the inner and outer hoop layers.

Acoustic emission data was recorded for each specimen and also showed a relative lack of activity compared to other six-ply specimens; however, no acoustic events were recorded during the last three-quarters of the loading history of Specimen 031392B. This was thought to be caused by ineffective coupling between the end plate and the transducer. A high-speed video camera system was used to record the failure of this specimen. High intensity lights were used to illuminate the specimen during testing which caused the couplant to dry out prematurely.

Selected results from the compression testing are listed in Table 6.9. The lower stiffness values observed in Specimens 031392A and 031392B was probably caused by the smaller thicknesses of these specimens compared to Specimens 031092A and 031092B. The smaller wall thickness was also reflected in the end-shortening displacement at failure of the shrink-tape cured specimens. Larger differences might have been expected when the fiber volume fraction and the magnitude of the geometric imperfections were examined; however, the imperfections observed in Cylinder 031092 were located in the resin rich layer on the outer surface which did not appreciably affect the load carrying capabilities of the shell.

Table 6.9: Compression results for the Heated Winding experimental program.

| Cylinder Number | Pressurization Method | t/r (%) | Stiffness (x10^-3 N/m) | End Short. Displ.@ Buck. (mm) | Buckling Stress (MPa) |
|---|---|---|---|---|---|
| 031092A | None | 1.7 | 12.2 | 1.56 | 260 |
| 031092B | None | 1.8 | 12.3 | 1.51 | 268 |
| 031392A | S.T.(4) | 1.6 | 11.4 | 1.37 | 261 |
| 031392B | S.T.(4) | 1.6 | 12.1 | 1.34 | 273 |

Comparison of the compressive performance of these specimens with cold wound, shrink-tape cured cylinders was difficult since different crossover-band spacings were used. When the failure stresses of Specimens 010891, 012592A, and 012592B were compared, a 14 percent reduction was observed which could be attributed to the crossover-band spacing since the quality parameters of these cylinders were similar. If the crossover-band spacing behavior of cylinders wound with $[90/\pm30_2/90]$ winding sequences is the same as $[\pm30/90_2/\pm30]$ cylinders, a failure stress of 231 MPa would be expected for the specimens in this experiment. Since the average failure stress of Specimens 031092A, 031092B, 031392A and 031392B was 265 MPa, and the thickness of these specimens was less than Cylinder 122990, filament winding at an elevated temperature seems to result in an improvement in the compressive performance.

## 6.5 Conclusions

The compressive performance of thin filament-wound cylinders is strongly dependent on several winding and curing parameters. These parameters include the placement of crossover-bands in the plane of the cylinder and through the thickness, the scale of the shell, sequence of plies, and the microstructural quality of the cured material. When the in-plane crossover-band spacing is small or very large, the buckling load is larger than when the winding pattern and buckling mode are of similar size. Relative placement of the crossover bands through the thickness of a multi-layered cylinder also affects the compressive behavior. If the circumferential-crossover bands are alternated through the thickness, and if different circumferential crossover-band spacings are used in the helical plies, improvements on the order of 20 percent can be obtained compared to a cylinder with a stacked configuration.

The scale of the cylinder also has a strong influence on the compressive response. Large diameter, thin cylinders buckle with little damage and large postbuckling strengths. When the thickness is maintained and the diameter is decreased, the cylinders still buckle; however, the induced damage level is greater and the postbuckling strength is smaller. As the thickness increases, the response begins to exhibit more damage associated with instability until buckling induces an immediate fracture which propagates through the structure. Further increases in thickness result in a change from buckling induced fracture to strength-type failure modes.

The sequence of layers and the use of an elevated winding temperature affects the compressive performance of filament-wound cylinders by changing the amount of damage before and during failure. Placing hoop-wound layers on the inner and outer surfaces of the cylinders tends to constrain the damage induced at buckling to smaller regions than when helical layers are placed on the outside of the laminate. If axial layers are used on the inner and outer layers, the final failure location is dictated by crossover locations in the helical plies. Winding at an elevated temperature was shown to reduce the void content and thickness of filament-wound cylinders by displacing air during winding. The compressive performance of these specimens exhibited less damage before final failure as observed by audible and ultrasonic acoustic emission due to the improved microstructural quality.

Two manufacturing parameters were found to have little affect on the compressive performance: mandrel material and symmetry of the laminated-shell regions. Changing the mandrel material from aluminum to steel while maintaining the same manufacturing procedures produced no noticeable changes in the compressive performance. Since helical layers are antisymmetric, the coupling behavior of these regions was thought to affect the compressive performance by altering the prebuckling behavior; however, the compressive load was nearly the same when compared to cylinders wound with symmetric laminated-shell regions.

PAGE 118 INTENTIONALLY BLANK

PRECEDING PAGE BLANK NOT FILMED

# 7.0 CLASSICAL BUCKLING AND STRENGTH ANALYSES

Many aspects of a cylindrical shell can affect its compressive stability and strength including the cylinder geometry, end constraints, material properties, and the level of geometric and material imperfections. In the previous chapter, the results of compressive buckling experiments were discussed with regards to many of these parameters; however, the influence of each parameter could often not be determined independently. To improve the understanding of the compressive buckling behavior of filament-wound cylinders, a classical buckling analysis was performed. The objectives of this analysis were to isolate the effects of material and geometric imperfections and to examine the validity of a relatively simple analysis. A strength analysis, based on classical lamination theory and the Tsai-Wu failure criterion, was used to predict the compressive strength of each cylinder since many specimens did not exhibit out-of-plane buckling displacements.

## 7.1 Buckling Analysis

A review of the current literature identified many sources which predict the stability of circular cylinders fabricated from composite materials. Excellent reviews have been written by Tennyson [2] for composite cylinders with an emphasis on experimental/theoretical correlations, Singer [1] for all material types, and Kapania [25] who focused on finite-element analyses. Currently, the technology exists to predict the prebuckling and postbuckling behavior of any shell geometry including many complicating factors such as; materials with anisotropic and/or non-linear constitutive behaviors, delaminations and sublaminate buckling, non-uniform boundaries, and geometric and material imperfections; however, these analyses are very complex.

### 7.1.1 Problem Formulation and General Solution Procedures

To maintain the manageability of the present analysis, the solution technique used by Cheng and Hou [26] was adopted. The authors perform an eigenvalue buckling analysis beginning with Flügge's equations. Although results for external pressure and torsional loading are presented in the companion paper by Hou and Cheng [27], the technique is applicable to axial loading and any kinematically admissible set of boundary conditions. This approach was adopted because it is relatively easy to perform, it can be used to satisfy the edge conditions used in the experiments, and is applicable for shells laminated from generally orthotropic layers. Three disadvantages limited the accuracy of this approach; the assumptions of a membrane prebuckled state, a geometrically perfect cylinder, and material homogeneity within the plane of the laminate.

Cheng and Hou [26] begin with Flügge's equations in differential form,

$$
\begin{aligned}
&R\frac{\partial N_{zz}}{\partial z}+\frac{\partial N_{\theta z}}{\partial \theta}-RN_z\frac{\partial^2 u}{\partial z^2}=0\\
&R^2\frac{\partial N_{z\theta}}{\partial z}+R\frac{\partial N_{\theta\theta}}{\partial \theta}+\frac{\partial M_{\theta\theta}}{\partial \theta}+R\frac{\partial M_{z\theta}}{\partial z}-R^2N_z\frac{\partial^2 v}{\partial z^2}=0\\
&R^2\frac{\partial^2 M_{zz}}{\partial z^2}+R\frac{\partial^2 M_{z\theta}}{\partial z\partial \theta}+R\frac{\partial^2 M_{\theta z}}{\partial z\partial \theta}+\frac{\partial^2 M_{\theta\theta}}{\partial \theta^2}-RN_{\theta\theta}-R^2N_z\frac{\partial^2 w}{\partial z^2}=0
\end{aligned}
\qquad (7.1)
$$

where the displacements in the axial, tangential, and radial directions are represented by $u$, $v$, and $w$ respectively, $N_{ij}$ and $M_{ij}$ are the resultant forces and moments in the $ij$ direction, $R$ represents the radius of the cylinder, and $N_z$ represents the critical buckling force. The coordinate system for the cylinder is shown in Figure 7.1. To begin the solution, the displacements are assumed to have the following form,

$$\begin{aligned} u &= A\sin\left(\frac{mz}{R}+n\theta\right) \\ v &= B\sin\left(\frac{mz}{R}+n\theta\right) \\ w &= C\cos\left(\frac{mz}{R}+n\theta\right) \end{aligned} \tag{7.2}$$

where, $A$, $B$, and $C$, represent the magnitude of the displacements, and $m$ and $n$ represent the axial and circumferential mode-shape numbers, respectively. When these displacements are inserted into the governing equations, a simultaneous set of three homogeneous equations results. For a non-trivial solution, the determinant of the coefficient matrix of these equations must vanish which results in the following characteristic equation,

$$\varsigma_1 m^8 + \varsigma_2 m^7 + \varsigma_3 m^6 + \varsigma_4 m^5 + \varsigma_5 m^4 + \varsigma_6 m^3 + \varsigma_7 m^2 + \varsigma_8 m + \varsigma_9 = 0 \tag{7.3}$$

The coefficients of the characteristic equation are functions of the circumferential mode number, $n$, and the buckling load, $N_z$. A detailed derivation of the governing equations is given in Claus, Hahn, and Jensen [19]. The solution of the characteristic equation results in 8 roots for $m$ corresponding to each combination of $n$ and $N_z$.

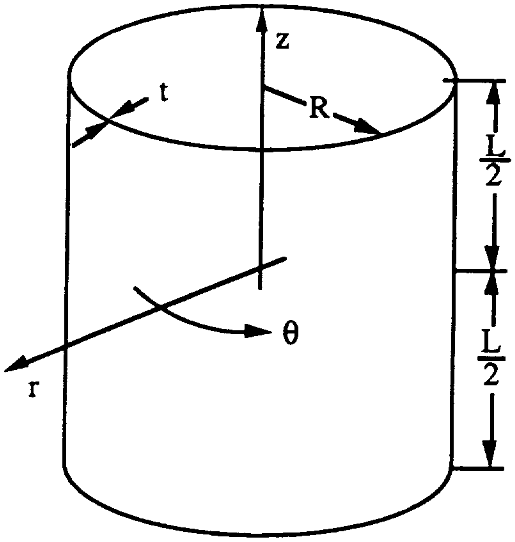

Figure 7.1: Geometry and coordinate system for Cheng and Hou's [26] analysis.

To satisfy the boundary conditions, the displacements are modified by superimposing the components from each root as follows,

$$\begin{aligned} u &= \sum_{j=1}^{8} \alpha_j C_j \sin\left(\frac{m_j z}{R}+n\theta\right) \\ v &= \sum_{j=1}^{8} \beta_j C_j \sin\left(\frac{m_j z}{R}+n\theta\right) \end{aligned} \tag{7.4}$$

$$w=\sum_{j=1}^{8} C_j \cos\left(\frac{m_j z}{R}+n\theta\right)$$

where, $\alpha_i$ and $\beta_i$ represent the amplitude ratios obtained from the equilibrium equations. For the present study, clamped boundaries, of the form,

$$u=v=w=\frac{\partial w}{\partial z}=0 \quad @ \quad z=\pm\frac{L}{2} \tag{7.5}$$

were assumed to exist at each end of the cylinder. Using the evenness and oddness of the displacements, the boundary conditions only need to be applied at one end of the cylinder. After inserting Equations 7.4 into 7.5, these equations become a set of eight homogeneous equations in the unknown displacement amplitudes $C_j$. For these equations to be satisfied, the determinant of the boundary-condition coefficient matrix must vanish.

To solve this problem, an iterative approach was adopted which searches for the lowest value of $N_z$ which satisfies the equilibrium characteristic and boundary condition equations. For several candidate values of $n$ and $N_z$, the values of m were determined from the equilibrium characteristic equation. Next, the boundary conditions were checked and the value of $N_z$ was adjusted until the determinant vanished. The smallest value of $N_z$ which satisfies both sets of equations was defined as the buckling load for the $n^{th}$ circumferential wave. The smallest solution for all possible circumferential wave numbers was defined as the critical buckling load for the cylinder.

Using the same solution procedure, Donnell's shell equations were also solved to investigate the accuracy of this shell theory. The equilibrium equations for this theory are,

$$\begin{aligned}
&R\frac{\partial N_{zz}}{\partial z}+\frac{\partial N_{\theta z}}{\partial \theta}=0\\
&R\frac{\partial N_{z\theta}}{\partial z}+\frac{\partial N_{\theta\theta}}{\partial \theta}=0\\
&R^2\frac{\partial^2 M_{zz}}{\partial z^2}+2R\frac{\partial^2 M_{z\theta}}{\partial z\partial\theta}+\frac{\partial^2 M_{\theta\theta}}{\partial\theta^2}-RN_{\theta\theta}-R^2N_z\frac{\partial^2 w}{\partial z^2}=0
\end{aligned} \tag{7.6}$$

Two computer programs were written to solve for the buckling loads with Donnell's and Flügge's buckling equations. An outline of the numerical solution procedures is discussed in the following section.

### 7.1.2 Numerical Solution Procedures

Fortran computer programs FLUGGE and DON were written to compute the critical buckling load and mode shape using the approach of Cheng and Hou [26]. Since the only difference between these programs was the shell theory on which they were based, the general form of the programs are the same and the following discussion can be considered to be applicable to both programs.

To begin the solution procedure, a value of the circumferential wave number, $n$, and the axial load, $N_z$, was chosen. The coefficients of the equilibrium characteristic equation and the displacement amplitude ratios were computed. The subroutines ZROOTS and LAGUER from Press [28] were used to find the roots of the equilibrium characteristic equation. Since the coefficients of the equilibrium-characteristic equation were real, if any root of the equation were complex, the complex conjugate must also be a root. Accuracy parameters within ZROOTS were adjusted so that the real and imaginary parts of the conjugate pairs were the same to at least eight significant digits.

The next stage of the computer programs was to formulate the coefficient matrix of the boundary condition equations. If the root $m_j$ was real, the coefficient $C_j$ must also be real for the displacements to be real valued functions. If the root $m_j$ was complex, and its conjugate was $m_{j+1}$, the coefficients $C_j$ and $C_{j+1}$ must also be complex conjugate pairs. To formulate the coefficient matrix corresponding to the boundary conditions, the displacements were rewritten in terms of the real and imaginary parts of the roots $m_j$, unknown magnitudes $C_j$, the amplitude ratios $\alpha_j$ and $\beta_j$, and their respective conjugates. By combining the complex conjugate portions, the unknown $C_j$'s were replaced with their real valued components. Each column of the boundary condition coefficient matrix corresponded to one unknown displacement magnitude: if the root was real, the column corresponds to that displacement magnitude, if the root was complex, the column corresponds to the real part of the displacement magnitude and the next column corresponds to the complex portion.

Rather than computing the determinant of the coefficient matrix, one equation was relaxed by assuming the magnitude of its unknown to be -1. The system of equations was then solved using subroutines LUBKSB and LUDCMP from Press [28]. Since all of the boundary conditions were homogenous, the error induced by making this assumption was related to the value of the relaxed equation. If this value was zero, then the determinant of the coefficient matrix was also zero. The error in the analysis was defined as the base 10 logarithm of the magnitude of the relaxed equation. Throughout this study, the cosine portion of the slope boundary-condition equation was used as the relaxed equation since the accuracy of the solution could be easily verified by visual examination of the buckled mode shape. This technique was advantageous since when the error is zero, the amplitude ratios for each mode are already known. These ratios are needed to compute the shape of the buckled cylinder.

The value the error for a particular combination of $n$ and $N_z$, was compared to the previous two values. If a local minimum was detected, the value of $N_z$ was assumed to be near a solution, as shown in Figure 7.2. The value of $N_z$ was then reset according to the following relationship,

$$N_{znew} = N_{zold} - 3d_{old} \tag{7.7}$$

were, $d_{old}$ represents the current step size, the step size was decreased, and the iterative procedure was restarted at $N_{znew}$. The solution was assumed to have converged when the smallest error was less than some prescribed value.

The numerical solution depends on two parameters: the initial step size, and the value of the convergence error (the error at which numerical convergence is assumed to occur). If the step size is to large, the computer program could miss a solution since the typical domain of convergence is small. To investigate the convergence behavior of the solution, the computer program DON was used with the material constants listed in Table 7.1 for a 152-mm diameter, 229-mm long, [±30/90$_2$/±30] cylinder with 0.227-mm thick layers. Step sizes of 1751, 876, 175, and 17.5 N/m were used to compute the buckling loads for circumferential mode numbers from 1 to 9. Convergence was assumed to occur when the error was less than 0. The buckling forces are listed in Table 7.2 for each value of $n$ and the error is plotted versus the axial force in Figure 7.3 for 6, 7, and 8 circumferential waves. Examination of the buckled surfaces, shown in Figures 7.4-7.7, was also made to ensure convergence. Based on this study, a step size of 175 N/m was considered sufficient for all 57 and 152-mm diameter cylinders using Donnell's equations.

To investigate the behavior of the solution with regards to the convergence error, the same problem was solved with a step size of 175 N/m and error parameters of 1, 0, -1, and -5. Since the computed critical buckling forces and mode shapes did not change, the solution is not particularly sensitive to the value of the convergence error. Since the algorithm converges very rapidly for small values of the convergence error, a value of -5 was often used in subsequent investigations to guarantee convergence.

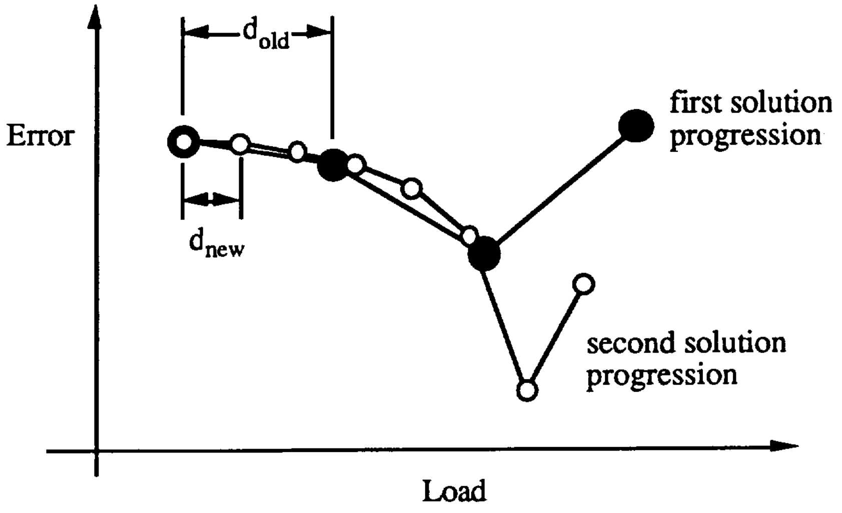
Error
$d_{old}$
$d_{new}$
first solution progression
second solution progression
Load

Figure 7.2: Comparison of sequential errors near a solution.

Table 7.1: Material constants used for the classical laminated-shell buckling analyses. The subscripts 1 and 2 refer to the fiber and transverse directions in the material respectively.

| Material Property | Magnitude |
|---|---|
| $E_1$ | 134 GPa |
| $E_2$ | 9.65 GPa |
| $\nu_{12}$ | 0.3 |
| $G_{12}$ | 5.52 GPa |

Table 7.2: Results of buckling force calculations computed to examine the step-size convergence of the computer program DON.

| Step Size (lb/in) | Buckling Force (kN/m) n=1 | n=2 | n=3 | n=4 | n=5 | n=6 | n=7 | n=8 | n=9 |
|---|---|---|---|---|---|---|---|---|---|
| 10 | 906.1 | 925.9 | 869.5 | 819.6 | 777.9 | 772.3 | 1963 | 779.5 | 1010 |
| 5 | 876.5 | 925.9 | 896.5 | 819.6 | 823.6 | 772.3 | 722.2 | 779.5 | 871.6 |
| 1 | 876.5 | 856.4 | 837.3 | 819.6 | 777.9 | 707.0 | 722.2 | 779.5 | 871.6 |
| 0.1 | 876.5 | 856.4 | 837.3 | 819.6 | 777.9 | 707.0 | 722.2 | 779.5 | 871.6 |

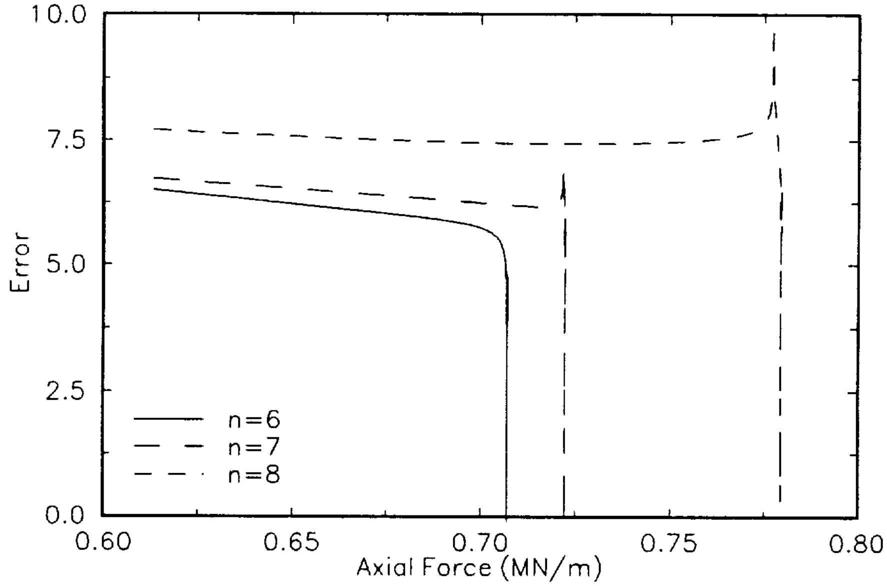

Figure 7.3: Error of the relaxed boundary condition as a function of the axial load. A step size of 175 N/m was used to produce this figure.

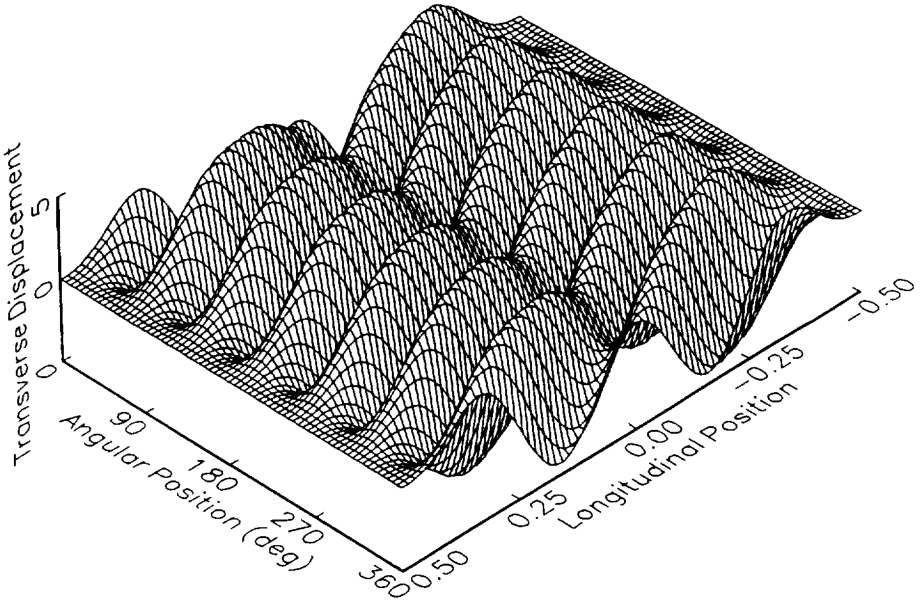

Figure 7.4: Buckled surface of [±30/$90_2$/±30] cylinder for a step size of 1750 N/m using Donnell's theory.

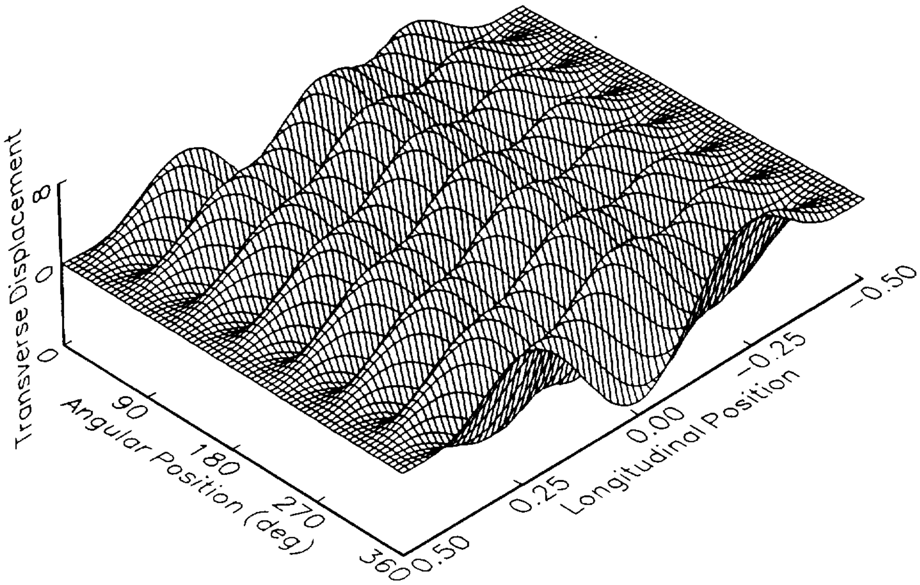

Figure 7.5: Buckled surface of [±30/$90_2$/±30] cylinder for a step size of 875 N/m using Donnell's theory.

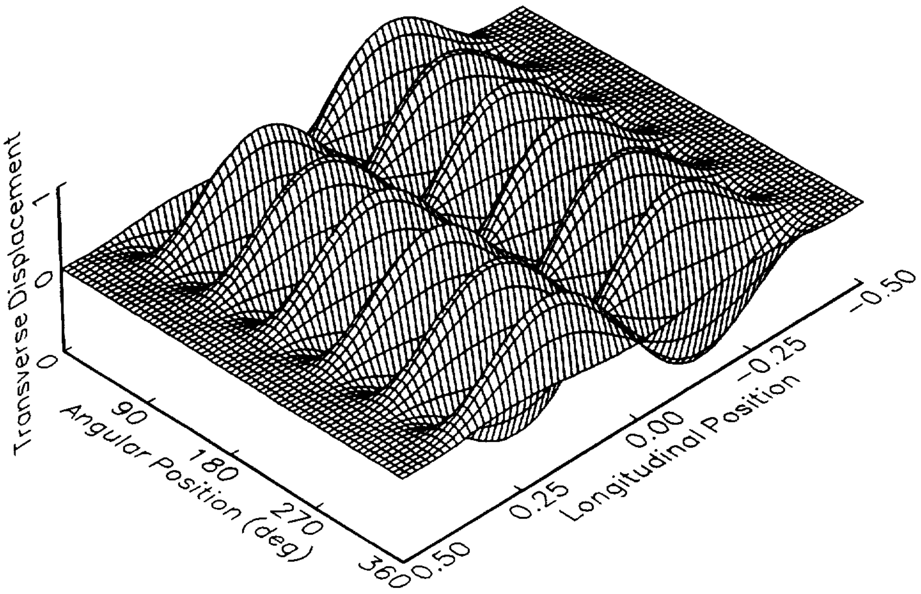

Figure 7.6: Buckled surface of [±30/$90_2$/±30] cylinder for a step size of 175 N/m using Donnell's theory.

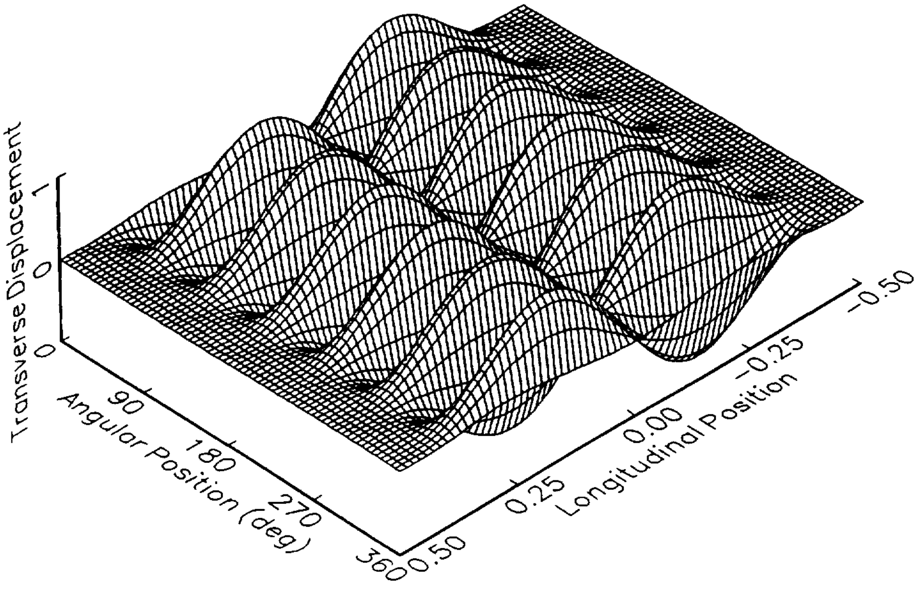

Figure 7.7: Buckled surface of [±30/$90_2$/±30] cylinder for a step size of 17.5 N/m using Donnell's theory.

A similar convergence study was performed with the computer program written to solve Flügge's equations. The material and geometric parameters for this study were the same as those used previously. Step sizes of 1751, 876, 175, and 17.5 N/m were used with a minimum error of 0 to obtain the results shown in Table 7.3. As observed from the buckling forces and the mode shapes, shown in Figures 7.8-7.11, this solution is slightly more sensitive than Donnell's theory; although, a step size of 175 N/m is still sufficient for convergence. A similar study was performed to investigate the solution behavior with regard to the convergence error. Since the buckling forces and mode shapes were identical, this solution is also not particularly sensitive to the value of convergence error.

Table 7.3: Results of buckling force calculations for the examination of step-size convergence for computer program FLUGGE.

| Step Size (lb/in) | Buckling Force (kN/m) n=1 | n=2 | n=3 | n=4 | n=5 | n=6 | n=7 | n=8 | n=9 |
|---|---|---|---|---|---|---|---|---|---|
| 10 | 915.9 | 851.1 | 862.3 | 883.2 | 726.6 | 1100 | 880.7 | 1088 | 851.5 |
| 5 | 872.7 | 851.1 | 862.3 | 810.7 | 726.6 | 682.5 | 702.3 | 757.2 | 851.5 |
| 1 | 872.7 | 851.1 | 830.4 | 810.7 | 726.6 | 671.4 | 695.4 | 757.2 | 872.3 |
| 0.1 | nc | nc | 830.4 | 810.7 | 726.6 | 671.4 | 695.4 | nc | nc |

nc -- not computed

### 7.1.3 Model Verification

Since the results reported in Hou and Cheng [27] are limited to combinations of external pressure and torsion, the work of Tasi, Feldman, and Stang [7] and Jensen and Pai [11] was used to verify the accuracy of the computer programs. Tasi, Feldman, and Stang [7] used the solution technique of Cheng and Hou [26] with Flügge's equations and clamped boundaries to predict the buckling loads for a variety of filament-wound cylinders. The cylinder used for verification of the present solution was wound with a [90/±8°49'/90] winding sequence on a 151-mm diameter mandrel with the material and geometry parameters listed in Table 7.4. Two slightly different analyses were performed by Tasi, Feldman, and Stang [7]. The first analysis consisted of solving the equilibrium characteristic equation for a large number of axial and circumferential wave numbers without consideration of the boundary conditions. The lowest buckling load computed in this fashion was 84.800 kN which corresponded to 8 circumferential and 9 longitudinal waves. The second type of analysis included the boundary conditions. A buckling load of 85.192 kN and 8 circumferential waves are the reported results for this analysis.

When the same cylinder was modeled with the computer program FLUGGE, a critical buckling load of 84.284 kN with 7 circumferential waves was computed. Although this only corresponds to a 1.06 percent difference in buckling load compared to Tasi, Feldman, and Stang [7], the difference in the number of circumferential waves is surprising. When the output from the present analysis was examined, the buckling load for 8 circumferential waves was determined to be 84.738 kN; a 0.5 percent smaller than Tasi, Feldman, and Stang [7]. The differences in the analyses are attributed to minor

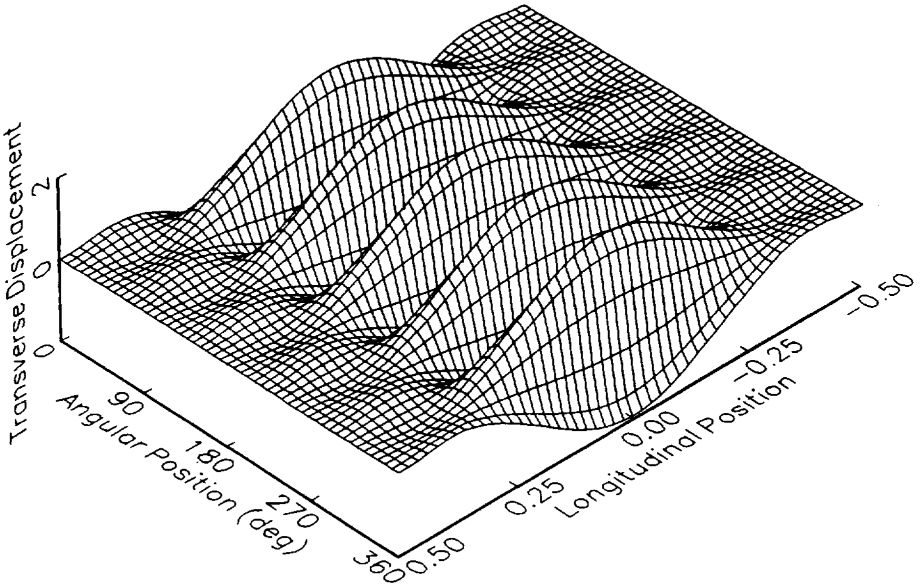

Figure 7.8: Buckled surface of [±30/$90_2$/±30] cylinder for a step size of 1750 N/m using Flügge's theory.

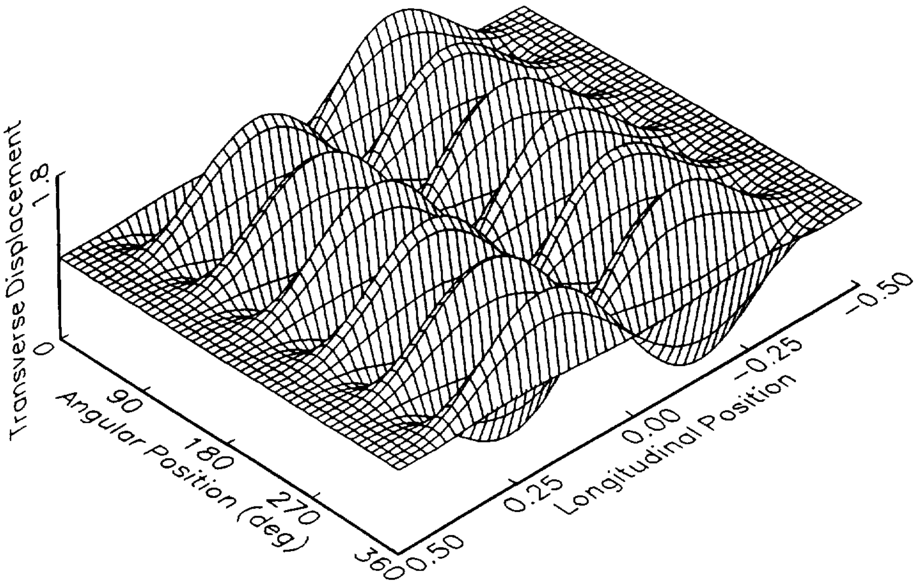

Figure 7.9: Buckled surface of [±30/$90_2$/±30] cylinder for a step size of 875 N/m using Flügge's theory.

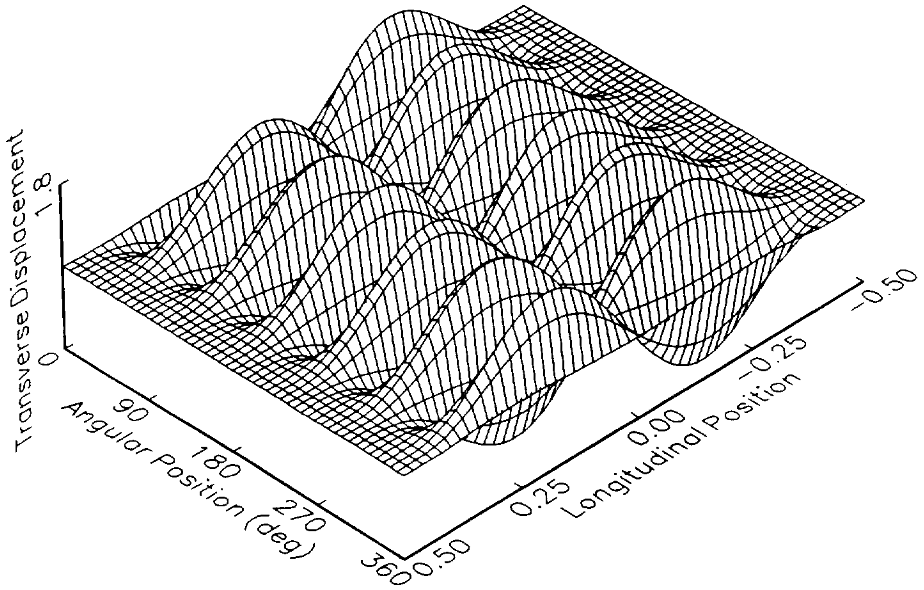

Figure 7.10: Buckled surface of [±30/$90_2$/±30] cylinder for a step size of 175 N/m using Flügge's theory.

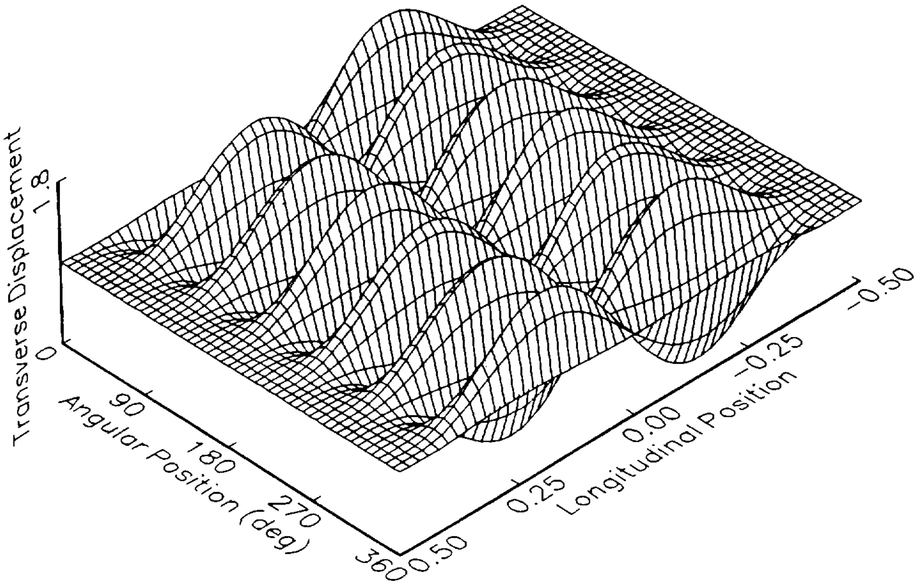

Figure 7.11: Buckled surface of [±30/$90_2$/±30] cylinder for a step size of 17.5 N/m using Flügge's theory.

Table 7.4: Material properties and cylinder geometry reported in Tasi, Feldman, and Stang [7] used for model verification. The subscripts 1 and 2 refer to the fiber and transverse directions in the material respectively.

| Material Property | Magnitude |
|---|---|
| $E_1$ | 61 GPa |
| $E_2$ | 20 GPa |
| $\nu_{12}$ | 0.35 |
| $G_{12}$ | 9.6 GPa |
| t/ply | 0.23 mm |
| Radius | 75 mm |
| Length | 170 mm |

computational differences and, possibly, a mistaken assumption by Tasi, Feldman, and Stang [7] that the critical buckling mode computed while satisfying the boundary conditions is the same as when only the equilibrium characteristic equation is used. Computer program DON was validated by computing the buckling response using the same conditions. The buckling load computed with Donnell's theory was identical to the results reported by Tasi, Feldman, and Stang [7]; however, the number of circumferential waves computed with DON was 7.

The accuracy of the present models was also compared to Jensen and Pai [11]. They model a clamped ($u=v=w=u,_z=v,_z=w,_z=0$ at $z=\pm L/2$) 152-mm diameter, 254-mm long, [±30] cylinder with the material properties listed in Table 7.1. The buckling load was computed with ABAQUS®, a commercial finite element package, using eight-noded quadrilateral-shell elements assuming a membrane prebuckling state and ignoring the microstructure within the crossover bands. Results from this analysis are nearly 8 percent larger than the present study using Donnell's equations. This difference may be attributed to the more highly constrained finite-element model and a possible difference in shell theories. Although the buckled mode shape of this cylinder is not presented by Jensen and Pai [11], geometries which include the effects of the helical and circumferential-crossover bands are predicted to buckle into a torsional mode shape which corresponds to the present study.

## 7.2 Comparison of Buckling Analyses and Experimental Results

The critical buckling loads and buckled mode shapes were computed with Flügge's and Donnell's theories for each cylinder manufactured and tested during the course of this research. Several effects which occurred in the actual cylinders could not be accounted for in either of the present analyses. These effects include geometric imperfections, prebuckling deformations, and nonhomogeneous composite materials. The material properties used for these analyses were obtained from the manufacturer and are listed in Table 7.1. The winding sequence, length, and thickness measured with the ball-end micrometer, were used to provide the best estimate of compressive performance. Each buckled mode shape computed from Donnell's and Flügge's theories are listed in Claus, Hahn, and Jensen [19]. As with the experimental results, the following discussion is divided into seven categories based on the parameters being investigated.

### 7.2.1 In-Plane Crossover-Band Spacing

Specimens in this study were wound with various circumferential-crossover band spacings. No correlation was found between the visual quality or geometric imperfection level and the winding pattern; however, the buckling load seemed to be the lowest when the winding pattern and buckled mode were the same size.

Results from both Flügge's and Donnell's theories are listed in Table 7.5. The accuracy of the analysis, $\varepsilon$, is defined as,

$$\varepsilon = \frac{N_{z(Experimental)}}{N_{z(Analytical)}} \tag{7.8}$$

For both analyses, the computed accuracies were between 40 and 60 percent for each cylinder. Donnell's and Flügge theories predicted most specimens to buckle with either two or three circumferential waves; whereas, 4, 5, or 6 waves were observed experimentally. In each case, the analyses predicted a torsional buckling mode, as shown in Figure 7.12. This mode shape may have been induced by an inaccurate simulation of the boundary conditions. During testing, the hemispherical aligner may have allowed some tangential rotation to occur which was constrained in the present analyses forcing the torsional mode to become the critical mode rather than the diamond-shaped mode observed experimentally. Substituting a zero torsional load for this boundary condition may improve the accuracy of the critical mode and load calculations. When identical cylinders were simulated with $-\beta/+\beta$ and $+\beta/-\beta$ lamination sequences, the critical loads were identical and the buckled mode shapes were similar except that the ridges were oriented in the opposite directions. Since filament-wound cylinders consist of both $+\beta/-\beta$ and $-\beta/+\beta$ regions, a model including these regions might buckle into a combination of these two modes.

The accuracy of each analysis was compared to the crossover-band spacing and the level of geometric imperfection. Little correlation between the buckling load and crossover-band spacing was observed, as shown in Figure 7.13, which indicates the behavior shown in Figure 5.15 was primarily the result of thickness and/or length effects. This conclusion is contrary to the results reported by Jensen and Pai [11] who included the micromechanical behavior of the crossover bands within a finite-element analysis of the buckling behavior. When the accuracy of the analytical predictions was compared to the root mean square, standard deviation, or range of the geometric imperfection, no trends were observed. Tennyson, Chan, and Muggeridge [29] used Koiter's special theory to determine the initial geometric imperfection sensitivity of $[+\beta/0/-\beta]$ cylinders and observed a rapid drop in accuracy over similar ranges of imperfection. This result suggest that the inaccuracy of the present analyses was caused by either some parameter which was not identified and is generally common to all cylinders, or, to non-membrane prebuckling behavior.

### 7.2.2 Mandrel Material

Specimens fabricated for this study were manufactured with aluminum and steel mandrels to study the influence of mandrel material on the compressive performance of filament-wound cylinders. The mandrel can only influence the analytical models indirectly; either through the thickness, material quality, or geometric imperfections. These parameters were not affected by the choice of mandrel material and there was no measurable difference in the results of either analysis, as shown in Table 7.6.

Table 7.5: Results of buckling load calculations for the In-Plane Crossover-Band Spacing experimental program.

| | Experiment | | Donnell's Theory | | | Flügge's Theory | | |
|---|---|---|---|---|---|---|---|---|
| Cylinder Number | Buck. Load (kN) | No. Cir. Waves | Buck. Load (kN) | ε (%) | No. Cir. Waves | Buck. Load (kN) | ε (%) | No. Cir Waves |
| 061991A | 8.29 | 4 | 14.7 | 57 | 2 | 14.5 | 57 | 2 |
| 061991B | 7.18 | 5 | 17.1 | 42 | 2 | 16.9 | 42 | 2 |
| 062091 | 6.15* | 4 | 13.4 | 46 | 2 | 13.3 | 47 | 3 |
| 062191A | 6.81* | 6 | 12.8 | 53 | 3 | 12.6 | 54 | 3 |
| 062191B | 6.72 | 6 | 13.9 | 49 | 2 | 13.7 | 49 | 3 |
| 062291A | 7.01 | 6 | 12.4 | 57 | 3 | 12.3 | 57 | 3 |
| 062291B | 6.62 | 5 | 12.9 | 51 | 3 | 12.8 | 52 | 3 |
| 062491A | 6.58 | 5 | 12.2 | 54 | 3 | 12.0 | 55 | 3 |
| 062491B | 5.56 | 5 | 13.3 | 42 | 2 | 13.2 | 42 | 3 |
| 062591A | 6.43 | 5 | 13.6 | 47 | 2 | 13.4 | 48 | 3 |
| 062591B | 5.70 | 5 | 13.6 | 42 | 2 | 13.5 | 42 | 3 |
| 063091A | 6.34 | 5 | 13.7 | 46 | 2 | 13.6 | 47 | 3 |
| 063091B | 6.65 | 5 | 13.2 | 50 | 2 | 13.0 | 51 | 3 |
| 070191A | 8.50 | 5 | 17.8 | 58 | 2 | 14.6 | 58 | 2 |
| 070191B | 8.80 | 5 | 15.1 | 58 | 2 | 15.0 | 59 | 2 |
| 011692A | 6.47* | -- | 13.4 | 48 | 2 | 13.2 | 49 | 3 |
| 011692B | 7.29 | 6 | 14.1 | 51 | 2 | 14.0 | 52 | 3 |

* first load cycle

### 7.2.3 Cylinder Scale

The scale of the filament-wound cylinders was varied by changing the thickness and diameter of the specimens while maintaining the same winding and curing procedures. Since the specimens with radius-to-thickness ratios of 18 (the 152-mm diameter, 18-ply cylinders) did not fail by buckling, only the [±30] specimens will be discussed in this section. The nominal radius-to-thickness ratios of the 152-mm and 57-mm diameter specimens, are 160 and 60, respectively. These specimens also differed in their length-to-thickness ratios from 3.01 to 2.67 for the 57-mm and 152-mm diameter specimens, respectively. The results from the present analyses are listed in Table 7.7. The buckled shapes for the 152-mm diameter [±30] specimens were the same as the smaller specimens.

The most striking differences between the analyses and the experimental performance are the accuracy and the number of circumferential waves. The average accuracy of Donnell's analysis is 48 percent with a range of ±6 percent for the small diameter specimens; whereas, a 36±3 percent accuracy was predicted for the 152-mm diameter specimens. Since all specimens contained only one circumferential-crossover band within the gage length, the amount of fiber undulation could not cause this difference in performance. The predicted number of circumferential waves for both sizes of cylinders is approximately half of the observed values. Consequently, the diameter of a filament-wound cylinder affects the compressive buckling load in a manner other than what is expected by classical, linear-buckling theory.

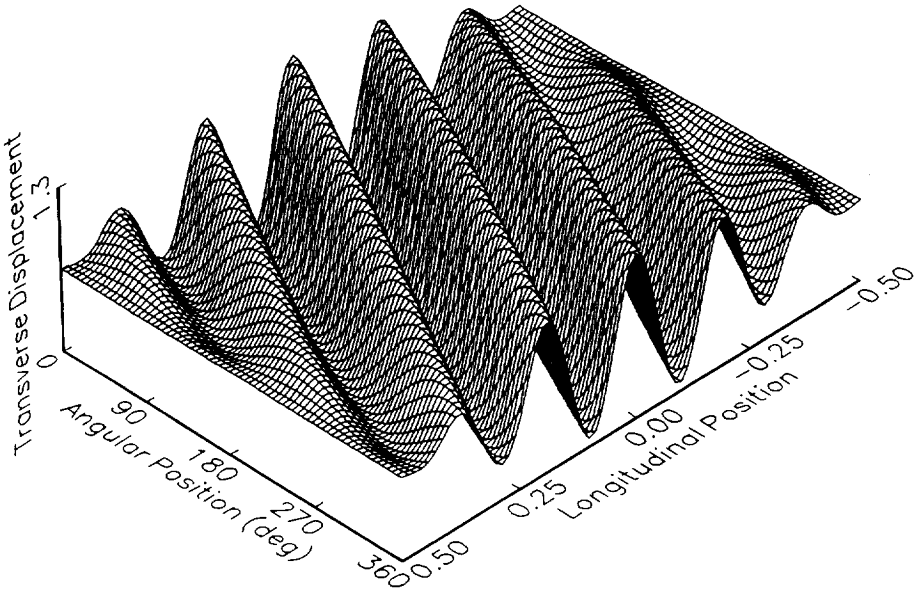

Figure 7.12: Torsional buckling mode shape typical for 57-mm diameter, [±30] cylinders.

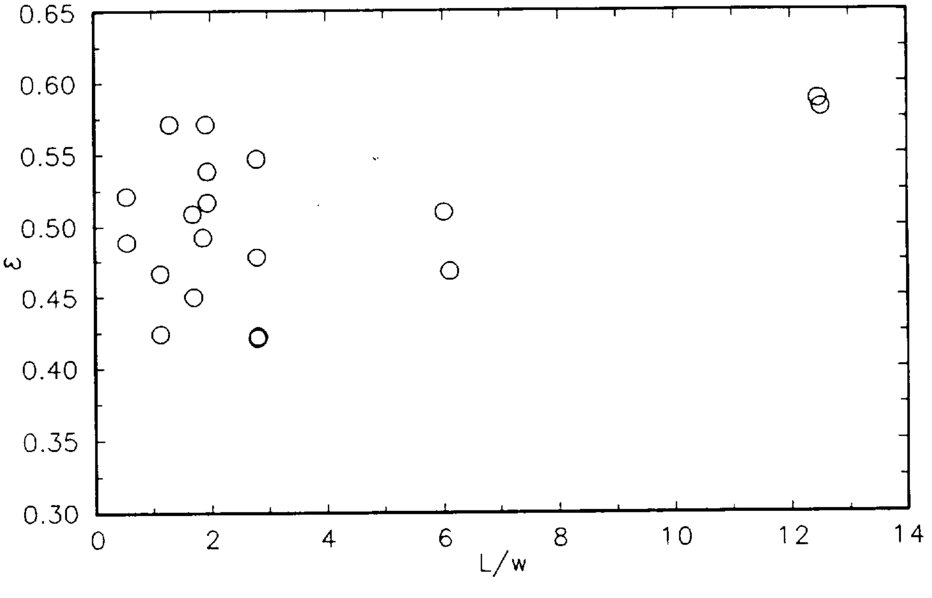

Figure 7.13: Accuracy of the In-Plane Crossover-Band Spacing specimens as a function of the normalized crossover-band spacing using Flügge's theory.

Table 7.6: Results of buckling load calculations for the Mandrel Material experimental program.

| Cylinder Number | Experiment | | Donnell's Theory | | | Flügge's Theory | | |
|---|---|---|---|---|---|---|---|---|
| | Buck. Load (kN) | No. Cir. Waves | Buck. Load (kN) | ε (%) | No. Cir. Waves | Buck. Load (kN) | ε (%) | No. Cir. Waves |
| 062191A | 6.81* | 6 | 12.8 | 53 | 3 | 12.6 | 54 | 3 |
| 062191B | 6.72 | 6 | 13.8 | 49 | 2 | 13.7 | 49 | 3 |
| 062391A | 6.30* | 4 | 14.1 | 45 | 2 | 14.0 | 45 | 3 |
| 062391B | 6.36* | 5 | 12.6 | 50 | 3 | 12.5 | 51 | 3 |

* first load cycle

Table 7.7: Results of buckling load calculations for the Cylinder Scale experimental program.

| Cylinder Number | Experiment | | Donnell's Theory | | | Flügge's Theory | | |
|---|---|---|---|---|---|---|---|---|
| | Buck. Load (kN) | No. Cir. Waves | Buck. Load (kN) | ε (%) | No. Cir. Waves | Buck. Load (kN) | ε (%) | No. Cir. Waves |
| 061991A | 8.29 | 4 | 14.7 | 57 | 2 | 14.5 | 57 | 2 |
| 061991B | 7.18 | 5 | 17.1 | 42 | 2 | 16.9 | 42 | 2 |
| 062091 | 6.15* | 4 | 13.4 | 46 | 2 | 13.3 | 47 | 3 |
| 081291A | 4.88 | 8 | 15.2 | 32 | 4 | 15.2 | 32 | 4 |
| 081291B | 5.29 | -- | 14.8 | 36 | 4 | 14.7 | 36 | 4 |
| 030692A | 5.71 | 8 | 15.1 | 38 | 4 | 15.0 | 38 | 4 |
| 030692B | 5.83* | -- | 15.3 | 38 | 4 | 15.3 | 38 | 4 |

* first load cycle

Since the material quality of the 57-mm and 152-mm diameter specimens were similar, the observed differences in performance were either caused by the geometric imperfections or non-membrane prebuckling deformations. The larger geometric imperfections observed in the 152-mm diameter specimens might indicate the probable cause of the reduced performance. However, this conclusion may be premature. Simitses, Shaw, and Sheinman [30] and Sheinman, Shaw, and Simitses [31] examine the effects of length-to-radius ratio on the imperfection sensitivity of [±45/±45] cylinders while including non-membrane effects. Their results indicate a decrease in geometric imperfection sensitivity with an increase in scale. If similar trends exist for [±30] laminated cylinders, the increased geometric imperfection observed in the large specimens may not be the cause of the reduced performance. Further analysis would be required to determine the effects of scale before the observed performance reduction can be fully explained.

### 7.2.4 Symmetry of the Laminated-Shell Regions

This experiment was designed to determine the effects of extension-bending coupling on the buckling behavior of filament-wound cylinders. Although the experimental results were nearly the same for the symmetric and antisymmetric configurations, the accuracy was approximately 18 percent better for the symmetric specimens, as shown in Table 7.8. Donnell's and Flügge's equations also predicted very different buckling modes. Each cylinder buckled in a torsional mode; however, the symmetric cylinder consisted of 5 circumferential waves in contrast to 1 circumferential wave for the antisymmetric cylinder.

Table 7.8: Results of buckling load calculations for the Symmetry of the Laminated-Shell Regions experimental program.

| | Experiment | Donnell's Theory | | | Flügge's Theory | | |
|---|---|---|---|---|---|---|---|
| Cylinder Number | Buck. Load (kN) | Buck. Load (kN) | ε (%) | No. Cir. Waves | Buck. Load (kN) | ε (%) | No. Cir Waves |
| 021192A | 48.0 | 70.6 | 68 | 5 | 70.4 | 68 | 5 |
| 021192B | 53.3 | 74.2 | 72 | 5 | 74.0 | 72 | 5 |
| 012092A | 50.8 | 87.0 | 58 | 1 | 86.7 | 59 | 1 |
| 012092B | 52.1 | 88.0 | 59 | 1 | 87.6 | 59 | 1 |

When the quality of the specimens was examined as a possible explanation for the differences in performance, both winding configurations had approximately the same root mean square, standard deviation, and range of initial geometric imperfection. Visual examination of the exterior and interior surfaces did not reveal sufficient cause for these discrepancies. From the laminate constitutive relations, out-of-plane deformations were expected prior to buckling for the antisymmetric configuration. This coupling behavior was assumed to be the major cause of the discrepancy between the accuracy of the predictions. Sheinman, Shaw, and Simitses [31] simulate the behavior of symmetric and antisymmetric cylinders ([+45/-45/+45/-45] and [+45/-45/-45/+45]) with length-to-radius ratios of 2 using an adaptation of Koiter's special theory. This theory includes the effects of geometric imperfections and prebuckling deformations. Their results indicate the symmetric cylinder was relatively insensitive to initial geometric imperfections and had a 6 percent larger buckling load.

### 7.2.5 Winding Sequence

Experimentally, the failure loads of Specimens 122990 and 010891 were approximately the same although they consisted of $[90/\pm30_2/90]$ and $[\pm30/90_2/\pm30]$ winding sequences, respectively. When the buckling behavior was analyzed using Donnell's and Flügge's theories, the accuracy was quite different for the different winding sequences, as shown in Table 7.9. Donnell's and Flügge's linear buckling theories were much more accurate for the case when the 90° plies are on the outside surfaces of the cylinder. When the buckled shapes were examined, they also show a substantial difference between the two types of specimens. Specimen 122990 was predicted to buckle in a torsional mode very similar to the shapes shown in Figure 7.12, whereas, Specimen 010891 buckled in a checkerboard pattern, as shown in Figure 7.14.

Table 7.9: Results of buckling load calculations for the Winding Sequence experimental program.

| | Experiment | Donnell's Theory | | | Flügge's Theory | | |
|---|---|---|---|---|---|---|---|
| Cylinder Number | Buck. Load (kN) | Buck. Load (kN) | ε (%) | No. Cir Waves | Buck. Load (kN) | ε (%) | No. Cir. Waves |
| 122990 | 174 | 228 | 76 | 5 | 226 | 77 | 5 |
| 010891 | 187 | 385 | 49 | 6 | 365 | 51 | 6 |
| 010191 | 845 | 2770 | 30 | 2 | 2720 | 31 | 3 |
| 030991 | 616 | 3420 | 18 | 4 | 3190 | 19 | 4 |

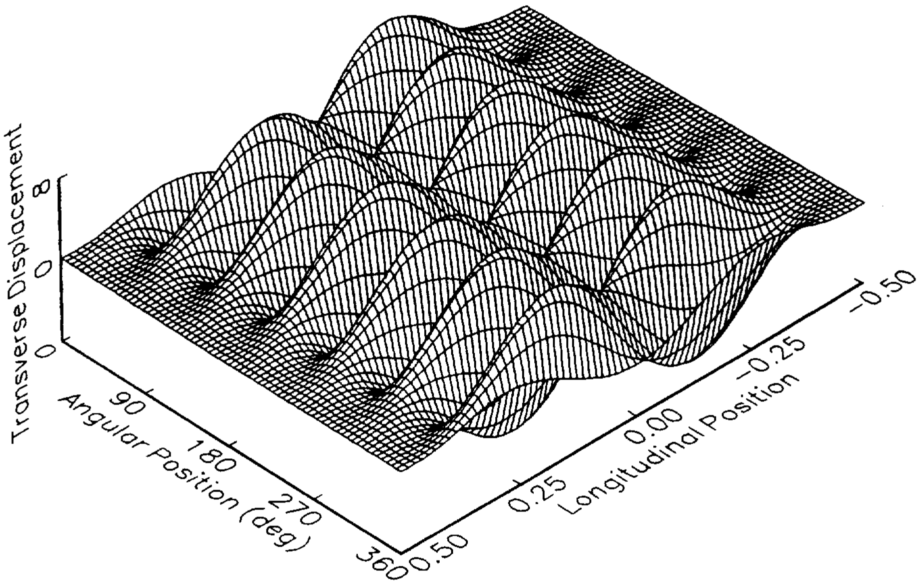

Figure 7.14: Checkerboard buckled shape observed for Specimen 010891 using Donnell's and Flügge's theories.

The differences in the accuracy between the two specimens was difficult to explain. Both specimens were wound with the same crossover-band spacing and appeared to have the same global geometric quality. Although Specimen 010891 contained more thickness deviations on the outer surface, this level of thickness imperfection in the [±30] specimens did not cause a substantial change in compressive performance. The differences in the accuracy was attributed to the bending stiffnesses of the laminates. The [90/±$30_2$/90] specimen had a large circumferential-bending stiffness while the [±30/$90_2$/±30] cylinder had a relatively large axial-bending stiffness. The results of the analyses seem to indicate that when the circumferential-bending stiffness is large, classical-buckling theories are better able to predict the compressive behavior. Simitses, Shaw, and Sheinman [30] report that stronger lamination sequences are more imperfection sensitive when non-membrane effects are considered. A cylinder with a winding sequence of [90/±30/$_2$90] has a 30 percent smaller buckling load, predicted by classical-buckling theories, than does a [±30/90$_2$/±30] cylinder with the same geometry.

### 7.2.6 Through-the-Thickness Crossover-Band Location

The objective of this study was to investigate the influence of the crossover-band placement through the thickness of multi-layered cylinders. Although the present analyses did not include the effects of the crossover bands, the accuracy of the analyses should reflect their presence and the relative amount of symmetrically-laminated material. The predicted number of circumferential waves for each cylinder and each analysis was 6, as shown in Table 7.10. Donnell's and Flügge's analyses predicted a checkerboard buckling mode with two rings of deformation, as shown in Figure 7.14, with one exception. Specimen 012592B was predicted to have a diamond-shaped buckling pattern, shown in Figure 7.15, with Flügge's theory. A contour plot of this buckling pattern is shown in Figure 7.16. This buckled shape is very similar to the postbuckled deformations observed in the [±30] specimens.

Table 7.10: Results of buckling load calculations for the Through-the-Thickness Crossover-Band Location experimental program.

| Cylinder Number | Experiment | Donnell's Theory | | | Flügge's Theory | | |
|---|---|---|---|---|---|---|---|
| | Buck. Load (kN) | Buck. Load (kN) | $\varepsilon$ (%) | No. Cir. Waves | Buck. Load (kN) | $\varepsilon$ (%) | No. Cir. Waves |
| 012592A | 144 | 330 | 44 | 6 | 313 | 46 | 6 |
| 012592B | 158 | 324 | 49 | 6 | 314 | 50 | 6 |
| 013092A | 181 | 339 | 53 | 6 | 321 | 56 | 6 |
| 013092B | 181 | 340 | 53 | 6 | 323 | 56 | 6 |
| 030592A | 164 | 339 | 48 | 6 | 321 | 51 | 6 |
| 030592B | 170 | 334 | 51 | 6 | 317 | 54 | 6 |
| 030992A | 188 | 325 | 58 | 6 | 308 | 60 | 6 |
| 030992B | 189 | 326 | 58 | 6 | 310 | 61 | 6 |

Geometric and material quality were approximately the same for all specimens except Cylinder 013092 which contained many tow twists and had a substantially higher buckling load. The results of Donnell's and Flügge's analyses only indicate a slightly higher load for this specimen which confirms the hypothesis discussed in the Winding Sequence experimental program that the bending stiffness of the material greatly influences the buckling load. No trends were observed for the other specimens when the accuracy of the analyses were compared to the geometric imperfection level. When the accuracy was compared to the winding pattern, a strong correlation was observed with the minimum distance between circumferential crossovers irrespective of layer, as shown in Figure 7.17. When the crossover bands were stacked through the thickness, the accuracy of the models

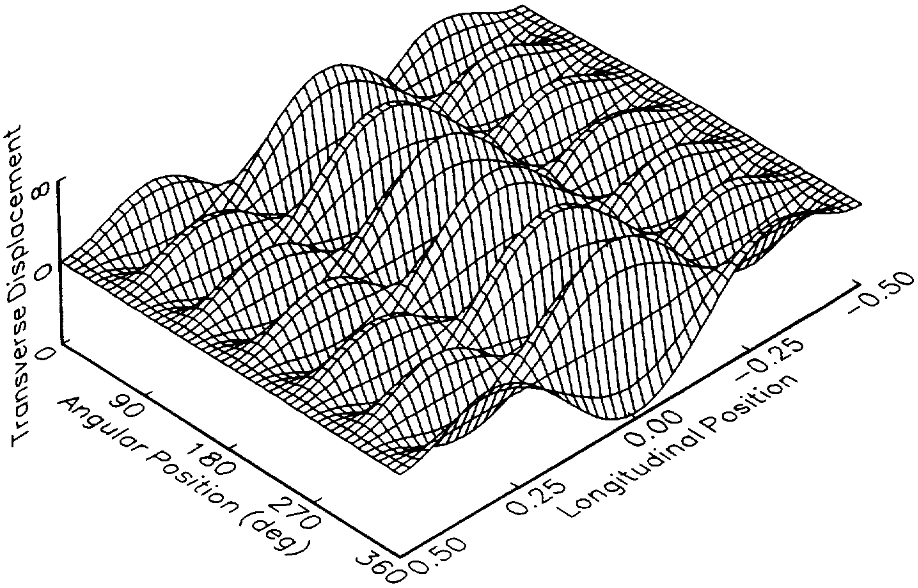

Figure 7.15: Buckled mode shape of Specimen 012592B computed with Flügge's theory: surface plot.

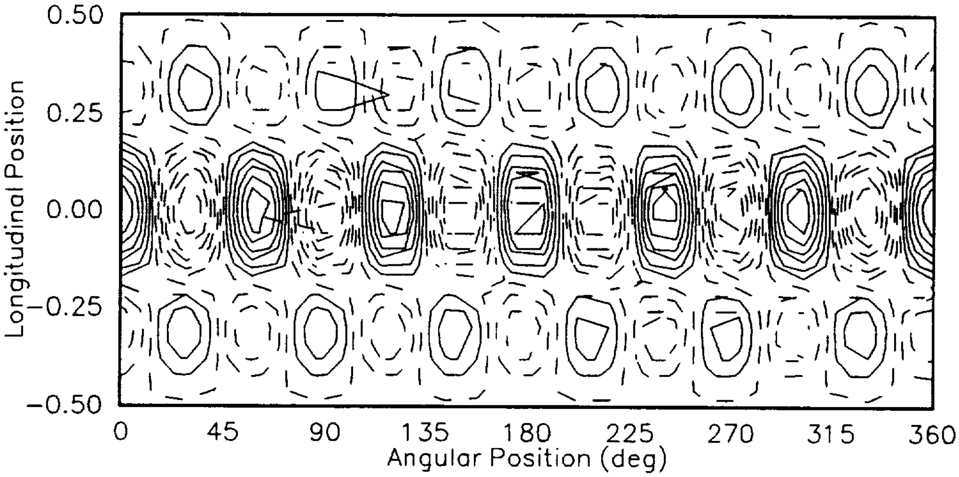

Figure 7.16: Buckled mode shape of Specimen 012592B computed with Flügge's theory: contour plot.

was approximately 46 percent. The alternating crossover-band configuration had a minimum crossover-band spacing of one-half of the stacked case and an average accuracy of 52 percent. Recall, this winding pattern also consisted of 62.5 percent symmetrically wound material. The final configuration, a combination of two crossover-band spacings, also had symmetric and antisymmetric regions and an average accuracy of 59 percent. As with the results of the Symmetry of the Laminated-Shell Regions experimental program, the suspected cause for the increase in accuracy is related to the amount of prebuckling deformation caused by the extension-bending coupling of the shell.

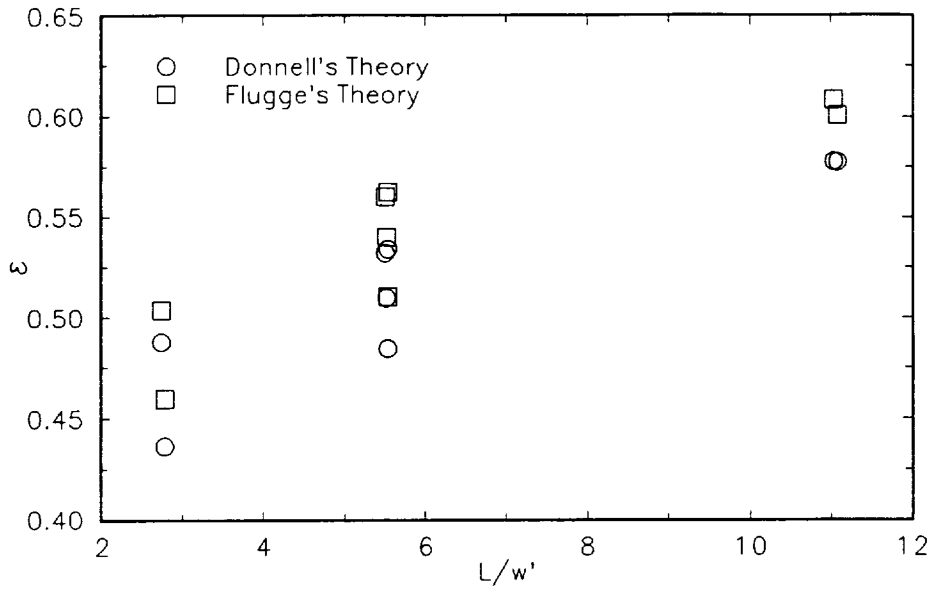

Figure 7.17: Accuracy of the Through-the-Thickness Crossover-Band Location specimens as a function of the minimum crossover-band spacing.

### 7.2.7 Heated Winding

The cylinders manufactured with the heated winding technique resulted in material with a lower void content but similar initial geometric imperfection levels as the cold-wound specimens. The accuracy of the buckling models of Cylinders 031092 and 031392 differ by nearly 10 percent although the number of circumferential waves is the same, as shown in Table 7.11. Each specimen was predicted to buckle with a torsional buckling mode. The difference in accuracy is probably due to the thickness variations around the circumference of Cylinder 031092 induced by non-uniform resin flow during cure.

If the results of this experiment are compared to Specimens 121490, 122990, and 011191, heated winding appears to improve the compressive performance by 10 percent. The cause of this improvement may be due to either a better correspondence between the manufacturer's published material properties and the wound specimens, a change in the crossover-band spacing, or the level of geometric imperfections. Unfortunately, the size of the geometric imperfections were not measured on the cold-wound specimens, although, visual examination indicated a similar level of quality. Additional experimentation with a cold-wound specimen with the same crossover-band spacing would be required to determine the actual effects of elevated temperature winding.

Table 7.11: Results of buckling load calculations for the Heated Winding experimental program.

| | Experiment | Donnell's Theory | | | Flügge's Theory | | |
|---|---|---|---|---|---|---|---|
| Cylinder Number | Buck. Load (kN) | Buck. Load (kN) | $\varepsilon$ (%) | No. Cir. Waves | Buck. Load (kN) | $\varepsilon$ (%) | No. Cir. Waves |
| 031092A | 166 | 222 | 75 | 5 | 220 | 76 | 5 |
| 031092B | 174 | 229 | 76 | 5 | 227 | 77 | 5 |
| 031392A | 153 | 185 | 83 | 5 | 184 | 83 | 5 |
| 031392B | 160 | 185 | 86 | 5 | 183 | 87 | 5 |

## 7.3 Strength Analysis

Since many of the specimens did not exhibit postbuckling deformations, an analysis was performed to compute the compressive strength of each specimen. The analysis was based on classical lamination theory using the Tsai-Wu failure criterion and the material properties listed in Table 7.12. Specimens which buckled during experimental testing were also examined with this analysis to aid in the development of design criteria to predict the compressive response of thin filament-wound cylinders. The following sections contain discussions of the accuracy of the strength analysis of each experimental program.

Table 7.12: Material constants used for the strength analysis.

| | Strength | |
|---|---|---|
| Direction | Tension (MPa) | Compression (MPa) |
| Longitudinal | 1860 | 1650 |
| Transverse | 62.1 | 138 |
| Shear | 82.7 | 82.7 |

### 7.3.1 In-Plane Crossover-Band Spacing

Each specimen in this experimental program buckled with visible out-of-plane deformations and significant postbuckling strength. Although cracks were heard and detected with the acoustic emission system prior to buckling, visible damage was not observed until after buckling. Consequently, the failure mode for these specimens was assumed to be compressive instability of the shell. When the buckling analyses were performed, the predicted buckling loads were between 40 and 60 percent of the experimentally measured loads. When the strength analysis was performed, the compressive failure predictions were an additional 15 to 20 percent above the predicted buckling loads, as shown in Table 7.13. Based on the buckling and strength analyses, the specimens in this experimental program should buckle rather than fail in compression.

Table 7.13: Results of compressive strength calculations for the In-Plane Crossover-Band Spacing experimental program.

| Cylinder Number | Exp. | Donnell | | Flügge | | Tsai-Wu | |
|---|---|---|---|---|---|---|---|
| | Buck. Load (kN) | Buck. Load (kN) | ε (%) | Buck. Load (kN) | ε (%) | Failure Load (kN) | ε (%) |
| 061991A | 8.29 | 14.7 | 57 | 14.5 | 57 | 21.8 | 38 |
| 061991B | 7.18 | 17.1 | 42 | 16.9 | 42 | 23.6 | 30 |
| 062091 | 6.15* | 13.4 | 46 | 13.3 | 47 | 20.9 | 29 |
| 062191A | 6.81* | 12.8 | 53 | 12.6 | 54 | 20.4 | 33 |
| 062191B | 6.72 | 13.9 | 49 | 13.7 | 49 | 21.2 | 32 |
| 062291A | 7.01 | 12.4 | 57 | 12.3 | 57 | 20.1 | 35 |
| 062291B | 6.62 | 12.9 | 51 | 12.8 | 52 | 20.5 | 32 |
| 062491A | 6.58 | 12.2 | 54 | 12.0 | 55 | 19.9 | 33 |
| 062491B | 5.56 | 13.3 | 42 | 13.2 | 42 | 20.8 | 27 |
| 062591A | 6.43 | 13.6 | 47 | 13.4 | 48 | 21.0 | 31 |
| 062591B | 5.70 | 13.6 | 42 | 13.5 | 42 | 21.1 | 27 |
| 063091A | 6.34 | 13.7 | 46 | 13.6 | 47 | 21.1 | 30 |
| 063091B | 6.65 | 13.2 | 50 | 13.0 | 51 | 20.7 | 32 |
| 070191A | 8.50 | 17.8 | 58 | 14.6 | 58 | 21.9 | 39 |
| 070191B | 8.80 | 15.1 | 58 | 15.0 | 59 | 22.2 | 40 |
| 011692A | 6.47* | 13.4 | 48 | 13.2 | 49 | 20.8 | 31 |
| 011692B | 7.29 | 14.1 | 51 | 14.0 | 52 | 21.4 | 34 |

* first load cycle

### 7.3.2 Mandrel Material

The goal of this experimental program was to investigate the effects of mandrel material on the compressive response. No effects were observed on the quality of the structure, experimental buckling load, or predicted buckling load. When the results from the strength analysis were examined, no effects of the mandrel material were observed, as shown in Table 7.14. Results from the experimental testing, buckling analysis, and strength analysis behave similar to those observed in the In-Plane Crossover-Band Spacing experimental program.

### 7.3.3 Cylinder Scale

Three different types of behavior were observed when the specimens for this experimental program were loaded to failure. The small and large diameter [±30] specimens buckled and postbuckled with little damage. The six-ply specimens appeared to buckle and fracture at the same instant while the 18-ply cylinders fractured without

Table 7.14: Results of compressive strength calculations for the Mandrel Material experimental program.

| Cylinder Number | Exp. Buck. Load (kN) | Donnell Buck. Load (kN) | Donnell ε (%) | Flügge Buck. Load (kN) | Flügge ε (%) | Tsai-Wu Failure Load (kN) | Tsai-Wu ε (%) |
|---|---|---|---|---|---|---|---|
| 062191A | 6.81* | 12.8 | 53 | 12.6 | 54 | 20.4 | 33 |
| 062191B | 6.72 | 13.8 | 49 | 13.7 | 49 | 21.2 | 32 |
| 062391A | 6.30* | 14.1 | 45 | 14.0 | 45 | 21.1 | 30 |
| 062391B | 6.36* | 12.6 | 50 | 12.5 | 51 | 20.3 | 31 |

* first load cycle

becoming unstable. When the strength analysis of the [±30] cylinders was performed, the predicted buckling loads were significantly smaller than the compressive strengths, shown in Table 7.15, which corresponds to the experimentally observed behavior. The level of damage in the 57-mm diameter specimens was significantly larger than the 152-mm diameter [±30] specimens. This might be related to difference between the buckling and strength analyses since the values for the small cylinders are closer together than the large diameter specimens.

When the analytical strength results for the six-ply specimens were examined, the difference between the buckling and failure loads ranged from approximately four percent for Cylinder 010891, to nearly 30 percent for Cylinder 122990; however, no buckling displacements were observed despite the large difference in these predictions. The level of visible damage for Cylinder 010891 was the largest for the six-ply specimens. The strength analysis predicts a compressive failure mode for each 18-ply specimen which confirms the experimental observations. The worst strength estimate occurred for Cylinder 053091 which exhibited delamination and sublaminate buckling without the development of a through-the-thickness fracture.

### 7.3.4 Symmetry of the Laminated-Shell Regions

When the strength analysis was performed for the symmetric and antisymmetric cylinders, the antisymmetric configuration was expected to be slightly stronger since the per-ply thickness for this cylinder was larger. For both winding configurations, the predicted buckling load was smaller than the predicted strength, as shown in Table 7.16, which corresponds to the experimental observations. The differences in the analyses is smaller than the [±30] specimens and the specimens in this experimental program exhibit substantially more damage and low postbuckling strengths.

### 7.3.5 Winding Sequence

Both specimens in this experimental program were predicted to buckle rather than fail in compression, as shown in Table 7.17. The difference between the buckling and strength analyses is quite large when the hoop layers are located on the exterior surfaces of the laminate. When the hoop layers are in the interior, the difference between the analyses is nearly zero and the cylinder contained more visible damage after failure.

Table 7.15: Results of compressive strength calculations for the Cylinder Scale experimental program.

| | Exp. | Donnell | | Flügge | | Tsai-Wu | |
|---|---|---|---|---|---|---|---|
| Cylinder Number | Buck. Load (kN) | Buck. Load (kN) | ε (%) | Buck. Load (kN) | ε (%) | Failure Load (kN) | ε (%) |
| 061991A | 8.29 | 14.7 | 57 | 14.5 | 57 | 21.8 | 38 |
| 061991B | 7.18 | 17.1 | 42 | 16.9 | 42 | 23.6 | 30 |
| 062091 | 6.15* | 13.4 | 46 | 13.3 | 47 | 20.9 | 29 |
| 081291A | 4.88 | 15.2 | 32 | 15.2 | 32 | 59.4 | 8.2 |
| 081291B | 5.29 | 14.8 | 36 | 14.7 | 36 | 58.5 | 9.0 |
| 030692A | 5.71 | 15.1 | 38 | 15.0 | 38 | 59.1 | 9.7 |
| 030692B | 5.83* | 15.3 | 38 | 15.3 | 38 | 59.7 | 9.8 |
| 121490 | 106 | 150 | 70 | 149 | 71 | 294 | 36 |
| 122990 | 174 | 228 | 76 | 226 | 77 | 363 | 48 |
| 010891 | 187 | 385 | 49 | 365 | 51 | 425 | 45 |
| 022591 | 163 | 291 | 56 | 280 | 58 | 445 | 36 |
| 010191 | 845 | 2770 | 30 | 2720 | 31 | 1370 | 53 |
| 030991 | 616 | 3420 | 18 | 3190 | 19 | 1290 | 47 |
| 053091 | 535 | 2880 | 19 | 2640 | 20 | 1290 | 41 |

* first load cycle

Table 7.16: Results of compressive strength calculations for the Symmetry of the Laminated-Shell Regions experimental program.

| | Exp. | Donnell | | Flügge | | Tsai-Wu | |
|---|---|---|---|---|---|---|---|
| Cylinder Number | Buck. Load (kN) | Buck. Load (kN) | ε (%) | Buck. Load (kN) | ε (%) | Failure Load (kN) | ε (%) |
| 021192A | 48.0 | 70.6 | 68 | 70.4 | 68 | 110 | 44 |
| 021192B | 53.3 | 74.2 | 72 | 74.0 | 72 | 113 | 47 |
| 012092A | 50.8 | 87.0 | 58 | 86.7 | 59 | 116 | 44 |
| 012092B | 52.1 | 88.0 | 59 | 87.6 | 59 | 117 | 45 |

### 7.3.6 Through-the-Thickness Crossover-Band Location

When the winding patterns for this experimental program were designed, an increase in the compressive response was expected if the crossover bands were not stacked through the thickness. Like the buckling analyses, the accuracy of the predicted strength increases when the crossover bands are distributed although the increase in strength is smaller, as shown in Table 7.18. Comparing the predicted buckling and failure loads, each specimen was expected to fail by buckling. The difference between the buckling and strength analyses is nearly the same although the visible damage in the failed specimens changed with the winding pattern.

Table 7.17: Results of compressive strength calculations for the Winding Sequence experimental program.

| | Exp. | Donnell | | Flügge | | Tsai-Wu | |
|---|---|---|---|---|---|---|---|
| Cylinder Number | Buck. Load (kN) | Buck. Load (kN) | ε (%) | Buck. Load (kN) | ε (%) | Failure Load (kN) | ε (%) |
| 122990 | 174 | 228 | 76 | 226 | 77 | 363 | 48 |
| 010891 | 187 | 385 | 49 | 365 | 51 | 425 | 45 |
| 010191 | 845 | 2770 | 30 | 2720 | 31 | 1370 | 53 |
| 030991 | 616 | 3420 | 18 | 3190 | 19 | 1290 | 47 |

Table 7.18: Results of compressive strength calculations for the Through-the-Thickness Crossover-Band Location experimental program.

| | Exp. | Donnell | | Flügge | | Tsai-Wu | |
|---|---|---|---|---|---|---|---|
| Cylinder Number | Buck. Load (kN) | Buck. Load (kN) | ε (%) | Buck. Load (kN) | ε (%) | Failure Load (kN) | ε (%) |
| 012592A | 144 | 330 | 44 | 313 | 46 | 395 | 36 |
| 012592B | 158 | 324 | 49 | 314 | 50 | 391 | 40 |
| 013092A | 181 | 339 | 53 | 321 | 56 | 400 | 45 |
| 013092B | 181 | 340 | 53 | 323 | 56 | 401 | 45 |
| 030592A | 164 | 339 | 48 | 321 | 51 | 400 | 41 |
| 030592B | 170 | 334 | 51 | 317 | 54 | 397 | 43 |
| 030992A | 188 | 325 | 58 | 308 | 60 | 392 | 48 |
| 030992B | 189 | 326 | 58 | 310 | 61 | 393 | 48 |

### 7.3.7 Heated Winding

The use of heat during winding improved the quality of the structure by reducing the number of voids and their size. When the buckling analyses were performed for these specimens, the predicted buckling loads were the closest to the experimentally measured loads of all specimens in this research program. The small out-of-plane deformations observed after failure in the specimens was caused by buckling which occurred just prior to fracture initiation. The strength analysis also predicts a buckling type failure, as shown in Table 7.19. Although the difference between the stability and strength analyses is nearly 30 percent, the substantial buckling displacements and large postbuckling strength observed in the Symmetry of the Laminated-Shell Regions specimens, is absent. The presence of hoop layers, which increases the circumferential bending stiffness and the thickness of the shell, could explain this difference in behavior.

Table 7.19: Results of compressive strength calculations for the Heated Winding experimental program.

| | Exp. | Donnell | | Flügge | | Tsai-Wu | |
|---|---|---|---|---|---|---|---|
| Cylinder Number | Buck. Load (kN) | Buck. Load (kN) | ε (%) | Buck. Load (kN) | ε (%) | Failure Load (kN) | ε (%) |
| 031092A | 166 | 222 | 75 | 220 | 76 | 358 | 47 |
| 031092B | 174 | 229 | 76 | 227 | 77 | 364 | 48 |
| 031392A | 153 | 185 | 83 | 184 | 83 | 327 | 47 |
| 031392B | 160 | 185 | 86 | 183 | 87 | 327 | 49 |

## 7.4 Design Criteria

One of the goals of this research program was to develop design criteria for use with compressively loaded filament-wound cylinders. Tennyson, Muggeridge, and Caswell [32] suggest that such design criteria include imperfection sensitivity where the imperfections are characterized by the root mean square of the imperfection normalized by the thickness of the cylinder. The analytical work by Tennyson, Muggeridge, and Caswell [32], Simitses, Shaw, and Sheinman [30], and Sheinman, Shaw, and Simitses [31] show a decrease in performance with increasing imperfection amplitude for many types of cylinders. When the experimental results of the present study are plotted in this fashion, the results follow a similar trend, as shown in Figure 7.18.

As discussed in the preceding sections, the most probable cause for reduced buckling loads compared to classical-buckling analyses, is geometric imperfections and/or prebuckling deformations due to the coupled extension, bending, shear, and twisting stiffnesses. Additional examination of the present experimental results with regard to these complexities would allow for improved compressive-buckling predictions. Until then, the design criteria developed by Tennyson, Muggeridge, and Caswell [32] will allow engineers to design composite cylinders with improved confidence when classical-shell theories are used as the basis for design.

An important addition to any prediction of the compressive behavior of composite cylinders can be made by using a strength approach. Classical lamination theory, coupled with the Tsai-Wu failure criterion, is able to predict compressive failure modes. Results from the Symmetry of the Laminated-Shell Regions, Cylinder Scale, and In-Plane Crossover-Band Spacing experimental programs seem to indicate that classical buckling and strength analyses can also be used to estimate the amount of damage induced in

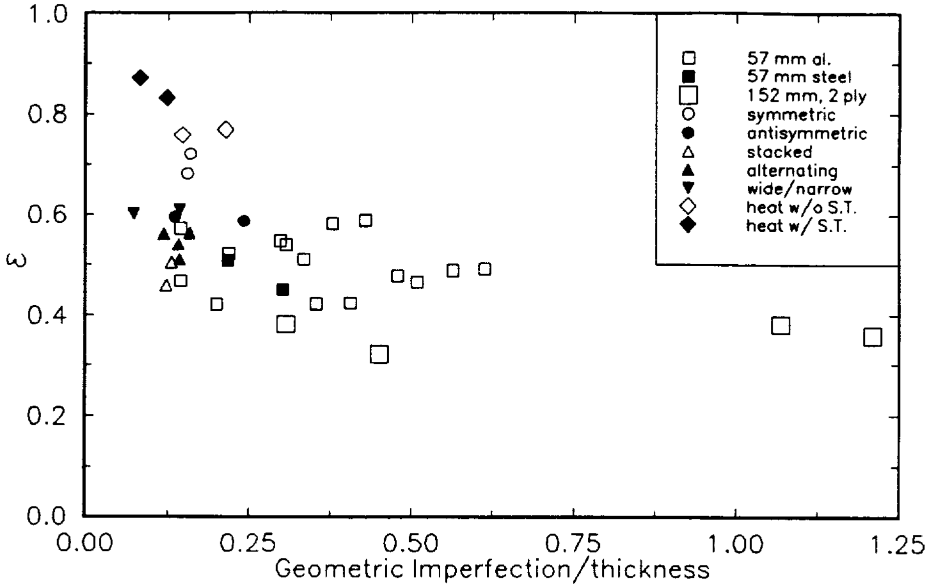

Figure 7.18: Accuracy of the buckling-load predictions as a function of the geometric imperfection amplitude using Flügge's theory.

cylinders with similar winding sequences: as the predicted compressive strength and buckling loads approach the same value, the amount of damage induced during buckling increases.

# 8.0 FINITE ELEMENT ANALYSIS

The filament-wound cylinder has a complex pattern of material distribution on the surface owing to changes in the layup from one triangular laminated shell region to the next. The presence of helical and circumferential crossover bands further complicate the material property distribution. These complications, coupled with residual thermal strains, lead to a highly nonlinear structural response of the filament-wound cylinders to compressive loads. The nonlinear structural response is not amenable to closed-form solution methods. Consequently, classical closed formed solutions such as those discussed in the previous chapter tend to overpredict the buckling load by as much as 175 percent. Hence, the implementation of finite element method was explored to predict the buckling response of the filament-wound cylinders.

The objectives of the present work were twofold. First, the effect of using progressively complicated levels of material distribution on the accuracy of buckling prediction was studied. Second, the importance of residual thermal strains in determining the buckling response was investigated. The finite element modeling and the results of this study are discussed below.

## 8.1 The Finite Element Model

Finite element models were developed and subjected to simulated compression using ABAQUS® software. The buckling loads were determined using the eigenvalue buckling analysis. Each of the 205.74 mm long by 152 mm diameter cylindrical models employed a single filament-wound layer oriented at +30°/-30°, with the diamond patterns placed symmetrically about the R-$\theta$ midplane (perpendicular to the longitudinal axis of the cylinder). A FORTRAN preprocessor was written to generate the nodal location and element connectivity for the various finite element models. At the present time, the geometric preprocessor is designed to generate cylinder models containing layers with a helical winding angle of +30°/-30°. The user can define the cylinder length, radius, material distribution, element mesh density and the number of repeating diamond patterns around the circumference. The models employ eight-noded quadrilateral and six-noded triangular curved shell elements in ABAQUS, designated S8R5 and STRI65 respectively. The formulation of these elements is based on thin shell theory, with the Kirchoff assumptions algebraically imposed in the development of the stiffness matrix [33]. A clamped-clamped boundary condition was used in all the models.

Before running the actual analyses, a mesh convergence study was performed. Five progressively finer meshes were used to demonstrate convergence of the buckling load. The details, including the number of nodes and elements, and the buckling loads are presented in Table 8.1. The convergence of the buckling load is shown in Figure 8.1, which is a plot of the buckling load versus the mesh density level.

The undeformed models and the mode shapes for the different mesh levels are shown in Figures 8.2 through 8.6. It can be observed that as the mesh density increases, the buckling mode shapes tend to exhibit a circular symmetry.

Table 8.1: Details of models used in mesh convergence study.

| Mesh Density Level | Number of Nodes | Number of Elements | Buckling Load (kN) |
|---|---|---|---|
| 3 | 1752 | 600 | 16.03 |
| 4 | 2408 | 824 | 15.32 |
| 5 | 3160 | 1080 | 14.89 |
| 6 | 4008 | 1368 | 14.70 |
| 7 | 4952 | 1688 | 14.61 |

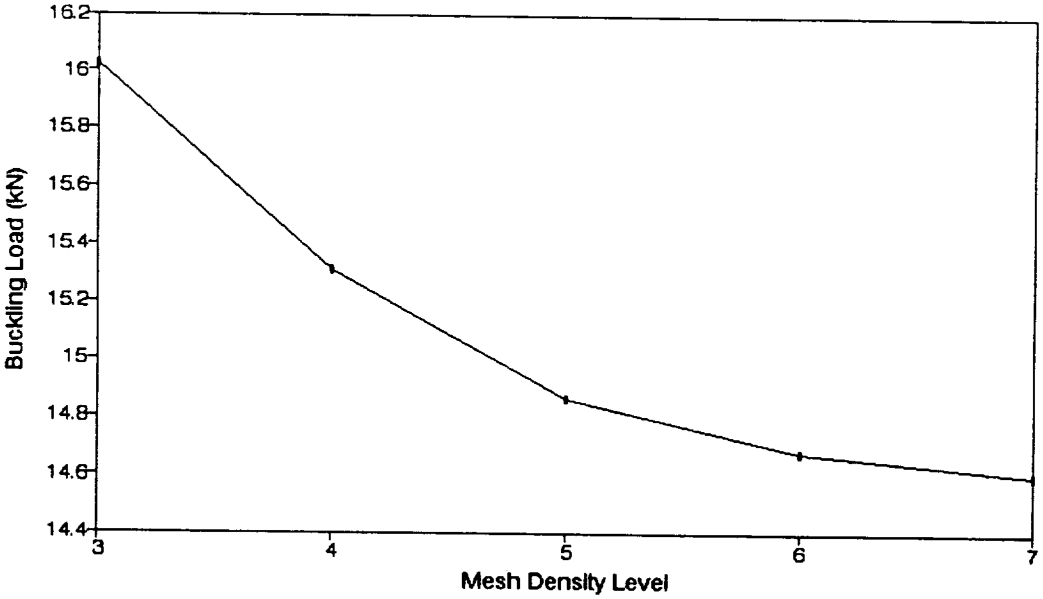

Figure 8.1: Convergence of the buckling load.

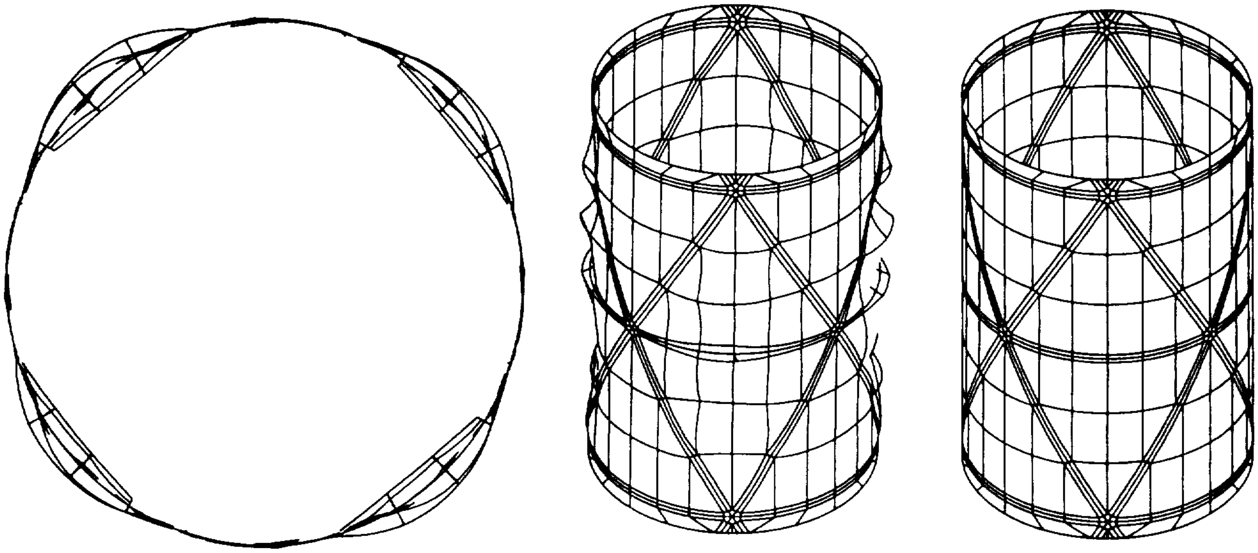

Figure 8.2: Model and mode shape with mesh level 3.

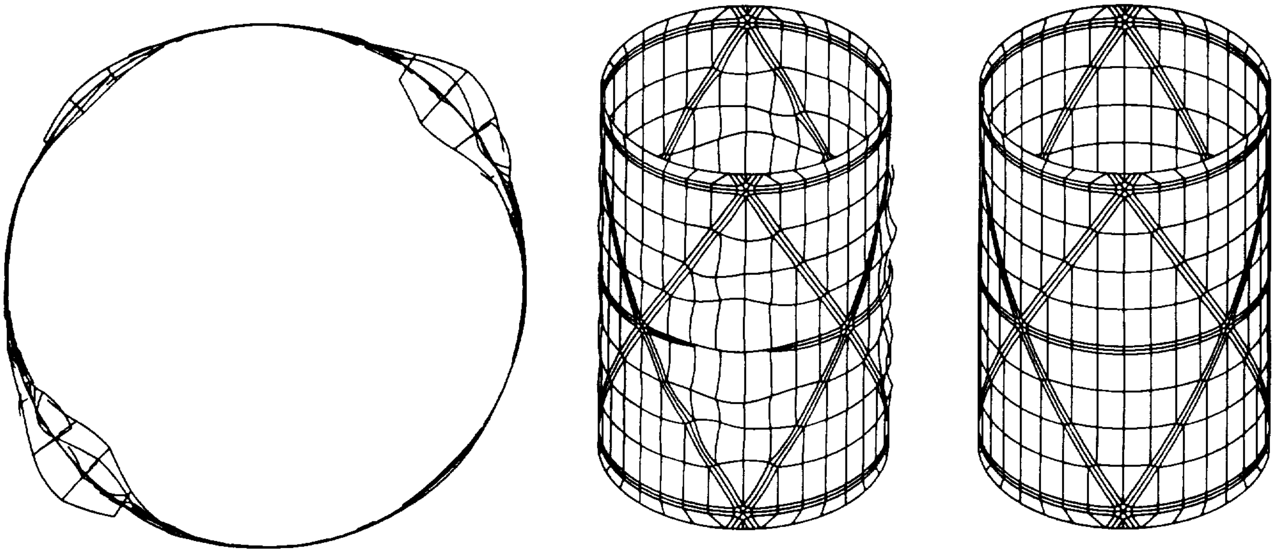

Figure 8.3: Model and mode shape with mesh level 4.

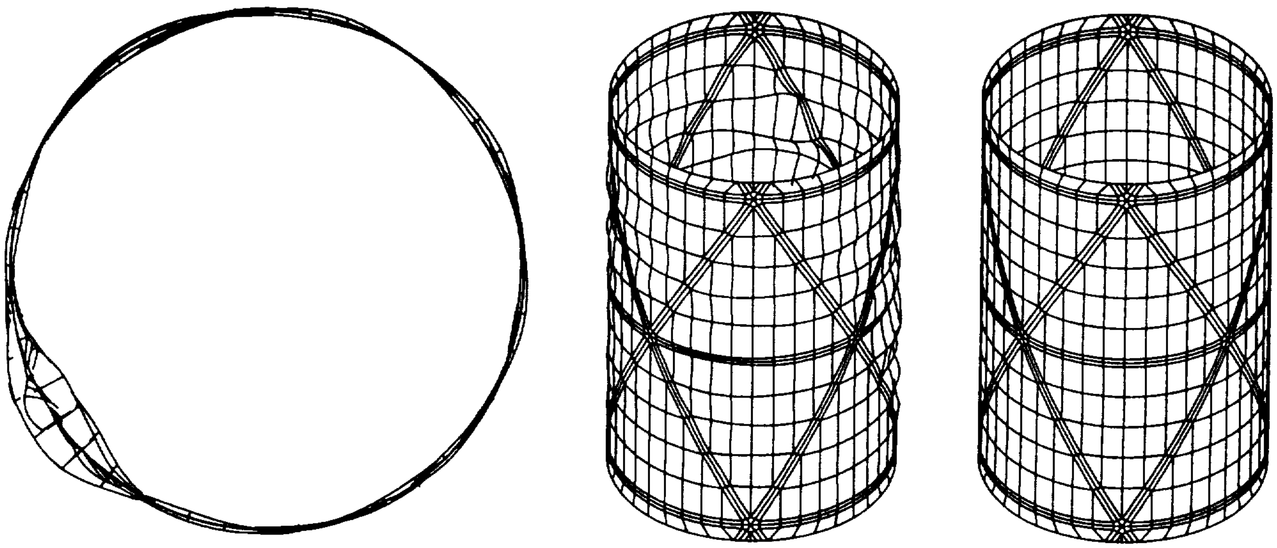

Figure 8.4: Model and mode shape with mesh level 5.

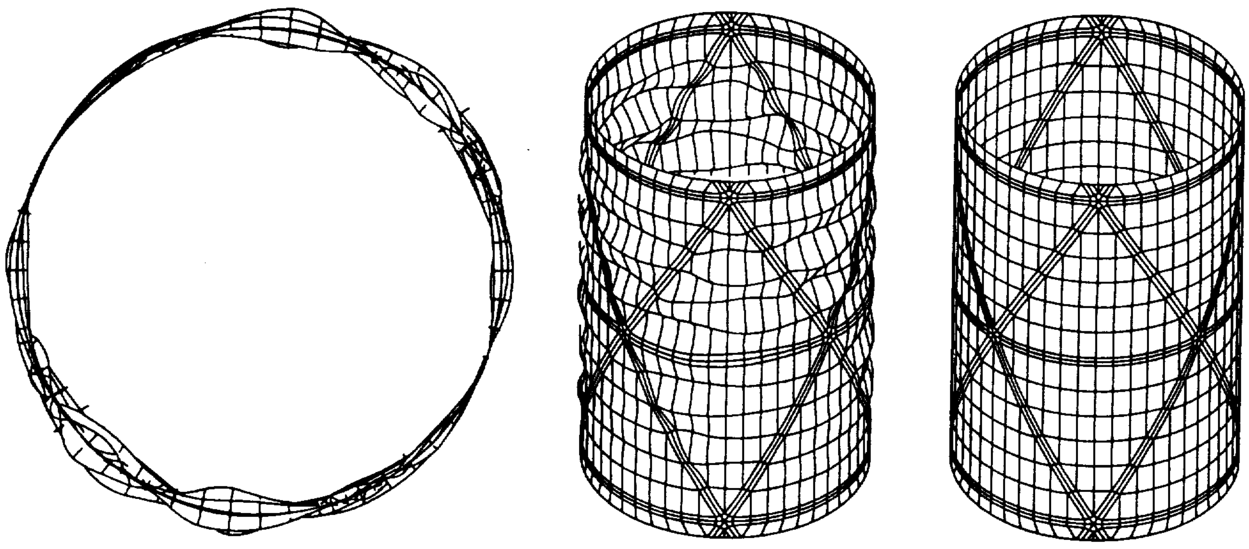

Figure 8.5: Model and mode shape with mesh level 6.

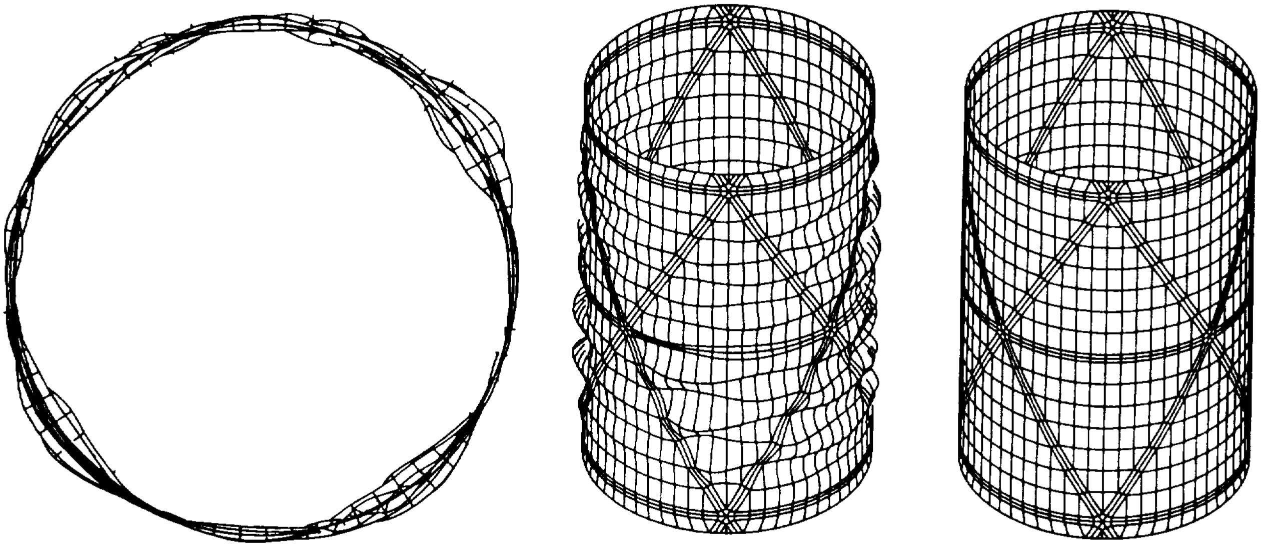

Figure 8.6: Model and mode shape with mesh level 7.

## 8.2 Effects of Material Modeling on Buckling Predictions

The effect of elastic couplings was studied using the cylindrical model with four circumferential repeating units. Three different sets of material constitutive properties based on the A, B, and D laminate stiffness matrices were analyzed and compared (see Table 8.2). First, the entire cylinder was modeled using the A, B, and D matrices of a +30°/-30° laminate, based on classical lamination theory. In the second material set, the A, B, and D for alternating +30°/-30° and -30°/+30° laminates were used in the two halves of each diamond repeating pattern. Finally, the modified A, B, and D matrices for the fiber undulation regions were used in the helical fiber crossover regions. The modified undulation properties, obtained from the analytical model developed by Jensen and Pai [17], were used to determine stiffness in the fiber undulation region. For the circumferential undulation band, the stiffness was obtained by averaging the respective stiffness terms of the +30°/-30° and -30°/+30° undulation region. The undulation properties were defined in addition to the alternating +30°/-30° and -30°/+30° laminate properties in the interior regions. Here, it is to be noted that the stretching-twisting/bending-shearing coupling values ($B_{16}$ and $B_{26}$) in the helical undulation bands are less than those for the corresponding flat (antisymmetric) laminates. This decrease is brought about by the averaging of the properties along the undulation length in the analytical model.

Table 8.2: Material constitutive property sets for the FEM model.

| Material Set | Description |
|---|---|
| 1 | +30/-30 Laminate |
| 2 | Alternating +30/-30 and -30/+30 Laminates |
| 3 | Set 2 with Modified Undulation Properties |

The stiffness values obtained for a +30°/-30° layup in the laminate and undulation regions using the material properties of Table 3.1 and the Modified Classical Lamination Theory are summarized in Table 8.3.

Table 8.3: Stiffness of laminate and undulation regions.

| Stiffness | Laminate Region | | | Undulation Region | | |
|---|---|---|---|---|---|---|
| $A_{ij}$ (MN/m) | 34.69 | 10.51 | 0.0 | 34.29 | 10.39 | -0.182 |
| | | 8.19 | 0.0 | | 8.15 | -0.070 |
| | sym. | | 11.63 | sym. | | 11.50 |
| $B_{ij}$ (kN) | 0.0 | 0.0 | 1.817 | -0.024 | -0.009 | 1.148 |
| | | 0.0 | 0.663 | | -0.004 | 0.419 |
| | sym. | | 0.0 | sym. | | -0.007 |
| $D_{ij}$ (Nm) | 0.535 | 0.162 | 0.0 | 0.532 | 0.161 | -0.098 |
| | | 0.127 | 0.0 | | 0.127 | -0.036 |
| | sym. | | 0.179 | sym. | | 0.178 |

The buckling loads for each of the three different material data sets are summarized in Table 8.4. It can be observed that the finite element model predicts a minimum buckling load when the stiffness properties of only the +30°/-30° laminate are included. It is interesting to note that the buckling load predicted using material set 2 (alternating +30°/-30° and -30°/+30° laminate properties) is lower than that predicted using material set 3 (alternating +30°/-30° and -30°/+30° laminate properties plus the modified undulation properties) is used. This implies that the stretching-twisting/bending-shearing couplings ($B_{16}$ and $B_{26}$) in an antisymmetric laminate tend to decrease the buckling load to a greater extent than the other coupling terms introduced by the fiber undulations. The buckling modes do not show any significant difference when the material sets are altered. The models and the mode shapes for Material Sets 1 and 3 are shown in Figures 8.7 and 8.8 respectively.

Table 8.4: Buckling Loads for Different Material Properties

| Material | Buckling Load (kN) |
|---|---|
| 1 | 13.7 |
| 2 | 14.1 |
| 3 | 14.6 |

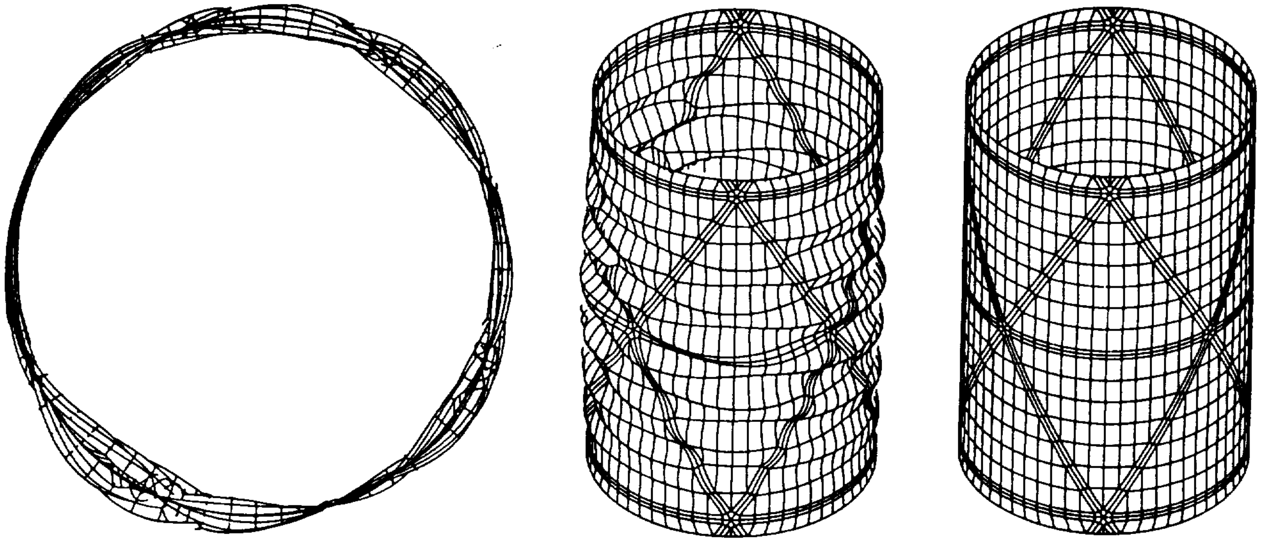

Figure 8.7: Buckling mode shape for Material Set 1.

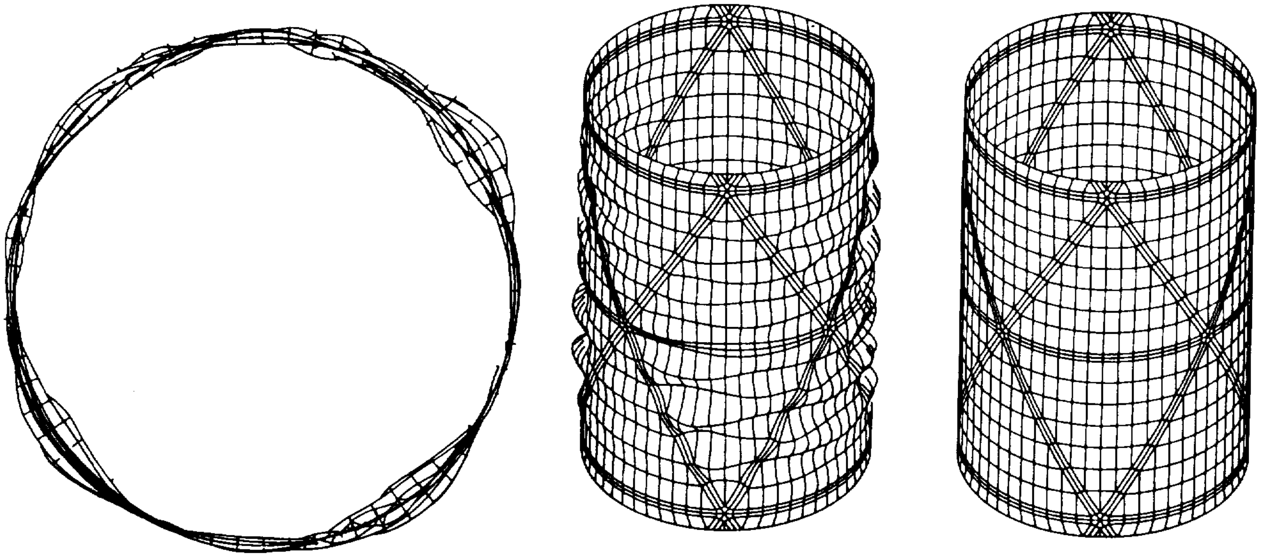

Figure 8.8: Buckling mode shape for Material Set 3.

## 8.3 Effects of Residual Thermal Strains on Buckling Predictions

The effect of residual thermal strains on the eigenvalue buckling analysis of the filament-wound cylinders was also studied. The thermal deformation incurred when the cured cylinder was cooled from the stress free temperature (121°C) to room temperature (21°C) was considered as an initial imperfection in the global geometry of the otherwise perfectly cylindrical shell during the eigenvalue analysis. The analysis was carried out in a two-step process. First, a thermal load was applied to the cylinder with four diamond patterns around the circumference. The model was defined using Material Set 3 and Mesh Level 6. Next, the thermally deformed cylinder shape was subjected to an eigenvalue buckling analysis. The thermal deformations are depicted in Figure 8.9. In the figure, the deformations are magnified five times the actual values. The maximum deformation of the shell was about 0.96 mm or approximately 2.25 times the average shell thickness. This value compares very well with experimentally observed geometric eccentricities of about 2.5 times the average shell thickness, discussed in Chapter 5. As seen in Figure 8.9, the residual stresses induce a quadrilateral shape to the cross section at the two ends. The quadrilaterals are out of phase by an angle of 45°. The midplane cross section (in the circumferential undulation band) is circular. This is the general pattern of deformation observed in the thin shell cylinders studied in the present work.

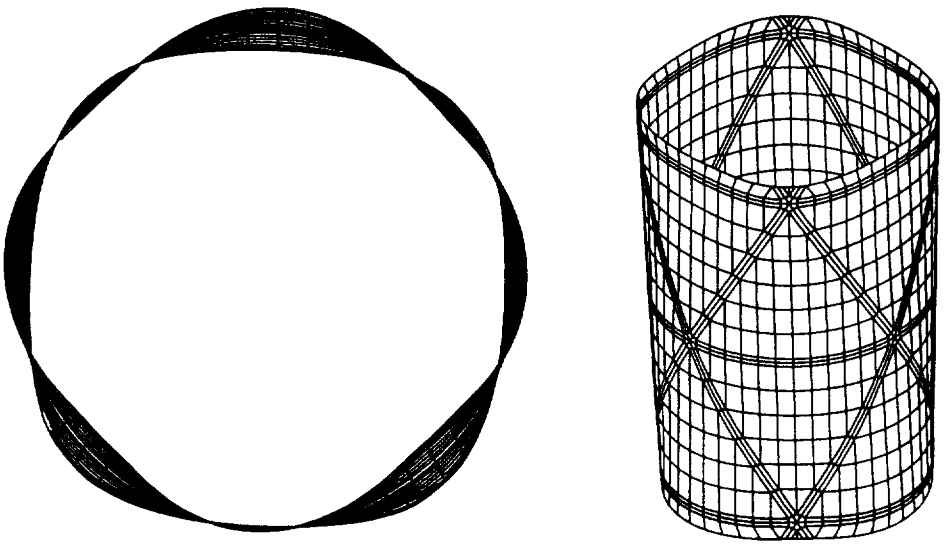

Figure 8.9: Thermally deformed shape of the cylinder.

The mode shape obtained from the eigenvalue buckling analysis of the thermally deformed cylinder is shown in Figure 8.10. The buckling load predicted by this two-step process was 5470 N which is within 5% of the experimentally observed value of 5720N (cylinder 030692A). Also, the mode shape shows vertical ridges, which have a very slight helical slant. This shape is much closer to experimentally observed modes when compared to the "crunched cylinder" shape predicted by the buckling analysis of cylinders with perfectly circular cross sections (Figures 8.7 and 8.8).

Hence, it can be concluded that the thermal deformations play a very significant role in determining the buckling loads and mode shapes of thin-shell filament-wound cylinders.

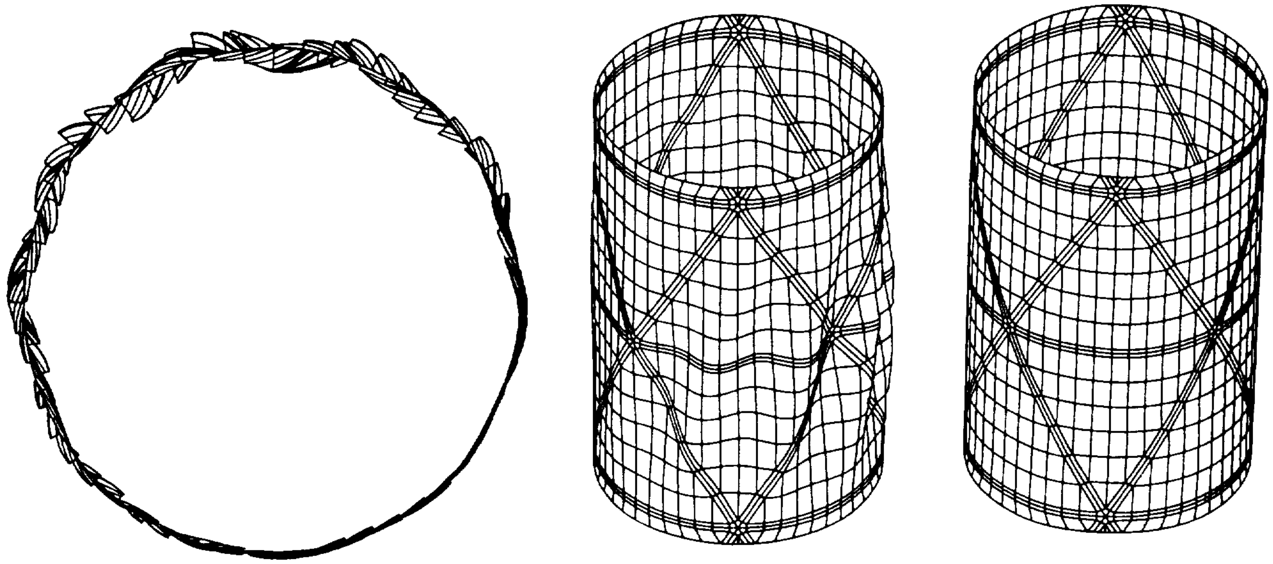

Figure 8.10: Buckling mode shape of thermally deformed cylinder.

[illegible] 156 [illegible]

PRECEDING PAGE BLANK NOT FILMED

# 9.0 CONCLUSIONS

The goal of the present research program was to improve the compressive buckling behavior of thin filament-wound cylinders by relating the manufacturing procedures to the quality and the compressive performance of the structure. Classical lamination theory for composites cannot predict the existence of all the stiffness couplings present in the undulation region. Modified classical lamination theories, which take into account the geometric eccentricity of the fibers in the undulation regions are required for an accurate material representation of the undulation. Even in modified lamination theories, the stiffness values are strongly dependent on the unit cell dimensions chosen to represent the undulation. Finite element modeling of the undulations confirms the drop in in-plane stiffness of the undulation region. Experimental results correlate quite well with analytical predictions regarding the decrease in the longitudinal stiffness in the undulation region. In general, the stiffness along the fiber undulation in the helical undulation band decreased by about 20%. The circumferential undulation band showed the maximum decrease in stiffness, by as much as 50%. The finite element analysis and experiments showed that the undulation regions initiated failure due to stress concentrations and microstructural defects.

During this investigation, winding and curing procedures have been developed which are capable of consistently producing high quality filament-wound cylinders using prepreg tows. With the use of simple mathematical relationships, the winding parameters can be related to the circumferential crossover-band spacing, number of diamond-shaped laminated-shell regions, and the amount of waste. The best manufacturing technique for thin multi-layered cylinders wound with prepreg tows is to wind at an elevated temperature and cure with high-temperature shrink tape. This technique promotes resin flow and improves consolidation resulting in nearly void free material without layer wrinkling or fiber waviness.

The quality of filament-wound cylinders determined by visual examination of the interior and exterior surfaces, is dependent on the accuracy of the rotation of the payout eye during winding, room humidity, winding temperature, and uniformity of the cure materials. Winding pattern and angle do not affect the visual quality of the cylinder. Microscopically, imperfections in the thickness are typically caused by tow twisting and nonuniform layers of shrink tape. The magnitude of these imperfections is typically less dramatic than the overlapping of prepreg layers which was observed by Chryssanthopoulos, Giavotto, and Poggi [22].

The quality parameter most often discussed in the literature with regard to compressive stability is the magnitude of the initial geometric imperfections. Global geometric imperfections in composite cylinders are caused by thermal residual stresses and deformations induced by attaching the loading fixtures to the cylinder. The magnitude of these imperfections is significant (often several times the thickness) in the thinner specimens; whereas, the increased stiffness of multi-layered cylinders reduces the magnitude of these imperfections. In general, filament-wound cylinders can be manufactured with the same or better level of quality obtained with cylinders manufactured from prepreg plies although the initial shape may be different.

The compressive performance of filament-wound cylinders is strongly influenced by the manufacturing procedures and quality level. The fiber microstructure within the crossover bands influences the location of postbuckling deformations and is the most common site of fracture. Small diameter [±30°] cylinders with various crossover-band spacings buckled with the same mode where the edges of the diamond-shaped buckled regions were parallel to, but slightly displaced from, the helical-crossover bands. Unlike the buckled shape, the stiffness of the cylinder and the buckling stress are not influenced by the crossover-band spacing. Although the mandrel material may affect the residual stress level within the composite material, the effects on the geometric imperfections and buckling load could not be observed in the [±30], 57-mm diameter specimens.

Laminated-shell regions within the winding pattern influence the prebuckling deformations through extension-bending coupling of the laminate. Significant gradients of the compression and bending strains are induced in helically-wound layers due to the presence of the helical and circumferential-crossover bands. These deformations can be measured with the use of strain gages and transversely mounted LVDTs. These techniques demonstrated that the prebuckled shape of the cylinder often differed dramatically from the postbuckled shape although the prebuckled deformations were very small.

One of the most influential effects on the compressive performance of filament-wound cylinders is the scale of the structure. Specimens examined in this study had a nominal length-to-radius ratio of 3 and radius-to-thickness ratios of 160, 86, 60, and 18. Single-layered specimens with radius-to-thickness ratios of 160 and 60 exhibited very stable postbuckling behavior. Less stable behavior was observed for specimens with radius-to-thickness ratios of 86. Multi-layered specimens with radius-to-thickness ratios of 60 failed by buckling induced fracture. Filament-wound cylinders with radius-to-thickness ratios of 18 did not exhibit buckling instabilities; rather, these specimens failed because the strength of the material was exceeded.

Multiple buckling of specimens which exhibit a stable postbuckling behavior cause changes in the compressive response of filament-wound cylinders. The first cycle results in the most acoustic emission and the largest buckling load, stiffness, and end-shortening displacement at buckling. During the next several cycles, the mechanical performance is degraded by an amount which depends on the degree of postbuckling induced damage. After the first few cycles, no further degradation in performance is observed. Greatly reduced acoustic emission activity also indicates cessation of the damage induced by buckling.

The effects of extension-bending coupling were investigated with the use of symmetric and antisymmetric cylinders wound with ±30° layers. Compared to classical laminated-shell stability theories, a degradation of 10 percent of the compressive buckling load was caused by initial geometric imperfections and non-membrane prebuckling deformations; an additional 10 percent degradation can be attributed to the material coupling behavior. The sequence of the wound layers also affects the compressive performance through a combination of prebuckling deformation, geometric imperfection sensitivity, and extent of damage.

The placement of crossover bands through the thickness of a filament-wound cylinder can dramatically affect its compressive performance. By changing the location of the crossover bands, either by altering the position of each layer or by changing the crossover-band spacing, the winding sequence can be changed from antisymmetric everywhere in the case of stacked crossover bands, to combinations of symmetric and antisymmetric with the other winding patterns. The buckling load was increased by 20 percent simply by changing the winding pattern from one containing stacked crossover bands to a configuration consisting of wide and narrow crossover-band spacings. The location of final fracture is also influenced by the through-the-thickness crossover-band spacing. Stacked configurations fracture directly on top of a circumferential-crossover band while alternating the crossover bands require the fracture to propagate between the bands, thereby increasing the crack length.

Elevated-temperature winding can improve the compressive response of filament-wound cylinders produced with prepreg tows. The reduced void content was responsible for a lack of prebuckling damage observed acoustically. Improvements in the accuracy of the classical laminated-shell theories were also observed and were probably caused by improvements in the material properties.

When the experimentally determined failure loads were compared to classical buckling theories and the Tsai-Wu failure criterion, the compressive failure mode was accurately determined. When the predicted buckling load is much smaller than the predicted strength, the cylinder will buckle and postbuckle in a stable fashion with little damage. As the difference between the predictions becomes smaller, the amount of damage associated with buckling becomes larger until postbuckling deformations are no longer visible and the cylinder fractures at the buckling load. The amount of damage induced during buckling is dependent on the winding sequence. When the predicted buckling load exceeds the ultimate strength, then the cylinders fail in compression without buckling.

Finite element models of the cylinders are used to study the effect of material property definition and residual strains on the accuracy of buckling prediction. The finite element models which use the stiffness material properties derived using classical lamination theory show better agreement with experimental results than when stiffness coupling and discontinuous material distribution in the materials are used in the simple eigenvalue buckling analysis. Sophistication levels in the material property definition do not seem to have much impact on the buckling load provided by an eigenvalue analysis. However, the sophistication in the material definition in the filament-wound cylinder model will gain significance in geometrically nonlinear large displacement analyses. The simple eigenvalue buckling analysis of a geometrically perfect filament-wound cylinder overpredicted the buckling load by about 175 percent of the value observed experimentally. However, when imperfections in the cylinders due to residual strains are included in the model for the buckling analysis, the predicted buckling load is within 5 percent of the experimentally observed value. This demonstrates the of the buckling analysis is relatively more sensitive to geometric imperfections than material coupling in the fiber undulation regions.

PRECEDING PAGE BLANK NOT FILMED

## 10.0 RECOMMENDATIONS FOR FUTURE WORK

Modifications are recommended to the experimental procedures to improve the measurement of geometric imperfections prior to loading. A device which incorporates stepper motors and linear bearings to accurately position the LVDT, similar to the one developed by Tennyson, Muggeridge, and Caswell [34], would allow improved accuracy of the initial geometric imperfection measurements. This system could also be fabricated to measure the prebuckling and postbuckling deformations on the outside surface of the cylinder while it is loaded, similar to the work performed by Yamaki [35] with isotropic cylinders. Additional techniques might be used to characterize the out-of-plane displacements in the prebuckling and postbuckling regimes including: multiple stationary LVDTs, moiré techniques similar to Krishnakumar and Foster [36], and holography. Experimental investigations of cylinders with different length-to-radius and radius-to-thickness ratios would yield additional insight into the phenomenon of scaling.

Further development of the analytical methods would yield important insight into the influence of initial geometric imperfections and non-membrane prebuckling behavior. Further correlation with carefully documented experiments is needed to validate future analytical studies. Any future analysis should include prebuckling deformations, geometric imperfections of the type actually observed in filament-wound cylinders, and the actual properties of the material within the crossover bands. A strength analysis coupled to the stability analysis could provide important insight into the failure progression of filament-wound cylinders when the buckling and compressive failure loads are similar.

The present results from the finite element analysis of the filament wound cylinders hint at their complex nonlinear response to applied loads. A significant amount of research has to be done in order to gain more confidence in predicting the structural response of these structures. In particular, the finite element modeling technique should be verified for various configurations of filament-wound cylinders, the variables being the winding sequence, the winding patterns, and dimensions. A robust structural response prediction capability can be used to further explore scaling effects and design optimization of these structures. The sophistication in defining material properties did not prove to be very significant in improving the accuracy of the eigenvalue buckling prediction of a perfect filament-wound cylinder. However, in the case of large deformation analysis, where the deformation state of the filament-wound cylinder at any instant of time is dependent on the previous state, the sophistication in the material definition might prove to be very significant. The effect of accuracy in material description in the case of nonlinear large deformation analysis has to be explored. Finally, the effects of residual thermal deformations and imperfections introduced during the manufacture should be quantified and incorporated into the finite element analysis for a more accurate prediction of the structural response of a filament-wound cylinder in compression.

PAGE 162 INTENTIONALLY BLANK

PRECEDING PAGE BLANK NOT FILMED

# 11.0 BIBLIOGRAPHY

## 11.1 Cited References

1. Singer, J., "Buckling Experiments on Shells -- A Review of Recent Developments," *Solid Mechanics Archives*, Vol. 7, 1982, pp. 213-313.

2. Tennyson, R.C., "Buckling of Laminated Composite Cylinders: A Review," *Composites*, Vol. 6, No. 1, Jan. 1975, pp. 17-24.

3. Tennyson, R.C., and Muggeridge, D.B., "Buckling of Laminated Anisotropic Imperfect Circular Cylinders under Axial Compression," *Journal of Spacecraft* , Vol. 10, No. 2, Feb. 1973, pp. 143-148.

4. Booton, M., and Tennyson, R.C., "Buckling of Imperfect Anisotropic Circular Cylinders under Combined Loading," *AIAA Journal*, Vol. 17, No. 3, March 1979, pp. 278-287.

5. Abu-Farsakh, G.A.F.R., and Lusher, J.K., "Buckling of Glass-Reinforced Plastic Cylindrical Shells under Combined Axial Compression and External Pressure," *AIAA Journal*, Vol. 23, No. 12, Dec. 1985, pp. 1946-1951.

6. Card, M.F., "Experiments to Determine the Strength of Filament-Wound Cylinders Loaded in Axial Compression," NASA TN D-3522, Aug. 1966.

7. Tasi, J., Feldman, A., and Stang, D.A., "The Buckling Strength of Filament-Wound Cylinders Under Axial Compression," NASA CR-266, 1965.

8. Boresi, A.P., Langhaar, H.L., and Miller, R.E., "Buckling of Axially-Compressed Bilayered Fiber-Reinforced Elastic Cylindrical Shell," *Developments in Theoretical and Applied Mechanics*, Vol. 2, Proceedings of the Second Southeastern Conference on Theoretical and Applied Mechanics, Atlanta, GA, W.A. Shaw ed., March 5-6, 1964, pp. 95-115.

9. Brito, F.M., "Influence of Interwoven Configuration on Mechanical Properties of Crossed Helicoidal Filament Winding Composites," Proceedings of the 6th International Conference on Composite Materials and 2nd European Conference on Composite Materials, Imperial College of Science and Technology, London, Matthews, Buskell, Hodgkinson, and Morton, J. eds., July 20-24, 1987, pp. 1.183-1.189

10. Hipp, P.A., and Jensen, D.W., "Design and Analysis of Filament-Wound Cylinders in Compression," Proceedings of the AIAA/ASME/ASCE/AHS/ASC 33rd Structures, Structural Dynamics and Materials Conference, Dallas, April 1992, pp. 2442-2452.

11. Jensen, D.W., and Pai, S.P., "Theoretical Sensitivity of Composite Cylinders in Compression to Filament-Winding Pattern," Proceedings of the 9th International Conference on Composite Materials, Madrid, A. Miravete ed., July 12-16, 1993, pp. 447-454.

12. Jensen, D.W., and Pickenheim, T.R., "Compressive Behavior of Undulations in Filament-Wound Composites," Proceedings of the AIAA/ASME/ASCE/AHS/ASC 34th Structures, Structural Dynamics and Materials Conference, La Jolla, CA, AIAA-93-1516-CP, April 1993, pp. 1796-1806.

13. Fedro, M., "Development of a Filament-Winding Process for Graphite/PPS Hybrid Yarn Composites," Masters Thesis, The Pennsylvania State University, Aug. 1989.

14. Hipp, P.A., "Influence of Intrinsic Imperfections on the Compression of Filament-Wound Cylinders," Masters Thesis, The Pennsylvania State University, Dec. 1991.

15. Chou, T.-W. and Ishikawa, T., "Analysis and Modeling of 2Dimensional Fabric Composites," Textile Structural Composites, Chou, T.-W. and Ko, F., Eds., Elsevier Science Publishing Co., New York, 1989, pp. 209-264.

16. Jensen, D. W. and Hipp, P. A., "Defect Sensitivity of Filament-Wound Structures in Compression," Development in Theoretical and Applied Mechanics, Hanagud, S. V., Kamat, M. P., and Ueng, C. E., Eds, Vol. XV, March 1990, pp. 669-676.

17. Jensen, D.W. and Pai, S.P., "Influence of Fiber Undulations on the Buckling Behavior of Filament-Wound Cylinders," Proceedings of the 7th Technical Conference on Composite Materials, American Society for Composites, University Park, PA, October 13-15, 1992, pp. 672-681.

18. Compositrak Programming/Operator Manual, McClean Anderson, Jan. 1987.

19. Claus, S.J., Hahn, H.T., and Jensen, D.W., "Experimental Test Results and Analytical Models of Thin Filament-Wound Cylinders," Composites Manufacturing Technology Center Report No. 9401, Jan. 1994.

20. Hahn, H.T., Jensen, D.W., Claus, S.J., and Hipp, P.A., "Structural Design Criteria for Filament-Wound Composite Shells--Annual Report," Composites Manufacturing Technology Center Report No. 9009, May 1990.

21. Standard Test Method for Fiber Content of Resin-Matrix Composites by Matrix Digestion, ASTM D 3171-76, Annual Book of ASTM Standards, Vol. 08.01, pp. 123-125.

22. Chryssanthopoulos, M.K., Giavotto, V., and Poggi, C., "Statistical Imperfection Models for Buckling Analysis of Composite Shells," Buckling of Shell Structures, on Land, in the Sea, and in the Air, A Collection of Papers Presented at the International Colloquium on Buckling of Shell Structures, on Land, in the Sea, and in the Air, Lyon, J.F. Jullien ed., Sept. 17-19, 1991, pp. 43-51.

23. Locan AT User's Manual, Rev. 1.0, Physical Acoustics Corporation, Princeton, 1988.

24. Pollock, A.A., *Practical Guide to Acoustic Emission Testing*, in Locan AT User's Manual, Rev. 1.0, Physical Acoustics Corporation, Princeton, 1988.

25. Kapania, R.K., “Analysis of Laminated Shells,” Recent Advances in the Macro- and Micro-Mechanics of Composite Material Structures, Winter Annual Meeting of the American Society of Mechanical Engineers, Chicago, IL, Nov. 27-Dec. 2, 1988, pp. 177-187.

26. Cheng, S., and Hou, B.P.C., "Stability of Heterogeneous Aeolotropic Cylindrical Shells under Combined Loading," *AIAA Journal*, Vol. 1, No. 4, April 1963, pp. 892-898.

27. Hou, B.P.C., and Cheng, S., “Some Problems in Stability of Heterogeneous Aeolotropic Cylindrical Shells under Combined Loading,” *AIAA Journal*, Vol. 1, No. 7, July 1963, pp. 1603-1607.

28. Press, W.H., Numerical Recipes, The Art of Scientific Computing, Cambridge University Press, 1989.

29. Tennyson, R.C., Chan, K.H., and Muggeridge, D.B., “The Effect of Axisymmetric Shape Imperfections on the Buckling of Laminated Circular Cylinders,” *C.A.S.I. Transactions*, Vol. 4, No. 2, Sept. 1971, pp. 131-139

30. Simitses, G.J., Shaw, D., and Sheinman, I., “Imperfection Sensitivity of Laminated Cylindrical Shells in Torsion and Axial Compression,” *Composite Structures*, Vol. 4, 1985, pp. 335-360.

31. Sheinman, I., Shaw, D., and Simitses, G.J., “Nonlinear Analysis of Axially-Loaded Laminated Cylindrical Shells,” *Computers and Structures*, Vol. 16, No. 1-4, 1983, pp. 131-137.

32. Tennyson, R.C., Muggeridge, D.B., and Caswell, R.D., "New Design Criteria for Predicting Buckling of Cylindrical Shells under Axial Compression," *Journal of Spacecraft*, Vol. 8, No. 10, Oct. 1971, pp. 1062-1067.

33. ABAQUS User's Manual, Version 4-8, Hibbit-Karlson-Sorensen Inc., 1990.

34. Tennyson, R.C., Muggeridge, D.B., and Caswell, R.D., "Buckling of Circular Cylindrical Shells Having Axisymmetric Imperfection Distributions," *AIAA Journal*, Vol. 9, No. 5, May 1971, pp. 924-930.

35. N. Yamaki, Elastic Stability of Circular Cylindrical Shells, Elsevier Science Publishers B.V., Amsterdam, 1984.

36. Krishnakumar, S., and Foster, C.G., "Buckling of Axially Compressed Cylindrical Shells with Local Geometric Imperfections," Buckling of Shell Structures, on Land, in the Sea, and in the Air, A Collection of Papers Presented at the International Colloquium on Buckling of Shell Structures, on Land, in the Sea, and in the Air, Lyon, J.F. Jullien ed., Sept. 17-19, 1991, pp. 33-42.

## 11.2 Summary of Relevant Publications

The following citations are based on research performed at the Composites Manufacturing Technology Center at The Pennsylvania State University under NASA grant NAG1-982.

### 11.2.1 Journal Papers

- Claus, S.J. and Hahn, H.T., "Manufacture-Quality-Performance Relationships for Filament-Wound Cylinders. Part I: Manufacturing Procedures," *Composites Manufacturing*, (submitted for review).
- Claus, S.J. and Hahn, H.T., "Manufacture-Quality-Performance Relationships for Filament-Wound Cylinders. Part II: Quality Assessment," *Composites Manufacturing*, (submitted for review).
- Claus, S.J. and Hahn, H.T., "Manufacture-Quality-Performance Relationships for Filament-Wound Cylinders. Part III: Compressive Performance," *Composites Manufacturing*, (submitted for review).
- Claus, S.J. and Hahn, H.T., "Manufacture-Quality-Performance Relationships for Filament-Wound Cylinders. Part IV: Analytical Predictions," *Composites Manufacturing*, (submitted for review).
- Jensen, D.W. and Pai, S.P., "Influence of Local Fiber Undulations on the Global Buckling of Filament-Wound Cylinders," *Journal of Reinforced Plastics and Composites*, Vol. 12, No. 8, 1993, pp. 865-875.
- Hipp, P.A. and Jensen, D.W., "Design and Analysis of Filament-Wound Cylinders in Compression," *AIAA Journal*, (submitted for review).

### 11.2.2 Conference Papers

- Hahn, H.T. and Claus, S.J., "Improved Manufacturing Techniques for Thin Filament-Wound Cylinders," Ninth International Conference on Composite Materials, Madrid - Spain, July 12-16, 1993, pp. 409-416.
- Jensen, D.W. and Pai, S.P., "Theoretical Sensitivity of Composite Cylinders in Compression to Filament-Winding Pattern," Ninth International Conference on Composite Materials, Madrid - Spain, July 12-16, 1993, pp. 447-454.
- Jensen, D.W. and Pickenheim, T.R., "Compressive Behavior of Undulations in Filament-Wound Composites," AIAA/ASME/ASCE/AHS/ASC 34th Structures, Structural Dynamics and Materials Conference, La Jolla, AIAA-93-1516-CP, April 1993, pp. 1796-1806.
- Pai, S.P., Claus, S.J., and Jensen, D.W., "Detecting Buckling in Filament-Wound Cylinders using Embedded Optical Fibers," SPIE's 1993 North American Conference on Smart Structures and Materials, Albuquerque, NM, February 1-4, 1993, pp. 118-126.

- Jensen, D.W. and Pai, S.P., "Influence of Fiber Undulations on the Buckling Behavior of Filament-Wound Cylinders," The 7th Technical Conference on Composite Materials, American Society for Composites, University Park, PA, October 13-15, 1992, pp. 672-681.
- Claus, S.J., "The Effects of Winding Pattern on the Compressive Behavior of Filament-Wound Cylinders," The 7th Technical Conference on Composite Materials, American Society for Composites, University Park, PA, October 13-15, 1992, pp. 258-265.
- Hipp, P.A. and Jensen, D.W., "Design and Analysis of Filament-Wound Cylinders in Compression," AIAA/ASME/ASCE/AHS/ASC 33th Structures, Structural Dynamics and Materials Conference, Dallas, April 1992, pp. 2442-2452.
- Claus, S.J. and Hahn, H.T., "Processing-Structure Relationships for Filament-Wound Composite Shells," The 6th Technical Conference on Composite Materials, American Society for Composites, Albany, NY, October 6-9, 1991, pp. 863-872.
- Jensen, D.W. and Hipp, P.A., "Compressive Testing of Filament-Wound Cylinders," Eighth International Conference on Composite Materials, Honolulu, July 1991, pp. 35-F-1 to 35-F-9.
- Jensen, D.W. and Hipp, P.A., "Design Considerations for Large-Scale Filament Wound Composite Structures," ASCE Engineering Mechanics Specialty Conference on Mechanics Computing in 1990's and Beyond, Columbus, May 1991, pp. 954-960.
- Jensen, D.W. and Hipp, P.A., "Defect Sensitivity of Filament-Wound Structures in Compression," Developments in Theoretical and Applied Mechanics, Vol. XV, Hanagud, Kamat, and Ueng eds., March 1990, pp. 669-676.

### 11.2.1 Theses

- Claus, S.J., "Manufacture-Structure-Performance Relationships for Filament-Wound Composite Shells," *Ph.D. Thesis*, The Pennsylvania State University, May 1994.
- Pickenheim, T.R., "Influence of Fiber Undulations on the Compressive Behavior of Filament-Wound Composites," *M.S. Thesis*, The Pennsylvania State University, Dec. 1993.
- Hipp, P.A., "Influence of Intrinsic Imperfections on the Compression of Filament-Wound Cylinders," *M.S. Thesis*, The Pennsylvania State University, Dec. 1991.
- Pai, S.P., "Measurement of Complex Strains in Filament-Wound Cylinders Using Embedded Fiber-Optic Sensors," *Ph.D. Thesis*, The Pennsylvania State University, In progress.